



<https://theses.gla.ac.uk/>

Theses Digitisation:

<https://www.gla.ac.uk/myglasgow/research/enlighten/theses/digitisation/>

This is a digitised version of the original print thesis.

Copyright and moral rights for this work are retained by the author

A copy can be downloaded for personal non-commercial research or study, without prior permission or charge

This work cannot be reproduced or quoted extensively from without first obtaining permission in writing from the author

The content must not be changed in any way or sold commercially in any format or medium without the formal permission of the author

When referring to this work, full bibliographic details including the author, title, awarding institution and date of the thesis must be given

Enlighten: Theses

<https://theses.gla.ac.uk/>  
[research-enlighten@glasgow.ac.uk](mailto:research-enlighten@glasgow.ac.uk)

**The Investigation of  
Blade-Vortex Interaction Noise  
Using Computational Fluid Dynamics  
by  
Romuald Morvant M.Eng.**

Thesis submitted to the Faculty of Engineering,  
University of Glasgow, for the Degree of Doctor of Philosophy  
Department of Aerospace Engineering  
University of Glasgow  
February 2004

© 2004  
Romuald Morvant

ProQuest Number: 10390656

All rights reserved

INFORMATION TO ALL USERS

The quality of this reproduction is dependent upon the quality of the copy submitted.

In the unlikely event that the author did not send a complete manuscript and there are missing pages, these will be noted. Also, if material had to be removed, a note will indicate the deletion.



ProQuest 10390656

Published by ProQuest LLC (2017). Copyright of the Dissertation is held by the Author.

All rights reserved.

This work is protected against unauthorized copying under Title 17, United States Code  
Microform Edition © ProQuest LLC.

ProQuest LLC.  
789 East Eisenhower Parkway  
P.O. Box 1346  
Ann Arbor, MI 48106 – 1346

GLASGOW  
UNIVERSITY  
LIBRARY:

13402

COPY 2

# Declaration

The author hereby declares that this dissertation is a record of work carried out in the Department of Aerospace Engineering at the University of Glasgow during the period from October 2000 to October 2003. The dissertation is original in content except where otherwise indicated.

February 2004

Romuald Morvant

# Abstract

This thesis presents the development and validation of numerical methods for the study of Blade-Vortex Interaction. Aspects addressed in this work include the aerodynamics and aeroacoustics of the interaction between a vortex and an aerofoil.

The phenomenon of Blade-Vortex Interaction (BVI) is central to the study of the aerodynamics of rotors as well as to the calculation of the acoustic field radiated by rotorcraft. The simulation of BVI is challenging since the solution scheme tends to alter the characteristics of the vortex which must be preserved until the interaction. The basis of the present thesis has been the code developed at the University of Glasgow. Some numerical improvements have been carried out to allow the simulation of BVI. First, the numerical developments concerned the time discretisation with the comparison of two different implicit schemes for their robustness and reliability. The implementation of an implicit unfactored method allowed better results in terms of convergence. Secondly, the Compressible Vorticity Confinement Method (CVCM) has been implemented into the solver to allow the preservation of vortical flows. The CVCM has been tested and validated on a benchmark problem for the case of vortex convection. The use of the CVCM was found to be capable of preserving the vortex characteristics assuming the optimum confinement parameter was chosen for a given grid. Hence the use of the CVCM made the simulation of BVI possible.

The capabilities of the CVCM were assessed with the simulation of head-on and miss-distance BVI cases. Results were compared against experimental surface pressure measurements and flow visualisation data. Good agreement was obtained. It appears that the CVCM is useful for preserving the characteristics of vortices on coarse grids. The use of the CVCM was not required for grid which were /fine enough and/or for weak vortices.

Inviscid and viscous calculations have been carried out for a well-known head-on two-dimensional BVI case. The influence of the vortex model, CVCM parameter, initial vortex location, spatial and time refinement, angle of attack and turbulence models has been assessed. The results obtained using the CVCM show a good agreement with the measurements. It was found that the BVI loads history could be well predicted for a vortex introduced at 1.5 chords ahead of the aerofoil whereas an acoustic study requires a vortex introduced at a least 4.5 chords ahead of the aerofoil for potential-like flow.

A parametric study was then conducted to highlight the importance of the aerofoil shape, freestream Mach number, vortex radius core, vortex circulation and miss-distance. The BVI aerodynamics were studied showing that BVI is primarily a leading-

edge phenomenon characterised by the oscillation of the stagnation point. The vortex-induced velocity modifies the apparent angle of attack of the aerofoil and influences the BVI response, especially for increased vortex strength or at larger freestream Mach numbers.

The acoustics of BVI were also investigated. The present work coupled CFD with Computational AeroAcoustics (CAA) and used the strength of both techniques in order to predict the nearfield and farfield noise. The nearfield acoustics were calculated and it was observed that the aerofoil shape and the vortex properties do influence the magnitude of the BVI noise. Three different acoustic mechanisms contribute to the acoustic signature of the BVI noise. The compressibility waves which propagate upstream below and above the aerofoil are generated due to the large flow deflection at the leading-edge of the aerofoil. They were found to dominate the overall noise in subsonic flow. The trailing-edge (TE) noise which originates from the passage of the vortex near the TE of the aerofoil was also present for both types of flow. The TE waves propagate upstream and were found to be of second order in terms of noise magnitude for the studied BVI cases. Another acoustical wave called the transonic wave appeared when a supersonic pocket was generated on the lower side of the aerofoil. It was found that this wave propagates upstream in a downward inclined direction and that it can be stronger than the compressibility wave. The directivity patterns of these waves was strongly influenced by the presence of the shocks which may modify the trajectory of the waves depending on their initial locations and by the loading of the aerofoil.

The Ffowcs Williams-Hawkings (FW-H) aeroacoustics method was used to predict the farfield noise. This method was preferred to the Kirchhoff method, which requires a very-accurate midfield acoustics prediction since the computed nearfield acoustics were found to dissipate relatively quickly. The FW-H module which used the BVI loads provided by CFD was first tested on a benchmark problem. Good agreement with the experiments was obtained.

The farfield noise was then computed for an observer located in front of and below the rotorcraft for all the different BVI configurations. The location of the observer was chosen carefully in order to be representative of the noise radiated by the compressibility wave into the farfield. The BVI noise levels of the compressibility wave were compared and the BVI directivity assessed. As for the nearfield acoustics study, the LE radius was found to be an important parameter in transonic flow. It was shown that the BVI noise intensity is a function of the freestream Mach number. The compressibility waves can be assimilated as dipole type sources as long as the transonic wave, if present, is negligible. Regarding the effects of the vortex properties, the relationship between the Sound Pressure Level (SPL) and the studied parameters were highlighted. The vortex strength was found to affect the BVI noise magnitude, the SPL decay rate decreasing for stronger vortices. The parametric study also showed the linear dependence of the BVI strength on the miss-distance when the miss-distance is greater than the vortex core radius. The vortex core radius was found to affect the BVI noise for both head-on and miss-distance BVI cases, the SPL decay rate increasing with larger core radii.

For the BVI directivity patterns, the size of the lobes of the radiated noise increases with the vortex core radius and the miss-distance. The compressibility effects which mainly depend on the freestream Mach number and the vortex strength were found

to delay the BVI and to change therefore its directivity. The loading induced by a cambered aerofoil and/or by the presence of asymmetrical shocks before the interaction was found to offset the values of the BVI loads, leading to BVI noise radiated at a different azimuthal position.

# Acknowledgements

I would like to thank my supervisor Dr. K.J. Badcock for providing me his guidance throughout the project and for allowing me to work in excellent conditions.

I would like to express my sincere gratitude to Dr. G.N. Barakos for his relentless enthusiasm and encouragements. His advices and help have been greatly appreciated.

It has been a pleasure to carry out my research in the CFD group and I would like to thank Prof. B.E. Richards for his major contribution to this stimulating environment.

I would also like to gratefully acknowledge the financial support of Westland Helicopter Limited and of the University of Glasgow.

Finally, I would like to thank my parents, Charles and Marie-Reine, for their support and the researchers in the CFD group, especially David and Punit, for being very helpful in many circumstances.

# Publications

## Conference papers

R. Morvant, K.J. Badcock and B.E. Richards. Comparison Between Two Time-Stepping Methods in an Euler Code for Helicopter Rotors. *Royal Aeronautical Society, Cambridge, England, June 2002.*

R. Morvant, K.J. Badcock, G.N. Barakos and B.E. Richards. Aerofoil-Vortex Interaction Simulation Using the Compressible Vorticity Confinement Method. *29<sup>th</sup> European Rotorcraft Forum, Friedrichshafen, Germany, Session 3, September 2003.*

R. Morvant, K.J. Badcock, G.N. Barakos and B.E. Richards. Study of Blade/Vortex Interaction Using Computational Fluid Dynamics and Computational Aeroacoustics. *American Helicopter Society, USA, San Francisco, January 2004.*

## Journal papers

R. Morvant, K.J. Badcock, G.N. Barakos and B.E. Richards. Aerofoil-Vortex Interaction Simulation Using the Compressible Vorticity Confinement Method. *Under revision for AIAA Journal.*

## Internal reports

G.N. Barakos and R. Morvant. An Efficient Approximate Method for Calculating Farfield BVI Noise. *Aerospace Engineering Report 0401, University of Glasgow, UK.*

# Contents

<b>1</b>	<b>Introduction</b>	<b>1</b>
1.1	Overview	1
1.2	Description of the rotorcraft flowfield	1
1.3	Rotorcraft noise sources	3
1.3.1	Noise characteristics of a rotorcraft	3
1.3.2	Blade-vortex interaction	7
1.3.3	BVI noise alleviation	10
1.4	Techniques to predict BVI aerodynamics	11
1.4.1	Experimental BVI Studies	11
	2D measurements	11
	3D measurements	12
1.4.2	Development of semi-empirical formula	12
1.4.3	Numerical simulation of BVI	14
1.5	Techniques to Predict BVI aeroacoustics	15
1.6	Scope of the study	16
<b>2</b>	<b>Mathematical models</b>	<b>18</b>
2.1	Introduction	18
2.2	The CFD solver	20
2.2.1	Model equations of the Euler code	20
2.2.2	The numerical schemes	20
	The finite volume method	20
	The spatial discretisation schemes	20
	The implicit dual-time method	21
	The implicit time-marching method	21
2.2.3	Navier-Stokes equations and turbulence models	22
	Governing equations and principles	22
	The Spalart-Allmaras turbulence model	24
	The $k-\omega$ turbulence model	25
	The Shear Stress Transport (SST) turbulence model	26
	The $Pk$ limiter turbulence model	28
2.3	The Aeroacoustical approach	28
2.3.1	Lighthill's acoustic analogy	28
2.3.2	Lighthill's formulation	29
2.3.3	Description of the types of noise sources	29
2.3.4	Review of the existing techniques	30
2.4	Conclusions	33

<b>3</b>	<b>Validation of CFD tools</b>	<b>34</b>
3.1	Introduction . . . . .	34
3.2	Evaluation of implicit schemes . . . . .	35
3.2.1	Description of the test cases . . . . .	35
3.2.2	Comparison between the UNFACTored and FUN methods . . . . .	35
	The Lann wing . . . . .	36
	The 7A model rotor in transonic hover non-lifting . . . . .	40
3.3	The Compressible Vorticity Confinement Method . . . . .	43
3.3.1	Principle of the VCM . . . . .	43
3.3.2	Compressibility modifications . . . . .	43
3.3.3	Implementation . . . . .	44
3.3.4	Modifications to the basic method . . . . .	44
3.3.5	Evaluation of the CVCM on a vortex convection test case . . . . .	45
3.4	Capabilities of the CVCM for flow simulation . . . . .	51
3.4.1	Characteristics and behaviour of the CVCM for the BVI simulation . . . . .	51
3.4.2	Blade-vortex interaction . . . . .	52
	Case 1 . . . . .	52
	Case 2 . . . . .	58
	Case 3 . . . . .	60
	Case 4 . . . . .	64
3.5	Conclusions . . . . .	70
<b>4</b>	<b>Optimisation of the BVI simulation</b>	<b>71</b>
4.1	Introduction . . . . .	71
4.2	Optimisation of the BVI Simulation using the CVCM . . . . .	71
4.2.1	Influence of the vortex models . . . . .	73
4.2.2	Influence of the CVCM . . . . .	81
4.2.3	Influence of the initial vortex location . . . . .	84
4.2.4	Influence of the spatial refinement . . . . .	85
4.2.5	Influence of the time refinement . . . . .	90
4.2.6	Influence of the angle of attack . . . . .	93
4.2.7	Influence of the turbulence models . . . . .	95
4.3	Conclusions . . . . .	104
<b>5</b>	<b>Parametric study of BVI aerodynamics</b>	<b>105</b>
5.1	Introduction . . . . .	105
5.2	Aerodynamics . . . . .	108
5.2.1	Influence of the aerofoil shape . . . . .	109
5.2.2	Influence of the freestream Mach number . . . . .	120
5.2.3	Influence of the vortex properties . . . . .	123
	Vortex core radius . . . . .	123
	Vortex strength . . . . .	129
	Miss-distance . . . . .	133
5.3	Conclusions . . . . .	138
<b>6</b>	<b>Parametric study of BVI aeroacoustics</b>	<b>139</b>
6.1	Introduction . . . . .	139
6.2	Parametric study of the nearfield noise . . . . .	139
6.2.1	Influence of the aerofoil shape . . . . .	140

6.2.2	Influence of the freestream Mach number . . . . .	156
6.2.3	Influence of the vortex properties . . . . .	157
	Vortex core radius . . . . .	157
	Vortex strength . . . . .	159
	Miss-distance . . . . .	162
6.3	Capabilities of the aeroacoustic module . . . . .	166
6.3.1	Coupling between CFD and the FW-H module . . . . .	166
6.3.2	Validation test . . . . .	167
6.4	Parametric study of the farfield noise . . . . .	170
6.4.1	Description of the rotor flight conditions . . . . .	170
6.4.2	Influence of the aerofoil shape . . . . .	172
6.4.3	Influence of the freestream Mach number . . . . .	177
6.4.4	Influence of the vortex properties . . . . .	179
	Vortex core radius . . . . .	179
	Vortex strength . . . . .	181
	Miss-distance . . . . .	182
6.5	Conclusions . . . . .	185
<b>7</b>	<b>Conclusions</b> . . . . .	<b>186</b>
7.1	Achievements . . . . .	186
7.2	Further work . . . . .	188
	<b>References</b> . . . . .	<b>190</b>

# List of Figures

1.1	Schematic of the rotorcraft elements influencing the aerodynamics (Brentner and Farassat [1]). . . . .	2
1.2	Schematic of the wake of a rotorcraft [2]. . . . .	3
1.3	Aeroacoustic noise sources for a rotorcraft (Edwards and Cox [3]). . . . .	4
1.4	Typical acoustical signature of BVI and HSI. . . . .	5
1.5	Sound Pressure Levels Spectrum of the rotational noise sources for a rotorcraft (Leverton [4]). . . . .	6
1.6	Directivity of the different components of the rotational noise [3]. . . . .	6
1.7	(a) Wake of the helicopter encountering the main rotor and creating BVI [5]. (b) Flight conditions likely to create BVI [6]. . . . .	7
1.8	(a) Locations of the BVI. (b) Differences between BVI on the advancing and retreating sides (Schmitz [6, 7]). . . . .	8
1.9	Creation of the blade-vortex interaction noise [1]. . . . .	9
1.10	Typical directivity of the sound for the BVI of a helicopter in descending flight [8]. . . . .	9
3.1	Grid used for the Lann case. The wing is represented in red colour. . . . .	36
3.2	Sectional normal force coefficient for the Lann wing. . . . .	37
3.3	Sectional chordwise force coefficient for the Lann wing. . . . .	37
3.4	Sectional pitching moment coefficient for the Lann wing. . . . .	37
3.5	Mean steady pressure for the Lann wing. . . . .	38
3.6	Real part of the 1 <sup>st</sup> harmonic pressure for the Lann wing. . . . .	38
3.7	Imaginary part of the 1 <sup>st</sup> harmonic pressure for the Lann wing. . . . .	38
3.8	Convergence histories for the steady preliminary run. . . . .	39
3.9	Convergence histories for the unsteady Lann wing case. . . . .	39
3.10	Grid used for the 7A-ONERA case. The blade is represented in red colour. . . . .	40
3.11	Convergence histories for the FUN and UNFACTored methods for the 7A hover flight. Coarse grid. . . . .	41
3.12	Pressure coefficient distribution and normal force coefficient for the 7A 4-bladed hover test case. Coarse grid. . . . .	42
3.13	(a) Schematic of the initial conditions of the benchmark problem and (b) time history of the $\omega/\rho$ ratio at the vortex core as predicted using the CVCMM method with or without gradient-based vorticity limiters. . . . .	46
3.14	Contours of the $\omega/\rho$ ratio after 20 cycles: (a) Effects of the artificial dissipation coefficient ( $\mu$ ) and (b) effect of the gradient-based vorticity limiter on the coarse grid. Laminar calculations ( $Re_c = 1000$ ). . . . .	47

3.15	History of the ratio $\omega/\rho$ at the vortex core on the coarse grid for laminar flow. (a) The confinement methods with constant $\epsilon$ and $\epsilon$ scaled with the grid cell are compared for a Reynold number of 1000. (b) Different Reynolds numbers are applied when the $\epsilon$ is scaled with the grid cell. Note that the vorticity gradient limiter is used. . . . .	48
3.16	Time history of the density at the vortex core using the vorticity gradient limiter and the density confinement. Inviscid calculations. . . . .	48
3.17	Contours of the density after 10 cycles for the inviscid calculations. (a) With vorticity gradient limiter. (b) With density confinement. . . . .	49
3.18	Contours of the density after 10 cycles for the inviscid calculations. (a) With vorticity gradient limiter. (b) With density confinement. . . . .	49
3.19	Contours of (a) the density $\rho$ and (b) the $\omega/\rho$ ratio for the initial vortex on the fine grid. (c) Time history of the density at the vortex core using different $\epsilon$ scalings. (d) Evolution of the $\omega/\rho$ ratio after 20 cycles with and without CVCM. Inviscid calculations. . . . .	50
3.20	Block topology of the 2D grid used for the simulation of the head-on BVI, NACA-0012 aerofoil. . . . .	52
3.21	Influence of the initial vortex location on the time history of the surface pressure coefficient. Head-on BVI problem, NACA-0012 aerofoil, viscous calculations, $Re = 1e + 6$ , $M_\infty=0.5$ , $\hat{\Gamma} = -0.283$ , $R_c = 0.018$ . . . . .	53
3.22	Lift and drag histories for head-on BVI with and without confinement. NACA-0012 aerofoil, viscous calculations, $M_\infty=0.5$ , $\hat{\Gamma} = -0.283$ , $R_c = 0.018$ . . . . .	54
3.23	Influence of the density confinement and of the vorticity gradient limiter on the time history of the surface pressure coefficient. Head-on BVI problem, NACA-0012 aerofoil, viscous calculations, $M_\infty=0.5$ , $x/c=0.02$ . The vortex was introduced at 4.5 chords ahead of the aerofoil. Note that $\epsilon$ and $\delta$ are the confinement and the density confinement parameters, respectively. . . . .	55
3.24	Influence of the density confinement and of the vorticity gradient limiter on the time histories of lift and drag. Head-on BVI problem, NACA-0012 aerofoil, viscous calculations, $M_\infty=0.5$ , $x/c=0.02$ . The vortex was introduced at 4.5 chords ahead of the aerofoil. . . . .	56
3.25	Comparison between (a-c) experimental holographic interferograms, (d-f) the density contours for the head-on BVI case and (g-i) the computational density gradient magnitude contours. The vortex was introduced 4.5 chords ahead of the aerofoil and the calculations were performed using the $k-\omega$ model. The time step is non-dimensionalised with the freestream velocity ( $U_\infty$ ) and the aerofoil chord (c). . . . .	57
3.26	Time history of the surface pressure coefficient for (a-b) the head-on and (c-d) miss-distance BVI cases. The vortex was introduced at 4.5 chords ahead of the aerofoil. NACA-0012 aerofoil, viscous calculations ( $k-\omega$ model), $Re = 1e + 6$ , $M_\infty=0.63$ , $\hat{\Gamma} = -0.25$ , $R_c = 0.162$ . . . . .	59
3.27	Time histories of (a) the $\omega/\rho$ ratio at the vortex core and of (b) the lift with and without CVCM. . . . .	59
3.28	Time histories of (a) the density at the vortex core and of (b) the $\omega/\rho$ ratio with and without CVCM. NACA-0012 aerofoil, viscous calculations ( $k-\omega$ model), $Re = 3.6e + 6$ , $M_\infty=0.8$ , $\hat{\Gamma} = -0.2$ , $R_c = 0.05$ , $y_0 = -0.26$ . . . . .	60

3.29	Time histories of the (a) lift and (b) drag with and without CVCM. The vortex was introduced at 5.0 chords ahead of the aerofoil. NACA-0012 aerofoil, viscous calculations ( $k-\omega$ model), $R_e = 3.6e + 6$ , $M_\infty=0.8$ . $\hat{\Gamma} = -0.2$ , $R_c = 0.05$ , $y_0 = -0.26$ . . . . .	61
3.30	Sonic lines at two different times. (a) Before the shock-vortex interaction, (b) after the shock-vortex interaction. NACA-0012 aerofoil, viscous calculations ( $k-\omega$ model), $R_e = 3.6e + 6$ , $M_\infty=0.8$ . $\hat{\Gamma} = -0.2$ , $R_c = 0.05$ , $y_0 = -0.26$ . . . . .	61
3.31	Shock-vortex mechanisms. Note that a weak expansion and compression develop respectively below and above the vortex, that is due to the downwash component of the vortex. Then, after the first half of the vortex passed the shock, the upwash component of the vortex creates similar pressure changes but of opposite signs this time, that is at the origin of the quadrupolar component. . . . .	62
3.32	Contours of pressure gradients streamlines and isomachs at two different times. The vorticity is shown along with the pressure gradient streamlines. NACA-0012 aerofoil, viscous calculations ( $k-\omega$ model), $R_e = 3.6e + 6$ , $M_\infty=0.8$ . $\hat{\Gamma} = -0.2$ , $R_c = 0.05$ , $y_0 = -0.26$ . . . . .	63
3.33	Contours of the absolute value of the acoustic pressure at two different times. NACA-0012 aerofoil, viscous calculations ( $k-\omega$ model), $R_e = 3.6e + 6$ . $M_\infty=0.8$ , $\hat{\Gamma} = -0.2$ , $R_c = 0.05$ , $y_0 = -0.26$ . The scale is exponential. . . . .	63
3.34	Density contours for miss-distance BVI case at four different times. NACA-0012 aerofoil, viscous calculations (SST model), $M_\infty=0.57$ , $\hat{\Gamma} = -1.8$ , $R_c = 0.10$ , $y_0 = -0.31$ . Note that the vortex location in the x-direction was not provided in the experiments (left). Therefore, the computed contours (right) were chosen in order to establish a comparison with the experiments . . . . .	65
3.35	Isobars ( $2p/q_\infty$ ) contours along with the streamlines for different miss-distances at time $t(U_\infty/c) = 4.90$ . Miss-distance BVI problem, NACA-0012 aerofoil, inviscid calculations, $M_\infty=0.57$ , $\hat{\Gamma} = -1.8$ , $y_0 = -0.31$ . . . . .	66
3.36	Total pressure loss at different instants. $t(U_\infty/c)=4.8$ (a-b), 4.9 (c-d), 5.0 (e-f). NACA-0012 aerofoil, head-on and miss-distance BVI problems, inviscid calculations, $M_\infty=0.57$ , $\hat{\Gamma} = -1.8$ . . . . .	66
3.37	Time history of the surface pressure coefficient at different chordwise locations for inviscid and viscous calculations (SST model). Miss-distance BVI problem, NACA-0012 aerofoil, $M_\infty=0.57$ , $\hat{\Gamma} = -1.8$ , $R_c = 0.10$ , $y_0 = -0.31$ . . . . .	67
3.38	Surface pressure coefficient at three different times. $t(U_\infty/c)=4.9$ . Head-on BVI problem, NACA-0012 aerofoil, inviscid and viscous calculations, $M_\infty=0.57$ , $\hat{\Gamma} = -1.8$ , $y_0 = -0.15$ . The horizontal black arrow and the oblique blue arrow indicate respectively the presence of a supersonic pocket and of a vortex. . . . .	68
3.39	Lift and drag histories for inviscid and viscous calculations (SST model), with and without CVCM. Miss-distance BVI problems, NACA-0012 aerofoil, $M_\infty=0.57$ , $\hat{\Gamma} = -1.8$ , $R_c = 0.10$ , $y_0 = -0.31$ . . . . .	69

3.40	Time histories of (a) the density and of (b) the $\omega/\rho$ ratio at the vortex core with and without CVCM. Miss-distance BVI problem, inviscid and viscous calculations (SST model), $\hat{\Gamma} = -1.8$ , $R_c = 0.10$ , $y_0 = -0.31$ . Note that a grid of 160k and 172k points were used for the inviscid and viscous runs, respectively. . . . .	69
4.1	(a) Schematic of the initial configuration of the head-on BVI problem, the initial location of the vortex is shown along with isobars ( $2p/q_\infty$ ) contours. (b) Locations of the pressure taps in the leading-edge region of the aerofoil. The locations correspond to the experiments by Lee and Bershader [9]. . . . .	72
4.2	Tangential velocity and density profile for four different vortex models. Vortex characteristics of the models which have the same density at the vortex core. . . . .	76
4.3	Tangential velocity and density profile for four different vortex models. Vortex characteristics of the models which have the same tangential velocity at the vortex core. . . . .	77
4.4	Surface pressure coefficient history for vortex models introduced initially with the same circulation. Viscous calculations ( $k-\omega$ model), $R_e = 1e+6$ , $M_\infty=0.5$ , $\hat{\Gamma} = -0.283$ , $R_c = 0.018$ . The vortex introduced at 2.5 chords ahead of the aerofoil. . . . .	78
4.5	Lift and drag histories for the Scully and the Vatistas models. The initial vortex has the same strength. Head-on BVI, viscous calculations ( $k-\omega$ model), $R_e = 1e+6$ , $M_\infty=0.5$ , $\hat{\Gamma} = -0.283$ , $R_c = 0.018$ . . . . .	79
4.6	Surface pressure coefficient history at the chordwise location $x/c=0.02$ for vortex models introduced initially with (a-b) the same density, (c-d) the same $\omega/\rho$ ratio and (e-f) the same tangential velocity at the vortex core. Viscous calculations ( $k-\omega$ model), $R_e = 1e+6$ , $M_\infty=0.5$ , $\hat{\Gamma} = -0.283$ , $R_c = 0.018$ . The vortex introduced at 2.5 chords ahead of the aerofoil. Note that no results are presented for the Lamb-like model in Figures c and d since it was not possible to obtain the initial $\omega/\rho$ ratio at the vortex core due to the velocity profile of the model. . . . .	80
4.7	Influence of the value of the confinement parameter $\epsilon$ on the time history of the surface pressure coefficient for inviscid and viscous calculations. The vortex was introduced at 4.5 chords ahead of the aerofoil. Head-on BVI problem, NACA-0012 aerofoil, inviscid calculations, $M_\infty=0.5$ , $\hat{\Gamma} = -0.283$ , $R_c = 0.018$ , $x/c=0.02$ . . . . .	82
4.8	Effect of the $\epsilon$ parameter on the vortex path and on the size of the vortex core for (a, c, e) inviscid and (b, d, f) viscous calculations. Density contours are shown along with streamlines at the same instant $t(U_\infty/c) = 4.0$ . The vortex was introduced 4.5 chords ahead of the aerofoil. Note that the lower value of density corresponds to the density at the vortex core. . . . .	83
4.9	Influence of the initial vortex location on the time history of the surface pressure coefficient. Head-on BVI problem, NACA-0012 aerofoil, inviscid calculations, $M_\infty=0.5$ , $\hat{\Gamma} = -0.283$ , $R_c = 0.018$ , $x/c=0.02$ . . . . .	86
4.10	Influence of the initial vortex location on the time history of the surface pressure coefficient. Head-on BVI problem, NACA-0012 aerofoil, viscous calculations, $M_\infty=0.5$ , $\hat{\Gamma} = -0.283$ , $R_c = 0.018$ , $x/c=0.02$ . . . . .	87

4.11	Influence of the spatial refinement on the time history of the surface pressure coefficient. Head-on BVI problem, NACA-0012 aerofoil, inviscid calculations, $M_\infty=0.5$ , $\hat{\Gamma} = -0.283$ , $R_c = 0.018$ , $x/c=0.02$ . . . . .	88
4.12	Pressure contours on the coarse grid at two different instants. Head-on BVI problem, NACA-0012 aerofoil, inviscid calculations, $M_\infty=0.5$ , $\hat{\Gamma} = -0.283$ , $R_c = 0.018$ , $x/c=0.02$ . Note that the pressure is non-dimensionalised against the dynamic pressure. . . . .	88
4.13	Influence of the spatial refinement on the time history of the surface pressure coefficient. Head-on BVI problem, NACA-0012 aerofoil, viscous calculations, $M_\infty=0.5$ , $\hat{\Gamma} = -0.283$ , $R_c = 0.018$ , $x/c=0.02$ . . . . .	89
4.14	Contours of pressure along with the velocity streamlines and of the turbulent Reynolds number for the $k-\omega$ model on the coarse and fine grid at $t(U_\infty/c)=2.65$ . The vortex was introduced at 2.5 chords ahead of the aerofoil. Head-on BVI problem, NACA-0012 aerofoil, viscous calculations, $M_\infty=0.5$ , $\hat{\Gamma} = -0.283$ , $R_c = 0.018$ . . . . .	90
4.15	Influence of the time refinement on the time history of the surface pressure coefficient for inviscid calculations. Head-on BVI problem, NACA-0012 aerofoil, $M_\infty=0.5$ , $\hat{\Gamma} = -0.283$ , $R_c = 0.018$ . (a-b) $x/c=0.02$ , (c-d) $x/c=0.05$ . The time step $\Delta t$ is non-dimensionalised with the freestream velocity ( $U_\infty$ ) and the aerofoil chord ( $c$ ). . . . .	91
4.16	Influence of the time refinement on the time history of the surface pressure coefficient for viscous calculations ( $k-\omega$ model). Head-on BVI problem, NACA-0012 aerofoil, $M_\infty=0.5$ , $\hat{\Gamma} = -0.283$ , $R_c = 0.018$ , $x/c=0.05$ . The time step $\Delta t$ is non-dimensionalised with the freestream velocity ( $U_\infty$ ) and the aerofoil chord ( $c$ ). . . . .	92
4.17	Influence of the time refinement on the lift histories for (a) the inviscid and (b) viscous calculations. Head-on BVI problem, NACA-0012 aerofoil, $M_\infty=0.5$ , $\hat{\Gamma} = -0.283$ , $R_c = 0.018$ . . . . .	92
4.18	Influence of the angle of attack on the time history of the surface pressure coefficient. Head-on BVI problem, NACA-0012 aerofoil, viscous calculations, $M_\infty=0.5$ , $\hat{\Gamma} = -0.283$ , $R_c = 0.018$ . (a) $x/c=0.02$ , (b) $x/c=0.05$ . . . . .	93
4.19	Influence of the angle of attack on the lift and drag time histories. Head-on BVI problem, NACA-0012 aerofoil, viscous calculations, $M_\infty=0.5$ , $\hat{\Gamma} = -0.283$ , $R_c = 0.018$ . (a) $x/c=0.02$ , (b) $x/c=0.05$ . . . . .	94
4.20	Effect of the angle of attack on the location of the stagnation point. Viscous calculations. Density contours are shown along with streamlines at the same time instant. The dotted red arrow indicates the location of the stagnation point and the plain black arrow shows the secondary vortex. . . . .	94
4.21	(a, c) Contours of the confinement parameter $\epsilon$ and (b, d) the magnitude of the velocity source term $S_{u,v} = (S_u, S_v)$ of the CVCM for a non-dimensionalised time $t(U_\infty/c) = 1.01$ . The grid is uniform along the vortex path. Head-on BVI problem, NACA-0012 aerofoil, viscous calculations, $M_\infty=0.5$ , $\hat{\Gamma} = -0.283$ , $R_c = 0.018$ . Note that no value appears on a horizontal line, the variables being cell-centered for the two blocks present along the vortex path. . . . .	96

4.22	(a, c) Contours of the confinement parameter $\epsilon$ and (b, d) the magnitude of the velocity source term $S_{u,v} = (S_u, S_v)$ of the CVCM for a non-dimensionalised time $t(U_\infty/c) = 2.01$ . The grid is uniform along the vortex path. Head-on BVI problem, NACA-0012 aerofoil, viscous calculations, $M_\infty=0.5$ , $\hat{\Gamma} = -0.283$ , $R_c = 0.018$ . Note that no value appears on a horizontal line, the variables being cell-centered for the two blocks present along the vortex path. . . . .	97
4.23	(a, c) Contours of the confinement parameter $\epsilon$ and (b, d) the magnitude of the velocity source term $S_{u,v} = (S_u, S_v)$ of the CVCM for a non-dimensionalised time $t(U_\infty/c) = 2.51$ . The grid gets refined when the vortex approaches the aerofoil. Head-on BVI problem, NACA-0012 aerofoil, viscous calculations, $M_\infty=0.5$ , $\hat{\Gamma} = -0.283$ , $R_c = 0.018$ , $t(U_\infty/c) = 2.51$ . Note that it can be observed that the CVCM was not applied up to a distance 0.1 chord from the aerofoil. . . . .	98
4.24	Time history of the surface pressure coefficient obtained with various turbulence models. Head-on BVI problem, NACA-0012 aerofoil, viscous calculations, $M_\infty=0.5$ , $\hat{\Gamma} = -0.283$ , $R_c = 0.018$ . . . . .	99
4.25	Contours of the pressure for (a) inviscid and (b) viscous calculations (k- $\omega$ model) at time $t(U_\infty/c) = 2.54$ . Head-on BVI problem, NACA-0012 aerofoil, $M_\infty=0.50$ , $\hat{\Gamma} = -0.283$ , $R_c = 0.018$ . Note that the pressure is non-dimensionalised against the freestream pressure. . . . .	100
4.26	Contours of the normal stress $\tau_{yy}$ along with the velocity streamlines at time $t(U_\infty/c) = 2.51$ for different $\epsilon$ for the SST model. The vortex was introduced at 2.5 chords ahead of the aerofoil. Head-on BVI problem, NACA-0012 aerofoil, $M_\infty=0.5$ , $\hat{\Gamma} = -0.283$ , $R_c = 0.018$ . . . . .	101
4.27	Time history of the surface pressure coefficient obtained with two confinement parameters for the SST model. Head-on BVI problem, NACA-0012 aerofoil, viscous calculations, $M_\infty=0.5$ , $\hat{\Gamma} = -0.283$ , $R_c = 0.018$ . . . . .	101
4.28	Contours of the isobars ( $2p/q_\infty$ ) and the shear stress at time $t(U_\infty/c) = 4.30$ for different $\epsilon$ for the k- $\omega$ model. The vortex was introduced at 4.5 chords ahead of the aerofoil. Head-on BVI problem, NACA-0012 aerofoil, $M_\infty=0.5$ , $\hat{\Gamma} = -0.283$ , $R_c = 0.018$ . . . . .	102
4.29	Time histories of the lift and drag for inviscid and viscous calculations. Different turbulence models have been used. The confinement parameter was set to 1.5 and the vortex was introduced at 2.5 chords ahead of the aerofoil. Head-on BVI problem, NACA-0012 aerofoil, $M_\infty=0.5$ , $\hat{\Gamma} = -0.283$ , $R_c = 0.018$ . . . . .	103
5.1	Schematic of the BVI parametric study. . . . .	106
5.2	Geometry of the different aerofoils. The aerofoils NACA-0012, NACA-0018, SC-1095, NACA-001234 and NACA-16018 are respectively offset by 0.2, 0.4, 0.6, 0.8 and 1.0 for clarity. . . . .	108
5.3	Time history of the surface pressure coefficient at different chordwise locations. Head-on BVI problem, six different aerofoils, viscous calculations, $M_\infty=0.50$ , $\hat{\Gamma} = -0.283$ , $R_c = 0.018$ . Note that the abbreviation "unl." means unloaded. . . . .	110

5.4	Time history of the surface pressure coefficient at different chordwise locations. Head-on BVI problem, six different aerofoils, viscous calculations, $M_\infty=0.50$ , $\hat{\Gamma} = -0.283$ , $R_c = 0.018$ . Note that the abbreviation "unl." means unloaded. . . . .	111
5.5	Isobars ( $2p/q_\infty$ ) along with the velocity streamlines for the NACA-0006 and NACA-001234 aerofoils. Head-on BVI problem, viscous calculations, $M_\infty=0.50$ , $\hat{\Gamma} = -0.283$ , $R_c = 0.018$ . . . . .	112
5.6	Surface pressure coefficient at time $t(U_\infty/c)=4.51$ for the NACA-0006 and NACA-001234 aerofoils. Head-on BVI problem, viscous calculations, $M_\infty=0.50$ , $\hat{\Gamma} = -0.283$ , $R_c = 0.018$ . . . . .	112
5.7	Time history of the surface pressure coefficient at different chordwise locations for the loaded and unloaded SC-1095 aerofoil. Head-on BVI problem, SC-1095 aerofoil, viscous calculations, $M_\infty=0.50$ , $\hat{\Gamma} = -0.283$ , $R_c = 0.018$ . . . . .	113
5.8	Time history of the surface pressure coefficient at different chordwise locations. Head-on BVI problem, six different aerofoils, viscous calculations, $M_\infty=0.80$ , $\hat{\Gamma} = -0.177$ , $R_c = 0.018$ . Note that abbreviation "unl." means unloaded. . . . .	114
5.9	Time history of the surface pressure coefficient at different chordwise locations. Head-on BVI problem, six different aerofoils, viscous calculations, $M_\infty=0.80$ , $\hat{\Gamma} = -0.177$ , $R_c = 0.018$ . Note that abbreviation "unl." means unloaded. . . . .	115
5.10	Isobars ( $2p/q_\infty$ ) and velocity vectors for (a) the clean case and (b) the vortex-shock interaction. Head-on BVI problem, NACA-0012 aerofoil, viscous calculations, $M_\infty=0.80$ , $\hat{\Gamma} = -0.177$ , $R_c = 0.018$ . . . . .	116
5.11	Isomachs at $t(U_\infty/c)=5.0$ for (a) inviscid and (b) viscous calculations. Head-on BVI problem, NACA-0012 aerofoil, $M_\infty=0.80$ , $\hat{\Gamma} = -0.177$ , $R_c = 0.018$ . . . . .	116
5.12	Isobars ( $2p/q_\infty$ ) for the clean case at two different time steps. It illustrates the movement of the shocks. Head-on BVI problem, NACA-0018 aerofoil, $M_\infty=0.8$ , $\hat{\Gamma} = -0.177$ , $R_c = 0.018$ . . . . .	117
5.13	Histories of the lift and drag coefficients at freestream Mach numbers of 0.50 and 0.80 for (a-b) the NACA-0006 aerofoil, (c-d) the NACA-0012 aerofoil, (e-f) the NACA-0018 aerofoil, (g-h) the loaded and unloaded SC-1095 aerofoil. $\hat{\Gamma} = -0.283$ at $M_\infty=0.50$ , $R_c = 0.018$ . Note that the drag is non-dimensionalised against $\frac{1}{2}\rho_\infty U_\infty^2 c$ . . . . .	118
5.14	(a, c) Lift history and (b, d) maximum difference of lift for different aerofoils of the same thickness or the same LE radius at freestream Mach number 0.80. $\hat{\Gamma} = -0.177$ , $R_c = 0.018$ . . . . .	119
5.15	Time history of the quantity $\omega/\rho$ for the four aerofoils at freestream Mach number 0.50 and 0.80. $\hat{\Gamma} = -0.283$ ( $M_\infty = 0.5$ ), $R_c = 0.018$ . . . . .	120
5.16	Time history of the surface pressure coefficients for different freestream Mach numbers at different chordwise locations. Head-on BVI problem, NACA-0012 aerofoil, inviscid calculations. $\hat{\Gamma} = -0.283$ ( $M_\infty = 0.5$ ), $R_c = 0.10$ . . . . .	121
5.17	Lift and drag histories for a vortex of fixed strength at different freestream Mach numbers. Head-on BVI problem, NACA-0012 aerofoil, inviscid calculations, $\hat{\Gamma} = -0.283$ ( $M_\infty=0.50$ ), $R_c = 0.10$ . . . . .	122

5.18	(a) Time histories of the density and of (b) the ratio vorticity-density at the vortex core. Head-on BVI problem, NACA-0012 aerofoil, inviscid calculations, $\hat{\Gamma} = -0.283$ ( $M_\infty=0.50$ ), $R_c = 0.10$ , various freestream Mach numbers. . . . .	122
5.19	Time history of the surface pressure coefficient at different tap locations. Head-on BVI problem, NACA-0012 aerofoil, inviscid calculations, $M_\infty=0.73$ , $\hat{\Gamma} = -0.42$ . . . . .	124
5.20	Time history of the surface pressure coefficient at different tap locations. Miss-distance BVI problem, NACA-0012 aerofoil, inviscid calculations, $M_\infty=0.73$ , $\hat{\Gamma} = -0.42$ , $y_0 = -0.15$ . . . . .	125
5.21	Time history of the density $\rho$ at the vortex core for vortices of different initial core radius. Head-on and miss-distance BVI problems, NACA-0012 aerofoil, inviscid calculations, $M_\infty=0.73$ , $\hat{\Gamma} = -0.42$ . (a) $y_0 = 0.0$ , (b) $y_0 = -0.15$ . . . . .	126
5.22	Time histories of the lift and drag for four vortices of different initial core radius. Head-on BVI problem, NACA-0012 aerofoil, inviscid calculations, $M_\infty=0.73$ , $\hat{\Gamma} = -0.42$ . . . . .	126
5.23	Time histories of the lift and drag for four vortices of different initial core radius. Miss-distance BVI problem, NACA-0012 aerofoil, inviscid calculations, $M_\infty=0.73$ , $\hat{\Gamma} = -0.42$ , $y_0 = -0.15$ . . . . .	127
5.24	Time history of the core radius along a vertical plane passing through the vortex core for four vortices of different initial core radius for two different BVI. $\hat{\Gamma}=-0.42$ . . . . .	127
5.25	History of the tangential velocity profile along a vertical plane passing by the vortex core at four different times. The vortex was introduced at 4.5 chords ahead of the aerofoil. Head-on BVI problem, NACA-0012 aerofoil, inviscid calculations, $M_\infty=0.73$ , $\hat{\Gamma} = -0.42$ . . . . .	128
5.26	Schematic of the vortex-induced angle on the aerofoil before and after the interaction. The vertical velocity component of the vortex induces an apparent angle of attack for the aerofoil. . . . .	129
5.27	Time history of the surface pressure coefficient at different tap locations. Head-on BVI problem, NACA-0012 aerofoil, inviscid calculations, $M_\infty=0.57$ , $R_c = 0.10$ . . . . .	130
5.28	Lift and drag histories for vortices of different strengths. Head-on BVI problem, NACA-0012 aerofoil, inviscid calculations, $M_\infty=0.57$ , $R_c = 0.10$ . . . . .	131
5.29	Time histories of (a) the density and of (b) the vorticity-density ratio at the vortex core. Head-on BVI problem, NACA-0012 aerofoil, inviscid calculations, $M_\infty=0.57$ , $R_c = 0.10$ , various vortex strengths. . . . .	131
5.30	Time history of the surface pressure coefficient at the chordwise location $x/c=0.02$ for a clockwise and anti-clockwise rotating vortex. Head-on BVI problem, NACA-0012 aerofoil, inviscid calculations, $M_\infty=0.50$ , $R_c = 0.018$ . . . . .	132
5.31	Lift and drag histories for clockwise and anti-clockwise rotating vortices. NACA-0012 aerofoil, head-on BVI, $M_\infty=0.50$ , $R_c = 0.018$ . . . . .	132
5.32	Time history of the surface pressure coefficient at different chordwise locations for different miss-distances. Head-on BVI problem, NACA-0012 aerofoil, inviscid calculations, $M_\infty=0.57$ , $\hat{\Gamma} = -1.8$ , $R_c = 0.10$ . . . . .	134

5.33	Time history of the surface pressure coefficient at different tap locations for different miss-distances. NACA-0012 aerofoil, inviscid calculations, $M_\infty=0.73$ , $\hat{\Gamma} = -0.42$ , $R_c = 0.10$ . . . . .	135
5.34	Pressure contours along with the velocity streamlines for miss-distances $y_0 = 0.00$ at time $t(U_\infty/c) = 5.50$ . Head-on BVI problem, NACA-0012 aerofoil, inviscid calculations, $M_\infty=0.57$ , $\hat{\Gamma} = -1.8$ , $R_c = 0.10$ . Note that the pressure is non-dimensionalised against the dynamic pressure. . . . .	136
5.35	Lift and drag histories for vortex of various miss-distances at two flow conditions. NACA-0012 aerofoil, inviscid calculations. . . . .	137
5.36	Time history of the density at the vortex core for different freestream Mach numbers. (a) $M_\infty=0.57$ , (b) $M_\infty=0.73$ . Head-on BVI problem, NACA-0012 aerofoil, inviscid calculations, various miss-distances. . . . .	138
6.1	Schematic of the probe locations at which the acoustic pressure was calculated for the four initial vortex locations. . . . .	141
6.2	Influence of the vortex location on the acoustical signature. The history of the acoustic pressure is given at point 1, 2, 3 and 4. The dotted lines indicates the presence of spurious waves. NACA-0012 aerofoil, viscous calculations, $M_\infty=0.5$ , $\hat{\Gamma} = -0.283$ , $R_c = 0.018$ . . . . .	141
6.3	Absolute value of the acoustic pressure at $t(U_\infty/c)=5.10$ and freestream Mach number of 0.5 for the NACA-0006, NACA-0012, NACA-0018, SC-1095. Head-on BVI, viscous calculations, $\hat{\Gamma} = -0.283$ , $R_c = 0.018$ . Note that the acoustic pressure is non-dimensionalised against the freestream pressure. . . . .	142
6.4	Pressure contours of the NACA-0012 aerofoil at two different instants. Head-on BVI case, NACA-0012 aerofoil, viscous calculations, $M_\infty=0.5$ , $\hat{\Gamma} = -0.283$ , $R_c = 0.018$ . Note that the pressure is non-dimensionalised against the dynamic pressure. . . . .	143
6.5	(a, c) Contours of the acoustic pressure along with the location of the four probes and (b, d) Time history of the acoustic pressure at the probes. The absolute value of the acoustic pressure is represented for the NACA-0012 at a freestream Mach number of 0.5 (a, b) and 0.8 (c, d). The scale is exponential. Note that the acoustic pressure is non-dimensionalised against the freestream pressure. . . . .	144
6.6	Acoustic pressure history for the aerofoils at points $P_1$ (a) and $P_2$ (b). Head-on BVI problem, viscous calculations, $\hat{\Gamma} = -0.283$ , $R_c = 0.018$ , $M_\infty=0.5$ . Note that the time is non-dimensionalised with $U_\infty/c$ and that the abbreviation "unl." means unloaded. . . . .	145
6.7	Acoustic pressure history for the aerofoils at points $P_3$ (a) and $P_4$ (b). Head-on BVI problem, viscous calculations, $\hat{\Gamma} = -0.283$ , $R_c = 0.018$ , $M_\infty=0.5$ . Note that the time is non-dimensionalised with $U_\infty/c$ and that the abbreviation "unl." means unloaded. . . . .	146
6.8	Acoustic pressure history for the aerofoils at points $P_1$ (a) and $P_2$ (b). Head-on BVI problem, viscous calculations, $\hat{\Gamma} = -0.177$ , $R_c = 0.018$ , $M_\infty=0.8$ . Note that the time is non-dimensionalised with $U_\infty/c$ and that the abbreviation "unl." means unloaded. . . . .	147

6.9	Acoustic pressure history for the aerofoils at points $P_3$ (a) and $P_4$ (b). Head-on BVI problem, viscous calculations, $\hat{\Gamma} = -0.177$ , $R_c = 0.018$ , $M_\infty=0.8$ . Note that the time is non-dimensionalised with $U_\infty/c$ and that the abbreviation "unl." means unloaded. . . . .	148
6.10	(a, c) Acoustic pressure and (b, d) isomachs at two different times. Head-on BVI problem, NACA-0006 aerofoil, viscous calculations, $M_\infty=0.80$ , $\hat{\Gamma} = -0.177$ , $R_c = 0.018$ . Note that the acoustic pressure is non-dimensionalised against the freestream pressure. . . . .	149
6.11	(a, c) Acoustic pressure and (b, d) isomachs at two different times. Head-on BVI problem, NACA-0012 aerofoil, viscous calculations, $M_\infty=0.80$ , $\hat{\Gamma} = -0.177$ , $R_c = 0.018$ . Note that the acoustic pressure is non-dimensionalised against the freestream pressure. . . . .	150
6.12	(a, c) Acoustic pressure and (b, d) isomachs at two different times. Head-on BVI problem, NACA-0018 aerofoil, viscous calculations, $M_\infty=0.80$ , $\hat{\Gamma} = -0.177$ , $R_c = 0.018$ . Note that the acoustic pressure is non-dimensionalised against the freestream pressure. . . . .	151
6.13	(a, c) Acoustic pressure and (b, d) isomachs at two different times. Head-on BVI problem, SC-1095 aerofoil, viscous calculations, $M_\infty=0.80$ , $\hat{\Gamma} = -0.177$ , $R_c = 0.018$ . Note that the acoustic pressure is non-dimensionalised against the freestream pressure. . . . .	152
6.14	Acoustic pressure history for the aerofoils at points $P_1$ (a-d) and $P_3$ (e-h) for the NACA-0006, NACA-0012, NACA-0018 aerofoils and the loaded and unloaded SC-1095 aerofoil at two different freestream Mach numbers. Head-on BVI, viscous calculations, $\hat{\Gamma} = -0.283$ , $R_c = 0.018$ . Note that the compressibility wave and the TE wave pass by points $P_1$ and $P_3$ , respectively. . . . .	153
6.15	Maximum Sound Pressure Level for the aerofoils at points $P_1$ (a-d) and $P_3$ (e-h) at two different freestream Mach numbers. Head-on BVI problem, viscous calculations, $M_\infty = 0.5$ , $\hat{\Gamma} = -0.283$ ( $M_\infty = 0.5$ ), $R_c = 0.018$ .	154
6.16	Acoustic pressure history at point $P_1$ and $P_2$ for the loaded and unloaded SC-1095 aerofoils at two freestream Mach numbers. Head-on BVI case, $\hat{\Gamma} = -0.283$ ( $M_\infty = 0.5$ ), $R_c = 0.018$ . Note that point $P_2$ is at the same distance from the aerofoil than point $P_1$ . . . . .	155
6.17	Isobars ( $2p/q_\infty$ ) at $t(U_\infty/c)=5.10$ for (a) the loaded and (b) unloaded SC-1095 aerofoils in transonic flow. Head-on BVI case, viscous calculations, $M_\infty=0.8$ , $\hat{\Gamma} = -0.177$ , $R_c = 0.018$ . . . . .	155
6.18	(a-b) Isobars ( $2p/q_\infty$ ) and (c-d) isolines of the acoustic pressure at $t(U_\infty/c)=5.10$ for head-on BVI at different freestream Mach numbers. NACA-0012 aerofoil, inviscid calculations, $\hat{\Gamma} = -0.283$ ( $M_\infty=0.5$ ), $R_c = 0.10$ . Note that the acoustic pressure is non-dimensionalised against the freestream pressure. . . . .	156
6.19	(a) Acoustic pressure history and (b) absolute value of the maximum acoustic pressure at point P for head-on BVI at different freestream Mach numbers. NACA-0012 aerofoil, inviscid calculations, $\hat{\Gamma} = -0.283$ ( $M_\infty=0.5$ ), $R_c = 0.10$ . . . . .	157
6.20	Isobars ( $2p/q_\infty$ ) at $t(U_\infty/c)=5.10$ for different core radii. NACA-0012 aerofoil, inviscid calculations. (a-b) $y_0 = 0.00$ , (c-d) $y_0 = -0.15$ . $M_\infty=0.73$ , $\hat{\Gamma} = -0.42$ . . . . .	158

6.21	(a, c) Isolines of the acoustic pressure at $t(U_\infty/c)=6.0$ for two miss-distance BVI cases. (b, d) Acoustic pressure history at point P. NACA-0012 aerofoil, inviscid calculations, $M_\infty=0.73$ , $\hat{\Gamma} = -0.42$ . Note that the acoustic pressure is non-dimensionalised against the freestream pressure for the isolines. . . . .	159
6.22	Isobars ( $2p/q_\infty$ ) at $t(U_\infty/c)=5.10$ . Head-on BVI problem, NACA-0012 aerofoil, inviscid calculations. $M_\infty=0.57$ , $R_c = 0.10$ . . . . .	160
6.23	(a-b) Isolines of the acoustic pressure at $t(U_\infty/c)=5.40$ for a vortices of different strengths. (c) Acoustic pressure history at point P. Head-on BVI problem, NACA-0012 aerofoil, inviscid calculations. $M_\infty=0.57$ , $R_c = 0.10$ . Note that the acoustic pressure is non-dimensionalised against the freestream pressure for the isolines. . . . .	161
6.24	(a) Sound Pressure Level and (b) acoustic pressure at point P for vortices of different strengths at time $t(U_\infty/c)=4.00$ . . . . .	161
6.25	Isobars ( $2p/q_\infty$ ) contours for different miss-distance BVI cases at time $t(U_\infty/c) = 5.10$ . Head-on BVI problem, NACA-0012 aerofoil, inviscid calculations, $M_\infty=0.57$ , $\hat{\Gamma} = -1.8$ , $R_c = 0.10$ . . . . .	162
6.26	Isobars ( $2p/q_\infty$ ) contours for different miss-distance BVI cases at time $t(U_\infty/c) = 5.10$ . Head-on BVI problem, NACA-0012 aerofoil, inviscid calculations, $M_\infty=0.73$ , $\hat{\Gamma} = -0.42$ , $R_c = 0.10$ . . . . .	163
6.27	Isolines of the acoustic pressure for different miss-distance BVI cases at time (a-b) $t(U_\infty/c) = 5.40$ . Head-on BVI problem, NACA-0012 aerofoil, inviscid calculations. (a-b) $M_\infty=0.57$ , $\hat{\Gamma} = -1.8$ , (c-d) $M_\infty=0.73$ , $\hat{\Gamma} = -0.42$ . Note that the acoustic pressure is non-dimensionalised against the freestream pressure. . . . .	164
6.28	Acoustic pressure history at point P at two freestream Mach numbers. (a) $M_\infty=0.57$ , $\hat{\Gamma} = -1.8$ , (b) $M_\infty=0.73$ , $\hat{\Gamma} = -0.42$ . NACA-0012 aerofoil, inviscid calculations, various miss-distances. Note that the acoustic pressure is of a larger magnitude before the interaction for the subsonic case. This is due to the fact that the initial vortex is much stronger for the subsonic case than the transonic one. . . . .	165
6.29	(a) Acoustic pressure history at points 1, 2, 3 above the aerofoil. (b) Acoustic pressure history at points 4, 5, 6 below the aerofoil. Head-on BVI problem, NACA-0012 aerofoil, viscous calculations, $M_\infty=0.5$ , $\hat{\Gamma} = -0.283$ , $R_c = 0.018$ . . . . .	166
6.30	Schematic of the BVI rotor test. . . . .	167
6.31	Schematic of the blade. The blade rotates anti-clockwise at $\omega/(2\pi)$ revolutions per second. The spherical coordinates of the observer are $(r, \theta, \Psi)$ . . . . .	168
6.32	(a) Evolution of the lift coefficient against the the revolution of the blade for different spanwise locations. (b) Distribution of the lift along the spanwise direction against the revolution of the blade. Head-on BVI problem, NACA-0012 section. . . . .	169
6.33	Acoustic pressure corresponding to the loading and thickness noises for (a-b) the head-on BVI and (c-d) the miss-distance BVI. $M_\infty=0.63$ , $\hat{\Gamma} = -0.25$ , $R_c = 0.162$ . . . . .	170
6.34	Schematic of the acoustical mapping for the helicopter. The OASPL is represented around a sphere passing by point P. The acoustic pressure has been calculated at point P (50, 0, -50) for the parametric study. . . . .	171

6.35	Distribution of the lift along the spanwise direction against the revolution of the blade. The BVI takes place at $90^\circ$ of azimuth. NACA-0012 section, $M_\infty=0.5$ . . . . .	172
6.36	Acoustic pressure for different aerofoils at the location (50.0,0.0,-50.0). (a) Slap noise, (b) thickness noise. . . . .	173
6.37	Acoustic pressure for different aerofoils at the point P (50.0,0.0,-50). Results corresponds to an azimuth angle of $180^\circ$ . . . . .	173
6.38	Acoustic pressure for different aerofoils at point P' (47.0,17.1,-50.0). Results corresponds to an azimuth angle of $200^\circ$ . The distance aircraft-observer is the same as point P. . . . .	174
6.39	Contours of the OASPL at the transonic freestream Mach number for the range of azimuth angles $\Psi$ where the BVI occurs. The elevation angle $\theta$ was fixed to $-30^\circ$ (below the aircraft) and the distance aircraft-observer to 50 metres. $\hat{\Gamma}=-0.177$ , $M_\infty=0.8$ - (a) NACA-0006, NACA-0012, (b) NACA-0018, SC-1095. . . . .	174
6.40	Maximum BVI noise amplitude in terms of Sound Pressure Level for different thicknesses of aerofoils at two freestream Mach numbers. The square points corresponds to the NACA-0006, NACA-0012, NACA-0018 and the SC-1095 sections. The cross corresponds to the unloaded SC-1095 aerofoil. Note the $\Delta SPL$ is deduced from the maximum value of the acoustic pressure at point P. . . . .	175
6.41	Acoustic pressure and maximum BVI noise amplitude at point (50,0,-50) in terms of Sound Pressure Level for (a-b) different thicknesses and (c-d) LE radii of aerofoil in subsonic flow. $M_\infty=0.5$ , $\hat{\Gamma} = -0.283$ , $R_c = 0.018$ . . . . .	176
6.42	Evolution of the OASPL against (a, c) the square of the distance observer-aircraft and the logarithm of the distance at $\Psi = 180^\circ$ for three different azimuth angles at two freestream Mach numbers. NACA-0012 section, $\hat{\Gamma} = -0.283$ ( $M_\infty=0.5$ ), $R_c = 0.018$ . (a) $M_\infty=0.5$ , (b) $M_\infty=0.8$ . . . . .	177
6.43	Acoustic pressure at different freestream Mach numbers at the location (50.0,0.0,-50.0). NACA-0012 section, $\hat{\Gamma} = -0.283$ at a freestream Mach number of 0.5, $R_c = 0.01$ . . . . .	177
6.44	(a) Maximum BVI noise amplitude in terms of Sound Pressure Level for different Mach numbers. (b) Slope of the SPL-Mach curves. $\hat{\Gamma} = -0.283$ , $M_\infty=0.50$ , $R_c = 0.10$ . . . . .	178
6.45	Acoustic pressure for different vortex core radii at the location (50.0,0.0,-50.0) for (a) head-on and (b) miss-distance BVI cases. $\hat{\Gamma} = -0.42$ , $M_\infty=0.73$ . (a) $y_0 = 0.00$ , (b) $y_0 = -0.15$ . . . . .	179
6.46	(a) Maximum BVI noise amplitude in terms of Sound Pressure Level for different vortex core radii at two flow conditions. (b) Slope of the SPL-viscous core radius. $\hat{\Gamma} = -0.42$ , $M_\infty=0.73$ . (a) $y_0 = 0.00$ , (b) $y_0 = -0.15$ . Note that $R_c$ is the non-dimensionalised core radius. . . . .	180
6.47	Contours of the OASPL for the range of azimuth angles $\Psi$ where the BVI occurs. The elevation angle $\theta$ indicates the directivity patterns of the BVI noise below ( $\theta < 0$ ) and above ( $\theta > 0$ ) the helicopter. Head-on BVI problem, NACA-0012 section, $\hat{\Gamma} = -0.42$ , $M_\infty=0.73$ . (a) $R_c=0.04$ , (b) $R_c=0.15$ . . . . .	180
6.48	Acoustic pressure for different vortex strengths at point P (50.0,0.0,-50.0). . . . .	181
6.49	(a) Maximum BVI noise amplitude in terms of Sound Pressure Level for different vortex strengths. (b) Slope of the SPL-vortex strength. . . . .	181

6.50	Contours of the OASPL for the range of azimuth angles $\Psi$ where the BVI occurs. The elevation angle $\theta$ indicates the directivity patterns of the BVI noise below ( $\theta < 0$ ) and above ( $\theta > 0$ ) the helicopter. NACA-0012 section, (a) $\hat{\Gamma} = -0.283$ , $M_\infty = 0.57$ - (b) $\hat{\Gamma} = -1.80$ , $M_\infty = 0.57$ . . . . .	182
6.51	Influence of the miss-distances on the farfield noise for two different BVI cases. (a-b) $\hat{\Gamma} = -0.42$ , $M_\infty = 0.73$ , (c-d) $\hat{\Gamma} = -1.8$ , $M_\infty = 0.57$ . (a, c) Acoustic pressure for different aerofoils at the location (50.0,0.0,-50.0). (b, d) Maximum BVI noise amplitude in terms of Sound Pressure Level for different miss-distances. Note that $y_0$ is non-dimensionalised with the chord of the aerofoil. . . . .	183
6.52	Slope of the SPL for two miss-distance BVI cases. NACA-0012 section. The acoustic pressure was taken for different miss-distance BVI cases at the location (50.0,0.0,-50.0). Note that $y_0$ is the non-dimensionalised miss-distance. . . . .	184
6.53	Contours of the OASPL for the range of azimuth angles $\Psi$ where the BVI occurs. The elevation angle $\theta$ indicates the directivity patterns of the BVI noise below ( $\theta < 0$ ) and above ( $\theta > 0$ ) the helicopter. NACA-0012 section, $M_\infty = 0.73$ , $\hat{\Gamma} = -0.242$ . (a) $y_0 = 0.00$ , (b) $y_0 = -0.60$ . . . . .	184

# List of Tables

3.1	The run test cases for the evaluation of the time-stepping implicit schemes.	35
3.2	Gain of the UNFACTored method against the FUN method.	41
3.3	Size of the grids used for the 2D BVI calculations. The first BVI is head-on and the three others are miss-distance BVI cases.	51
4.1	Size of the grids used for the inviscid and viscous calculations with different vortex locations.	73
5.1	List of the parameters examined. $M_{\infty}$ , $R_c$ , $\hat{\Gamma}$ , $(x_0, y_0)$ represent respectively the freestream Mach number, the vortex core radius non-dimensionalised against the chord, the vortex strength non-dimensionalised against the product freestream velocity-chord and the miss-distance non-dimensionalised against the chord. A Mach number of 0.8 was chosen to highlight the differences of behaviour for the different aerofoils. Note that a negative strength $\hat{\Gamma}$ corresponds to a clockwise-rotating vortex and that the distance from the aerofoil to the vortex core is called miss-distance.	107
5.2	Size of the grids used for the inviscid and viscous calculations for different types of BVI. The vortex was introduced at 4.5 chords ahead of the aerofoil.	108

# Nomenclature

Symbols	Definition
$a$	Speed of the sound
$a_0$	Speed of the sound of the undisturbed medium
$b$	Wingspan
$c$	Chord length of the aerofoil
$c_{b1}, c_{b2}$	Closure coefficients for the SA turbulence model
$c_p$	Specific heat capacity at constant pressure
$c_{t1}, c_{t2}, c_{t3}, c_{t4}$	Closure coefficients for the SA turbulence model
$c_v$	Specific heat capacity at constant volume
$c_{v1}$	Closure coefficients for the SA turbulence model
$c_{w1}, c_{w2}, c_{w3}$	Coefficients for the SA turbulence model
$C_p$	Surface pressure coefficient, $C_p = \frac{p - p_{\infty}}{\frac{1}{2} \rho_{\infty} U_{\infty}^2}$
$C_{p0}$	Mean steady pressure
$C_{p1}$	First harmonic pressure
$C_D$	Drag coefficient
$C_L$	Lift coefficient
$C_{P,L}$	Surface pressure coefficient on the lower surface of the aerofoil
$C_{P,U}$	Surface pressure coefficient on the upper surface of the aerofoil
$C_T$	Rotor thrust coefficient
$C_1$	Confinement parameter when the grid scaling is applied
$\tilde{C}$	Constant used in the Povitsky vortex model
$d$	Distance to the wall
$d_t$	Distance from the field point to the trip (which is on a wall)
$dC_{MP}$	Sectional pitching moment coefficient
$dC_N$	Sectional normal force coefficient
$dC_T$	Sectional chordwise force coefficient
$e$	Specific internal energy
$E$	Total energy of the fluid
$\vec{f}_b$	Body force term
$f_i$	Function of indice $i$ (Section 3.3.3), body forces (everywhere else)
$f'_i$	Derivative of a function for the indice $i$
$f_{t1}, f_{t2}, f_{v1}, f_w, f_{\mu}$	Functions used in the SA turbulence model
$F_i$	Forces vector
$F$	Fluxes
$g_i$	Functions used in the SA turbulence model
$G$	Fluxes

$h_{proj}$	Characteristic length
$Im$	Imaginary part
$k$	Reduced frequency of oscillation (Section 3.2.2), turbulent kinetic energy, $k \equiv \overline{u'_i u'_i} / 2$ (everywhere else)
$K$	Heat transfer coefficient
$L$	Width of the grid
$\dot{L}_i$	Time derivative of the lift forces
$L_T$	Lift forces in the radiation direction
$\vec{L}$	Cell size vector
$M$	Mach number
$M_\infty$	Freestream Mach number
$M_{tip}$	Tip Mach number
$M_r$	Mach number vector in the radiation direction
$\dot{M}_i$	Time derivative of the Mach number vector
$\frac{\partial}{\partial M}$	Gradient
$\mathbf{n}$	Normal vector to the surface $\Sigma$
$\bar{\mathbf{n}}$	Normalised vorticity gradient vector to the surface $\Sigma$
$p$	Pressure
$p_0$	Pressure of the undisturbed medium
$p_\infty$	Pressure at the freestream conditions
$P_k$	Production term
$\mathbf{P}_{ij}$	Compressive stress tensor
$P'_L$	Loading acoustic pressure
$P'_T$	Thickness acoustic pressure
$Pr_T$	Turbulent Prandtl number, $Pr_T = \rho \mu_T c_p / k$
$P'$	Acoustic pressure
$q_i$	Heat flux vector
$q_\infty$	Dynamic pressure
$Q$	Mass fluxes
$r$	Distance from the source to the observer (Sections 2.3.3-2.3.4), ratio of the magnitude of the rate-of-strain, and vorticity tensors (Section 2.2.3), distance from the vortex core (everywhere else)
$r_i$	Radiation vector
$\hat{r}_i$	Unit radiation vector
$R$	Ideal gas law constant (Section 2.2.3), residual (Section 2.2.2), rotor radius (everywhere else)
$Re$	Real part
$Rev$	Revolution, $Rev = 1$ when the blade has rotated for $360^\circ$ .
$R_c$	Non-dimensionalised core radius
$Re$	Reynolds number based on aerofoil chord
$R_0$	Outer radius of the vortex
$R^*$	Pseudo-residual
$S$	Magnitude of the vorticity (Section 2.2.3), source term tensor (everywhere else)
$S_c$	Confinement source term for the energy
$S_u$	Confinement source term for the u velocity

$S_v$	Confinement source term for the $v$ velocity
$S_{u,v}$	Confinement source tensor for the velocity components
$S_\rho$	Confinement source term for the density
$\tilde{S}$	Variable used for the SA turbulence model
$t$	Instant
$T$	Temperature of the fluid
$T_{ij}$	Acoustic stress
$u$	Velocity
$\bar{u}_i$	Averaged velocity component
$u_i'$	Velocity fluctuating component
$\overline{u_i' u_i'}$	Reynolds-stress tensor
$U_{res}$	Vortex-induced velocity
$U_{vortex}$	Vertical component of the tangential velocity
$U_\infty$	Freestream velocity
$v_n$	Normal velocity at the body
$V_c$	Maximum velocity magnitude
$v_\theta$	Tangential velocity
$\mathcal{V}$	Control Volume
$\vec{V}$	Velocity vector
$x, y$	Chordwise and vertical distances
$x_{A1}$	Wing pitch axis origin
$\vec{x}$	Observer vector
$y_0$	Miss-distance
$W$	Conservative variables
$W^n$	Conservative variables at the time level $n \cdot \Delta t$

## Acronyms

## Definition

ADI	Alternating Direction Implicit (method)
BEM	Boundary Element Method
BILU	Block-Incomplete Lower-Upper
BL	Boundary Layer
BVI	Blade-Vortex Interaction
CAA	Computational AeroAcoustics
CFD	Computational Fluid Dynamics
CFL	Courant-Friedrichs-Lewy (number)
CPU	Computer
CVCM	Compressible Vorticity Confinement Method
EROS	European Rotorcraft Software
FAR	Federal Air Regulations
FUN	Factored-UNfactored
FW-H	Ffowcs Williams - Hawkings
GCG	General Conjugate Gradient (method)
GEROS	Grid generator for European Rotorcraft Software
HHC	High Harmonic Control
HSI	High-Speed Impulsive
IBC	Independent Blade Control
ICAO	International Civil Aviation Organisation

LE	Leading-Edge
LHS	Left Hand Side
MUSCL	Monotone Upwind Scheme for Conservation Laws
NLR	National Research Laboratory
NS	Navier-Stokes (equations)
OASPL	Overall Sound Pressure Level
ONERA	Office Nationale d'Études et Recherches Aéropatiales
PIV	Particle Image Velocimetry
PMB	Parallel Multi-Block (code)
RANS	Reynolds Averaged Navier-Stokes (equations)
RHS	Right Hand Side
SA	Spalart-Allmaras turbulence model
SPL	Sound Pressure Level
SST	Shear Stress Transport (model)
TE	Trailing-edge
TPL	Total Pressure Loss
TPP	Tip Path Plane
TVD	Total Variation Diminishing (scheme)
TU	Technical University
2D	Two-Dimensional
3D	Three-Dimensional

## Greek Symbols Definition

$\alpha_{PPP}$	Descent angle
$\alpha$	Closure coefficient for the $k - \omega$ turbulence model (Section 2.2.3), angle of attack of the aerofoil (everywhere else)
$\alpha^*$	Closure coefficient for the $k - \omega$ turbulence model
$\beta$	Closure coefficient for the $k - \omega$ turbulence model
$\beta^*$	Closure coefficient for the $k - \omega$ turbulence model
$\delta$	Density confinement parameter
$\delta_{ij}$	Kronecker Symbol
$\delta$	Boundary layer thickness (Section 2.2.3), density confinement parameter (everywhere else)
$\Delta t$	Real time step
$\Delta t^*$	Pseudo-time step
$\Delta x, \Delta y, \Delta z$	Cell size in the x, y, z directions
$\Delta SPL$	BVI noise amplitude in terms of Sound Pressure levels
$\Delta U$	Difference between the velocity at the field point and that at the trip
$\Delta x$	Grid spacing along the wall at the trip
$\epsilon$	Confinement parameter
$\gamma$	Ratio of specific heats, $\gamma = c_p/c_v$
$\Gamma$	Vortex strength
$\bar{\Gamma}$	Vortex strength non-dimensionalised against $V_\infty R_c$
$\hat{\Gamma}$	Vortex strength non-dimensionalised against $V_\infty c$
$\mu$	Molecular viscosity (Section 2.2.3), artificial viscosity (Section 3.3), advance ratio (everywhere else)
$\mu_T$	Kinematic turbulent viscosity

$\nabla$	Gradient
$\nu$	Molecular eddy viscosity
$\nu_T$	Turbulent eddy viscosity
$\tilde{\nu}$	Variable used in the SA turbulence model
$\chi$	Variable used in the SA turbulence model, $\chi = \tilde{\nu}/\nu$
$\omega$	Specific dissipation rate (Sections 2.2.3) vorticity (everywhere else)
$\omega_t$	Wall vorticity at the trip
$\Omega$	Vorticity invariant
$\Omega_{ij}$	Vorticity tensor
$\Psi$	Azimuthal angle
$\rho$	Density
$\rho_\infty$	Density at the freestream conditions
$\rho_0$	Density of the undisturbed medium
$\sigma$	Solidity
$\sigma_{ij}$	Viscous stress
$\sigma_k$	Closure coefficient in the $k - \omega$ and SST turbulence models
$\sigma_\omega$	Closure coefficient in the $k - \omega$ and SST turbulence models
$\Sigma$	Surface
$\tau$	Magnitude of the shear stress (Section 4.2.7), retarded time (everywhere else)
$\tau_{ij}$	Viscous stress tensor, total stress tensor
$\tau_{yy}$	Shear stress in the y direction
$\theta$	Polar angle (when related to the velocity component), elevation angle (everywhere else)
$\theta_0$	Mean angle of attack
$\theta_1$	Oscillation pitch angle
$\theta(t)$	Wing pitching angle
$\phi$	Blending function for the SST turbulence model
$\phi_1, \phi_2$	Blending coefficients for for the SST turbulence model
$\varepsilon$	Dissipation rate of the turbulence for the $k - \varepsilon$ model
$\vartheta$	Volume

## Superscripts

*	Pseudo
-	Time-averaged quantity
$n, m$	Time indice
Prime (')	Fluctuating quantity

## Subscripts

$i, j, k$	Spatial indices
$t$	Trip
$w$	Wall
$T$	Turbulent value
$\infty$	Farfield value

## Definition

## Definition

# Chapter 1

## Introduction

### 1.1 Overview

The performance of the helicopter in terms of manoeuvrability and speed has been considerably enhanced through an understanding of fluid dynamics. The flowfield has been studied for decades towards reducing the vibration levels and controlling the turbulent flow generated around the rotors and the fuselage. The diversity and complexity of the flowfield makes the development of new designs difficult. This explains why research in the last ten years has mainly focused on the understanding of the flow phenomena which have an impact on the performances of a helicopter.

Environmental concerns have raised the interest in noise. The major noise sources of a helicopter have been identified and it is known that blade-vortex interaction (BVI) highly contributes to the perceived noise levels. BVI needs to be considered when simulating the acoustics of a helicopter and this work is devoted to the study of BVI.

BVI takes place on both the main and tail rotors of helicopters with the vortex axis being parallel or orthogonal to the blades and noise is generated when the blade tip vortices collide or come close to the rotor blades [10]. As explained by Schmitz *et al.* [6], the pressure disturbances generated by the passage of a vortex close to a blade radiate a part of their energy as sound. Depending on the phase delay between the emitted acoustic waves, the BVI sound can propagate directionally and far from the rotor. It is therefore essential to understand the mechanisms of BVI due to its dominance on the acoustic signature of a helicopter, particularly in descending flight [4, 11].

### 1.2 Description of the rotorcraft flowfield

The flowfield of a rotorcraft induces unsteady aerodynamics and vibratory loads. Due to the complexity of the flow, many difficulties in studying the aerodynamics and the aeroelasticity are encountered. Research in these fields is aimed at easing the task of the pilot and increasing passenger comfort by reducing the levels of vibration and

perturbations caused by the flow. One of the reasons for the complexity of the flowfield derives from the trim requirements of a rotorcraft. The lateral cyclic pitch control of the helicopter is aimed at balancing the lateral lift distribution [1]. The advancing blade experiences a high-speed flow whereas the retreating one is characterised by a flow at lower speed. The difference in lift is managed by altering the angle of attack of the retreating blade. Also, transonic flow is experienced in the advancing blade leading to critical flow characteristics. Shock-vortex interaction may occur as well as shock-boundary layer interaction depending on the configuration. Studies have been carried out to understand the different mechanisms (see Figure 1.1) which trigger these unwanted flowfield modifications to be able to improve the manoeuvrability and the control of the aircraft.

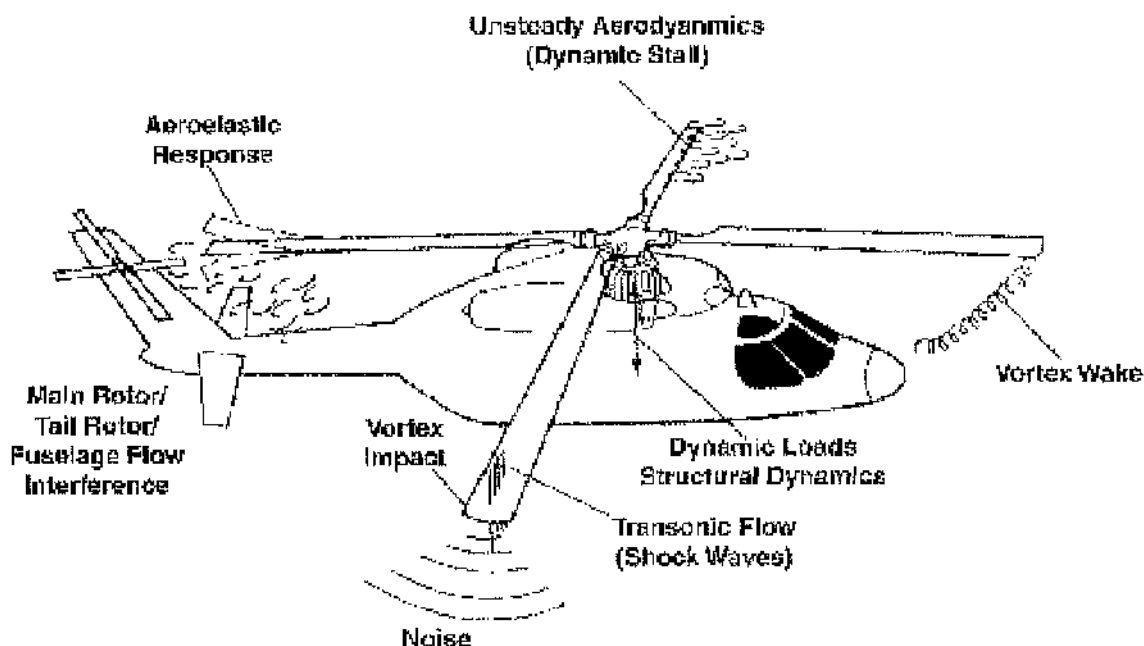


Figure 1.1: Schematic of the rotorcraft elements influencing the aerodynamics (Brentner and Farassat [1]).

Furthermore the rotor operates very close to its own wake implying interactions with the fuselage and the main and tail rotor blades, as illustrated by Figure 1.2. It is recognised [8] that the rotor wakes are the most important feature to generate BVI noise. The diversity and complexity of the flow encountered around the rotorcraft and the difficulties of predicting the wake make the prediction of the rotorcraft aerodynamics very challenging.

## 1.2. DESCRIPTION OF THE ROTORCRAFT FLOWFIELD

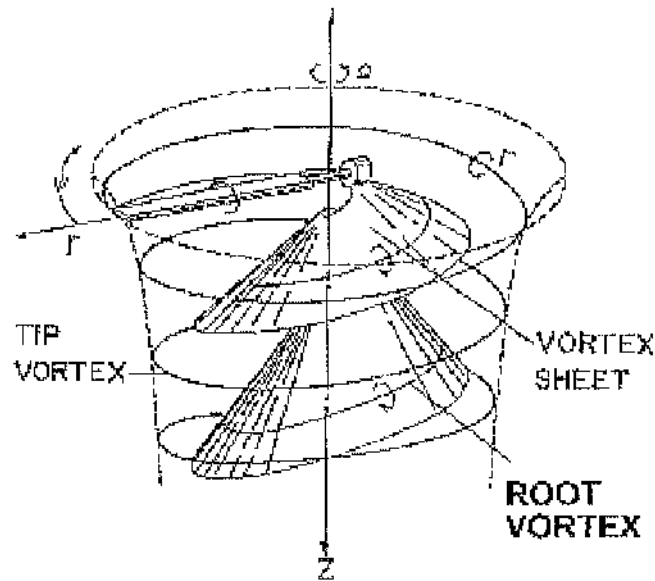


Figure 1.2: Schematic of the wake of a rotorcraft [2].

Helicopter noise continues to be very difficult to predict due to the complexity of the helicopter aerodynamics [4]. Any acoustical analysis towards alleviation requires the inclusion of all possible noise sources and isolation of the type of noise which contributes the most to the perceived noise levels. A description of the rotorcraft noise sources is given in the next section.

### 1.3 Rotorcraft noise sources

The expanding civil use of helicopters renewed the interest in aeroacoustics [4]. New noise regulations such as the Convention on International Civil Aviation of the ICAO (Chapter 8 of Annex 16) and the United States FAR (Part 36) demanded that industry achieve low noise levels when a helicopter passes close to an inhabited area. Indeed, a recent investigation of the public acceptance of helicopter noise [12] led to the conclusion that directives for flight conditions, i.e. time schedule and flight routes should be addressed. The concern of the public for helicopter noise forced the rotorcraft industry to develop more acoustically friendly designs without compromising performance.

#### 1.3.1 Noise characteristics of a rotorcraft

The engine exhaust noise is the loudest in helicopters powered by piston internal combustion engines [4]. This is due to its impulsive character. The introduction of gas turbines to power helicopters in the early 1960s reduced considerably the engine noise and revealed the high contribution of the rotor to the overall noise [1]. The rotor noise is characterised by turbulent phenomena which may modify the loads of the blades, e.g. for the case of BVI which occurs when a blade encounters a vortex trailed by a previous blade as explained in section 1.3.2. Advanced helicopters were prone

### 1.3. ROTORCRAFT NOISE SOURCES

to generating high levels of blade slap noise since improved blade sections replaced the standard NACA-0012, leading to higher performances. The rotor noise was then needed to be treated because of its important contribution to the overall noise levels. It is interesting to note that the rotational noise sources can be split into 3 different types:

- The thickness noise which is related to the displacement of the fluid by the rotor blade. The acoustical pressure can be regarded as the sum of sources over the blade surface, the shift in observer time causing the sources not to cancel [11].
- The loading noise which is induced by the unsteady loads of the blade.
- The quadrupole noise which represents the noise produced, for example, by turbulence.

The loudest and the most annoying sounds are impulsive in nature [11]. The impulsive rotational noise is composed of the high-speed impulsive (HSI) noise and of the blade-vortex interaction. Figure 1.3 shows the different types of aerodynamic noise for a helicopter. The source terms of BVI and HSI noise differ from the ordinary loading and thickness noises by their impulsive nature [13]. For HSI, the blade tip volume and shape are the major parameters contributing to noise generation [8]. For BVI, the strength of the vortex and the miss-distance are the most important parameters.

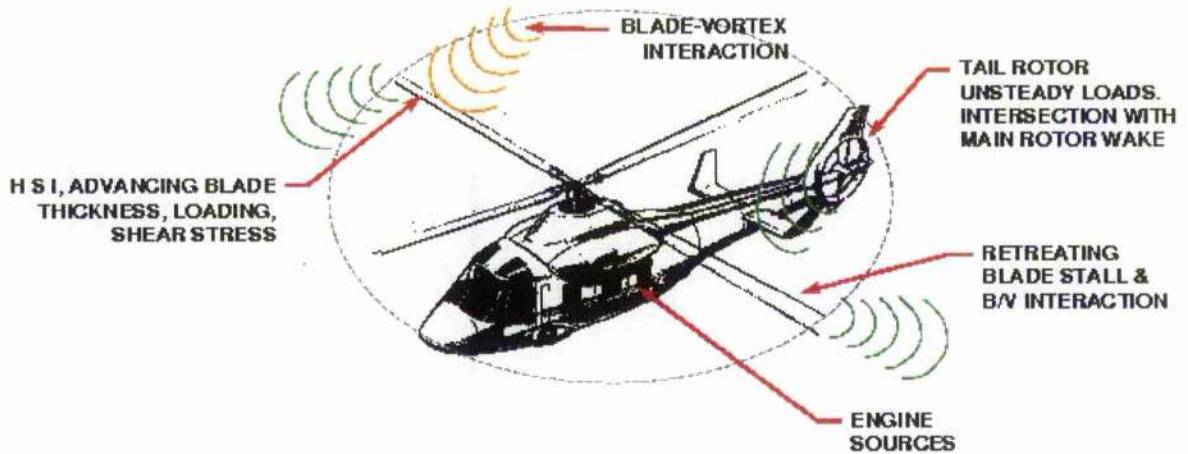


Figure 1.3: Aeroacoustic noise sources for a rotorcraft (Edwards and Cox [3]).

HSI produces blade thickness and quadrupole noise whereas BVI is characterised by blade thickness and loading noise. The typical acoustical signature of the BVI and HSI noise are different as depicted by Figure 1.4.

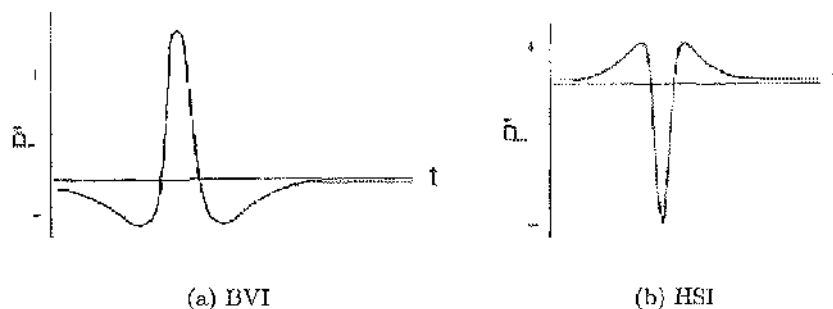


Figure 1.4: Typical acoustical signature of BVI and HSI.

Unlike the slap noise, the thickness noise is more intense ahead of the rotor in the plane of the rotor [11] and varies only slightly in a horizontal plane ahead of the rotor axis [14]. The thickness noise is driven by tip Mach number. However, it dominates only for forward speed at high advance ratio. The importance of BVI became particularly apparent as a result of the introduction of the Bell UH-1 range of helicopters, with their highly loaded/high tip speed two-bladed main rotor, and the Boeing Vertol V107, and later Chinook, range of tandem rotor helicopters. Helicopter tip speed was afterwards not considered as the primary noise source for civil helicopters and the interest in BVI in descent increased, especially with the development of modern helicopters with high blade loading.

A comparison by Wagner [15] between the thickness noise and the BVI noise signatures is depicted in Figure 1.5. This reveals that BVI is the most annoying type of noise for at least two reasons. First, it occurs in the middle of the audible frequency range as mentioned in [16] (see Figure 1.5). Secondly, as shown in figure 1.6, BVI is present during rotorcraft approach landings, which is very likely to affect populated areas. It also raises the issue of acoustic detectability of the helicopter for military operations [13]. Since BVI is a limiting factor in public acceptance of helicopter operations [17], it is thus relevant to try to understand the mechanisms.

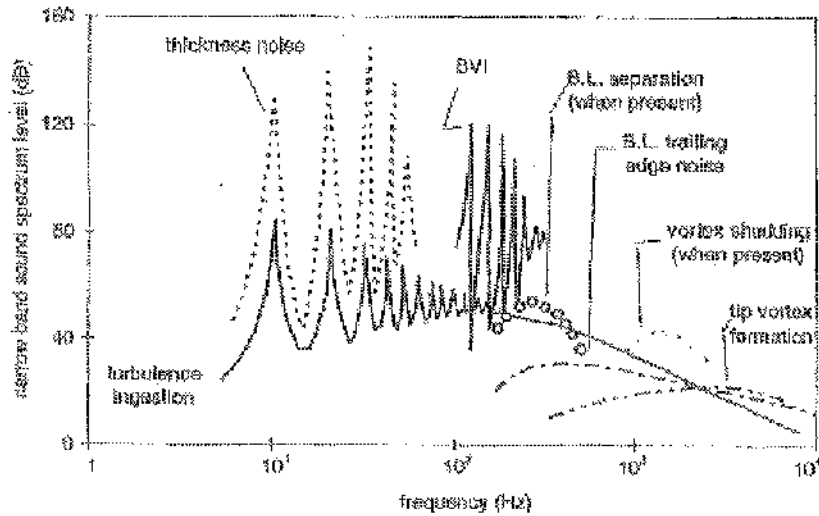


Figure 1.5: Sound Pressure Levels Spectrum of the rotational noise sources for a rotorcraft (Levertan [4]).

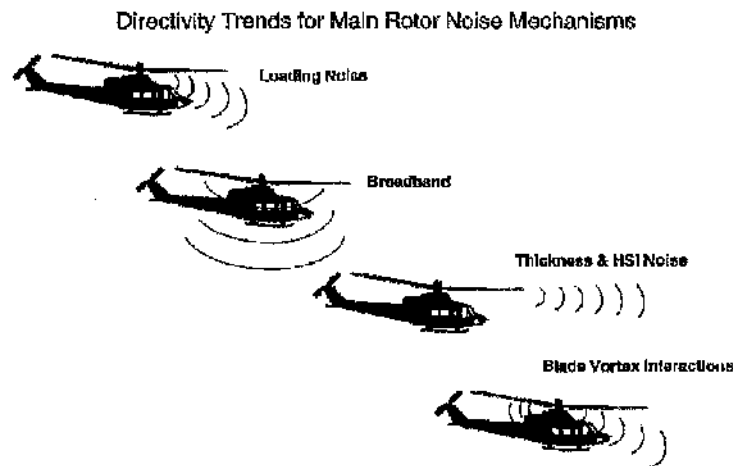


Figure 1.6: Directivity of the different components of the rotational noise [3].

BVI noise is characterised by different acoustical waves [18]. First, acoustical waves are generated due to the oscillation of the stagnation point at the LE of the aerofoil. These waves, named compressibility waves, propagate upstream and away from the LE and are present for all types of BVI at high subsonic flow. Trailing-edge acoustical waves or "Kutta" waves [19] also propagate upstream away from the trailing-edge but their contribution to the BVI noise is secondary. This is not the case for the transonic wave which can dominate when the the vortex-induced velocity is severe enough to generate a supersonic pocket. This results in a shock wave which propagates upstream in a downwards inclined direction. The contribution of these acoustical waves which are characterised by different directivity patterns explains the difficulties encountered for the prediction of BVI noise.

### 1.3.2 Blade-vortex interaction

BVI is triggered by the collision of the rotorcraft wake and the blade. The tip vortices produced by a blade roll-up, leading to the formation of a wake of vortices. Then the wake may propagate and cross the trajectory of a blade. For a rotor operating in a steady descending flight, a positive inflow tends to force the epicycloid-type pattern into the rotor disk plane, causing strong BVI (see Figure 1.7(a)). The wake is then located in the tip path plane of the rotorcraft, i.e. in the plane which is delimited by the disc described by the blades. BVI occurs any time the wake passes by the tip path plane such as for landing approach. Stronger BVI noise is found for a back tilted rotor which is constantly operating in its own wake [6] and occurs mainly for forward and descending flights. Figure 1.7(b) indicates the flight conditions in terms of the rate likely to create BVI.

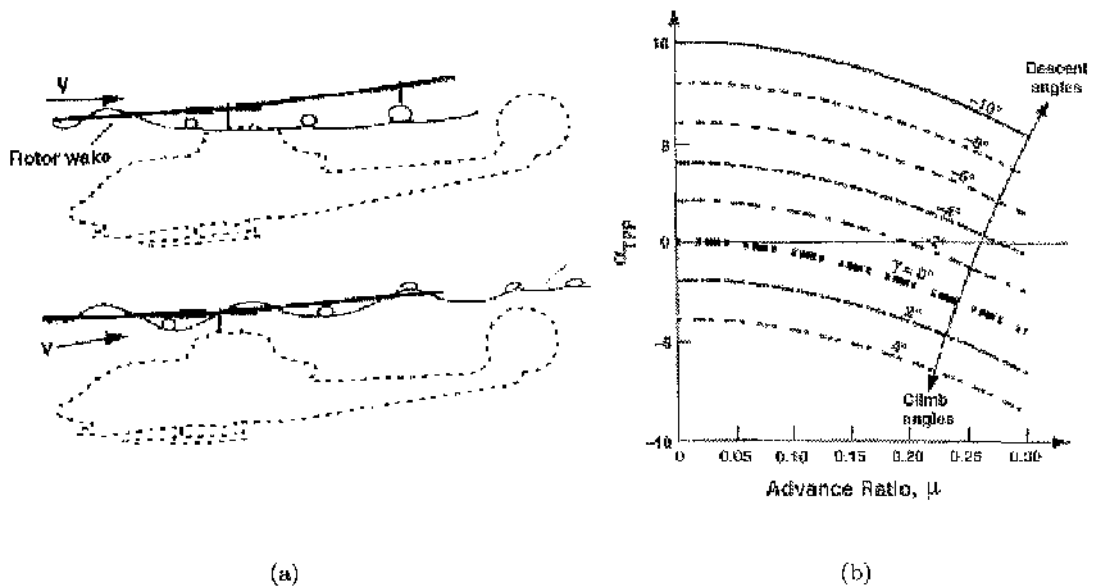


Figure 1.7: (a) Wake of the helicopter encountering the main rotor and creating BVI [5]. (b) Flight conditions likely to create BVI [6].

Depending on the flight conditions, the number and the nature of the interactions vary as depicted in Figure 1.8(a). The type of BVI which can occur both on the advancing and retreating sides of the helicopter rotor are generally not of the same nature. Indeed, on the advancing side, the vortex is more likely to encounter the blade with its axis of rotation parallel to the spanwise direction of the blade. On the retreating side, parallel BVI may also occur. However, the vortex is more likely to rotate anti-clockwise and the flow velocity is of a lower magnitude than on the advancing side over each blade section. Figure 1.8(b) shows the difference between BVI on the advancing and retreating side. Note that "four different types of BVI have been identified on the

advancing side of the rotor” by Sim and Schmitz [7]. The same remark is valid for the retreating side. Their respective acoustic radiation and directionality features are different. This is attributed to their different phasing characteristics.

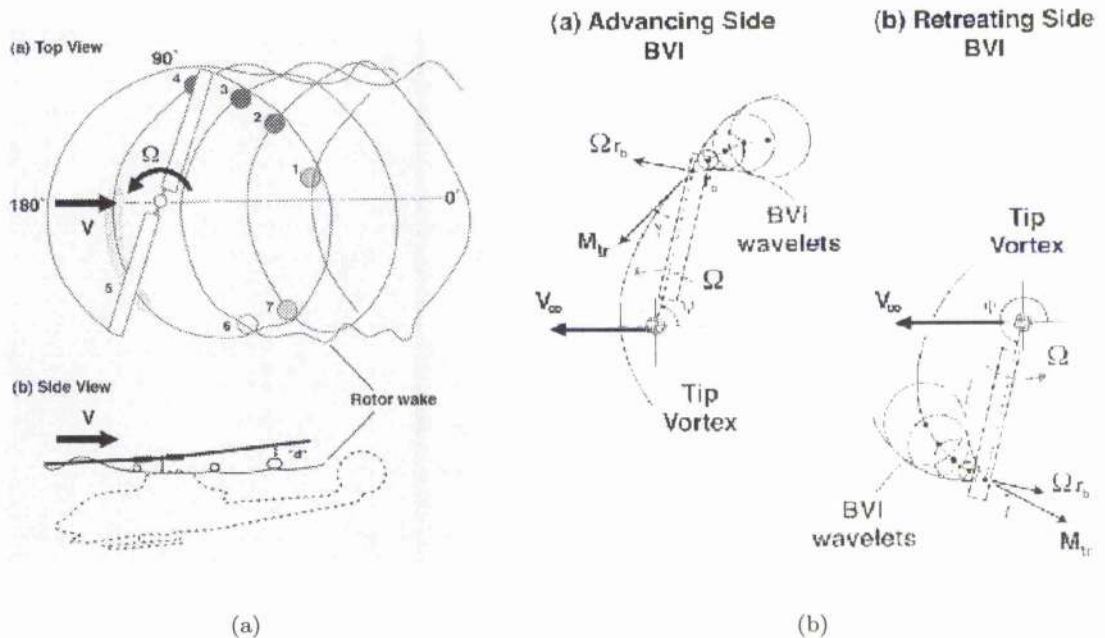


Figure 1.8: (a) Locations of the BVI. (b) Differences between BVI on the advancing and retreating sides (Schmitz [6, 7]).

The BVI noise generated on the advancing side of the aerofoil is generally considered as the main noise source for BVI as mentioned by Brentner and Farassat [1] (see Figure 1.9). Indeed, parallel BVI occurs on the advancing side of the blade and results in the strongest noise radiation while retreating side BVI is much less intense, radiating downward and rearward [7, 11]. Different experimental and computational studies prove that the parallel BVI occurring on the advancing side contributes significantly to the noise levels. Furthermore, in transonic flow, the supersonic pocket which may be generated by the passage of the vortex can contribute significantly to the overall noise levels. This illustrates why helicopter blades which operate at transonic tip Mach numbers are the most likely to be affected by BVI due to the presence of the shock waves and local supersonic regions.

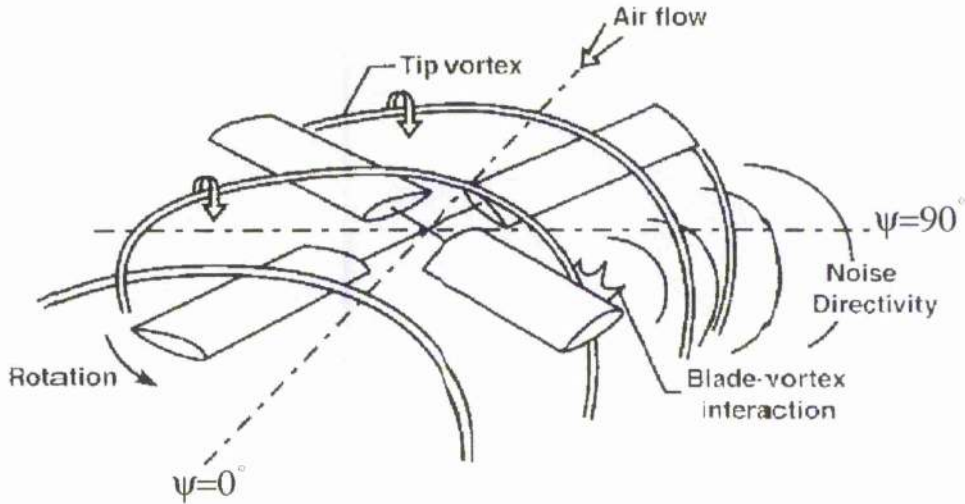


Figure 1.9: Creation of the blade-vortex interaction noise [1].

The BVI noise directivity pattern given by Hu [8] is depicted in Figure 1.10 for a descending flight. The high directivity of BVI which is a function of the lift forces underlines the importance of the prediction of the load pressure distribution if the acoustics of BVI is to be studied. Hence the simulation of BVI noise requires the exact determination of the blade loading distribution and of the geometry of the wake which will determine the location of the BVI.

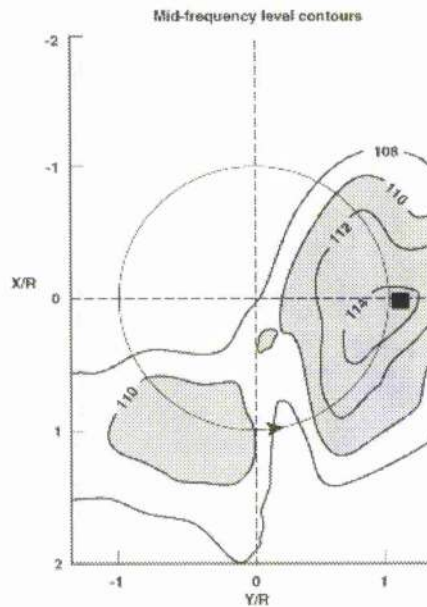


Figure 1.10: Typical directivity of the sound for the BVI of a helicopter in descending flight [8].

### 1.3.3 BVI noise alleviation

There are several BVI parameters which are known to influence its aerodynamic and acoustic signature: the airfoil shape (thickness, leading-edge radius, camber), the vortex properties (vortex core radius, vortex strength, miss-distance) and the location of the vortex impact on the blade (spanwise location of the interaction, interaction angle in the blade-shaft plane, interaction angle in the disk plane). Some studies [20] also considered the influence of parameters such as the blade thickness, the twist distribution, the chord length distribution and the quarter chord line geometry. The influence of some of these parameters have been assessed in the literature.

The modification of the effective thickness and camber [21] is a possibility for BVI reduction. The reduction of the vortex strength [5] and of the modification of the turbulence along the blades via the use of surface blowing-suction [21] have also been identified as viable techniques for BVI reduction. The impact location is also considered as a very important parameter [22]. Indeed, it was shown that the shaft plane interaction angle affects the interaction length of the BVI, reducing the BVI noise. This is one of the reasons why anhedral tips were found to be able to reduce BVI noise and to improve hover performance. In a similar way, BVI reduction can be obtained by avoiding or delaying parallel interactions [8]. Oblique interactions are actually more gradual and affect more the vibratory loading [23], leading to lower levels of BVI noise.

Although different techniques exist for reducing the BVI radiated noise, it is still not clear if it is feasible from a commercial point of view [5]. Hence industry started to be interested in active models which are nowadays preferred. So far, the increase of the miss-distance seems to be "the most effective in reducing noise whereas a decrease of the vortex strength is most effective in reducing vibration" [22]. The wake geometry depends strongly on the motion of the blade. As stated by Tung *et al.* [24], the change in the distance from the blade to the vortex is the major factor for BVI noise alleviation. A mechanical control can be exerted on the blade motion which influences strongly the wake geometry, the miss-distance being influenced by tip vortex trajectory, blade elastic deformation and induced velocity distribution [8]. Some different approaches have been conducted and are currently the most realistic and the most likely to be used by the industry:

- The control of the orientation of the helicopter blades, e.g. the High Harmonic Control (HHC) system [25, 26] allows an increase of the distance between the vortex and the blade (for more details, see [27]). Note that a technique named Independent Blade Control (IBC) which defines the pitching angle of the blade has promising capabilities for BVI alleviation. The appropriate modification of the blade angle of attack can compensate the vortex-induced angle of attack, leading to a reduction of the typical BVI waves at high subsonic and transonic flows [28]. Both techniques HHC and IBC have been proved to be respectively very efficient for reducing BVI vibration and BVI

### BVI noise alleviation

noise.

- Another way of controlling BVI is actually via the control of the flight conditions. The concept proposed by Schmitz [5] is to alter the near-zero inflow conditions by adding a force which modifies the tip-path plane angle. An adapted use of the acceleration and deceleration of the helicopter can have a significant effect on the BVI noise.

However, both approaches require a good understanding and high level of skill from the helicopter pilot. A design challenge is to find a workable system for the BVI reduction which does not complicate the piloting. BVI alleviation passes by a complete understanding of the mechanisms which are involved in the BVI aerodynamics and acoustics [18] for subsonic and transonic flows. This explains why it is still the subject of numerous experimental and theoretical investigations [29, 30, 31].

## 1.4 Techniques to predict BVI aerodynamics

As mentioned by Brentner and Farassat [1], the challenge consists mainly of determining the wake and predicting accurately the tip-vortex. Great progress has been made in the analysis of rotorcraft performance and characteristics through theoretical research and experimental investigation. The next section presents a review of the progress made in the experimental and computational research areas for BVI.

### 1.4.1 Experimental BVI Studies

#### 2D measurements

Two different set-ups have been used for experimental investigation [18]; i.e. through use of the wind tunnel or the shock tube, using pressure measurements and interferometric techniques respectively. The output data from the wind tunnels are usually of better quality but a real single vortex with no interactions caused by wall effects is difficult to obtain. Vortex filaments created by a vortex generator implied that the condition for an isolated encounter is also not always met [32]. The shock tube allows single vortex studies, however, shock wavelets resulting from reflections of the primary shock leads to less accurate results. The use of both wind tunnel and shock tube experiments [9, 18] has been preferred by some experimentalists.

Two-dimensional measurements represent a simplified problem since the structure of the near wake depends on the blade loading distribution, meaning that a fixed wing and a blade do not interact with a vortex in the same way [33]. Indeed, a large spanwise velocity variation which is due to centrifugal effects exists on the pressure side of the rotor. Experiments are also difficult to conduct due to the importance of the 3D effects when a vortex is present. However, they allow the decoupling of the various acoustical phenomena which allows an easier interpretation of the mechanisms. An upstream

---

## 1.4. TECHNIQUES TO PREDICT BVI AERODYNAMICS

vortex can be generated in a wind tunnel by a pitching aerofoil or in a shock tube, the initial vortex being produced by the interaction of a shock with an aerofoil [23].

### 3D measurements

3D experimental data are very valuable since they include all the flow non-linearities. Different techniques exist for the flow visualisation. The Projected Grid Method is one of the measurement techniques. A projected video grid image is taken at different times. It is used for determining the deflection and deformation of the blade. The Laser Light Sheet uses a light sheet which is positioned into the flow field. An interferometric system is then used to detect how the light is scattered and refracted from individual flow particles in the light sheet which is imaged onto a camera. It allows the visualisation of the flow structures, more particularly of the vortex geometry and blade-vortex miss-distance. Particle Image Velocimetry (vortex velocity fields - PIV) [21] is another flow visualisation system which allows the calculation of the velocity field. A laser highlights individual particles of the flow at different times. Then the calculations of the distance between the particles allows the recomposition of the velocity field. The flow may also be visualized with Schlieren techniques which consist of recording the density gradient in the flow direction. The rays of a light source which are beamed by the flow inhomogeneities allows the determination of the density gradient via the use of an optical system. In most experiments, models are used to simulate the flow around an aircraft, to take some acoustic measurements [1]. On one hand, the experiments are still difficult and expensive to conduct. On the other hand, although more accurate than for 2D, the flow data have to be carefully interpreted since the flow around the model may not be representative of the full-scale flow. Hence the rotorcraft industry uses 2D experiments to get an insight into the flow mechanisms and uses the 3D data for the development of techniques such as prediction methods as design tools.

#### 1.4.2 Development of semi-empirical formula

The prediction of BVI airloads necessitates accurate prediction of the blade motion and the wake geometry [24]. The wake geometry and vortex strength are actually two major parameters affecting the BVI noise signature. Kitaplioglu and Caradonna [34] proved that most methods assuming that the wake and the tip vortex geometry and strength are known are capable of predicting correctly the airloads and the noise of a helicopter. The accuracy of the rotor wake remains therefore crucial but difficult to obtain.

Wake models are used to simulate the vortex disturbances on loads computations. They are aimed at predicting the tip vortex structure and the flowfield velocity in the rotor wake. The wake is usually decomposed into two parts: a near wake of trailed and shed vorticity behind the wake and a far wake comprising tip vortices which roll-up downstream of each blade [35]. In many rotor codes, the tip vortex and the inboard

#### Development of semi-empirical formula

sheet are modelled as a collection of straight vortex segments. The velocity induced by the wake is calculated from the Biot-Savart law which may be modified to account for the effects of the viscosity. The rotor blade aerodynamics are generally modelled using either a lifting line or lifting surface approach [2]. In these panel-like methods, each blade is discretised into aerodynamic segments with a bound vortex the strength of which is determined with the wake induced airloads. Then the integration of the segments loads along the span and around the azimuth gives the aerodynamic coefficients of the rotor, e.g. the BVI loads. Note that the Biot-Savart law is only valid for incompressible flow. Therefore, the compressibility effects are included by the use of the Prandtl-Glauert compressibility corrections [2].

Several wake models of different complexity can be used for the determination of the wake geometry. Since it is known that the contraction of the wake must be accounted for, some wake models utilise experimental data or numerical results to locate the wake position. Such models are termed prescribed wake models. Although they are very efficient computationally, they can only be applied provided that experimental data exist for the specific flight conditions. Models such as the Beddoes/Leishman model also use empirical factors which are chosen following the comparison between experiment and calculations. However, wake models may give different blade-to-vortex distances, which is of great importance for the BVI noise study as shown by Schmitz [6].

Another method is the free wake analysis which avoids the difficulty of prescribing a wake geometry. Free wake models have been developed since wake models should be adapted to complete helicopter configurations. The geometry of the wake is calculated using the local velocity field which is induced by each vortex lattice. This model presents the advantage of allowing the wake to develop in time [35]. The unconstrained wake is permitted to move freely with the local velocities which exist in the wake. Therefore, the effects of all the wake components and the influence of the blade determine directly the vortex system motion. It has to be pointed out that the free wake model requires a Partial Differential Equation to be solved in the time domain. They are therefore more expensive computationally than the prescribed vortex models, although this is more and more affordable for the rotorcraft industry due to the increasing performances of the computers in terms of memory and speed.

These wake models are still being enhanced in conjunction with the use of experimental data by research institutes. The wake model for the aerodynamic analysis by ONERA improved its vortex core radius evolution law based on the preliminary analysis of the laser Doppler velocimetry measurements [27]. A good example of what can be achieved in terms of aerodynamics and noise prediction is illustrated by Gallman *et al.* [27]. It was found that an improvement of the reorientation of the wake geometry with respect to the tip-path-plane allowed better aeroacoustic predictions [27]. However, it is important to note that the current wake models still contains various simplifications and approximations and that they are also prone to numerical problems. As shown by

Rahier and Delrieux [36], the whole lattice approach appears not to be capable of correctly simulating the local wake rolling-up and the vortical concentration, the model of which leads to better qualitative and quantitative aerodynamic and acoustic prediction. Furthermore, it also remains more difficult to develop free wake models for transonic flow. Any prediction tools have to be tested against experiments as Caradonna *et al.* [37] did for their acoustic predictions. Models often need enhancement so that they can be applied to a larger range of problems, therefore simulation of the full problem is advisable.

### 1.4.3 Numerical simulation of BVI

The simulation of BVI requires the accurate prediction of the loads [4] which results from the interaction between the vortex and the aerofoil. It is therefore necessary to account for the non-linearities of the flow if the compressibility effects are strong. Different techniques can be used for the prediction of the blade loads. Different models were compared [30]: indicial methods, vortex cloud, 3D full-potential methods, Boundary Element Method (BEM) and compressible Euler/NS CFD methods. The existing methods differ in the way that non-linearities of the flow are taken into account. A brief description of three methods which have been used by the industry is given.

First, one of the methods used the most in the industry is the indicial method. It is based on indicial models using semi-empirical coefficients for the prediction of aerodynamic loads [38]. Lifting line theory is used to predict the lift on the blade as it traverses around the azimuth. The main advantage of this method is the important saving in computational cost. A more advanced technique which can also provide the BVI loads is the semi-Lagrangian method called cloud-in-cell method [39]. It decomposes the vortices into small eddies and the cloud of eddies behaves like a vortex when some specific conditions are respected. Although it is incompressible, it accounts for the vortex deformation [40].

Secondly, helicopter aerodynamic researchers have generally given their attention to full potential methods. Although the full-potential model assumes that the flowfield is both irrotational and inviscid, transonic flow prediction remains accurate for transonic flow [41] since the flow in this case is driven by inviscid effects and since the shocks are not strong enough to generate vortices with large effects on the flowfield. However, this may lead to errors in the calculations of blade aerodynamic characteristics.

Thirdly, BEM offers the advantage of ease of understanding and use combined with minimal computation requirements. Although BEM methods are still popular for wind turbine designers as explained by Wang [42], they are unlikely to be useful for rotorcraft simulations because of the wide range of flow conditions that a helicopter can encounter.

Finally, the recent development of CFD allows the simulation of the helicopter flowfield [1, 43]. CFD remains a very attractive tool since its progress has opened new

possibilities of the simulation of the time evolution of the rotor flow-field. The main difficulty of most CFD solvers remains the preservation of the vortex characteristics which is crucial for simulating BVI. Indeed, CFD solvers tend to dissipate small disturbances in the flow field. Upwind and dissipative schemes work fairly well in problems where acoustic or vortical disturbances are not of interest since in most of the cases the flow physics of the problem is not altered by the inherent numerical dissipation. In aeroacoustics problems, however, this situation is not acceptable. Not only acoustic disturbances but flow structures may be affected by the properties of numerical schemes. A well-known example is the convection of vortices where the core properties are altered during calculation.

Such problems can be tackled by the use of new and powerful algorithms which can capture accurately the pressure changes along the blade. Different methods have been applied in the literature to preserve vortices. The prescribed-disturbance method, which modifies the velocity components according to the vortex properties, was used to overcome the dissipation of the vortex by the solver [44]. Local grid refinement [16] and unstructured adaptive meshes [45, 46] can also be used to preserve the convected vortex. Another technique is however preferred at present, with better properties both in terms of acoustics and dissipation of vortices offering substantial improvements over conventional second/third order schemes. This consists of calculating the flow gradients very accurately to limit the inherent dissipation of the solver, resulting in well-preserved vortices. Various different spatial schemes have been developed. They can be separated into two groups: Essentially Non-Oscillatory schemes [47, 48, 49] and compact schemes [50, 51, 52, 53, 54, 55, 56, 57]. Both types of schemes allow a spatial accuracy of five orders or more and have successfully been used for BVI simulation [58, 59]. However, their implementation is not trivial and requires a significant investment. Furthermore, problems of robustness can be encountered when calculations are run on coarse grids. In practice, this may result in loss of efficiency and stability during calculation. The adopted approach is therefore to calculate BVI using a method called the Compressible Vorticity Confinement which allows the conservation of vorticity on coarse grid with a minimal overhead in CPU time. The advantage of the CVCM is that it allows the use of relatively coarse grids along the vortex path and refined grids near the aerofoil so that accurate predictions of the surface pressure and reasonably well-preserved near-field acoustical waves can be obtained.

## 1.5 Techniques to Predict BVI aeroacoustics

Aeroacoustic research has been marked by considerable achievements since its foundation by Lighthill [60] in 1952. The study of various fields of interest such as helicopter and propeller acoustics, and the fan noise has led to the enhancement of models and numerical methods for noise prediction. Hence the development of vibro-acoustic models

allowed the evaluation of different kinds of control systems to reduce noise and vibration for the interior noise of propellers and helicopters. The development of semi-empirical prediction method for the broadband noise of subsonic fans can also be mentioned [61]. Such improvements were made possible by the conclusion of some important research programs [29] which provided valuable databases for testing acoustics code. Indeed, some experiments have been conducted in wind tunnels [29, 30] and at full scale using arrays of microphones for the determination of the farfield noise. An important set of experimental data was therefore generated for the BVI study, not only for the aerodynamics, but also for the acoustics. This was motivated by the determination of the rotorcraft industry to understand what are the most effective techniques for BVI alleviation.

A better understanding of the BVI mechanisms gave some insight on how the farfield noise could be more accurately predicted. It is known that it is imperative to consider the effects of non-linearities of the flow which are contained in the acoustical BVI response. These effects are usually represented by the time evolution of the BVI loads as long as no shock waves are present. Linear theories for the noise propagation can then be applied for the prediction of the farfield noise, using the BVI loads. They present two advantages. Not only are they cheap in terms of computation, but also their formulation is exact. Two different formulations have been used in the literature: the Kirchhoff [41] and the Ffowcs Williams-Hawkings (FW-H) [62] methods. The choice between these two methods mainly depends on the quality of the nearfield acoustics predicted by the solver. Note that, even though the BVI loads may not be representative of the BVI aerodynamics at high subsonic or transonic conditions, depending on the severity of the BVI, they are used intensively by industry since they are reliable for the other cases and since they allow a relative comparison between the different types of BVI.

## 1.6 Scope of the study

The dissertation is composed of seven chapters as follows

The introductory chapter presents the scope of the dissertation and outline.

Chapter 2 describes the features of the employed CFD and CAA solvers. The time-stepping method and the Compressible Vorticity Confinement are described. The formulation of the CAA module is given.

Chapter 3 illustrates the capabilities of the CFD solver for the prediction of rotorcraft flowfields. It presents the results of 3D calculations which were run to highlight the robustness and the reliability of the implemented time stepping scheme. Then the

---

## 1.6. SCOPE OF THE STUDY

capabilities of the Vorticity Confinement Method for preserving the characteristics of the vortices are assessed. The method is tested for 2D flows and several BVI cases are simulated using CFD, the results being compared against experimental data.

Chapter 4 discusses the optimisation of the two-dimensional BVI simulation. Parameters such as vortex models, initial vortex location, spatial and time refinement, angle of attack and turbulence models have been examined. The influence of the Vorticity Confinement Method on the results is also investigated.

Chapter 5 is dedicated to the presentation of the inviscid and viscous calculations for the BVI study. The investigation is confined to simplified 2D flow geometries. A parametric study is undertaken to highlight the difference of aerodynamic behaviour between different aerofoils and flow conditions. The influence of the Mach number, vortex strength, vortex core radius and miss-distance on the BVI is also assessed.

Chapter 6 reviews the aeroacoustic approach and discusses the prediction of the nearfield and farfield acoustics for the different types of BVI simulated. Results are analysed and discussed.

Chapter 7 draws the conclusions from the present work and discusses further work.

With the exception of the opening and concluding chapters, every chapter is composed of an introduction to its topics, a presentation of the results followed by a discussion and a conclusion based on the content of the chapter.

## Chapter 2

# Mathematical models

This chapter describes the characteristics of the CFD solver along with the aeroacoustic methods currently available for the prediction of the farfield BVI noise.

### 2.1 Introduction

The EROS project [63] was a European project involving industries, universities and research establishments in Italy, United Kingdom, France, Germany and the Netherlands. This code started from the industrial requirement for a CFD tool adapted for the study of helicopters. The objective was to develop a CFD solver for the European Rotorcraft industry. It was aimed at correctly predicting unsteady blade pressures over a range of different flight conditions, from hover to high speed forward flight.

A grid generator called GEROS [64, 65] was developed within the EROS project. The grid generation is an essential part of such a simulation system because of the unique requirements that have to be fulfilled for rotorcraft simulations. Since GEROS contains all the adaptive geometry facilities for rotating configurations, it is fully developed for rotorcraft study. With this code, the blades can be designed to reduce pilot control-loads, increase the performance of the helicopter, and quantify aerodynamic noise sources.

For the high vorticity regions of the flow, the farfield conditions have to be constantly adapted to capture the helical rotor wake over large distances from the rotor blade tip plane. These requirements justify the use of moving geometry characteristics for the grids. The GEROS code is adapted to multiblade calculations and is capable of generating overlapping grids called Chimera grids with respect of the above conditions. Each domain of the individual rotorcraft components and each interesting flow-field region can be covered by high quality grids, making the Chimera method very flexible. O, C, H topologies can be used. Each of the topologies has its own characteristics for capturing shock waves and tip vortices (for more details, see [63]).

The EROS code solves the Euler equations using a finite volume approach and an implicit dual-time method. Implicit dual-time allows an implicit discretisation to be used in real-time, but at each time step, the solution in a pseudo time marches to steady state. This not only permits the use of acceleration techniques but also allows the choice of real time step based on accuracy requirements only, an important aspect for Euler codes.

The second order Roe discretisation coupled with the time-stepping Factored - Unfactored method (FUN) was initially used. This implicit time-marching method [66] was proposed as an alternative to the Alternating Direction Implicit (ADI) method for three-dimensional flows: it was shown that better efficiency was obtained when compared with the standard ADI method. This method results in a two-factor linear system, the system being treated as unfactored for each spanwise slice and as factored in the spanwise direction. The linear system is solved using a Conjugate Gradient Method (CG) with a preconditioning strategy based on a Block Incomplete Lower-Upper (BILU) factorisation. It presents the advantage of preserving its stability properties in three dimensions and of reducing the factorisation error effects.

A stability analysis [67] has shown that the method has similar stability properties to the two-factor ADI method in two dimensions, which represents a significant improvement on the behaviour of the three-factor ADI method in three dimensions. However, it was suggested that the factorization error of the FUN method could be significant. Therefore, the UNFACTored method which solves the three-dimensional system of equations without factorization was proposed as an alternative. The objective was to improve the Euler solver in the EROS code, which resulted in the implementation of a new time-marching implicit scheme. Indeed, a satisfactory resolution of the BVI physics requires high fidelity numerics to represent correctly the aerodynamics and the dynamics of the helicopter and the resulting noise.

Different approaches can be used for the prediction of BVI noise. One approach for predicting the noise is based on a series of steady-state conditions. The resulting method [6] is quite attractive but has a drawback: it cannot take into account the acceleration effects of the helicopter. The adopted approach consists of using the CFD data along with an aeroacoustic module based on the Lighthill's analogy [60] for the prediction of the farfield noise. This is rendered possible since the radiated noise is related to the aerodynamic characteristics of the blade, i.e. the load pressure distribution along the blade.

The objective of this chapter is to review the main characteristics of the CFD and CAA solvers. The governing equations along with the time and spatial discretisations are presented for the Euler solver for clarity. The characteristics of the different turbulence models are also given for the Reynolds Averaged Navier-Stokes (RANS) equations. Once the CFD solver has been described, the features of the Computational Aeroacoustic (CAA) solver are discussed. The way the CFD data can be used by CAA

## 2.1. INTRODUCTION

for the prediction of the farfield noise is examined. Existing techniques are reviewed and finally the model used is given.

## 2.2 The CFD solver

### 2.2.1 Model equations of the Euler code

The model is based on the standard Euler equations but contains some extra-terms due to the use of the different frames of reference. The inertial frame of reference is used for the computation of the fluid velocity. The non-inertial frame linked to each blade makes the calculation of the fluxes less expensive. Since the speed of the relative frame does not have to be considered, the grids around the blade do not change in time. Then, the computation time for a set of Chimera grids is shorter. The Euler equations can be written in integral form:

$$\int_{\mathcal{V}(t)} W d\mathcal{V} + \int_{\Sigma(t)} [F.n - W(v.n)] d\Sigma = \int_{\mathcal{V}(t)} S(W) d\mathcal{V}. \quad (2.1)$$

Each term of this equation represents a specific aspect of the physics. The volume integral  $\int_{\mathcal{V}(t)} W d\mathcal{V}$  concerns the amount of conserved quantities in the volume  $\mathcal{V}(t)$ . The surface integral  $\int_{\Sigma(t)} [F.n - W(v.n)] d\Sigma$  represents the convective change in the same volume. Finally, the source term  $\int_{\mathcal{V}(t)} S(W) d\mathcal{V}$  is necessary to consider the change of frame for the calculations.

### 2.2.2 The numerical schemes

The three-dimensional Euler solver uses a cell-centred finite-volume method with a dual-time implicit scheme. This is now described.

#### The finite volume method

According to the finite volume method, Equation 2.1 can be discretised for each cell as follows

$$\frac{d}{dt} (W\mathcal{V}_{i,j,k}) + R_{i,j,k} = 0. \quad (2.2)$$

Three conditions have to be respected for this method. First, the surfaces related to the cell volume have to be closed; secondly, the blade surface, the inboard cylinder and the farfield boundary conditions have to be applied carefully; finally, the Geometric Conservation Law has to be respected in the case of a deforming grid. Note that the last condition defines the relation between the volume change due to the grid speeds and the size of the time step.

#### The spatial discretisation schemes

The calculations of the surface integrals require the use of spatial discretisation schemes. Two of them can be used in the EROS solver: central and upwind differencing.

## 2.2. THE CFD SOLVER

The central scheme is the most common one and uses the average of the conservative variables to calculate the flux vector on the volume cell face. This scheme is not stable and some artificial dissipation is needed according to Jameson [68]. This is necessary to damp the high frequency oscillations.

An upwind scheme has also been implemented: the Roe flux-splitting scheme [69] with the TVD modified flux approach of Yee and Harten [70]. This scheme is based on the theory of the wave propagation and uses a MUSCL interpolation for the conservative variables to give second-order accuracy. The limiter is of Albada type. The LHS has been constructed to first order accuracy and the RHS at a higher one: it was shown that a reduction in the convergence time [71] was obtained for this approximate linearisation.

### The implicit dual-time method

The implicit dual-time method proposed by Jameson [72] is used for time accurate calculations. The residual is redefined to obtain a steady state equation which can be solved using acceleration techniques. The system of equations which is considered is the following:

$$\frac{dW_{i,j,k}^{n+1}}{dt^n} + \frac{1}{V_{i,j,k}} R_{i,j,k}^* (W^{n+1}) = 0,$$

with

$$R_{i,j,k}^* (W^{n-1}) = \frac{3V_{i,j,k}^{n+1} W_{i,j,k}^{n+1} - 4V_{i,j,k}^n W_{i,j,k}^n + V_{i,j,k}^{n-1} W_{i,j,k}^{n-1}}{2\Delta t} + R_{i,j,k} (W^{n+1}) = 0.$$

Therefore,  $W^{n+1}$  becomes the solution of the Euler equation at the new time level when the pseudo-residual  $R_{i,j,k}^* (W^{n+1})$  is equal to zero. Moreover it is possible to use acceleration techniques to accelerate convergence.

### The implicit time-marching method

A previous study [63] showed that the spatial Roe discretisation coupled with the implicit Factored-UNfactored method (FUN) was the more capable numerical scheme for aerodynamic prediction of the blades. This two-factor method solves the linear system by using a conjugate gradient type method with preconditioner as explained in [63]. The linear system is solved via a matrix inversion which is calculated at a lower cost using the ADI approximation. After the preconditioning, the conjugate gradient method is used to determine an approximation of the solution of the system by minimizing the residual error (for more details, see [66]). One implicit step can be

written as

$$\begin{aligned} & \left[ \left( \frac{\nu}{\Delta t^*} + \frac{3\nu}{2\Delta t} \right) I + \frac{\partial R_i}{\partial W} + \frac{\partial R_k}{\partial W} \right] \\ & \left[ \left( \frac{\nu}{\Delta t^*} + \frac{3\nu}{2\Delta t} \right) I \right]^{-1} \left[ \left( \frac{\nu}{\Delta t^*} + \frac{3\nu}{2\Delta t} \right) I + \frac{\partial R_j}{\partial W} \right] \Delta W \\ & = -R^* W^m. \end{aligned}$$

Regarding the three-dimensional flows, the FUN method consists of a factorisation in the spanwise direction (see [67]). The system is therefore solved successively in one dimension (spanwise direction) and in two dimensions (streamwise direction). The main advantage of the FUN method is the small size of the matrices, that means a reduced memory requirement. However a comparison of the EROS code with the University of Glasgow PMB3D code pointed out that slow convergence behaviour in the FUN method could come from the factorisation error. Another comparison of different test cases confirmed that the UNFACTored method used at the University of Glasgow could be considered as one of the alternatives to remedy such a problem.

The UNFACTored method solves the system of equations in three dimensions. The UNFACTored system of equations can be represented by

$$\begin{aligned} & \left[ \left( \frac{\nu}{\Delta t^*} + \frac{3\nu}{2\Delta t} \right) I + \frac{\partial R_i}{\partial W} + \frac{\partial R_j}{\partial W} + \frac{\partial R_k}{\partial W} \right] \Delta W \\ & = -R^* W^m. \end{aligned} \quad (2.3)$$

The advantage of such a scheme is the absence of the factorization error, the drawback is the use of larger matrices at the cost of an increased memory.

### 2.2.3 Navier-Stokes equations and turbulence models

Only inviscid calculations could be run at the time of the present work within the framework of the EROS project. Therefore, the Parallel Multi-Block (PMB) code of the University of Glasgow was used for the 2D BVI simulations since it allows the use of various turbulence models. The way the Navier-Stokes (NS) equations are handled is presented now.

#### Governing equations and principles

The governing equations of a viscous fluid in motion are the flow conservation laws and the fluid properties laws.

- Continuity equation

$$\frac{\partial \rho}{\partial t} + \frac{\partial (\rho u_i)}{\partial x_i} = 0. \quad (2.4)$$

- Conservation of momentum

$$\frac{\partial(\rho u_i)}{\partial t} + \frac{\partial(\rho u_i u_j)}{\partial x_j} = \rho f_i - \frac{\partial p}{\partial x_i} + \frac{\partial \tau_{ij}}{\partial x_j}. \quad (2.5)$$

with

$$\begin{cases} \tau_{ij} = \mu \left[ \left( \frac{\partial u_i}{\partial x_j} + \frac{\partial u_j}{\partial x_i} \right) - \frac{2}{3} \delta_{ij} \frac{\partial u_k}{\partial x_k} \right] \\ \mu = 1.458 \times 10^{-6} \left[ \frac{T^{3/2}}{T+110.4} \right]. \end{cases} \quad (2.6)$$

- Conservation of energy

$$\frac{\partial E}{\partial t} + \frac{\partial}{\partial x_j} [u_j (E + p)] - \frac{\partial}{\partial x_j} (u_i \tau_{ij} - q_j) = 0. \quad (2.7)$$

with

$$\begin{cases} e = \frac{p}{\gamma-1} \\ E = e + \rho \frac{1}{2} u_i u_i \\ q_i = -k \frac{\partial T}{\partial x_i}. \end{cases} \quad (2.8)$$

- Perfect gas equation of state

$$p = R\rho T. \quad (2.9)$$

Note that the expression of the molecular viscosity  $\mu$  is given by the Sutherland's law.

Since the full resolution of the NS equations requires the consideration of a vast range of length and time scales, the RANS equations are used to limit the computer costs. These are obtained by decomposing the quantities into a mean component, which is time-averaged, and a fluctuating term which represents the effects of the turbulence as

$$u = \bar{u} + u'. \quad (2.10)$$

The RANS equations then become

$$\frac{\partial(\bar{\rho} \bar{u}_i)}{\partial t} + \frac{\partial(\bar{\rho} \bar{u}_i \bar{u}_j)}{\partial x_j} = \bar{\rho} \bar{f}_i - \frac{\partial \bar{p}}{\partial x_i} + \frac{\partial}{\partial x_j} \left( \bar{\tau}_{ij} - \overline{\rho u'_i u'_j} \right). \quad (2.11)$$

An extra term called the Reynolds Stress,  $\overline{\rho u'_i u'_j}$  appears in the momentum equation due to the non-linearity of the convection term. The main problem in turbulence modelling is to calculate the Reynolds stresses from the known mean quantities. The Reynolds stresses are modelled, using the Boussinesq hypothesis, as being proportional to the product of the mean strain tensor and the kinematic eddy viscosity  $\mu_T$ . The Boussinesq hypothesis states that:

$$-\overline{\rho u'_i u'_j} = \mu_T \left[ \frac{\partial \bar{u}_i}{\partial x_j} + \frac{\partial \bar{u}_j}{\partial x_i} - \frac{2}{3} \delta_{ij} \frac{\partial \bar{u}_k}{\partial x_k} \right] - \frac{2}{3} \bar{\rho} \delta_{ij} k. \quad (2.12)$$

where  $k$  represents the specific kinetic energy of the fluctuations and is given by:

$$k = \frac{\overline{u'_i u'_i}}{2}. \quad (2.13)$$

## Navier-Stokes equations and turbulence models

Further modelling is required to compute  $\mu_T$  for the eddy-viscosity models and this is the point where turbulence models come into play. The models used differ from each other with the number of transport equations and the applied constants. The models used in this work are of the one-equation and two-equation models. For both types, the first equation concerns the kinetic energy  $k$ . The 1-equation turbulence models scale the turbulence using dimensional analysis and empirical results whereas the 2-equation models use a second transport equation with variables such as the dissipation rate of turbulence  $\varepsilon$  ( $k$ - $\varepsilon$  model) or the  $k$ -specific dissipation rate  $\omega$  ( $k$ - $\omega$  model). A brief description of the turbulence models is given in this chapter for the RANS equations. Note that the density, velocity components, total energy represent the averaged quantities in the next sections and that a more complete description of the models can be found in [73, 74, 75].

### The Spalart-Allmaras turbulence model

The Spalart-Allmaras (SA) turbulence model is a 1-equation model [76]. The eddy-viscosity ( $\nu_T$ ) is calculated by:

$$\nu_T = \tilde{\nu} \cdot f_{v1}. \quad (2.14)$$

where

$$f_{v1} = \frac{\chi^3}{\chi^3 + c_{v1}^3}, \quad \chi = \frac{\tilde{\nu}}{\nu}. \quad (2.15)$$

$c$  and  $\nu$  are respectively a constant and the molecular viscosity. The variable  $\tilde{\nu}$  is deduced from the transport equation:

$$\begin{aligned} \frac{D\tilde{\nu}}{Dt} &= c_{b1} (1 - f_{t2}) \cdot \tilde{S}\tilde{\nu} + \frac{1}{Pr_T} \left( \nabla \cdot ((\nu + \tilde{\nu}) \nabla \tilde{\nu}) + c_{b2} (\nabla \tilde{\nu})^2 \right) \\ &- \left( c_{w1} f_w - \frac{c_{b1}}{K^2} f_{t2} \right) \left( \frac{\tilde{\nu}}{d} \right)^2 + f_{t1} \Delta u^2. \end{aligned} \quad (2.16)$$

The subscript  $w$  refers to *wall* and  $t$  stands for *trip* which represents the transition between the laminar and turbulent flow. The turbulence Prandtl number  $Pr_T$  is set to 0.9,  $d$  is the distance to the wall, and  $S$  is the magnitude of the vorticity. The variable  $\tilde{S}$  is defined as

$$\tilde{S} = S + \frac{\tilde{\nu}}{k^2 d^2} f_{v2}. \quad (2.17)$$

with

$$f_{v2} = 1 - \frac{\chi}{1 + \chi f_{v1}}. \quad (2.18)$$

The function  $f_w$  is

$$f_w = g \left( \frac{1 + c_{w3}^6}{g^6 + c_{w3}^6} \right)^{1/6}. \quad (2.19)$$

## Navier-Stokes equations and turbulence models

with

$$g = r + c_{w2} (r^6 - r), \quad r = \frac{\tilde{\nu}}{\tilde{S}k^2d^2}. \quad (2.20)$$

The  $f_{t2}$  function is defined as:

$$f_{t2} = c_{t3} \cdot e^{-c_{t4}\chi^2}. \quad (2.21)$$

The trip function  $f_{t1}$  is defined as follows:

$$f_{t1} = c_{t1}g_t \cdot e^{-c_{t2} \frac{\omega_t^2}{\Delta u^2} (d^2 + g_t^2 d_t^2)}. \quad (2.22)$$

with

$$g_t = \min(0.1, \Delta u / \omega_t \Delta x), \quad c_{w1} = \frac{c_{b1}}{K^2} + \frac{(1 + c_{b2})}{\sigma}. \quad (2.23)$$

where  $d_t$  is the distance from the field point to the trip (which is on a wall),

$\omega_t$  is the wall vorticity at the trip and

$\Delta u$  is the difference between the velocity at the field point and that at the trip.

$\Delta x$  is the grid spacing along the wall at the trip.

The closure coefficients for the SA turbulence model are:

$$\left\{ \begin{array}{l} c_{b1} = 0.1355 \\ \sigma = 2/3 \\ c_{b2} = 0.622 \\ K = 0.41 \\ c_{w2} = 0.3 \\ c_{w3} = 2 \\ c_{v1} = 7.1 \\ c_{t1} = 1 \\ c_{t2} = 2 \\ c_{t3} = 1.1 \\ c_{t4} = 2 \end{array} \right. .$$

### The $k$ - $\omega$ turbulence model

The main reference to this model is given by Wilcox [77]. The  $k$ - $\omega$  model uses the  $k$ -specific dissipation rate as a second variable. The eddy viscosity is given by

$$\mu_T = \rho \frac{k}{\omega}. \quad (2.24)$$

The transport equation of the turbulent kinetic energy is

$$\frac{\partial}{\partial t} (\rho k) + \frac{\partial}{\partial x_j} (\rho u_j k) = \frac{\partial}{\partial x_j} \left[ \left( \mu + \frac{\mu_t}{\sigma_k} \right) \frac{\partial k}{\partial x_j} \right] + \rho (P_k - \beta^* \omega k). \quad (2.25)$$

### Navier-Stokes equations and turbulence models

where  $P_k$  stands for the production term and is expressed as :

$$P_k = \tau_{ij} \frac{\partial u_i}{\partial x_j}. \quad (2.26)$$

The  $k$ - $\omega$  determines the turbulent eddy viscosity as the ratio of the kinetic energy over its dissipation rate as follows

$$\frac{\partial}{\partial t}(\rho\omega) + \frac{\partial}{\partial x_j}(\rho u_j \omega) = \frac{\partial}{\partial x_j} \left[ \left( \mu + \frac{\mu_T}{\sigma_\omega} \right) \frac{\partial \omega}{\partial x_j} \right] + \rho \left( \frac{\alpha}{\nu_T} P - \frac{\beta}{\beta^* \omega^2} \right) + \rho S_l. \quad (2.27)$$

The closure coefficients for the  $k$ - $\omega$  turbulence model are:

$$\begin{cases} \beta^* = \frac{9}{100} \\ \alpha = \frac{5}{9} \\ \beta = \frac{3}{40} \\ \sigma_k = 2 \\ \sigma_\omega = 2 \\ S_l = 0 \end{cases}.$$

### The Shear Stress Transport (SST) turbulence model

The SST model was developed by Menter [78, 79]. It is constructed as a “blend” of the  $k$ - $\epsilon$  model which uses the second transport equation to model the dissipation rate of the turbulent kinetic energy [80] and of  $k$ - $\omega$  model. The models coefficients denoted with the symbol  $\phi$  are defined by blending the coefficients of the original  $k$ - $\omega$  model, denoted as  $\phi_1$ , with those of the transformed  $k$ - $\epsilon$  model, denoted  $\phi_2$ . This is given by

$$\phi \begin{pmatrix} \phi_1 \\ \phi_2 \end{pmatrix} \equiv F_1 \phi_1 + (1 - F_1) \phi_2. \quad (2.28)$$

The blending function is

$$F_1 = \tanh(\text{arg}_1^4), \quad (2.29)$$

$$\text{arg}_1 = \min \left[ \max \left( \frac{k^{1/2}}{\beta^* \omega d}, \frac{500\nu}{d^2 \omega} \right), \frac{2k\omega}{d^2 \max(\nabla k \cdot \nabla \omega, 0.0)} \right]. \quad (2.30)$$

The function  $F_1$  is designed to blend the coefficients of the original  $k$ - $\omega$  model in Boundary Layer (BL) zones with the transformed  $k$ - $\epsilon$  model in the free-shear layer freestream zones. This function takes the value of one on no-slip surfaces and near one over a large portion of the BL. Note that the transport equations are modified to take into account the use of the function  $\phi$  as illustrated by the blended values of the coefficients  $\alpha$ ,  $\beta$ ,  $\sigma_k^{-1}$  and  $\sigma_\omega^{-1}$  (see [74] for more details).

### Navier-Stokes equations and turbulence models

The closure coefficients for the SST turbulence model are:

$$\left\{ \begin{array}{l} \beta^* = 0.09 \\ \alpha = \phi \begin{pmatrix} 0.553 \\ 0.440 \end{pmatrix} \\ \beta = \phi \begin{pmatrix} 0.075 \\ 0.083 \end{pmatrix} \\ \sigma_k = \frac{1}{\phi \begin{pmatrix} 0.5 \\ 1.0 \end{pmatrix}} \\ \sigma_\omega = \frac{1}{\phi \begin{pmatrix} 0.5 \\ 0.856 \end{pmatrix}} \\ S_l = \phi \begin{pmatrix} 0 \\ \frac{1.71}{\omega} \nabla k \cdot \nabla \omega \end{pmatrix} \end{array} \right. .$$

Furthermore, the SST model places an additional vorticity-dependent limiter on the shear stress, with

$$F_2 = \tanh (arg_2^2), \quad arg_2 = \max \left( \frac{2k^{1/2}}{\beta^* \omega y}, \frac{500\nu}{y^2 \omega} \right). \quad (2.31)$$

The turbulent eddy viscosity is redefined as

$$\mu_T = \frac{\rho a_1 k}{\max (a_1 \omega, \Omega F_2)}. \quad (2.32)$$

with the vorticity invariant  $\Omega$  being defined as

$$\left\{ \begin{array}{l} \Omega \equiv (\Omega_{ij} \Omega_{ij} / 2)^{1/2} \\ \Omega_{ij} \equiv \partial u_i / \partial x_j - \partial u_j / \partial x_i \end{array} \right. . \quad (2.33)$$

This limits the values of the eddy viscosity in the turbulent boundary layer.

The closure coefficients for the SST model are:

$$\left\{ \begin{array}{l} a_1 = 0.31 \\ \beta^* = 0.09 \\ \alpha = \phi \begin{pmatrix} 0.553 \\ 0.440 \end{pmatrix} \\ \beta = \phi \begin{pmatrix} 0.075 \\ 0.083 \end{pmatrix} \\ \sigma_k = \frac{1}{\phi \begin{pmatrix} 0.85 \\ 1.0 \end{pmatrix}} \\ \sigma_\omega = \frac{1}{\phi \begin{pmatrix} 0.5 \\ 0.856 \end{pmatrix}} \\ S_l = \phi \begin{pmatrix} 0 \\ \frac{1.71}{\omega} \nabla k \cdot \nabla \omega \end{pmatrix} \end{array} \right. .$$

### The $Pk$ limiter turbulence model

The  $Pk$  limiter [81] is a modified version of the  $k$ - $\omega$  model suggested by Brandsma *et al.* [82] for vortical flows. The production term is expressed as follows:

$$P_k = \min [P_k^u, (2.0 + 2.0 \min(0, r - 1)) \rho \beta^* k \omega]. \quad (2.34)$$

with  $P_k^u$  the unlimited production of  $k$  and  $r$  the ratio of the magnitude of the rate-of-strain and vorticity tensors. The production of  $k$  is reduced for regions of pure rotation and high vorticity, i.e. at the vortex core [83].

## 2.3 The Aeroacoustical approach

Blade-Vortex Interaction (BVI) is one of the most challenging problems encountered in modern rotorcraft since it affects both the aerodynamic performance of rotors, as well as, the acoustic signature of the aircraft. Researchers started to be interested in the mechanisms of the propagation of sound generated aerodynamically decades ago. Much effort was put into the development of sound propagation theories which allows the prediction of the farfield noise from the near-midfield acoustic. The objective was to understand how the aircraft noise was perceived by an observer on the ground. The basis of the actual aeroacoustic work is the acoustic analogy theory of sound which was developed by Lighthill [60] in 1952.

### 2.3.1 Lighthill's acoustic analogy

In Lighthill's theory, the sound is expected to be a sufficiently small element of the motion that its interaction with the mean flow can be neglected. The acoustic analogy lies in the separation between the source and the sound, the sound being defined as the linear response of the source's environment. It is then possible to determine the acoustic fluctuations from the source, i.e. from the flow characteristics.

The acoustic analogy is particularly easy to apply at low Mach numbers. For this case, it is possible to assume that the sound radiation surfaces are acoustically compact, i.e. the linear scales are much smaller than any in the sound field. It becomes reasonable in this case to scale surface stresses on hydrodynamic variables. Analytical treatment is then made possible [84] for the noise generated by a flow interacting with rigid and elastic structures via the use of the compact acoustic Green's function when the source dimensions are small compared to the acoustic wavelength. The source flow can then be first estimated by ignoring the production and propagation of the sound.

The acoustic analogy assumes that the solution is non-causal, meaning that the sound is the linear response of the flow. However, at large Mach numbers, compressibility effects or motion coupled with a resonating system makes this assumption inexact. The unsteadiness of the flow determines the nature of the response which may quickly grow to become non-linear. Acoustic sources may also generate turbulence into the

flow, leading to a coupling between the acoustic and hydrodynamic modes. This is the case for a large enough aerofoil at low Mach number [84] and for a non-uniform flow of density-inhomogeneous fluid which cannot be steady and creates noise [85]. This noise which can be dominant for very hot jets is not covered by Lighthill's theory. Indeed, the airflow cannot be represented any more in terms of acoustics by a distribution of quadrupoles in the absence of resonators and boundaries when there is a singularity, or abrupt flow change. This implies that Lighthill's analogy has also to be used carefully for flows over helicopter blades on the advancing side where shocks can be present.

### 2.3.2 Lighthill's formulation

The Lighthill theory lies on the reformulation of the NS equations with the use of the continuity equation. It is valid for an ideal stationary acoustic medium on which is applied a stress distribution, the Lighthill stress tensor  $T_{ij}$ . The fundamental equation describing the noise generation is expressed as

$$\frac{\partial^2 \rho}{\partial t^2} - a_0^2 \nabla^2 \rho = \frac{\partial Q}{\partial t} + \frac{\partial F_i}{\partial x_i} + \frac{\partial^2 T_{ij}}{\partial x_i \partial x_j} \quad (2.35)$$

with

$$T_{ij} = \rho u_i u_j + [(p - p_0) - a_0^2 (\rho - \rho_0)] \delta_{ij} - \sigma_{ij}. \quad (2.36)$$

The sound produced by mass introduction is represented by  $\frac{\partial Q}{\partial t}$ . The sound produced by force acting upon the acoustic medium is expressed by  $\frac{\partial F_i}{\partial x_i}$ . The acoustic stress,  $T_{ij}$ , includes the effects of temperature, refraction, diffraction and inhomogeneity. The first term of  $T_{ij}$ , the Reynolds stress  $\rho u_i u_j$  expresses the rate of change momentum, the viscous stress on its boundary and its convection across the boundary [84]. The second term represents "the excess of momentum transfer by pressure over that in a ideal fluid" which can be caused by nonlinearity and entropy fluctuations. Finally the third term accounts for the attenuation of the sound. Note that in the case of a helicopter, extra noise sources appear [86]. This is due to the centrifugal accelerations which give rise to additional radiating noise.

### 2.3.3 Description of the types of noise sources

A physical explanation of the impulsive noise motion for a helicopter is now given. The characteristics of the loading noise are first described. Loading noise is caused by the fluctuating momentum which could be interpreted as the result of a fluctuation force. The variation of the apparent angle of attack during BVI induces a change in the lift, which results in a radiated noise given by:

$$P'(\vec{x}, t) = -\frac{\partial}{\partial x_i} \int \int \left[ \frac{\mathbf{P}_{ij} \mathbf{n}_j}{r|1 - M_r|} \right]_\tau d\Sigma \quad (2.37)$$

where  $P'$ ,  $\mathbf{P}_{ij}$ ,  $\mathbf{n}_j$ ,  $M_r$ ,  $\Sigma$  are respectively the acoustic pressure, the compressive stress tensor, the outward normal vector to surface, the Mach number in the radiation direction and the surface. Note that that acceleration causes additional sound generation. Indeed, it appears that accelerated turbulent eddies produce more noise than eddies moving at constant speed.

The thickness noise results from the movement of the fluid. It is a function of the normal velocity components at the body as shown by its expression  $\iint \left[ \frac{\rho_0 v_n}{r|1 - M_r|} \right] d\Sigma$ . The factor  $1/(1 - M_r)$  represents the Doppler amplification of acoustic signals and is a strong function of  $M_r$  [86]. Since  $M_r$  becomes a maximum when the azimuthal angle is around  $90^\circ$ , the thickness noise is expected to originate at this position. Due to the convection of the turbulent eddies, the Doppler effect modifies the frequency and the sound is preferentially beamed in the direction in which the frequency shift is greatest.

Only the surface noises, i.e. the loading and the thickness noise will be considered for two reasons: they are sufficient to get a good estimation of the BVI noise and their calculation is not as time consuming as the quadrupole noise [86] which requires the calculations of volume integrals.

### 2.3.4 Review of the existing techniques

Two different approaches are common for determining the farfield noise: the Kirchhoff method [87] and the Ffowcs Williams-Hawkings (F'W-H) [85, 88, 89, 90].

The use of the Kirchhoff method requires that all the non-linearities of the flow are inside a control surface which is supposed to be representative of the flow phenomena occurring during the BVI. In this case, using Green's theorem, it is possible to calculate exactly the pressure distribution outside the surface. The method also requires knowledge of the time history of the flow quantities. Although the method is easy to adopt in potential-like flows, cases with strong vortices traveling in the flow domain or higher Mach numbers require a larger surface since the nonlinearities prevail longer in all spatial directions [91, 92, 93]. This is a hard requirement to be met since CFD methods lose resolution of the flow field in coarse grids far away of the main area of interest in the flow. This implies that a judicious choice of the Kirchhoff surface [41] is necessary.

As reported by Brentner [1], the Kirchhoff approach for moving surfaces can lead to erroneous results for two reasons. First, the integrations over the control surface do not represent the physics of the BVI when the vortex passes through the surface and predictions can be misleading unless the integration surface is large enough to include the vortex before or during the interaction. Furthermore, the Kirchhoff method requires the use of a nearfield which is usually distant by at least one chord from the aerofoil to include the non-linear effects of the flow on the acoustics. This makes the Kirchhoff method unreliable for most CFD solvers which tend to dissipate the pressure waves unless adaptive grid refinement or/and high-order spatial schemes are used to preserve

### Review of the existing techniques

the acoustical waves for longer. Nevertheless, the determination of the farfield noise remains possible with the use of the FW-H method [40] which can be formulated to include surface properties only.

At subsonic flow, the FW-H method has the advantage of only requiring the accurate prediction of the loads on a lifting surface and even though the surface has to be carefully chosen when simulating transonic BVI, little difference in the region of maximum BVI noise intensity was noticed by Singh and Baeder [94] when quadrupole noise is neglected. The contribution of the quadrupole noise was actually found to be negligible in the out-plane of the rotor. This implies that the farfield noise can be well-predicted using the BVI loads as an input for the FW-H method as long as the observer is located in the out-plane region. The FH-W method also decomposes the noise into different sources making the analysis of the obtained results easier. The BVI is then classified as an impulsive loading noise. Due to the above reasons the FW-H method has gained popularity and it is possible to predict the thickness and loading noises from the FW-H equations provided the surface loads are known [13].

Following Farassat's 1A formulation [10, 62] which is suitable for moving bodies such as helicopter blades and assuming the blades are rigid, the FW-H equation can be reformulated as follows:

$$4\pi P'(\vec{x}, t) = \frac{1}{a} \frac{\partial}{\partial t} \int_{f=0} \left[ \frac{\rho_0 a v_n + L_r}{r(1-M_r)} \right]_{ret} d\Sigma + \int_{f=0} \left[ \frac{L_r}{r^2(1-M_r)} \right]_{ret} d\Sigma. \quad (2.38)$$

In the above,  $P'$  represents the acoustic pressure at point  $\vec{x}$  and time  $t$ . The symbols  $\Sigma$ ,  $L_r$  and  $M_r$  are respectively the FW-H surface, the loading forces and the Mach number in the radiation direction. The speed of the sound is noted by  $a$  and the velocity normal to the surface by  $v_n$ .

In the Farassat formulation 1A, it is possible to use the retarded time as a reference:

$$\left( \frac{\partial}{\partial t} \right)_x = \left[ \left( \frac{1}{1-M_r} \frac{\partial}{\partial \tau} \right)_x \right]_{ret}. \quad (2.39)$$

Then the loading and thickness acoustic pressure  $P'_L$  and  $P'_T$  are deduced from Equations 2.38 and 2.39. Their respective expression is

$$4\pi P'_L(\vec{x}, t) = \frac{1}{a} \int_{f=0} \left[ \frac{\dot{L}_i \hat{r}_i}{r(1-M_r)^2} \right]_{ret} d\Sigma + \int_{f=0} \left[ \frac{L_r - L_i M_i}{r^2(1-M_r)^2} \right]_{ret} d\Sigma \quad (2.40)$$

II

$$+ \frac{1}{a} \int_{f=0} \left[ \frac{L_r (r \dot{M}_i \hat{r}_i + a M_r - a M^2)}{r^2 (1 - M_r)^3} \right]_{ret} d\Sigma.$$

III

$$4\pi P'_T(\vec{x}, t) = \frac{1}{a} \int_{f=0} \left[ \frac{\rho_0 v_n (r \dot{M}_i \hat{r}_i + a M_r - a M^2)}{r^2 (1 - M_r)^3} \right]_{ret} d\Sigma. \quad (2.41)$$

Note that the dot on  $M_i$  and  $L_i$  denotes the time derivative of each vector and that  $\hat{r}_i = (x_i - y_i/r)$  is the unit radiation vector.

The acoustic pressure is expressed as the sum of the loading and thickness noise sources:

$$P'(\vec{x}, t) = P'_L(\vec{x}, t) + P'_T(\vec{x}, t). \quad (2.42)$$

The thickness term [95] which considers the disturbance of the fluid medium caused by the aerofoil is determined by the blade characteristics and the forward velocities. The loading terms which represents the noise caused by the aerofoil exerting a force on the fluid [14] requires the calculation of the forces acting on the blade.

It is interesting to note that "the loading noise depends on the projection of the forces onto the direction from the blade to the observer" [62]. Term  $I$  is supposed to be the dominant term of the loading noise. Therefore, only term  $I$  of Equation 2.40 is estimated. Note that the distance from the aircraft to the observer was also approximated so that the aircraft was seen as a source point.

According to [62], only subsonic motion of the blade is allowed, i.e. for low forward speed (20m/s). Discrepancies appear in the prediction at high forward speeds ( $V=67\text{m/s}$ ) due to the large contribution of the quadrupolar noise [96] for higher tip Mach numbers, which is created by the velocity perturbation along the blade chord. Furthermore, the presence of shocks, i.e. strong discontinuity in pressure, are also a possible source of noise. Both quadrupole and shock noise are assumed to be at the origin of the noise discrepancy.

For acoustic prediction, the integration of the lift force (term  $I$  of Equation 2.38) over the chordwise direction is often realised assuming that the blade can be seen as a point source ( $r/c \ll 1$ ). The force is then applied at the quarter chord and the BVI is said to be chordwise compact [7]. The compactness of the chordwise loading distribution is justified as long as the aspect ratio of the blade is high and the flow which is considered 2D locally make the frequency range of BVI low enough for the observer not to perceive any chordwise variations [96]. Indeed, the generation of an acoustic wave is associated with a particular phase [21]. Each section wave can be characterised by a phase which corresponds to a fixed section of the blade. The radiated noise therefore depends on

the phase delay between all the acoustic pressures for a fixed chordwise section, which implies that the noise levels may be overpredicted.

The modification of the phase delay is also an important parameter of the BVI noise generation since BVI acoustic phasing influences the directionality of the radiated noise [97]. A comparison between the non-compact and the compact modelling has been undertaken by Sim and Schmitz [7]. They found that a lower peak value and a larger acoustic pulse width is obtained for the non-compact modelling. However, the difference in terms of noise levels between the two methods appears especially near the plane of the rotor and decreases underneath it. Although non-compact chord assumptions does not overpredict the noise levels as the compact does, the directivity patterns or trends of the noise remains similar.

## 2.4 Conclusions

The main features of the EROS code have been given along with a description of the CAA methods. It appears that the quality of the BVI noise prediction is related to the accuracy of the aerodynamics of BVI provided by CFD. Therefore, it is desirable to test the capabilities of the CFD code in terms of robustness and reliability for both time and spatial schemes. This will help in addressing the possibilities and the limitations of the present approach which combines CFD and CAA for the study of BVI noise.

## Chapter 3

# Validation of CFD tools

This chapter illustrates the capabilities of the CFD code for flow simulation and the improvements carried out for the BVI simulation.

### 3.1 Introduction

In recent years, Computational Fluid Dynamics (CFD) has made a significant impact in the design of modern rotors. Yet, the ability of most CFD codes to preserve vortices over long periods of calculation on grids of moderate density still remains questionable. This is mainly due to the amount of numerical dissipation and dispersion inherent in most numerical schemes. The PMB code of the University of Glasgow [66] is the basis for the present work. This is a parallel, structured, multi-block code with implicit time stepping. It is based on the Osher and Roe schemes and uses a preconditioned Krylov solver for high efficiency.

To extend the capability of the code for predicting flows with strong vortical structures the Compressible Vorticity Confinement Method (CVCM) [98, 99, 100] has been implemented. This method is particularly attractive from a practical point of view since it is economic in terms of memory and CPU time and relatively simple to implement in existing CFD solvers. This method has been successfully used for tracking vortices [101, 102] and more specifically for rotorcraft simulations [103, 104]. Application of the method is also reported for several other flow cases including flows over complex bodies [105], massively separated flows [106] and even flow visualization [107]. Recently, it was applied to allow the simulation of blade-vortex interaction [98] which is the main focus of this paper.

This chapter will first present a comparison between the FUN and UNFACTored methods in terms of efficiency and flow solutions. Indeed, a good convergence behaviour is to be obtained, especially for unsteady flows. Both implicit time-stepping methods which were described in Chapter 2 are tested for different cases. The solutions and the convergence behaviour of the different schemes are compared for each test case.

The same Courant-Friedrichs-Lewy (CFL) number is used for the two first test cases to highlight the importance of the factorisation error and the CFL numbers used for the other test are chosen to get a good convergence behaviour.

Then this chapter will show the capabilities of the Vorticity Confinement Method using a simple benchmark problem of vortex convection in an infinite domain. Once confidence in the method has been established, four different BVI cases will be simulated. These flow simulations will demonstrate the capabilities of the code in terms of robustness and reliability. The influence of the CVCM on the aerodynamic results will be assessed on both counts.

## 3.2 Evaluation of implicit schemes

The UNFACTored method has been implemented and compared with FUN for a range of test cases. It is important to point out that, even though most calculations presented in the next chapters are 2D, 3D calculations have been carried out in order to highlight the differences between the methods in terms of efficiency and robustness. Note that a good starting solution is required for the implicit method. This is obtained using a small number of explicit time steps from the freestream solution.

### 3.2.1 Description of the test cases

The reference tests which have been carried out are the following: unsteady Lann wing and 7A 4-bladed model rotor in transonic hover flight. The Lann tests were run on an AMD Athlon 1009 Mhz with 524 Mbyte RAM and the 7A hover flight case on a Pentium 750 MHz. Details of test cases are given in Table 3.1.

<i>Model</i>	<i>Description</i>	<i>Aero Cond.</i>
Lann Wing	Unsteady case (3D)	$M_\infty = 0.822$ $\theta_0 = 0.6^\circ$ $\theta_1 = 0.25^\circ$ $k = 0.102$ $x_{A1} = 0.621$
7A 4-bladed	Transonic HOVER flight – <i>Single block grid</i>	$M_{tip} = 0.66117$ $\theta_{.70} = 7.49^\circ$ $C_T/\sigma = 0.08178$

Table 3.1: The run test cases for the evaluation of the time-stepping implicit schemes.

### 3.2.2 Comparison between the UNFACTored and FUN methods

The following section provides some results. The algorithms are compared for two main aspects: solution accuracy and convergence characteristics.

## 3.2. EVALUATION OF IMPLICIT SCHEMES

### The Lann wing

This test case concerns a wing in pitching motion. The pitching angle is defined as

$$\theta(t) = \theta_0 + \theta_1 \sin\left(\frac{2V_\infty k}{a_0} t\right) \quad (3.1)$$

where  $\theta_0$ ,  $\theta_1$ ,  $V_\infty$ ,  $k$ ,  $a_0$  are respectively the mean angle of attack, the oscillation pitch angle, the freestream velocity, the reduced frequency and the speed of sound. Note that the wing motion parameters are given in Table 3.1. The grid used for this test was the TU Delft/NLR single block 120 x 31 x 23 C-H grid described in Renzoni *et al* [63]. This is given in Figure 3.1.

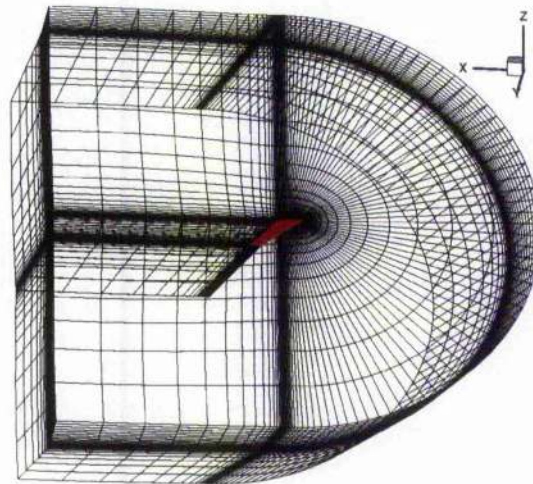


Figure 3.1: Grid used for the Lann case. The wing is represented in red colour.

The sectional force coefficients and the sectional pitching moment coefficients which are depicted in Figures 3.2-3.4 are similar for both methods. The layout of the mean steady pressure distribution and of the first harmonic pressure (see Figures 3.5-3.7) also show indistinguishable results, confirming that both schemes solve the Euler system of equations in an identical way at convergence for this case.

For this test case, a steady run is carried out in order to get an initial solution for the unsteady calculation. The convergence histories for the preliminary runs are given in Figure 3.8. The evolution of the number of pseudo-time steps per real time step is given in Figure 3.9: the convergence criterion was set to a residual reduction of four orders of magnitude. Eleven pseudo-time steps per iteration are required for the UNFACTored method against fifty four for the FUN method. The resulting CPU advantage is of a ratio of four, that can be considered as a substantial improvement.

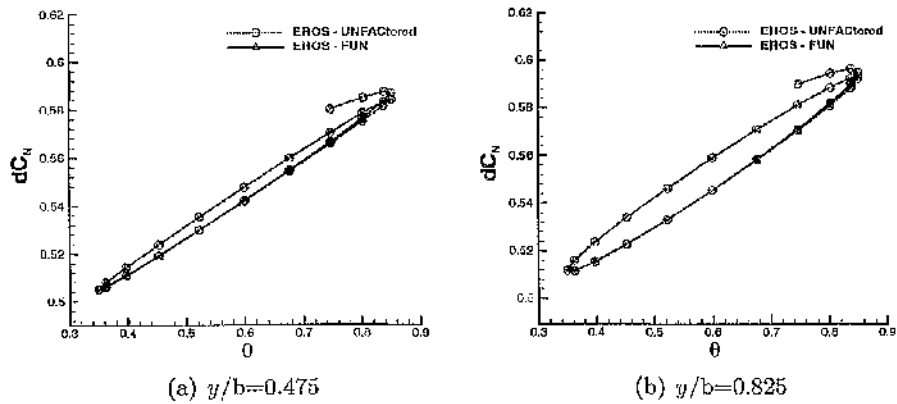


Figure 3.2: Sectional normal force coefficient for the Lann wing.

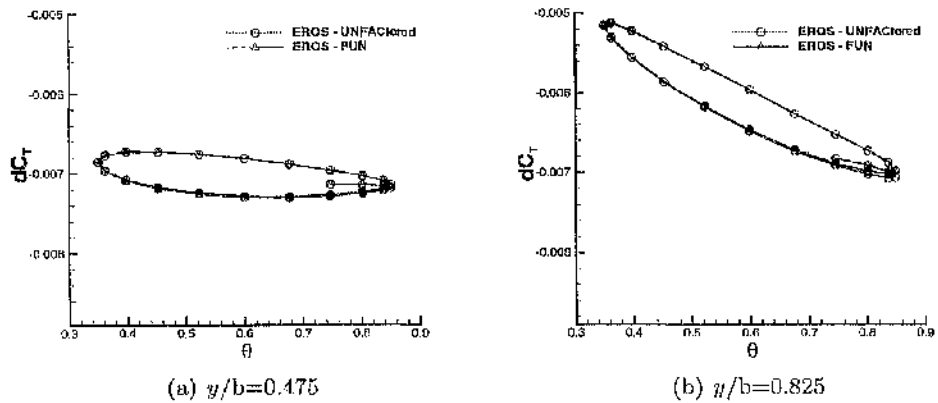


Figure 3.3: Sectional chordwise force coefficient for the Lann wing.

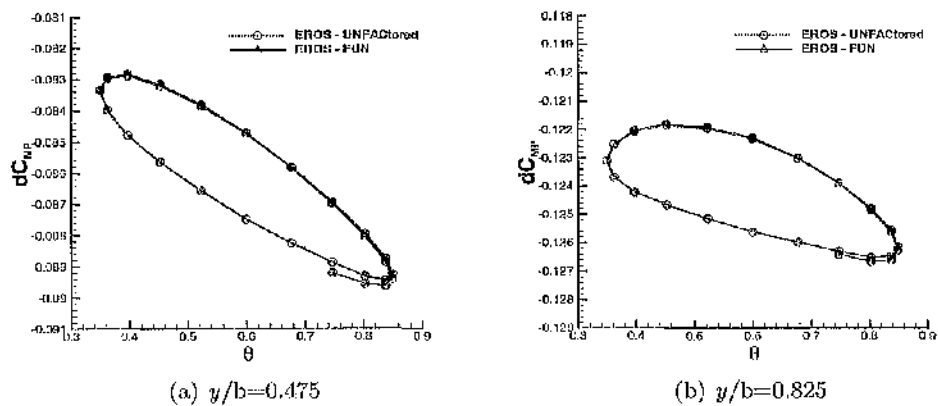


Figure 3.4: Sectional pitching moment coefficient for the Lann wing.

Comparison between the UNFACTORED and FUN methods

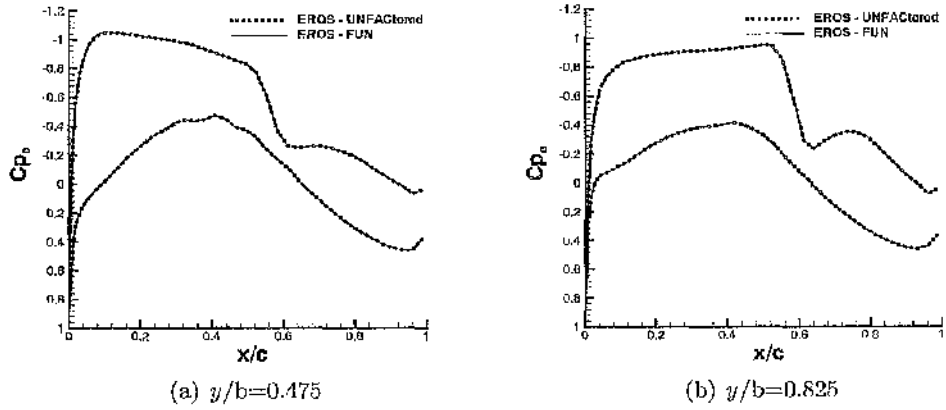


Figure 3.5: Mean steady pressure for the Lann wing.

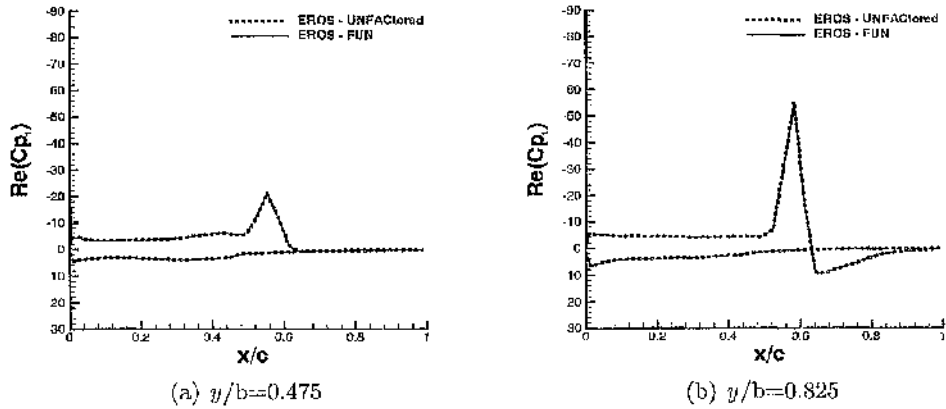


Figure 3.6: Real part of the 1<sup>st</sup> harmonic pressure for the Lann wing.

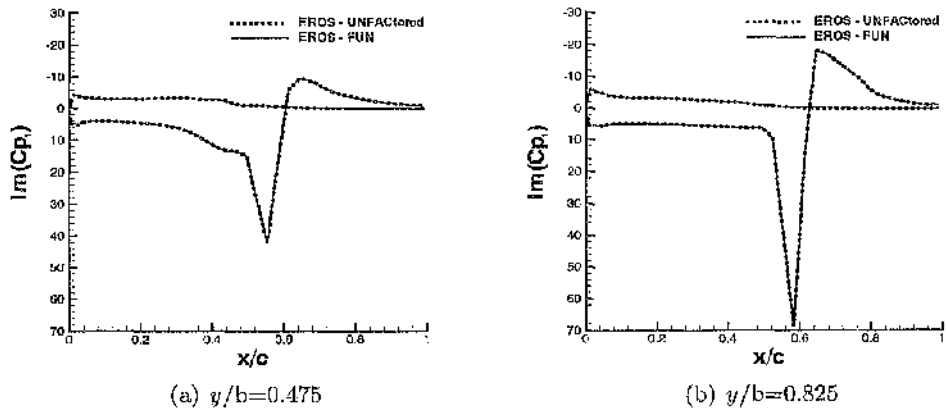


Figure 3.7: Imaginary part of the 1<sup>st</sup> harmonic pressure for the Lann wing.

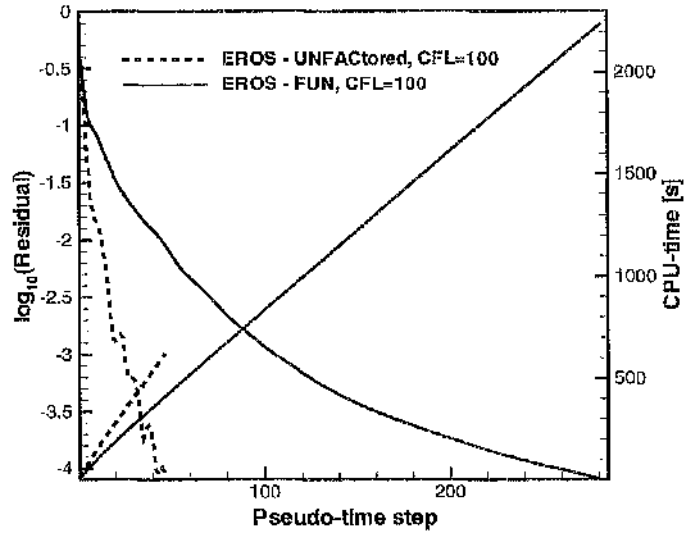


Figure 3.8: Convergence histories for the steady preliminary run.

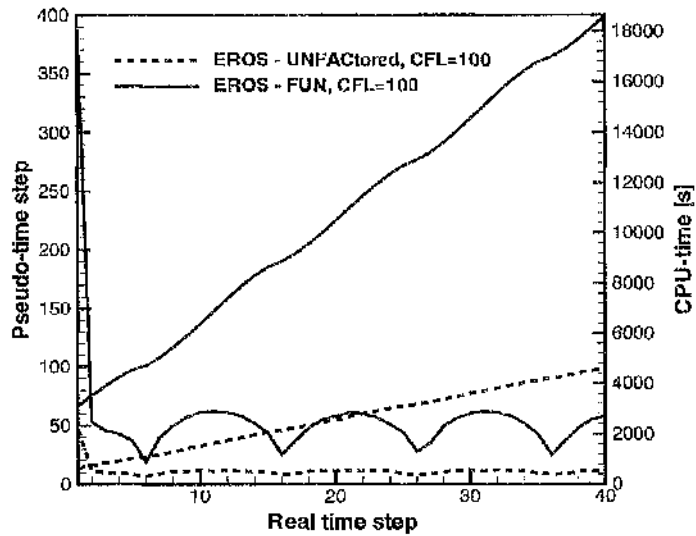


Figure 3.9: Convergence histories for the unsteady Lann wing case.

The Lann wing test case shows the importance of the factorization error in the FUN method. Since the CFL numbers were set to 100 for both methods, the convergence behaviour of the FUN method compared to the UNFACTored method proves that the factorisation error was indeed significant. The fact that both schemes are similar in their manner of handling the Euler equations and that only the UNFACTored scheme solves the full unfactored system confirms the importance of this factorization error in the FUN method.

### The 7A model rotor in transonic hover non-lifting

The coarse grid generated by the GEROS code was a  $84 \times 60 \times 32$  O-H grid with 40 chords (2.67 rotor aspect ratio) for radial dimension and 40 chords for vertical dimension above and below the rotor plane. The grid is given in Figure 3.10.

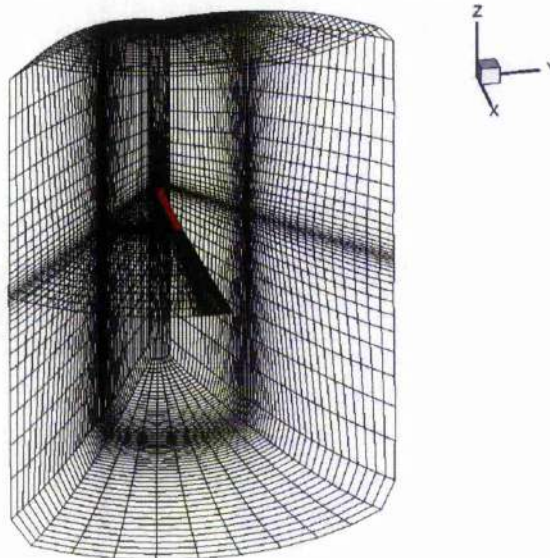


Figure 3.10: Grid used for the 7A-ONERA case. The blade is represented in red colour.

The solution which is fully converged (see Figure 3.11) is again similar regarding the surface pressure coefficient distribution and the normal force coefficient as depicted in Figure 3.12. However, the results present some problems for the area close to the tip blade. Indeed, some previous studies on finer grids [63] gave a higher peak in the area near the leading edge. The obtained solution depends in fact on the grid resolution since the tip vortices are better captured on finer grids.

The UNFACTored method (CFL=100) is also 3.7 times faster than the FUN method (CFL=70) in achieving a reduction of five orders in the residual (see Figure 3.11). The CFL numbers were set to obtain the best compromise between stability and efficiency in terms of execution time. However, the convergence bottoms out when the residual has been reduced 3.6 orders for the FUN method and five orders for the UNFACTored method. While reaching a residual decreased by an order of six, an improvement by

a factor of two is achieved, which is quite satisfactory considering the low number of required pseudo-time steps for this test case using FUN.

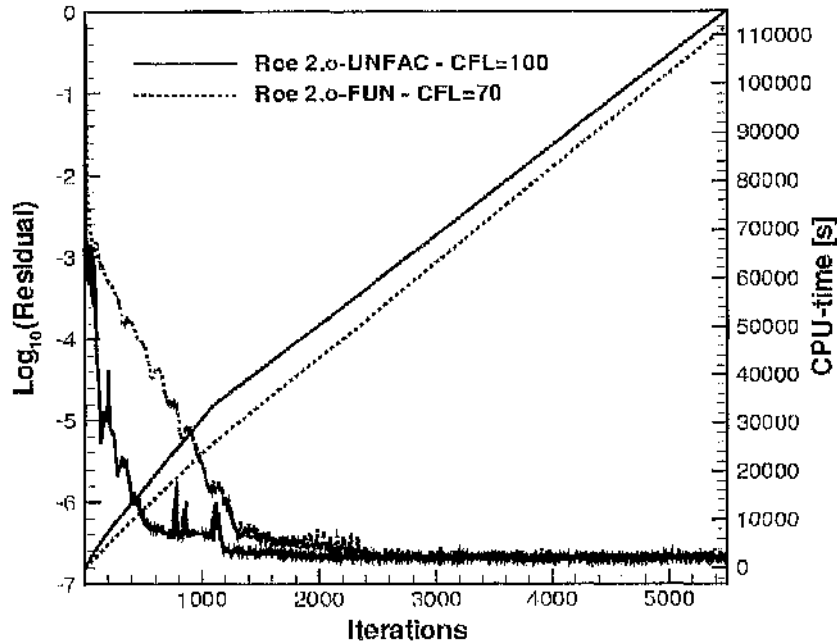


Figure 3.11: Convergence histories for the FUN and UNFACTored methods for the 7A hover flight. Coarse grid.

Results from both schemes agree with each other and show that the UNFACTored method yields faster convergence than the FUN method for each of these test cases. The convergence obtained was indeed four times faster for the Lann wing study and 3.7 faster for the 7A 4-bladed model rotor on a single block grid. The performance of both schemes for each test case is summarised in Table 3.2.

Note that the UNFACTored method uses more memory since the equations are solved in three dimensions. However, the UNFACTored method gives better performance for the convergence behaviour since no factorisation errors occur. The implicit scheme can then be chosen according to the grids and the memory capabilities of the particular computer used. Note that the UNFACTored method was used for all the next CFD calculations presented in the dissertation.

<i>TESTcases</i>	<i>Grid</i>	<i>Gain</i>	<i>Memory</i>
Lann Wing	Single	0.25	4.5
7A Transonic hover flight	Single	0.27	5.4

Table 3.2: Gain of the UNFACTored method against the FUN method.

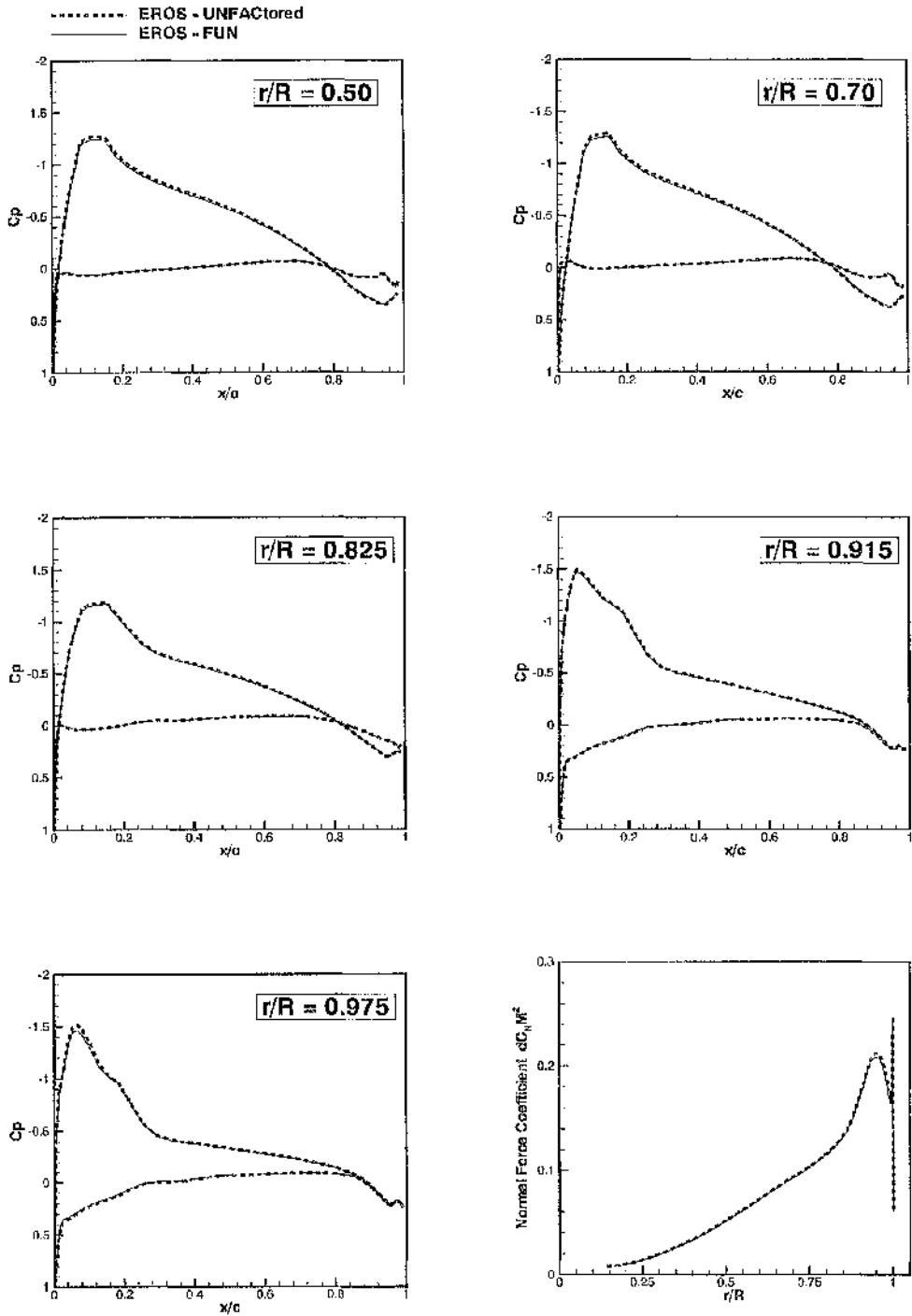


Figure 3.12: Pressure coefficient distribution and normal force coefficient for the 7A 4-bladed hover test case. Coarse grid.

Comparison between the UNFACTored and FUN methods

### 3.3 The Compressible Vorticity Confinement Method

#### 3.3.1 Principle of the VCM

The Vorticity Confinement Method (VCM) developed by Steinhoff [99] is aimed at countering the dissipation of the spatial scheme. The VCM is based on the observation that conventional schemes tend to dissipate the vortices in the flow. Therefore the VCM adds a source of momentum to overcome this in regions of the flowfield where vorticity is concentrated. Regardless of the nature of the flow, the CVCM allows the vortex core to be modelled. It has been therefore used as a turbulence model in previous studies [98, 100]. The basic modification is to add a body force term  $\mathbf{f}_b^*$  to the momentum transport equations which for incompressible flow read:

$$\rho \frac{\partial \vec{V}}{\partial t} + \rho(\vec{V} \cdot \nabla) \vec{V} + \nabla p = \mu \nabla^2 \vec{V} + \mathbf{f}_b^*. \quad (3.2)$$

In the original version, the body force term  $\mathbf{f}_b^*$  is given by  $-\epsilon \rho \frac{\nabla |\vec{\omega}|}{|\nabla |\vec{\omega}||} \times \vec{\omega}$  where  $\epsilon$ ,  $\mu$  and  $\vec{\omega}$  are respectively the confinement parameter, an artificial dissipation coefficient and the vorticity. It is important to note that the CVCM was employed to circumvent the issue of dissipation of the CFD solver and not for modelling turbulence.

#### 3.3.2 Compressibility modifications

The extension of the VCM to the compressible Navier-Stokes (NS) equations has been realised by including the work of the body source term in the energy equation [108]. The integral form of the Euler's equations can be rewritten for a two-dimensional problem as

$$\frac{d}{dt} \int_V W dV + \int_\Sigma F \cdot \vec{n} d\Sigma + \int_\Sigma G \cdot \vec{n} d\Sigma = - \int_V S dV. \quad (3.3)$$

where the conservative variables  $W$ , the fluxes  $F$ ,  $G$  and the source term  $S$  can be expressed as

$$W = \begin{Bmatrix} \rho \\ \rho u \\ \rho v \\ \rho e \end{Bmatrix}, F = \begin{Bmatrix} \rho u \\ \rho u^2 + p \\ \rho uv \\ \rho uh \end{Bmatrix}, G = \begin{Bmatrix} \rho v \\ \rho uv \\ \rho v^2 + p \\ \rho vh \end{Bmatrix},$$

$$S = \begin{Bmatrix} S_\rho \\ S_u \\ S_v \\ S_e \end{Bmatrix} = \begin{Bmatrix} 0 \\ \epsilon \rho (\vec{n} \times \vec{\omega}) \cdot \vec{i} \\ \epsilon \rho (\vec{n} \times \vec{\omega}) \cdot \vec{j} \\ \epsilon \rho (\vec{n} \times \vec{\omega}) \cdot \vec{V} \end{Bmatrix} \text{ with } \begin{cases} \vec{n} = \frac{\nabla |\vec{\omega}|}{|\nabla |\vec{\omega}||} \\ \vec{\omega} = \frac{\partial}{\partial M} \times \vec{V} \end{cases}. \quad (3.4)$$

The term  $-\epsilon \rho \frac{\nabla |\vec{\omega}|}{|\nabla |\vec{\omega}||} \times \vec{\omega}$  is added to the transport equations of the momentum components, while  $\epsilon$ ,  $\rho$  and  $\vec{\omega}$  represent the confinement parameter, the density and the

vorticity, respectively. In order to include the work done by the body source term in the energy conservation law, the term  $-\epsilon\rho(\vec{n} \times \vec{\omega})$  also contributes as a part of the residual. A complete review of the Compressible Vorticity Confinement Method is given in the thesis by Hu [109].

### 3.3.3 Implementation

The vorticity gradient is required for the source term  $S$ . The derivatives were calculated from their curvilinear form. It was found that the robustness of the method depends strongly on the order of accuracy of the calculated gradients. Therefore the derivatives  $f'_i$  were estimated using the fourth-order finite difference approximation from

$$f'_i = \frac{-f_{i+2} + 8f_{i+1} - 8f_{i-1} + f_{i-2}}{12} \quad (3.5)$$

The use of high-order derivatives provides a better estimate of the vorticity gradients particularly in the wake of the airfoil. In addition, some Laplacian smoothing to the vorticity and its gradient was applied. The Jacobians in the implicit formulation (see Equation 3.3) were left unchanged. Experience with the test cases presented in Section 3.4 will show that the stability and convergence of the scheme is not affected by the CVCN.

### 3.3.4 Modifications to the basic method

Different methods have been used to set the values for the parameters  $\epsilon$  and  $\mu$ .

- (a) Parameters  $\epsilon$  and  $\mu$  set to constants.

The constants  $\epsilon$  and  $\mu$  were respectively chosen so as to control the amount of momentum injected into the flow and to remove any excessive momentum which may create artificial vortices. The value of  $\epsilon$  ranges typically from 0.001 to 0.1 whereas the parameter  $\mu$  was set to a value between 0.1 to 1.0.

- (b) Use of a vorticity gradient based limiter.

It has been attempted to reduce the production of spurious vortices via the use of a limiter based on the vorticity gradient. Indeed, it was observed that some of the secondary vortices stem from the vector  $\vec{n}$ . The cross product of the vector  $\vec{n}$  and the vorticity  $\vec{\omega}$  allows the concentration of the anti-dissipation term in the areas where the magnitude of the vector  $\vec{n}$  is significant. However, the vector  $\vec{n}$  may have a large magnitude even in areas of low vorticity and this may result in artificial vortices. Therefore, the vorticity  $\omega$  was set to zero when the magnitude of the vorticity gradient  $|\nabla|\vec{\omega}||$  was low.

- (c) Parameter  $\epsilon$  scaled with the grid.

Different formulations of the CVCN have been tested [101, 110, 111]. Since the confinement parameter  $\epsilon$  is homogeneous to a velocity, it is possible to scale it

### Implementation

with the grid size. The formulation proposed by [101] expresses the confinement parameter as  $\epsilon = h_{proj}^2 |\nabla |\vec{\omega}||$  with  $h$  the characteristic length which is equal to the scalar product of the cell size vector  $\vec{l} = (\Delta x, \Delta y, \Delta z)$  with the vector  $\vec{n}$ . This formulation has been tested and compared against the constant scaling  $\epsilon$ . Results are shown in section 3.3.5.

(d) Density confinement.

The density confinement method was proposed by Costes and Kowani [110]. It consists of adding a source term to the continuity equation. The source term  $S$  (see Equation 3.4) has a component  $S_\rho$  which is expressed as

$$S_\rho = \delta \frac{1}{|\vec{\omega}|} \left( S_u \frac{\partial \rho}{\partial x} + S_v \frac{\partial \rho}{\partial y} \right). \quad (3.6)$$

The non-dimensionalised parameter  $\delta$  allows the modification of the density in the vortex.

### 3.3.5 Evaluation of the CVCM on a vortex convection test case

The CVCM has been tested on the benchmark problem of vortex convection in an infinite domain. A 2D isentropic vortex is introduced into the flow and convected at the freestream velocity. Periodic boundary conditions were applied to enable the vortex to convect for many cycles. The Scully model was chosen due to its wide acceptance in the literature [9]. According to this model, the expression for the tangential velocity component is

$$\frac{v_\theta}{U_\infty} = \left( \frac{\hat{\Gamma}}{2\pi r} \right) \left( \frac{r^2}{r^2 + R_c^2} \right) \quad (3.7)$$

with  $U_\infty$ ,  $\hat{\Gamma}$ ,  $R_c$  being respectively the freestream velocity, the non-dimensionalised circulation and the core radius. The non-dimensionalised circulation  $\hat{\Gamma}$  is equal to  $\frac{\Gamma}{U_\infty L}$ ,  $L$  being the width of the grid. Note that the pressure and density are calculated from the approximation of the Euler equations  $\frac{dp}{dr} = \rho \frac{v_\theta^2}{r}$  and the isentropic relation  $p = a\rho^\gamma$  [109].

The influence of the different method (a-d) is examined for the case  $R_c = 0.018$ ,  $\hat{\Gamma} = -0.283$ ,  $M_\infty = 0.5$ . The calculations were carried out on two uniform grids: a coarse grid with  $51 \times 102$  points and a finer grid of  $139 \times 278$ . Note that one core radius represents a length of 0.018 in the x or y direction.

First, the effects of the confinement parameter and of the artificial dissipation coefficient on the vortex convection are investigated. Different values for the confinement coefficient  $\epsilon$  have been used, the artificial dissipation coefficient  $\mu$  being set to zero. The flow was first considered as laminar with a Reynolds number of 1000. The initial condition and the vorticity divided by the density are plotted in Figure 3.13. Figure 3.13(a) highlights the grid density of the coarse grid. The full grid extends from -0.5 to 0.5 in the x direction and from -1.0 to 1.0 in the y direction. Figure 3.13(b) shows that the  $\omega/\rho$  ratio is maintained constant when the CVCM is used while it is significantly reduced when  $\epsilon = 0$ .

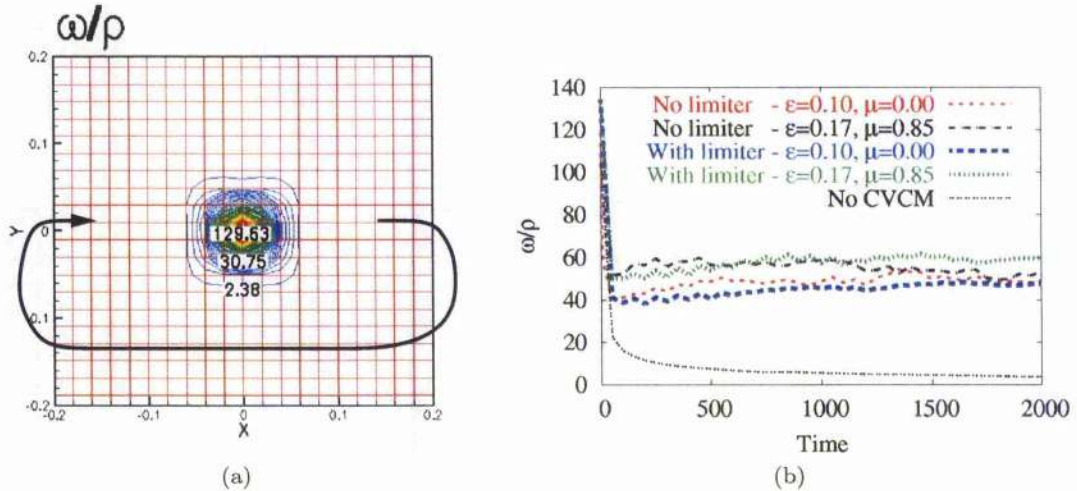


Figure 3.13: (a) Schematic of the initial conditions of the benchmark problem and (b) time history of the  $\omega/\rho$  ratio at the vortex core as predicted using the CVCM method with or without gradient-based vorticity limiters.

It was also noticed that the method leads to the formation of artificial secondary vortices when the artificial dissipation coefficient  $\mu$  is set to zero. As depicted in Figure 3.14(a), the artificial dissipation term (method (a)) reduces the creation of artificial vortices and results in better preservation of the shape of the original vortex. Results with the use of the vorticity gradient based limiter (method (b)) are presented in Figure 3.14(b). It can be seen that the vortex is shifted when  $\mu = 0$ . This can be explained by the fact that, when some artificial dissipation is added at the vortex core, the influence of the farfield on the vortex decreases. The gradient based limiter was used to replace the artificial dissipation so that only the confinement term  $\epsilon$  remains as a parameter of the CVCM. The shape of the vortex is better preserved, even when the artificial dissipation coefficient  $\mu$  is set to zero.

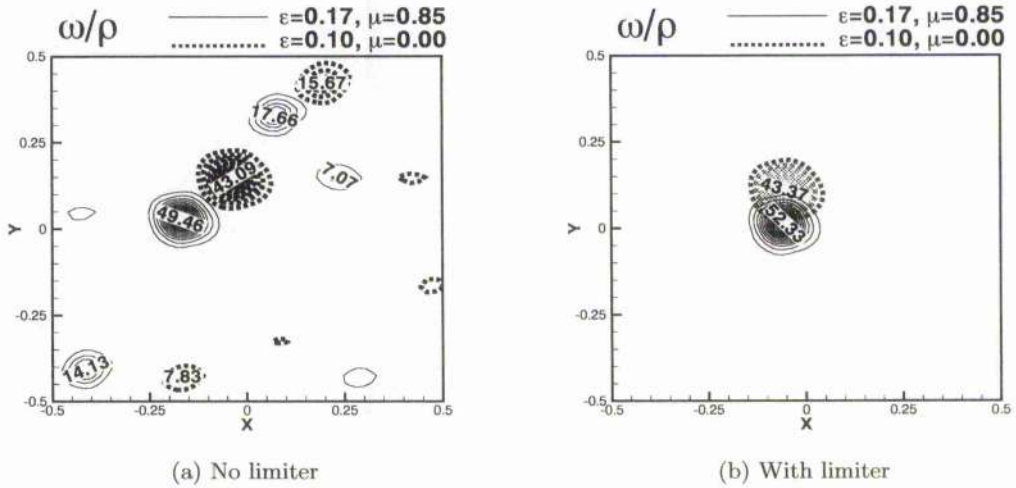


Figure 3.14: Contours of the  $\omega/\rho$  ratio after 20 cycles: (a) Effects of the artificial dissipation coefficient ( $\mu$ ) and (b) effect of the gradient-based vorticity limiter on the coarse grid. Laminar calculations ( $Re = 1000$ ).

Comparison between the results given by method (c) (grid scaling) and method (b) ( $\epsilon$  set to a constant) was established for laminar flow. It can be noticed from Figure 3.15(a) that the vortex strength depends on the applied value of the confinement parameter and is different for the two methods. It appears that the convected vortex loses a part of its strength in the first steps on a coarse grid for method (b), the grid scaling having the advantage of better preserving the vortex. However, the vortex dissipates relatively faster after 10 cycles since the vortex core radius tends to increase.

It is relevant to know how the optimum  $\epsilon$  parameter is to be modified for different  $Re$  numbers. It can be seen from Figure 3.15(b) that a lower Reynolds number necessitates the use of a higher value of  $\epsilon$  since the vortex is more viscous at the vortex core and is more affected by the freestream conditions. For any Reynolds numbers, it is possible to preserve the vortex characteristics and to get the desirable values of vorticity before its interaction with the blade in the case of BVI simulations. This was expected since the CVCM is aimed at modelling the vortex core. It should also be pointed out that the vortex is expected to diffuse at low  $Re$  number.

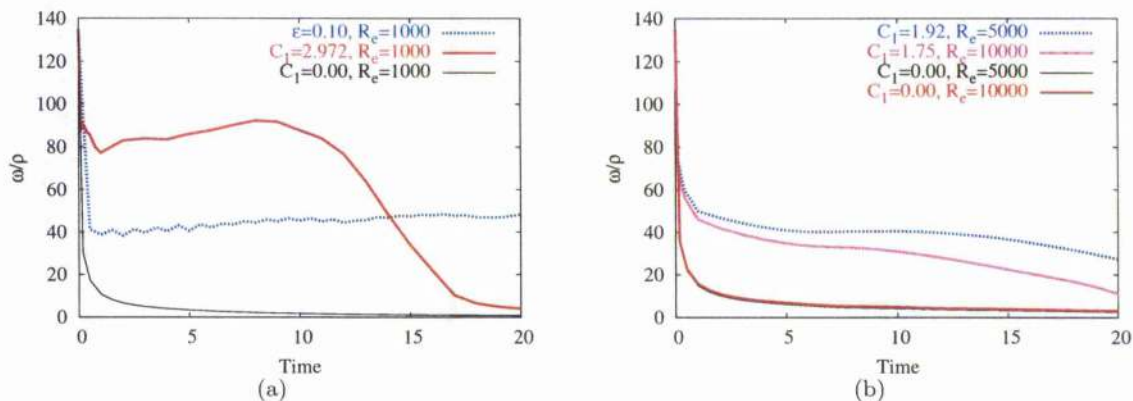


Figure 3.15: History of the ratio  $\omega/\rho$  at the vortex core on the coarse grid for laminar flow. (a) The confinement methods with constant  $\epsilon$  and  $\epsilon$  scaled with the grid cell are compared for a Reynolds number of 1000. (b) Different Reynolds numbers are applied when the  $\epsilon$  is scaled with the grid cell. Note that the vorticity gradient limiter is used.

The density confinement method (method d) has been tested with the use of the grid scaling (method c). The influence of the  $\delta$  parameter has been evaluated on a coarse grid. Figure 3.16 gives respectively the history of the density at the vortex core for different values of  $\delta$  with vorticity gradient limiter and with density confinement. As mentioned by Costes and Kowani [110], the density confinement allows a better preservation of the vortex eye as shown in Figures 3.17-3.18. Regarding the vortex shape preservation, it seemed that a parameter  $\delta$  set to 5.0 was the best option. It is interesting to note that the vorticity gradient limiter helps to preserve the characteristics of the vortex.

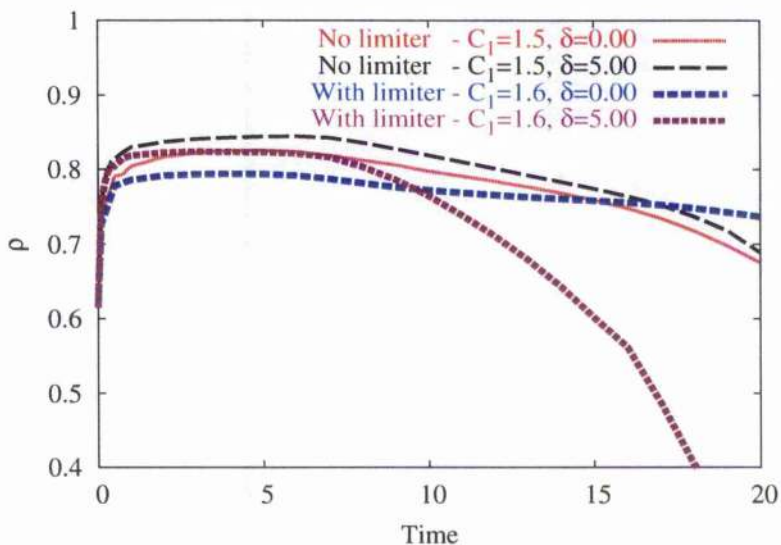


Figure 3.16: Time history of the density at the vortex core using the vorticity gradient limiter and the density confinement. Inviscid calculations.

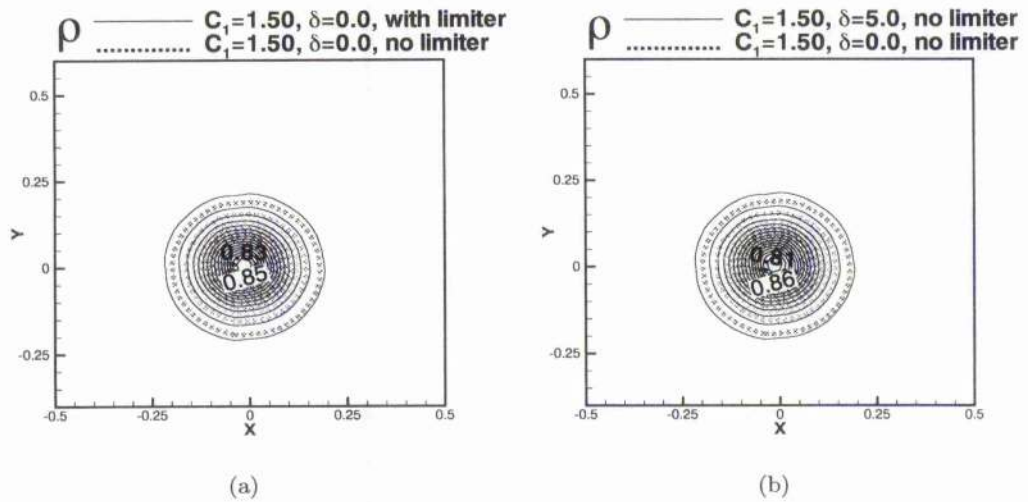


Figure 3.17: Contours of the density after 10 cycles for the inviscid calculations. (a) With vorticity gradient limiter. (b) With density confinement.

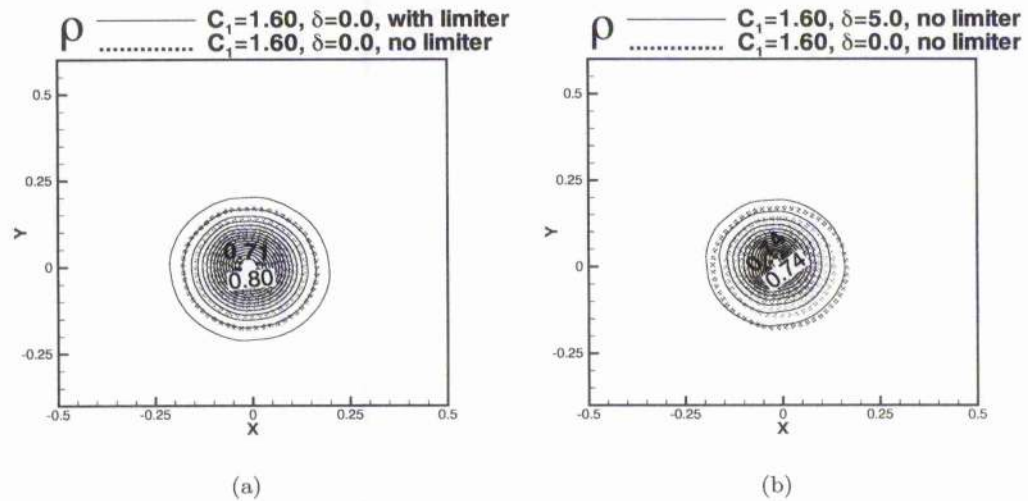


Figure 3.18: Contours of the density after 10 cycles for the inviscid calculations. (a) With vorticity gradient limiter. (b) With density confinement.

The use of the CVCM allows the tracking of the vortex for several cycles. The initial characteristics of the vortex are given in Figure 3.19(a-b). As illustrated in Figure 3.19(c), on the coarse grid, the vortex is reasonably preserved after twenty cycles whereas it disappears after only two cycles without CVCM. On the fine grid and without CVCM, the vortex is five times weaker in terms of the  $\omega/\rho$  ratio at the vortex core after twenty cycles of convection (see Figure 3.19(d)). It can be noticed (Figure 3.19(c)) that the vortex is better captured on a fine grid than on a coarse grid since the number of cells across the core radius is larger. The combination of methods (b) and (c) gives the best results for preserving the vortex characteristics and was therefore preferred to method (a). It is interesting to note that the coefficient  $C_1$  on the fine grid was set to almost half the value of the confinement parameter on

the coarse grid. The expression used for the  $\epsilon$  was actually found to be related to the number of cells per core radius. Since the fine grid has double the number of cells in the  $x$  and  $y$  directions, the optimum  $\epsilon$  was set to 0.75, its values on the coarse grid being 1.5. This suggests that a full optimisation of the method may be possible with the use of the spatial scheme properties and some of the vortex characteristics such as the vortex core size. Note that the CPU time incurred by the use of the CVCM is minimal.

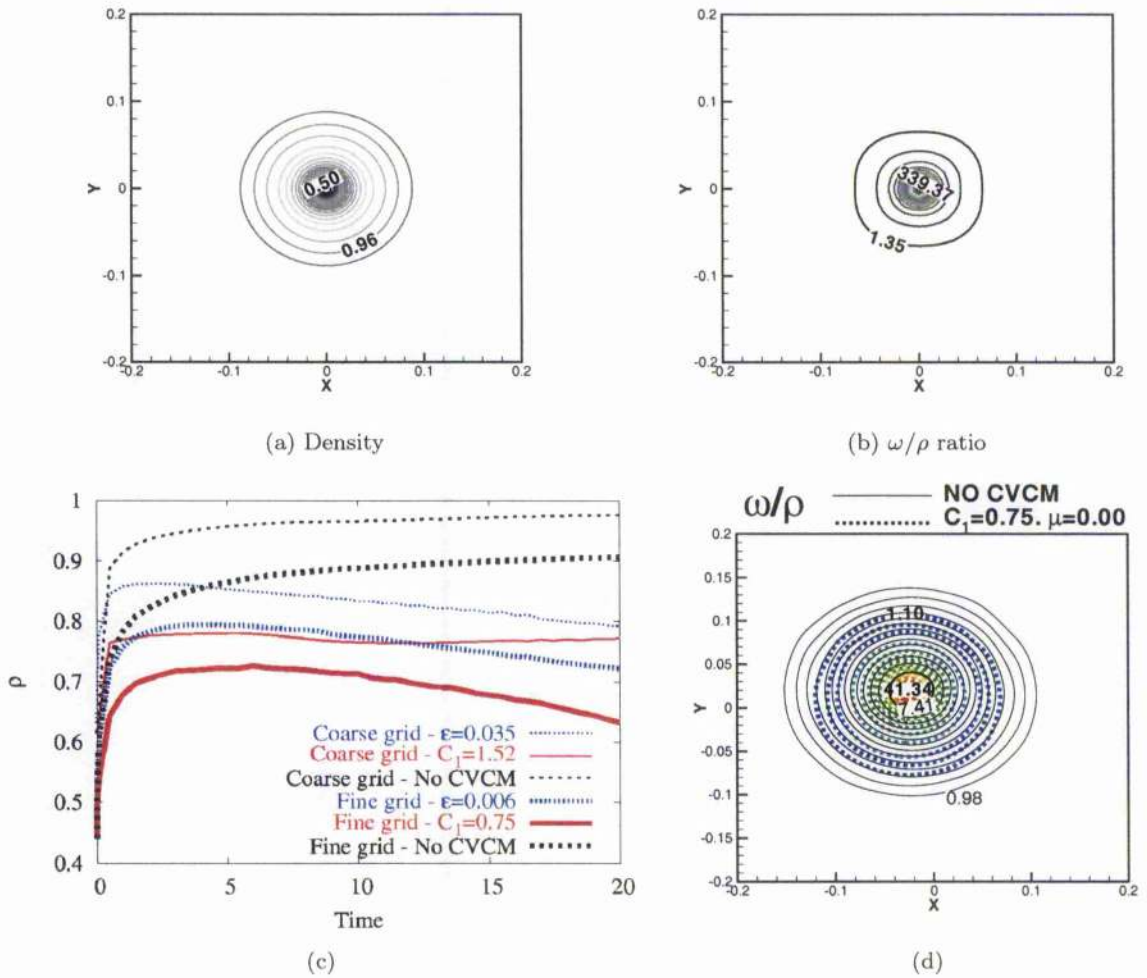


Figure 3.19: Contours of (a) the density  $\rho$  and (b) the  $\omega/\rho$  ratio for the initial vortex on the fine grid. (c) Time history of the density at the vortex core using different  $\epsilon$  scalings. (d) Evolution of the  $\omega/\rho$  ratio after 20 cycles with and without CVCM. Inviscid calculations.

### 3.4 Capabilities of the CVCM for flow simulation

#### 3.4.1 Characteristics and behaviour of the CVCM for the BVI simulation

The simulation of blade-vortex interaction requires the use of a non-uniform grid. Scaling with cell size was therefore combined with the vorticity gradient limiter for the calculations. The grids used for the BVI simulation were carefully generated so that spacing along the expected path of the vortex is as uniform as possible. The grid densities along with the nature of the BVI calculations are given in Table 3.3. It is important to note that the calculations were run 2D in order to gain some insight into the behaviour of the CVCM for unsteady problems.

Some robustness problems were encountered when running the calculations for values of  $\epsilon$  which are too large. Indeed, the use of the CVCM tends to modify the profile of the boundary layer and to amplify the wake which is characterised by a large value of vorticity. One approach is then to use the surface confinement method [112]. The used approach consisted in using zones to restrict the effect of the source term to vortices, avoiding wakes and boundary layers: the confinement method was not applied up to a distance 0.1 chords from the aerofoil and also when the vorticity gradient exceeded a cut-off value. No confinement was applied near the aerofoil and so the CVCM does not alter the behaviour of the turbulence model during the interaction. Furthermore, the CVCM is not needed near the aerofoil since the grid is fine enough in this area to capture the vortices. Another advantage of the limiter is that it can be used for both inviscid and viscous calculations. The optimum  $\epsilon$  parameter was also found to depend on which spatial scheme is used and dissipation properties vary with the grid cell length, the time step and the nature of the flow. Since most of the calculations were run at a fixed Reynolds number of a million, the influence of the Reynolds number ( $R_e$ ) on the CVCM behaviour (see Section 3.3.5) was not considered, meaning that no specific limiter based on  $R_e$  was used. This is expected since the physical viscosity is negligible in this case. Note that the confinement parameter will be noted  $\epsilon$  for clarity.

Unsteady case	BVI conditions	Number of points
Viscous	$M_\infty = 0.50, \hat{\Gamma} = -0.283, y_0 = 0.00$	240k
Viscous (coarse) (fine)	$M_\infty = 0.80, \hat{\Gamma} = -0.2, y_0 = -0.26$	66k
	$M_\infty = 0.80, \hat{\Gamma} = -0.2, y_0 = -0.26$	140k
Viscous	$M_\infty = 0.63, \hat{\Gamma} = -0.42, y_0 = 0.00$	172k
	$M_\infty = 0.63, \hat{\Gamma} = -0.42, y_0 = -0.25$	172k
Inviscid	$M_\infty = 0.57, \hat{\Gamma} = -1.8, y_0 = -0.31$	160k
Viscous		172k

Table 3.3: Size of the grids used for the 2D BVI calculations. The first BVI is head-on and the three others are miss-distance BVI cases.

### 3.4.2 Blade-vortex interaction

The four test cases concern the interaction between a vortex and an NACA-0012 aerofoil at different freestream Mach numbers. The calculations used the  $k-\omega$  model for the three first cases and the SST model for the last case. More detail about the use of the CVCMM with a turbulence model is given in the next chapter. The grid sizes used are given in Table 3.3 along with the initial conditions. The Reynolds number given for each case is non-dimensionalised against the chord whereas the vortex strength and the vortex core radius are non-dimensionalised against the product of the freestream velocity with the chord of the aerofoil and the chord, respectively. Note that the density confinement has been assessed for the first case of BVI.

#### Case 1

This experiment concerns the head-on parallel BVI between a vortex and a NACA-0012 aerofoil. This was taken from Lee and Bershader [9]. Since detailed measurements of the surface pressure on the upper and lower sides of the blade are available for this experiment, this case has been previously used as a benchmark. The head-on BVI has been simulated using the CVCMM. The non-dimensionalised vortex strength and core radius were respectively set to  $-0.283$  and  $0.018$ . The Reynolds number ( $Re$ ) was fixed to a million. The block topology of the grids used along with the dimensions of the blocks is given for case 1 in Figure 3.20. Note that the commercial package ICEMCFD was used to generate the grids employed for the BVI study.

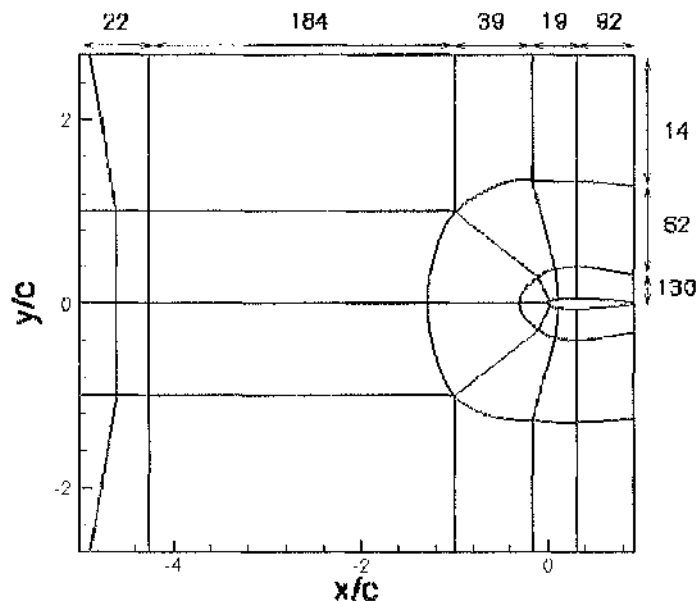


Figure 3.20: Block topology of the 2D grid used for the simulation of the head-on BVI, NACA-0012 aerofoil.

The computed surface pressure coefficient is given in Figure 3.21 and they are compared to the experiments. It is observed that the peaks are underpredicted when the CVCM is not used, especially for  $x/c=0.02$ . The use of the CVCM allows the preservation of the vortex characteristics. This can also be observed for the histories of the lift and drag coefficients given in Figure 3.22.

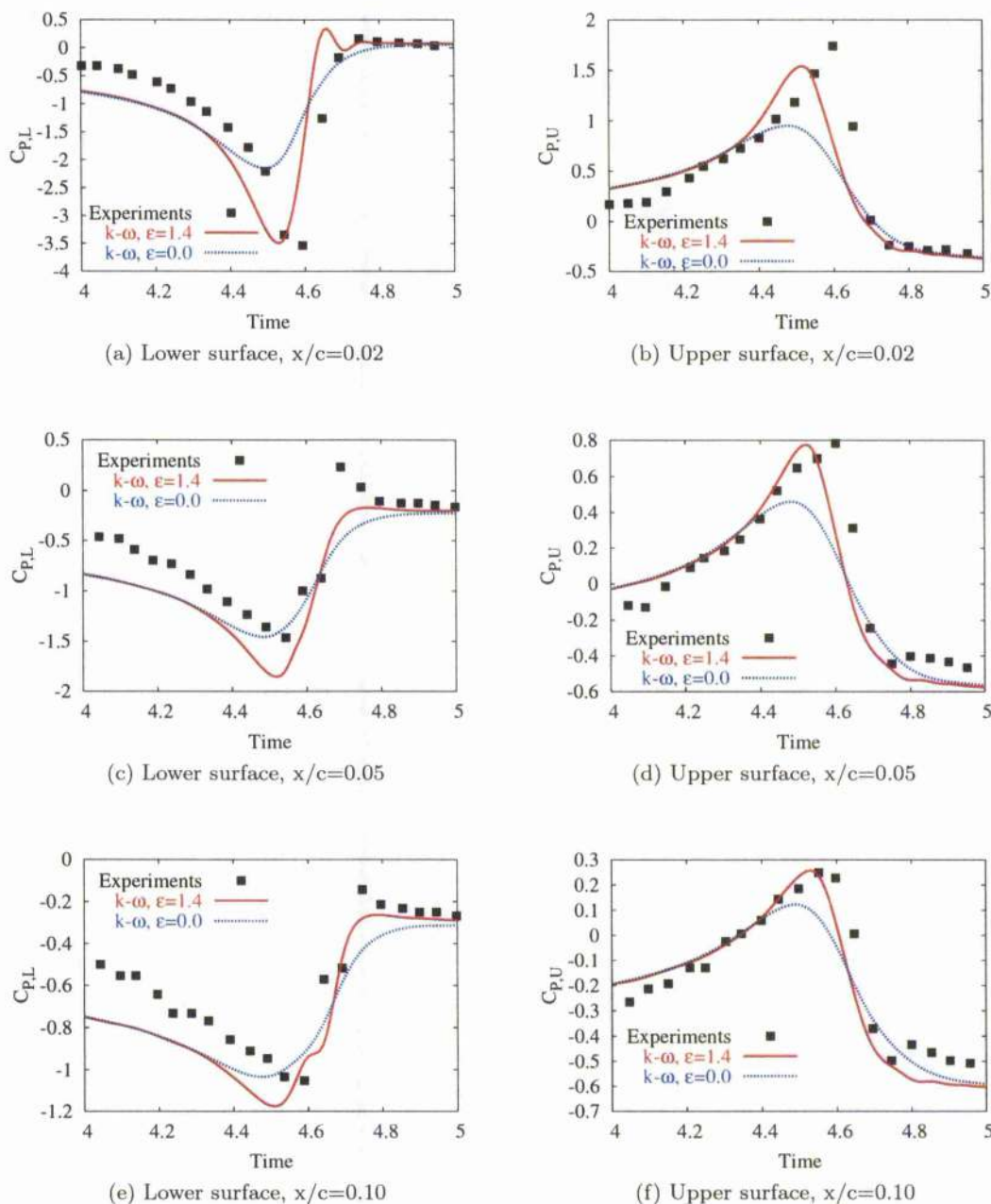


Figure 3.21: Influence of the initial vortex location on the time history of the surface pressure coefficient. Head-on BVI problem, NACA-0012 aerofoil, viscous calculations,  $Re = 1e + 6$ ,  $M_\infty=0.5$ ,  $\hat{\Gamma} = -0.283$ ,  $R_c = 0.018$ .

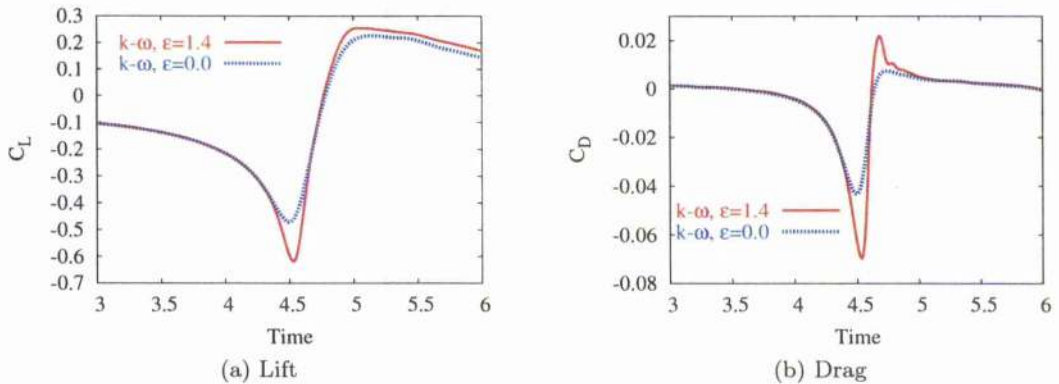


Figure 3.22: Lift and drag histories for head-on BVI with and without confinement. NACA-0012 aerofoil, viscous calculations,  $M_\infty=0.5$ ,  $\hat{\Gamma} = -0.283$ ,  $R_c = 0.018$ .

It has been checked if the vorticity gradient limiter coupled with the density confinement (methods (b) and (d)) could help in obtaining a better match with the experiments for viscous calculations when  $\epsilon$  is equal to 1.5. Viscous calculations using the density confinement have been run for a parameter of 1.4 which gave the best results with the use of the vorticity gradient limiter. The use of density confinement gave similar results for this test case which also illustrates that better predictions are obtained with the use of either the vorticity gradient limiter or the density confinement. It can be noticed from Figure 3.23 that the combination of methods (b) and (d) yields similar results to method (a) and (b).

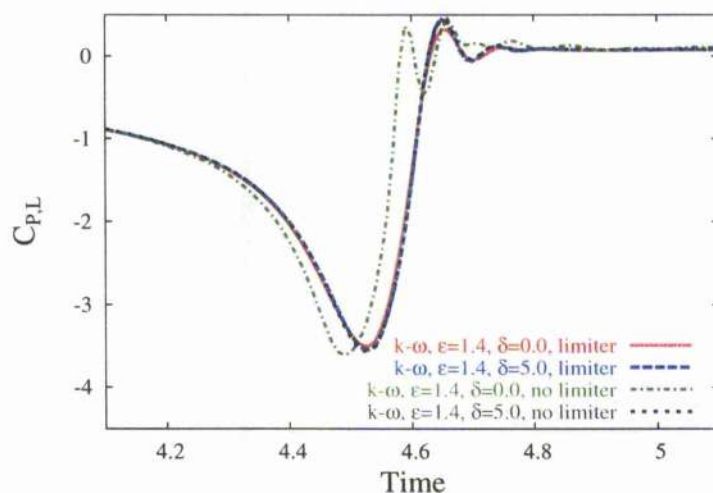
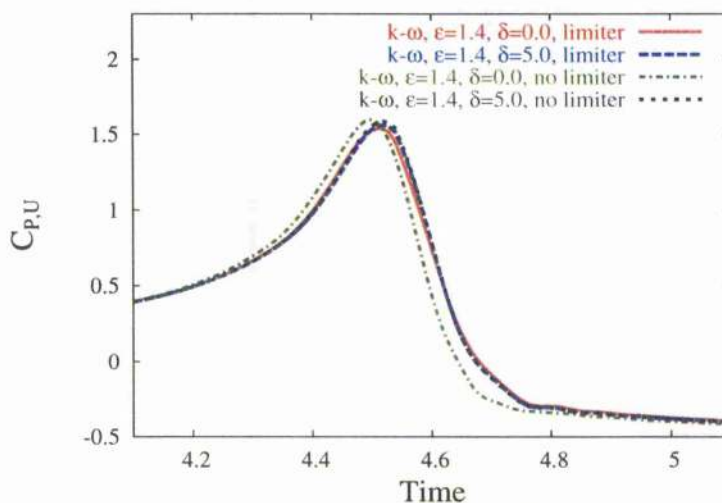
(a) Lower surface,  $x/c=0.02$ (b) Upper surface,  $x/c=0.02$ 

Figure 3.23: Influence of the density confinement and of the vorticity gradient limiter on the time history of the surface pressure coefficient. Head-on BVI problem, NACA-0012 aerofoil, viscous calculations,  $M_\infty=0.5$ ,  $x/c=0.02$ . The vortex was introduced at 4.5 chords ahead of the aerofoil. Note that  $\epsilon$  and  $\delta$  are the confinement and the density confinement parameters, respectively.

A comparison for the lift and drag histories is given in Figure 3.24 for the different methods. The lift and drag coefficients are similar for all the methods except for the method when neither the density confinement nor the vorticity-based limiter is used. The use of the limiter seems to be sufficient as long as the vortex is not introduced too far away from the aerofoil. Although it is suspected that the use of the density confinement will be useful if the vortex is to be well-captured for long distances, the use of the vorticity gradient limiter for the confinement parameter was preferred for our study, the  $\epsilon$  term remaining the only parameter of the CVCM. This choice was

made since it allows the use of the CVCM with only a single parameter to calibrate, the confinement parameter  $\epsilon$ . Note that the confinement parameter was found to be inversely proportional to the core radius on a given grid when the grid scaling was used.

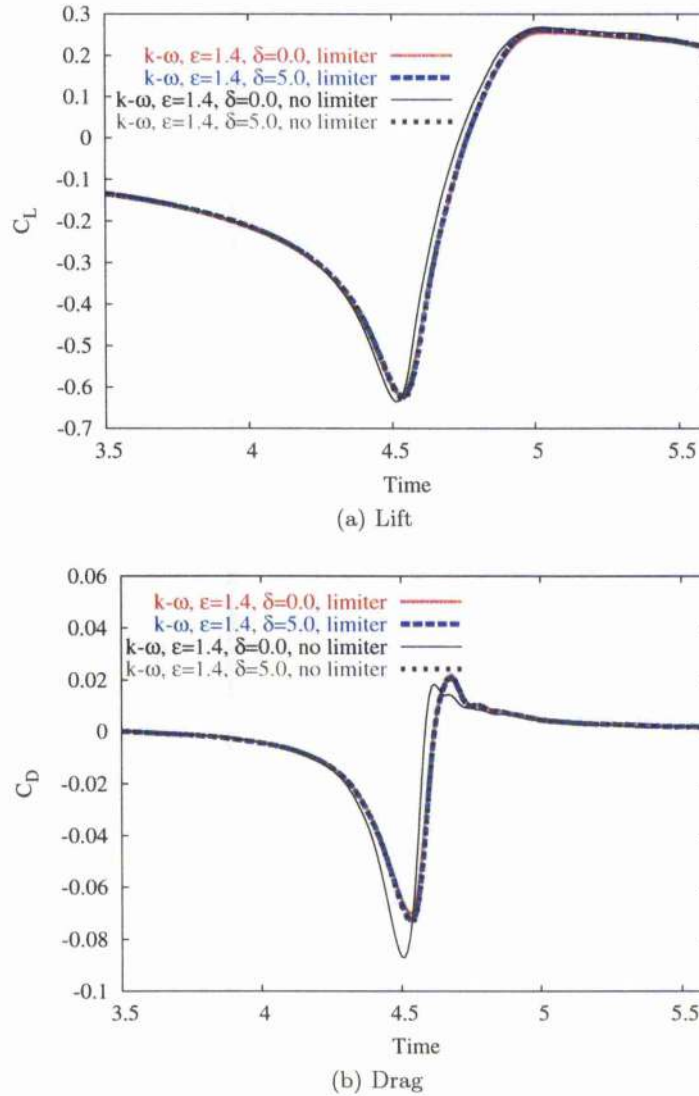


Figure 3.24: Influence of the density confinement and of the vorticity gradient limiter on the time histories of lift and drag. Head-on BVI problem, NACA-0012 aerofoil, viscous calculations,  $M_\infty=0.5$ ,  $x/c=0.02$ . The vortex was introduced at 4.5 chords ahead of the aerofoil.

The quality of the BVI simulation in terms of flow visualisation is now assessed. The computed flow is compared against the holographic interferograms taken during the experiments. As explained in [113, 114], the holographic interferograms can be represented by one of the density contours. Figure 3.25 shows the contours of the density gradient magnitude along with the density contours. They compare well against the experiments, proving that the main features of the flow are well-captured.

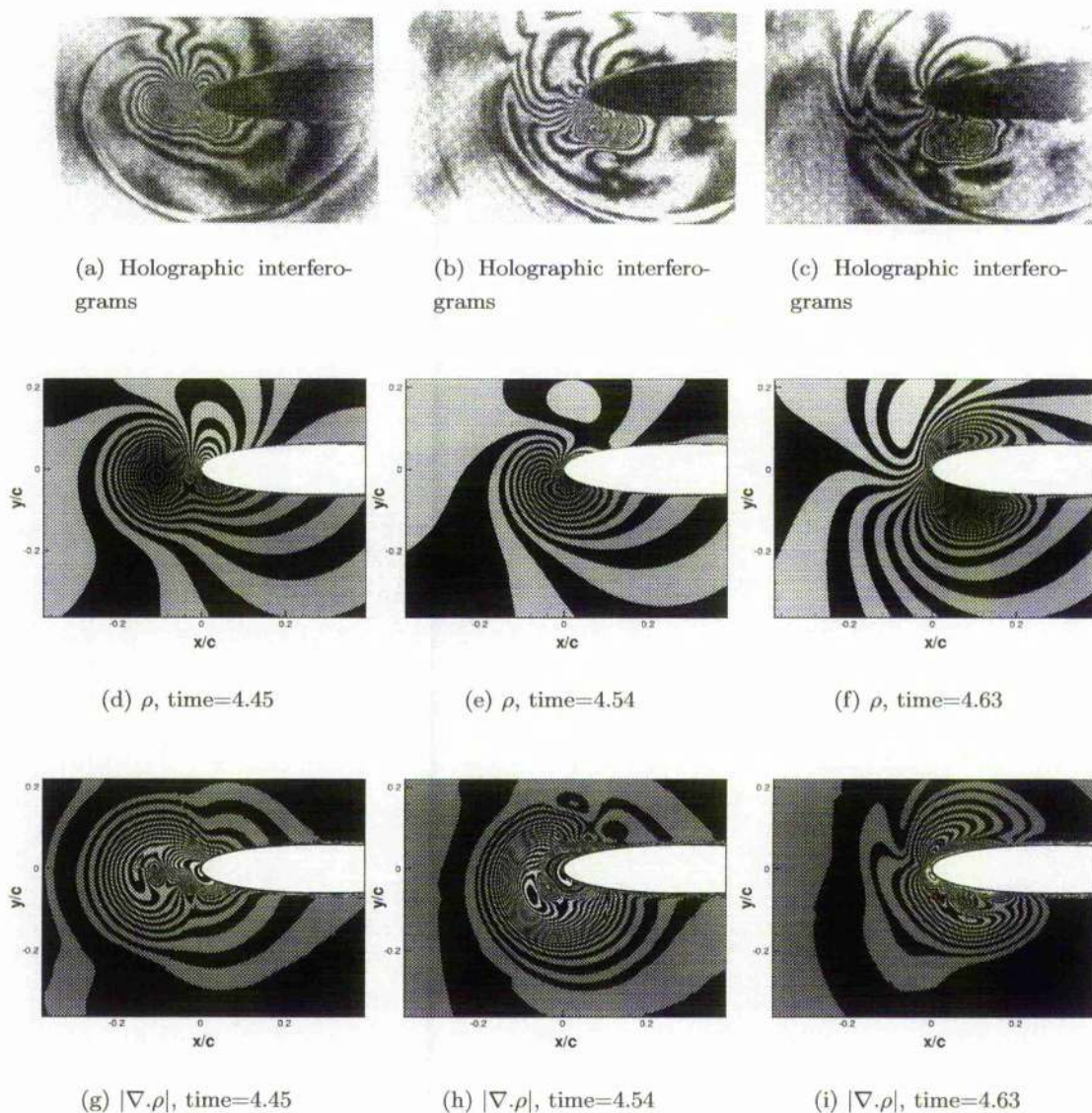


Figure 3.25: Comparison between (a-c) experimental holographic interferograms, (d-f) the density contours for the head-on BVI case and (g-i) the computational density gradient magnitude contours. The vortex was introduced 4.5 chords ahead of the aerofoil and the calculations were performed using the  $k-\omega$  model. The time step is non-dimensionalised with the freestream velocity ( $U_\infty$ ) and the aerofoil chord ( $c$ ).

### Case 2

The experiments from Kitaplioglu *et al.* [30] were used as second BVI test cases for head-on and miss-distance BVI ( $y_0 = -0.25$ ). A two-bladed rotor operating at zero thrust to minimize the influence of the rotor's wake was used in a wind tunnel to simulate the aerodynamics and the acoustics of a parallel BVI. The vortex was generated upstream of a rotor of section NACA-0012 using a pitching NACA-0015 aerofoil with an incidence of  $\pm 12$  degrees. The hover tip Mach number was set to 0.712 and the advance ratio 0.197. The blade surface pressure distribution was measured at the spanwise radius  $R/r = 0.876$ . Note that the contribution of the second blade was neglected since the vortex was supposed to dissipate after its interaction with the first blade.

The characteristics of the vortex, not initially measured, was estimated from the work of McAlister and Takahashi [115] who obtained the necessary measurements on a wing of nearly identical geometry as the vortex generator [23]. A comparison of the velocity distributions with experiment of McAlister and Takahashi motivated Bridgeman [116] to recommend a higher value of vortex strength [41]. The vortex strength  $\hat{\Gamma}$  was set to -0.25 for a dimensionless core radius of 0.162 at a freestream Mach number of 0.63.

Viscous calculations were run with a Reynolds number of a million. The loads history is given in Figure 3.26 at different chordwise locations. It is thought that the computed results are satisfactory for two reasons. First, similar results are obtained with and without the CVCM. This suggests that the loads and the lift histories can be well-simulated by CFD without the CVCM as long as the initial vortex is weak. Indeed, the dissipation of a relatively weak vortex affects less the BVI loads than that of a strong initial vortex. Figure 3.27(a) confirms that the inherent dissipation of the solver is minimal for a weak vortex, explaining why different methods were capable of reproducing the BVI test case [30]. As expected, the lift history is similar with and without CVCM as shown in Figure 3.27(b). Secondly, the accuracy of the lift prediction was found to be good since the predicted farfield noise which uses the lift history was correctly predicted as shown in Chapter 6.

Note that the vortex generated by the pitching aerofoil is actually not typical for a rotor [23] since its radius is too large and its velocity peak too low. This means that the CVCM is of interest for the simulation of more critical BVI with a stronger vortex. This is further discussed for case 4.

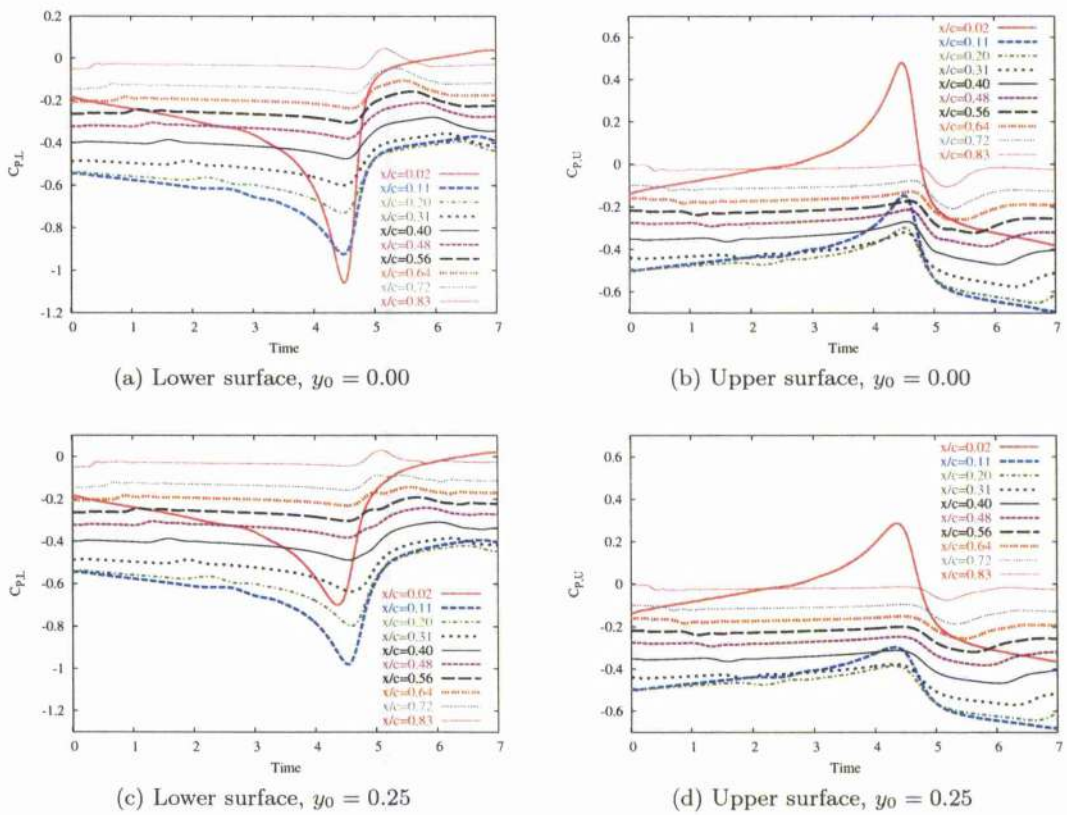


Figure 3.26: Time history of the surface pressure coefficient for (a-b) the head-on and (c-d) miss-distance BVI cases. The vortex was introduced at 4.5 chords ahead of the aerofoil. NACA-0012 aerofoil, viscous calculations ( $k-\omega$  model),  $Re = 1e+6$ ,  $M_\infty = 0.63$ .  $\hat{\Gamma} = -0.25$ ,  $R_c = 0.162$ .

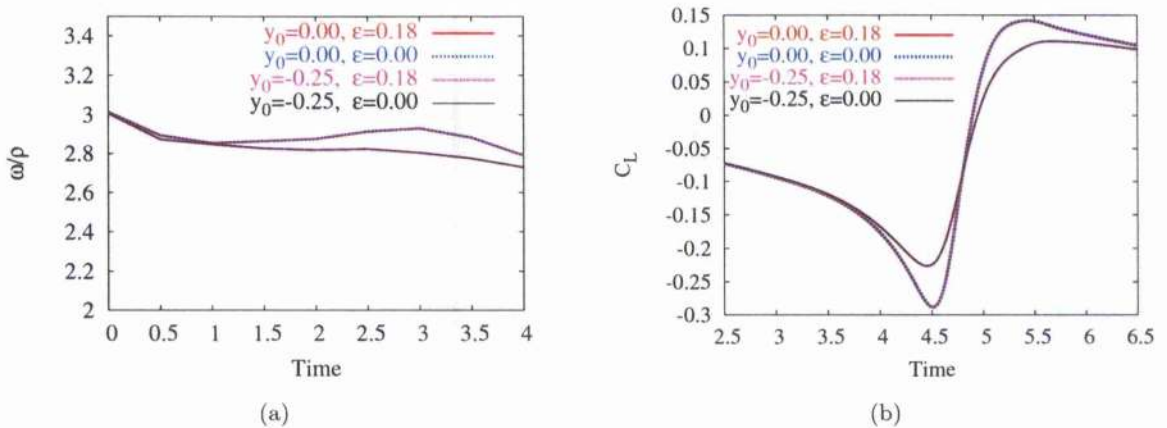


Figure 3.27: Time histories of (a) the  $\omega/\rho$  ratio at the vortex core and of (b) the lift with and without CVCM.

## Case 3

This test case is a miss-distance BVI at transonic flow. It has been previously used as a benchmark for CFD calculations [46, 117]. This BVI is interesting since it allows the robustness of the solver to be tested due to the presence of a shock-vortex interaction. The non-dimensionalised vortex strength and the core radius are respectively  $-0.2$  and  $0.05$ . The location of the vortex was set to 5 chords upstream of the aerofoil and  $0.26$  chord beneath the mean chord. Viscous calculations were run on two grids of 65k points and 140k points for a freestream Mach number of  $0.8$  and a Reynolds number of  $3.6$  millions.

The BVI has been simulated with and without the CVCM for two grid densities. It can be noticed that the vortex dissipates faster on both grids when no CVCM is applied as Figure 3.28 shows. However, the results are very similar. The initial vortex is actually relatively weak in terms of density at its core, which implies that the preservation of the vortex characteristics does not modify significantly the lift coefficient, suggesting that a weak vortex is less affected by the inherent dissipation of the solver.

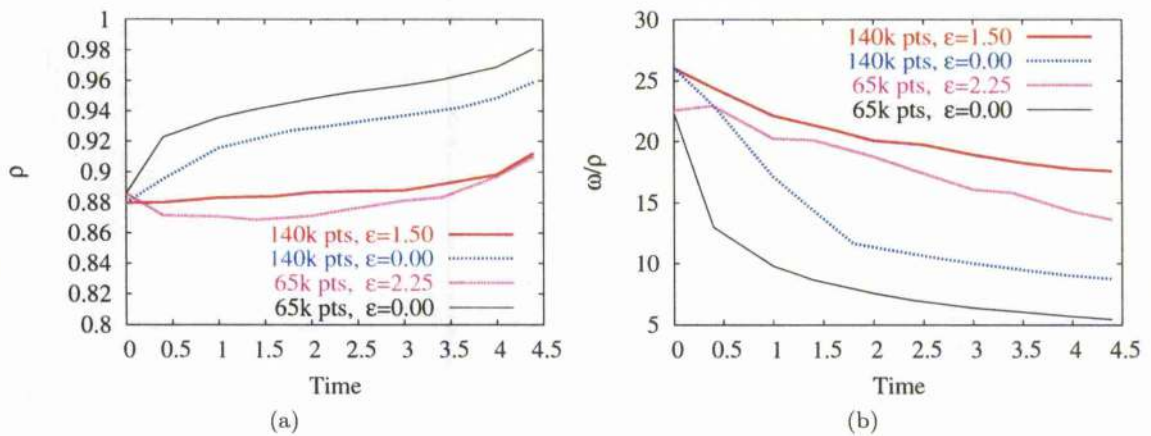


Figure 3.28: Time histories of (a) the density at the vortex core and of (b) the  $\omega/\rho$  ratio with and without CVCM. NACA-0012 aerofoil, viscous calculations ( $k-\omega$  model),  $R_e = 3.6e + 6$ ,  $M_\infty = 0.8$ .  $\hat{\Gamma} = -0.2$ ,  $R_c = 0.05$ ,  $y_0 = -0.26$ .

Figure 3.29 presents the lift and drag histories. The maximum lift matches with the NS results of Oh *et al.* [46] for the same test case. It is also in good agreement with numerical inviscid results of Damodaran and Caughey [117]. Note that a difference occurs at the shock-vortex interaction: a slight overshoot can be observed on both grids with the use of the CVCM at time  $t(U_\infty/c) = 5.60$ .

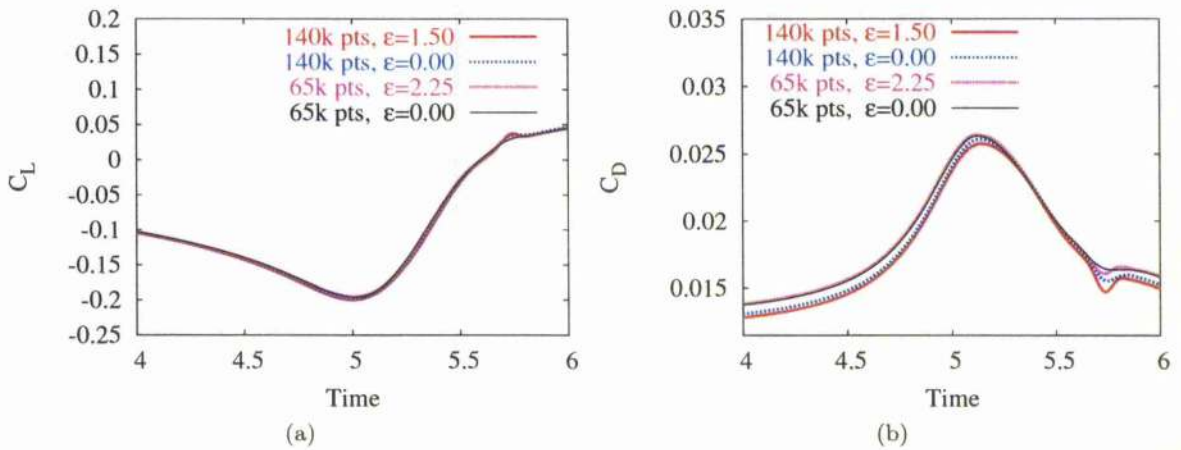


Figure 3.29: Time histories of the (a) lift and (b) drag with and without CVCM. The vortex was introduced at 5.0 chords ahead of the aerofoil. NACA-0012 aerofoil, viscous calculations ( $k-\omega$  model),  $R_e = 3.6e + 6$ ,  $M_\infty=0.8$ .  $\hat{\Gamma} = -0.2$ ,  $R_c = 0.05$ ,  $y_0 = -0.26$ .

This case is characterised by a shock-vortex interaction. As depicted in Figure 3.30, the presence of the vortex before and after its interaction with the shock modifies the structure of the latter. The vortex which passes through the shock has been studied in the literature. The theory of such interaction is illustrated by the schematic of Figure 3.31 [118].

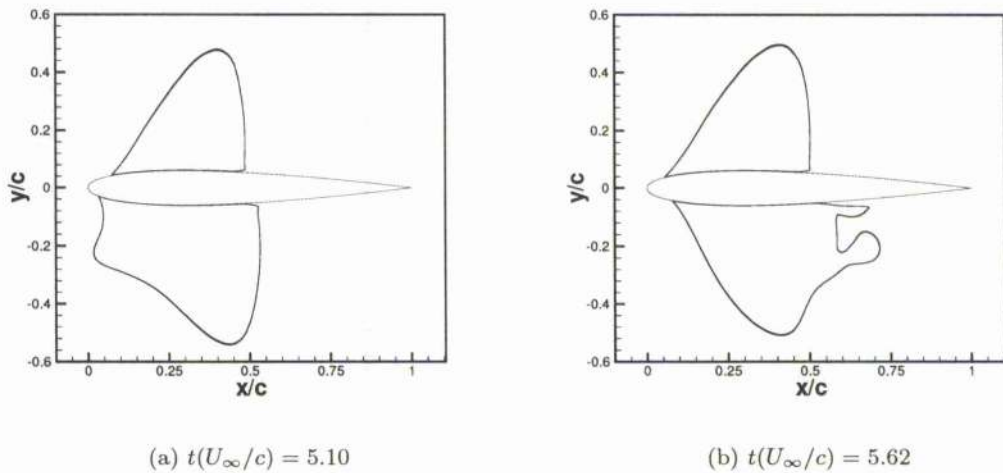


Figure 3.30: Sonic lines at two different times. (a) Before the shock-vortex interaction, (b) after the shock-vortex interaction. NACA-0012 aerofoil, viscous calculations ( $k-\omega$  model),  $R_e = 3.6e + 6$ ,  $M_\infty=0.8$ .  $\hat{\Gamma} = -0.2$ ,  $R_c = 0.05$ ,  $y_0 = -0.26$ .

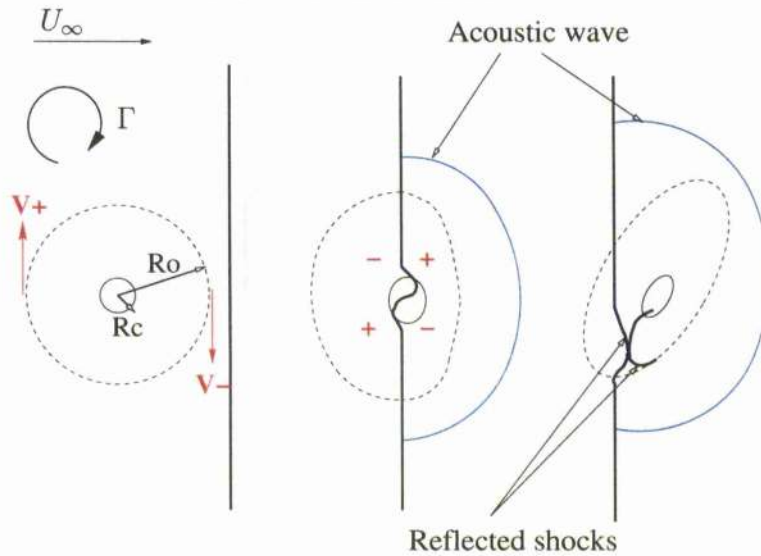


Figure 3.31: Shock-vortex mechanisms. Note that a weak expansion and compression develop respectively below and above the vortex, that is due to the downwash component of the vortex. Then, after the first half of the vortex passed the shock, the upwash component of the vortex creates similar pressure changes but of opposite signs this time, that is at the origin of the quadrupolar component.

The interaction of a shock with a vortex produces a quadrupolar acoustic wave [119]. The quadrupolar component propagates radially outward and behind the shock. The shock compresses the vortex into an elliptical vortex [118]. As a consequence of the vortex-shock interaction, the shock splits into two parts as illustrated by Figure 3.32. The pressure gradients change after the passage of the vortex and the structure of the shock is then altered, leading to a distortion of the shock. The alternation of expansions and compressions is at the origin of the formation of the quadrupolar component which interacts with the shocks. The shock distorts and reflects on the body, meaning that the quadrupolar component and the reflected shocks form an acoustical wave.

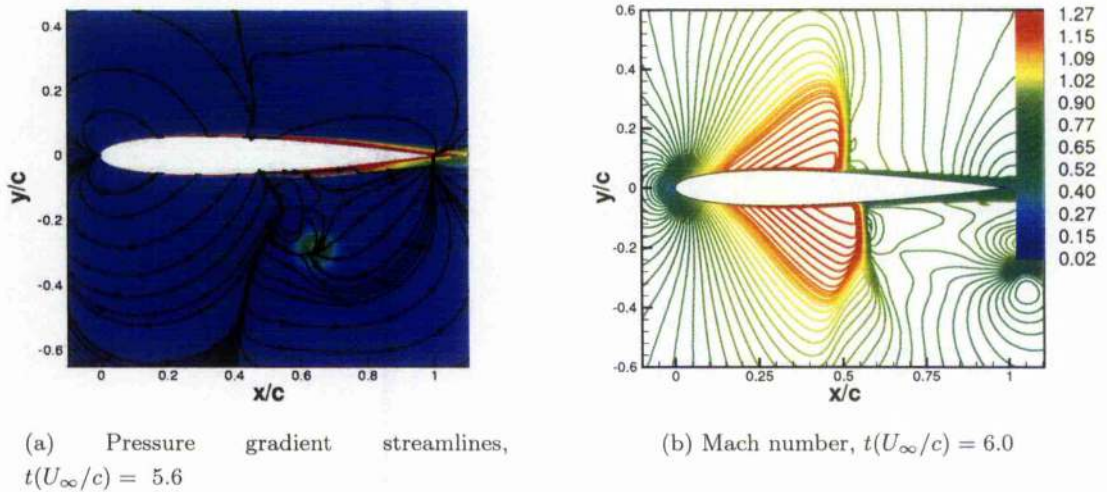


Figure 3.32: Contours of pressure gradients streamlines and isomachs at two different times. The vorticity is shown along with the pressure gradient streamlines. NACA-0012 aerofoil, viscous calculations ( $k-\omega$  model),  $R_e = 3.6e + 6$ ,  $M_\infty=0.8$ .  $\hat{\Gamma} = -0.2$ ,  $R_c = 0.05$ ,  $y_0 = -0.26$ .

Furthermore, this interaction is characterised by the generation of acoustical waves [119]. Figure 3.33 shows three different acoustic waves. The waves denoted by A-B, and E are respectively called the compressibility waves and the transonic wave. The waves C and D correspond to the trailing-edge noise. The compressibility waves start to propagate after the oscillation of the stagnation point and the transonic wave stems from the generation of a supersonic pocket below the aerofoil. The trailing-edge waves originate from the diffraction of the pressure field by the trailing-edge of the aerofoil. The mechanisms of the acoustics will be studied in more detail in Chapter 6.

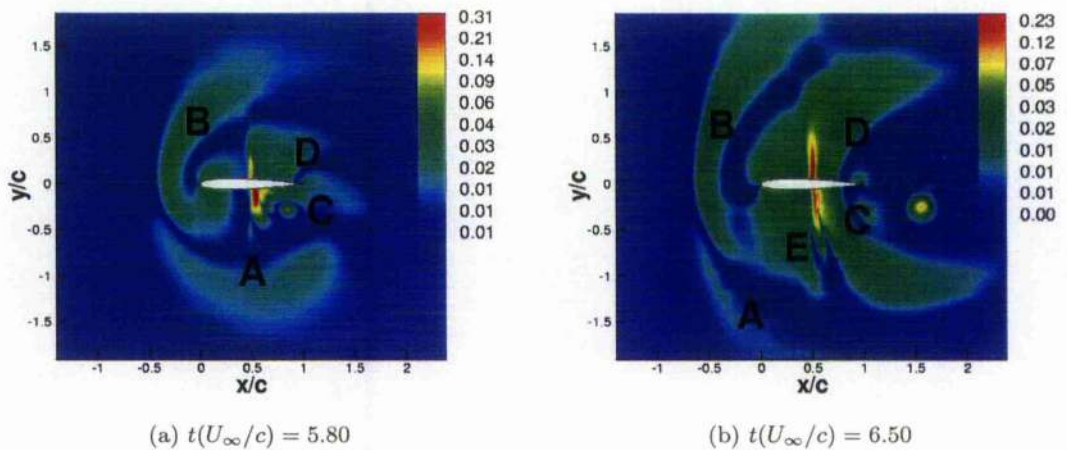


Figure 3.33: Contours of the absolute value of the acoustic pressure at two different times. NACA-0012 aerofoil, viscous calculations ( $k-\omega$  model),  $R_e = 3.6e + 6$ .  $M_\infty=0.8$ ,  $\hat{\Gamma} = -0.2$ ,  $R_c = 0.05$ ,  $y_0 = -0.26$ . The scale is exponential.

#### Case 4

The BVI concerns the interaction of a strong vortex with the NACA-0012 at a miss-distance  $-0.31c$ . Flow visualisation was obtained in the experiments conducted by Nellessen *et al.* [28]. The vortex was generated in a shock tube and its strength was large enough to generate a supersonic pocket on the lower side of the aerofoil. The vortex strength and the core radius were respectively set to  $-1.8$  and  $0.1$  at a freestream Mach number of  $0.57$ .

Inviscid and viscous calculations were carried out. In contrast to the inviscid calculations, some convergence problems were met for the viscous runs. The flow was therefore set to laminar till  $5\%$  chord ahead of the aerofoil, meaning that the turbulence model was applied just before the interaction. Such a choice was made due to the severity of the test case, the vortex being very strong at its core. The computed density contours are compared against the experimental ones in Figure 3.34 at four different times. Good agreement in terms of flow visualisation was obtained, which suggests that the BVI was satisfactorily simulated. Note that the Reynolds number was fixed to a million for the viscous calculations and that the grid density for inviscid and viscous calculations were similar along the vortex path.

A comparison between the aerodynamics of both inviscid and viscous calculations was established. It was found that secondary vortices appear for the viscous calculations due to the detachment of the Boundary Layer (BL) and that this is also the case for the inviscid calculations although no BL should develop. The presence of vortices is shown in Figure 3.35. The vortices originate from the way the solver handles the Euler equations. The properties of the flow are altered due to the fact that the Euler equations are discretised [120]. As in any solver, boundary conditions are used to get a physical flow and the order of accuracy of the scheme is lowered when discontinuities are present. When the solver is not capable of capturing accurately high velocity gradients for severe cases such as the studied one, the entropy gradient rises. This causes vorticity to be generated, e.g. at the vortex core and on the lower surface of the aerofoil as depicted in Figure 3.36.

Differences between the flow structures given by the inviscid and viscous runs are observable. Although special care should be taken if the transonic effects have to be accurately simulated, the mentioned differences may be small enough for a reasonable prediction of the integrated loads using Euler calculations. Therefore it is important to check whether inviscid calculations can provide reliable aerodynamic coefficients for such severe BVI cases.

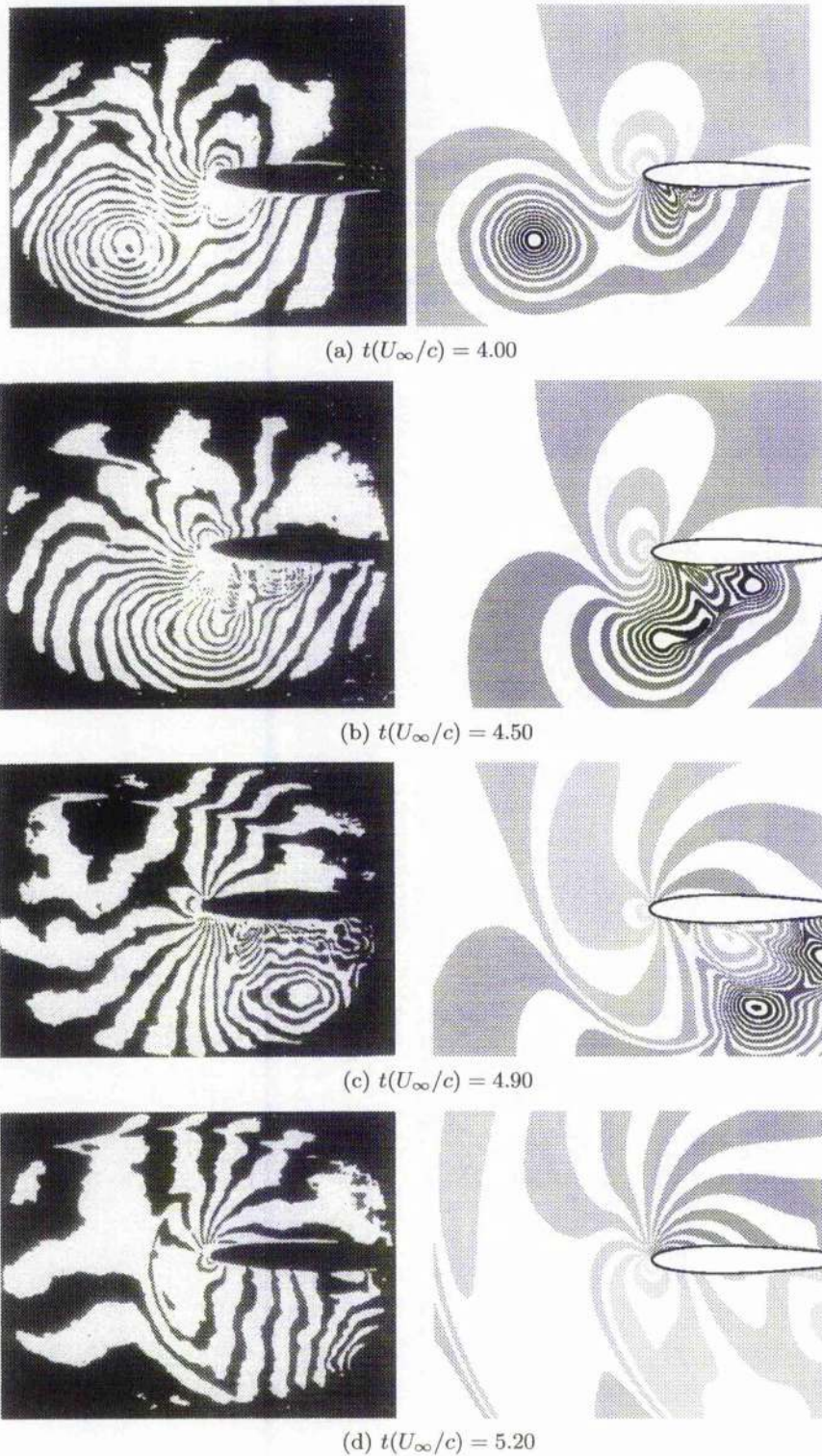


Figure 3.34: Density contours for miss-distance BVI case at four different times. NACA-0012 aerofoil, viscous calculations (SST model),  $M_\infty=0.57$ ,  $\hat{\Gamma} = -1.8$ ,  $R_c = 0.10$ ,  $y_0 = -0.31$ . Note that the vortex location in the x-direction was not provided in the experiments (left). Therefore, the computed contours (right) were chosen in order to establish a comparison with the experiments .

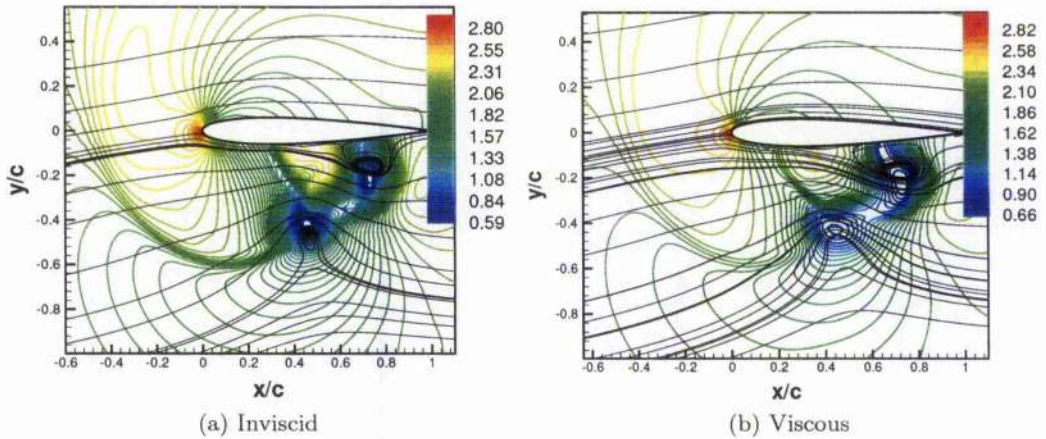


Figure 3.35: Isobars ( $2p/q_\infty$ ) contours along with the streamlines for different miss-distances at time  $t(U_\infty/c) = 4.90$ . Miss-distance BVI problem, NACA-0012 aerofoil, inviscid calculations,  $M_\infty=0.57$ ,  $\hat{\Gamma} = -1.8$ ,  $y_0 = -0.31$ .

A valuable quantity to find out the importance of the numerical dissipation is the Total Pressure Loss  $TPL$  which indicates the entropy rises. This is defined as

$$TPL = 1 - \frac{p \left(1 + \frac{\gamma-1}{2} M^2\right)^{\frac{\gamma}{\gamma-1}}}{\frac{1}{\gamma M_\infty^2} \left(1 + \frac{\gamma-1}{2} M_\infty^2\right)^{\frac{\gamma}{\gamma-1}}} \tag{3.8}$$

where  $p$  is the non-dimensionalised pressure,  $M$  is the local Mach number and  $M_\infty$  is the freestream Mach number. As depicted in Figure 3.36, excessive total pressure loss is generated at the body of the aerofoil. Vorticity is then created artificially and vortices appear. The vortices then keep growing due to the numerical diffusion [121] and to the fact that the only dissipation present in the Euler equations is the inherent dissipation of the solver; mainly stemming from the spatial scheme.

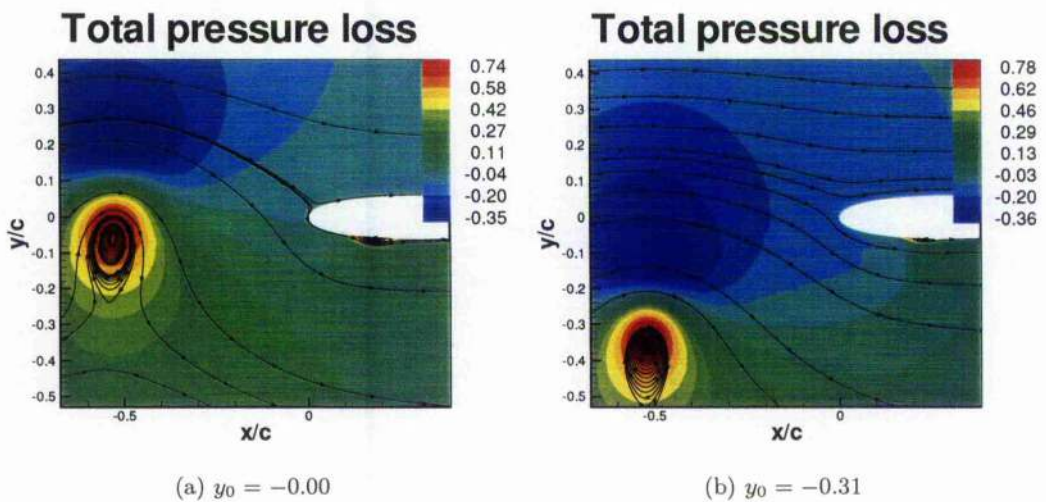


Figure 3.36: Total pressure loss at different instants.  $t(U_\infty/c)=4.8$  (a-b), 4.9 (c-d), 5.0 (e-f). NACA-0012 aerofoil, head-on and miss-distance BVI problems, inviscid calculations,  $M_\infty=0.57$ ,  $\hat{\Gamma} = -1.8$ .

Inviscid and viscous results are now compared in terms of surface pressure coefficients and lift coefficients. A particular attention has to be paid to the quality of the aerodynamic loads, i.e. the lift coefficient when inviscid calculations are run. The surface pressure coefficient is given in Figure 3.37 for both inviscid and viscous calculations. They are very similar up to 10% chord length.

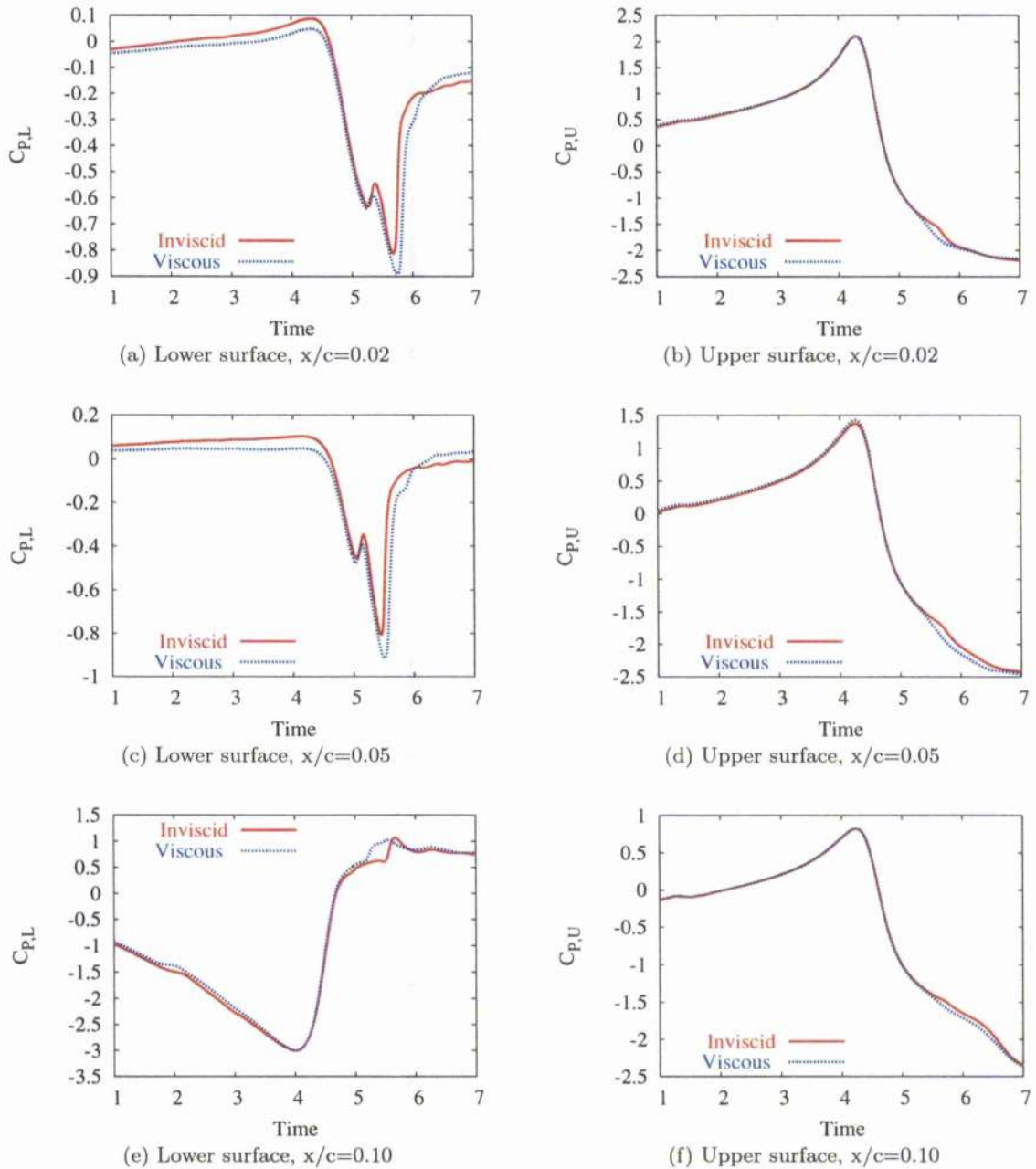


Figure 3.37: Time history of the surface pressure coefficient at different chordwise locations for inviscid and viscous calculations (SST model). Miss-distance BVI problem, NACA-0012 aerofoil,  $M_\infty=0.57$ ,  $\hat{\Gamma} = -1.8$ ,  $R_c = 0.10$ ,  $y_0 = -0.31$ .

Differences appear at the aft of the aerofoil as shown in Figure 3.38 which depicts the  $C_p$  chordwise variation at the time  $t(U_\infty/c) = 4.9$ . It shows that BVI modifies the loads up to 30% chord length for both inviscid and viscous calculations, which was also observed by Booth and Yu [32]. Furthermore, it also indicates the presence of vortices. It can be noticed that the secondary vortex, although stronger on the case of the inviscid run, affects more the lower surface coefficient for viscous calculations as observed in [98]. This results from the thickening of the BL induced by the presence of the secondary vortex.

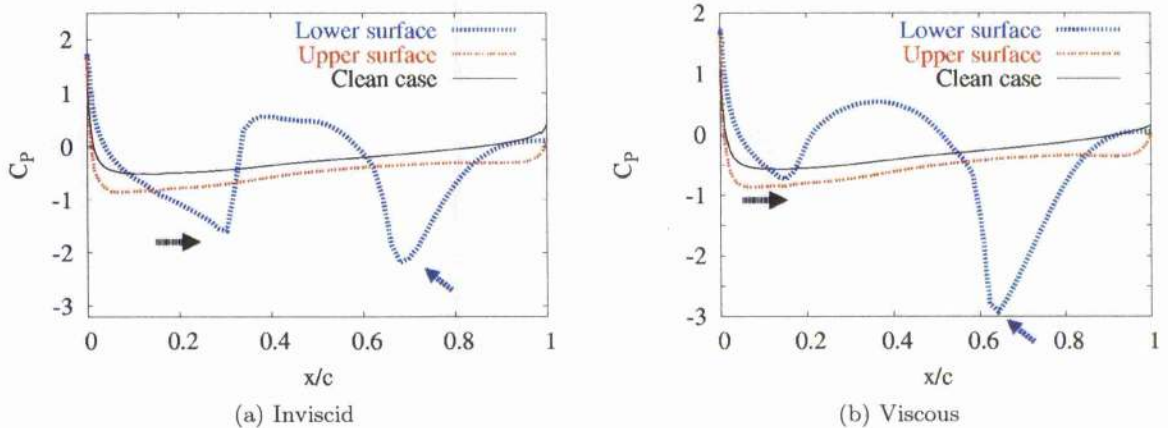


Figure 3.38: Surface pressure coefficient at three different times.  $t(U_\infty/c)=4.9$ . Head-on BVI problem, NACA-0012 aerofoil, inviscid and viscous calculations,  $M_\infty=0.57$ ,  $\hat{\Gamma} = -1.8$ ,  $y_0 = -0.15$ . The horizontal black arrow and the oblique blue arrow indicate respectively the presence of a supersonic pocket and of a vortex.

Figure 3.39 shows the histories of the lift and drag. Although the presence of vortices affects the  $C_p$  for both inviscid and viscous calculations, very close agreement was obtained between both calculations in terms of BVI loads. Indeed, the integrated loads are not affected much by the presence of the vortices which are only generated on the lower side of the aerofoil. This means that, even for such a severe case, BVI cases can be correctly simulated with inviscid runs as long as only BVI loads are to be predicted. Inviscid calculations can be run to allow a relative comparison between the different BVI cases in terms of aerodynamic coefficients. It has to be pointed out that the head-on BVI was also simulated for inviscid and viscous calculations. The same remarks could be made for the secondary vortices, the lift and drag coefficients remaining similar for both cases. Note that a more complete comparison between inviscid and viscous results along with the use of the CVCVM is carried out in Chapter 4.

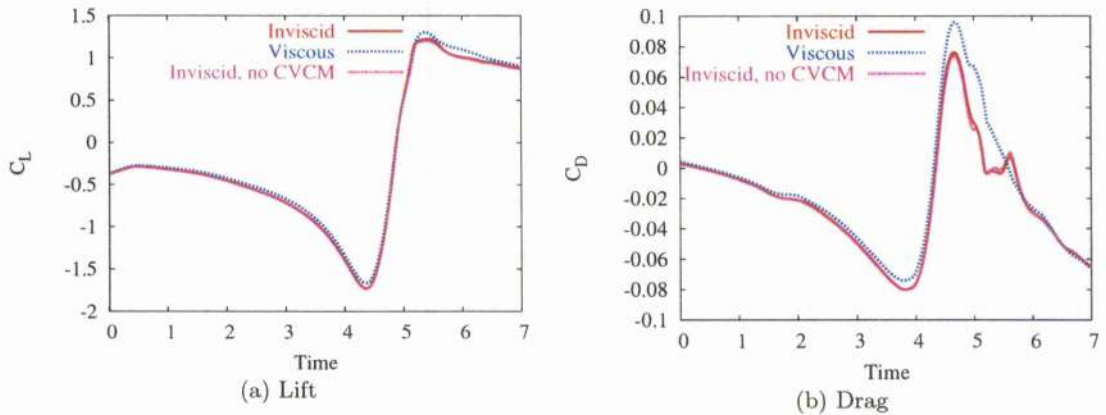


Figure 3.39: Lift and drag histories for inviscid and viscous calculations (SST model), with and without CVCM. Miss-distance BVI problems, NACA-0012 aerofoil,  $M_\infty=0.57$ ,  $\hat{\Gamma} = -1.8$ ,  $R_c = 0.10$ ,  $y_0 = -0.31$ .

Figure 3.40 illustrates all the interest of the CVCM. Although the loads are also reasonably predicted without CVCM as shown in Figure 3.39, the vortex is found to diffuse very quickly on the given grid when no CVCM is applied. On one hand, this illustrates the capabilities of the code in terms of robustness and efficiency. On the other hand, it implies that the BVI loads are affected by the vortex-induced velocity up to a certain limit. It is suspected that the supersonic pocket generated along the shoulder of the aerofoil gets stronger when the vortex is well-captured, meaning that the transonic wave is much stronger when the CVCM is applied.

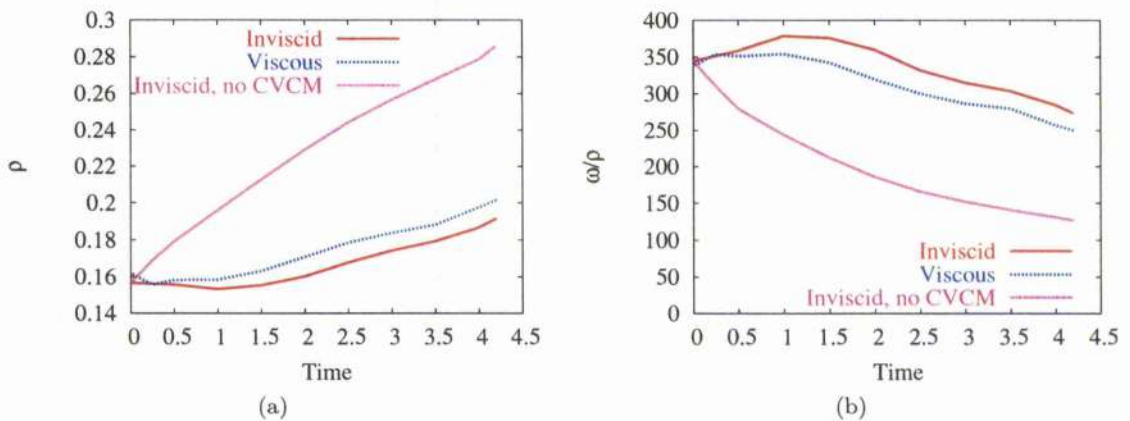


Figure 3.40: Time histories of (a) the density and of (b) the  $\omega/\rho$  ratio at the vortex core with and without CVCM. Miss-distance BVI problem, inviscid and viscous calculations (SST model),  $\hat{\Gamma} = -1.8$ ,  $R_c = 0.10$ ,  $y_0 = -0.31$ . Note that a grid of 160k and 172k points were used for the inviscid and viscous runs, respectively.

### 3.5 Conclusions

A comparison between the performance of two implicit time-marching schemes coupled with an upwind spatial scheme has been carried out. The UNFACTored method is in good agreement with the FUN method regarding the results of the test cases. Despite a higher average CPU time per iteration, the UNFACTored method presents the advantage of getting a faster convergence. The possibility of using a higher CFL number enables a faster convergence. The fact that no factorisation error occurs is also another explanation for the better performance of the UNFACTored method.

The use of the CVCM allows the preservation of the vortex. The characteristics of the vortices can be preserved as long as the confinement parameter is optimum. The CVCM made possible the simulation of BVI using an existing CFD code and the overhead in terms of CPU time and memory was minimal. Results compared well with experiments when the CVCM is used for preserving strong vortices and the predicted acoustic field is in qualitative agreement with experimental observations. However, further investigation is needed to make the method as independent as possible of the value of the confinement parameter, this could be possibly achieved by taking into account the properties of the scheme of the solver and some of the characteristics of the vortex.

## Chapter 4

# Optimisation of the BVI simulation

This chapter identifies the effects of various parameters on the BVI results. The consistency of the CFD results is assessed for inviscid and viscous calculations.

### 4.1 Introduction

It has been shown in the previous chapter that the simulation of BVI is possible via the use of the CVCM. The simulation of the head-on BVI is now attempted along with comparisons between CFD results and experiment. The well-know experiment of Lee and Bershader [9] is used as the test case. This experiment concerns the head-on parallel BVI between a vortex and a NACA-0012 aerofoil. Different techniques such as high-order schemes [9, 58], local grid refinement [16] and more recently unstructured adaptive meshes [45, 46] have been used to preserve the convected vortex. CVCM allows the use of relatively coarse grids along the vortex path and refined grids near the aerofoil so that accurate prediction of the surface pressure and well-preserved near- and mid-field acoustical waves can be obtained without an excessive number of grid points.

In this chapter, comparison of the CFD results against the experiments of Lee and Bershader [9] are shown. Parameters which are likely to influence the convergence of the method as well as the BVI results will be studied: vortex models, vortex location, spatial and time refinement, the influence of corrections to the angle of attack and of the turbulence models. The influence of the CVCM on the results is also assessed.

### 4.2 Optimisation of the BVI Simulation using the CVCM

The test case is the parallel BVI between a clockwise-rotating vortex and the NACA-0012 aerofoil. The radius of the vortex, which is non-dimensionalised against the chord, and its circulation  $\hat{\Gamma} = \frac{\Gamma}{U_{\infty}c}$  are set respectively to 0.018 and -0.283 as for the benchmark

problem of Chapter 3. A schematic of the problem is presented in Figure 4.1. Results will be shown for the head-on BVI at freestream Mach numbers of 0.5 and 0.8.

Both inviscid and viscous calculations were attempted and the freestream Reynolds number, based on the chord, was set to one million for the viscous case, within the range of values 0.9-1.3 million given for the experiments. The viscous calculations were expected to predict better the pressure coefficient on the lower part of the aerofoil. As will be shown, it is important to include the viscosity effects for head-on BVI since they effect the transfer of energy between vortices as well as between a vortex and the boundary-layer flow (see Körber and Ballmann [122]). The best parameters for simulating BVI will be determined by examining the results obtained for the subsonic case (freestream Mach number 0.5). Then the simulation of a similar head-on BVI at a freestream Mach number of 0.8 is presented.

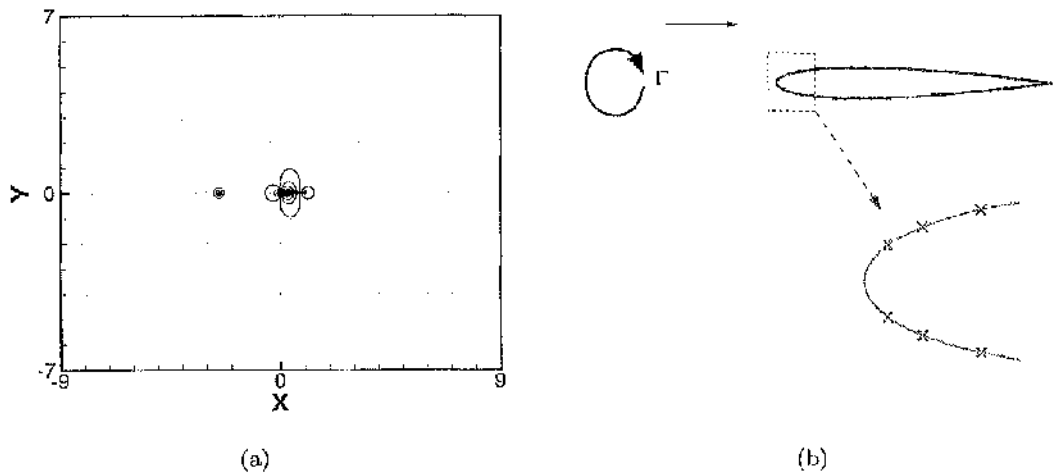


Figure 4.1: (a) Schematic of the initial configuration of the head-on BVI problem, the initial location of the vortex is shown along with isobars ( $2p/q_\infty$ ) contours. (b) Locations of the pressure taps in the leading-edge region of the aerofoil. The locations correspond to the experiments by Lee and Bershader [9].

Fine and coarse versions of inviscid and viscous grids were generated, as summarised in Table 4.1. All the viscous calculations were run using the  $k-\omega$  model in the next sections except for the section where the influence of the turbulence model along with the use of the CVCM is investigated. Note that the grid densities along the vortex path were kept the same for the different vortex locations but that they were different around the aerofoil for the inviscid and viscous calculations.

Unsteady case	Grid density	Vortex location (in chord)	Number of points
Inviscid	Coarse	1.5	126k
		2.5	140k
	Fine	1.5	490k
		2.5	512k
		3.5	549k
		4.5	578k
Viscous	Coarse	1.5	203k
		2.5	211k
		3.5	221k
		4.5	230k
	Fine	2.5	819k

Table 4.1: Size of the grids used for the inviscid and viscous calculations with different vortex locations.

#### 4.2.1 Influence of the vortex models

Several different models for an isentropic vortex exist, all of which assume that the radial velocity is negligible. The pressure and density are calculated using the approximation of the Euler equations  $\frac{dp}{dr} = \rho \frac{v_\theta^2}{r}$  and the isentropic relation  $p = a\rho^\gamma$  (see [109]). An expression of the tangential velocity  $v_\theta(r)$  with  $r$  the radial distance from the vortex centre is given in the next paragraphs. In this work, the following models were considered.

(1) The Scully model [123]

This model has been widely used for numerical simulation. The expression of the velocity is

$$\frac{v_\theta}{U_\infty} = \left( \frac{\hat{\Gamma}}{2\pi r} \right) \left( \frac{r^2}{r^2 + R_c^2} \right). \quad (4.1)$$

$U_\infty$ ,  $\hat{\Gamma}$ ,  $R_c$  are respectively the freestream velocity, the non-dimensionalised circulation ( $\hat{\Gamma} = \frac{\Gamma}{U_\infty c}$ ) and the core radius.

The density of the vortex, which is non-dimensionalised against the freestream density, is expressed as

$$\rho_{Scully} = \left( 1.0 - \frac{\gamma - 1}{2} \left( \frac{\hat{\Gamma}}{2\pi} \right)^2 \frac{M^2}{r^2 + R_c^2} \right)^{\frac{1}{\gamma-1}} \quad (4.2)$$

(2) The Vatistas model [124]

This model [42] is supposed to give a better vortex profile than the Scully model, which has already been used for simulations [22]. The profile is the following:

$$\frac{v_\theta}{U_\infty} = \frac{\hat{\Gamma}}{2\pi r} \frac{r^2}{(r^4 + R_c^4)^{\frac{1}{2}}} \quad (4.3)$$

The non-dimensionalised density is given by

$$\rho_{Vatistas} = \left( 1.0 - \frac{1}{2R_c^2}(\gamma - 1) \left( \frac{\hat{\Gamma}}{2\pi} \right)^2 M^2 \left( \operatorname{atan} \left( \frac{\sqrt{2}r}{R_c} - 1 \right) - \operatorname{atan} \left( \frac{\sqrt{2}r}{R_c} + 1 \right) \right) \right)^{\frac{1}{\gamma-1}} \quad (4.4)$$

(3) The Povitsky model

The Povitsky model was used in [109] and it has the advantage of using an outer radius in addition to the core radius. Its expression is:

$$v_\theta(r) = \begin{cases} U_c r / R_c, & 0 \leq r < R_c \\ \tilde{C} \left( \frac{R_0}{r} - \frac{r}{R_0} \right), & R_c \leq r \leq R_0 \end{cases} \quad (4.5)$$

with  $U_c$  the maximum velocity magnitude,  $R_c$  the viscous radius core,  $R_0$  the outer radius and  $\tilde{C} = \frac{U_c R_0 R_c}{(R_0^2 - R_c^2)}$ .

Note that the outer radius is set to  $10 \times R_c$ .

The non-dimensionalised density is as follows

•  $0 < r < R_c$

$$\rho_{Povitsky} = \left( 1.0 - \frac{1}{2}(\gamma - 1)U_c^2 \left( 1 - \left( \frac{r}{R_c} \right)^2 \right) \right)^{\frac{1}{\gamma-1}} \quad (4.6)$$

•  $0 < r < R_c$

$\rho_{Povitsky} =$

$$\left[ 1.0 - (\gamma - 1)\tilde{C}^{\frac{2}{\gamma-1}} \left( 0.5 \left( 1 - \left( \frac{r}{R_0} \right)^2 \right) - 0.5 \left( 1 - \left( \frac{R_0}{r} \right)^2 \right) - 2 \left( \ln \left( \frac{R_0}{r} \right) \right) \right) \right]^{\frac{1}{\gamma-1}} \quad (4.7)$$

## (4) The Lamb-like model

This model has been replaced by the Scully model but is presented here for completeness. The radial velocity is of the form:

$$\frac{v_\theta}{U_\infty} = \bar{\Gamma} r e^{-0.5 \times r^2 / R_c^2}, \quad (4.8)$$

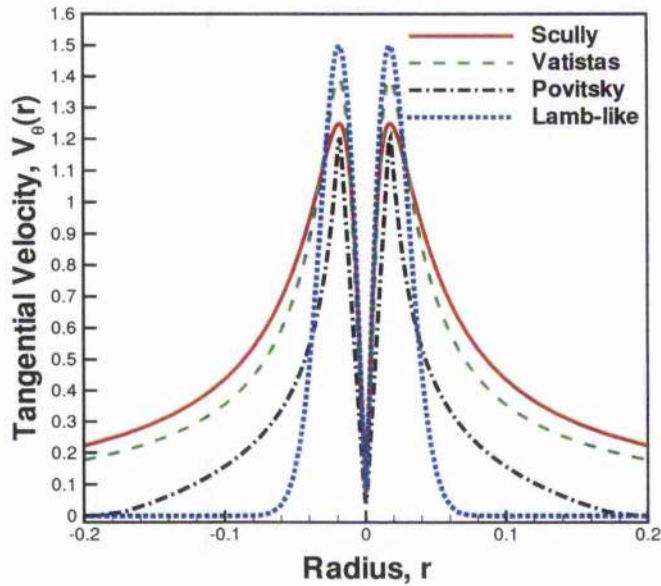
with  $\bar{\Gamma} = \frac{1}{U_\infty R_c}$

The non-dimensionalised density is written as

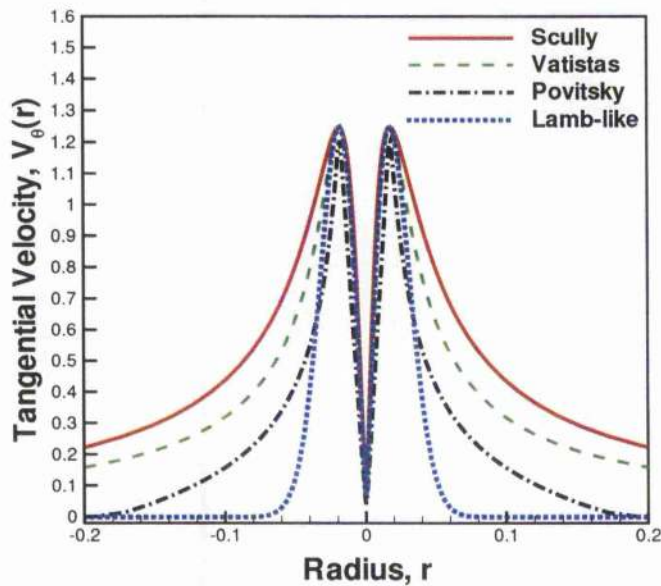
$$\rho_{Lamb} = \left( 1.0 - \frac{1}{2} (\gamma - 1) \bar{\Gamma}^2 M^2 e^{-\frac{r^2}{R_c^2}} \right)^{\frac{1}{\gamma-1}}. \quad (4.9)$$

Figures 4.2-4.3 show how different the models are in terms of tangential velocity and density. The same density at the vortex core could be obtained for the four models as well for the maximum velocity. However, the circulation and the ratio  $\omega/\rho$  is not similar for all the models. The circulation parameter of the Potvistky and Lamb-like models can only be set to a lower value than the Scully and Vatistas. This stems from the integration domain of the velocity profile which depends on the vortex model.

Srinivasan *et al.* [125] showed the importance of the model which should give the correct tangential velocity within the vortex core. A comparison between the Scully model and the other models has been carried out in order to check the influence of the vortex profile on the results. The time history of the surface pressure coefficients has been examined for the four different vortex models. However, it was only possible to get a vortex with the appropriate vortex strength and core radius for the Scully and the Vatistas models. Indeed, the sharp velocity profile of the Povitsky and Lamb models does not allow the introduction into the flow of a non-dimensionalised vortex strength of -0.283 with a core radius of 0.018. Therefore, the surface pressure coefficient at the chordwise locations  $x/c=0.02, 0.05$  and  $0.10$  is only given in Figure 4.4 for the Scully and the Vatistas models. Good results were obtained for both models as expected since they match very well the experimental data profile of the introduced vortex for this well known acrofoil-vortex interaction test case. The lift and the drag history remains very similar for the Vatistas and the Scully models as shown in Figure 4.5, meaning that they are both suitable for the simulation of BVI.

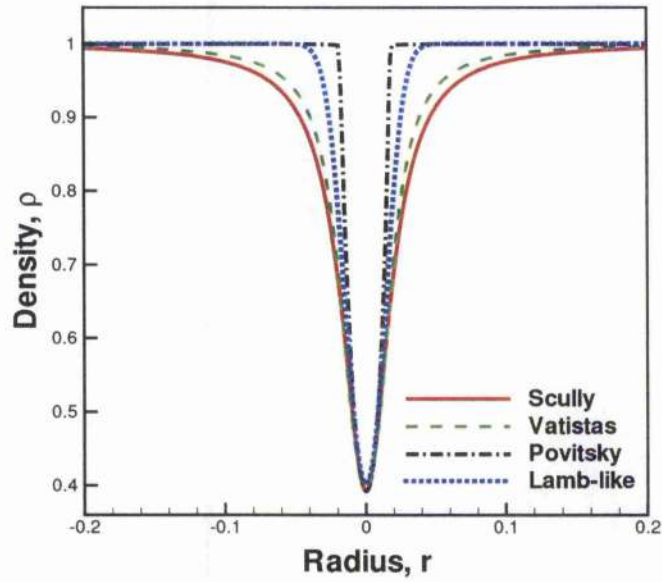


(a) Same initial density at the vortex core

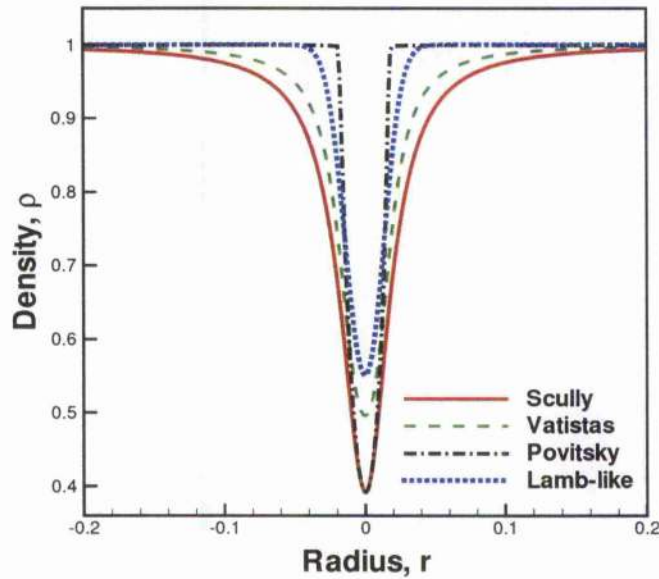


(b) Same initial tangential velocity at the vortex core

Figure 4.2: Tangential velocity and density profile for four different vortex models. Vortex characteristics of the models which have the same density at the vortex core.



(a) Same initial tangential velocity at the vortex core



(b) Same initial density at the vortex core

Figure 4.3: Tangential velocity and density profile for four different vortex models. Vortex characteristics of the models which have the same tangential velocity at the vortex core.

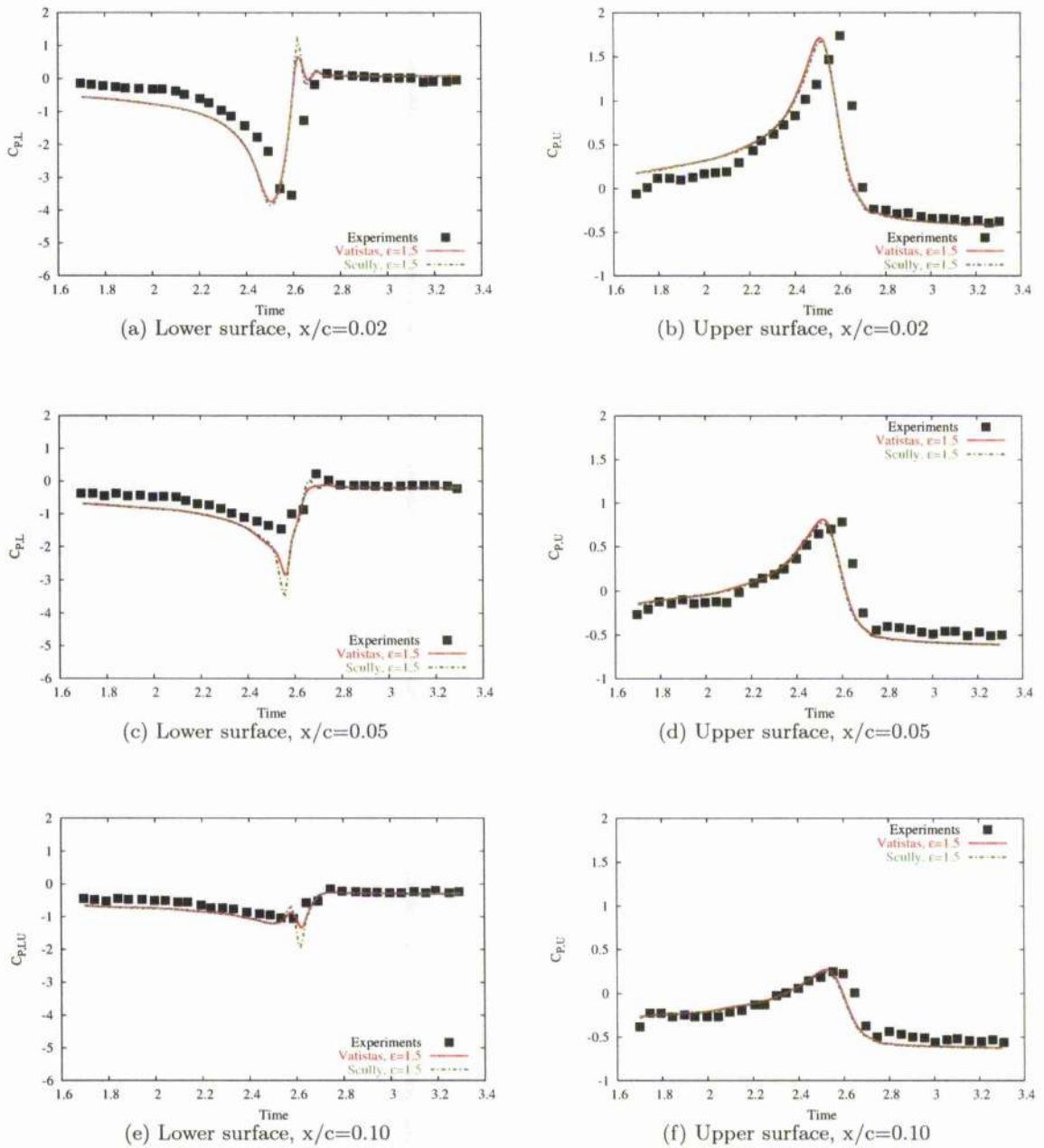


Figure 4.4: Surface pressure coefficient history for vortex models introduced initially with the same circulation. Viscous calculations ( $k-\omega$  model),  $R_e = 1e + 6$ ,  $M_\infty=0.5$ ,  $\hat{\Gamma} = -0.283$ ,  $R_c = 0.018$ . The vortex introduced at 2.5 chords ahead of the aerofoil.

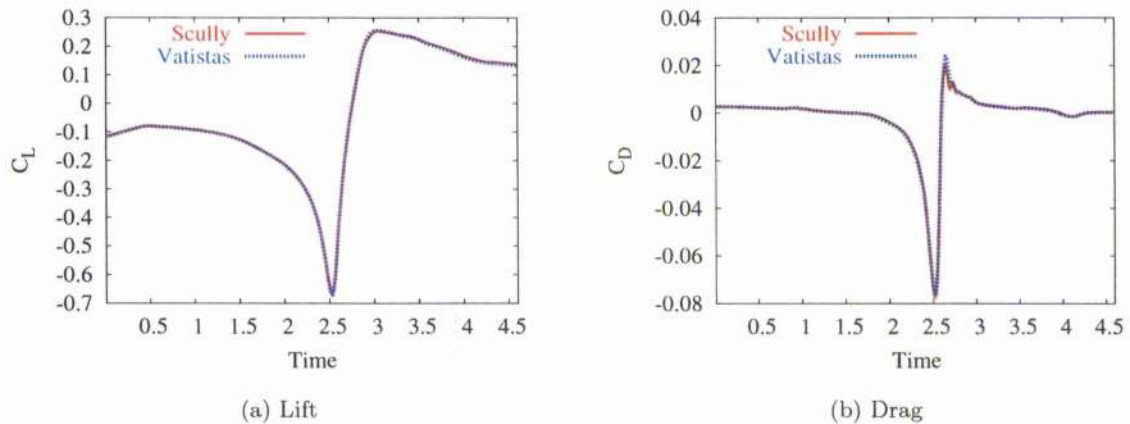
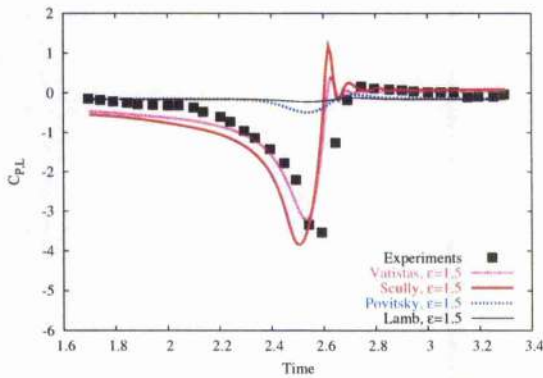


Figure 4.5: Lift and drag histories for the Scully and the Vatistas models. The initial vortex has the same strength. Head-on BVI, viscous calculations ( $k\text{-}\omega$  model),  $R_e = 1e + 6$ ,  $M_\infty = 0.5$ ,  $\hat{\Gamma} = -0.283$ ,  $R_c = 0.018$ .

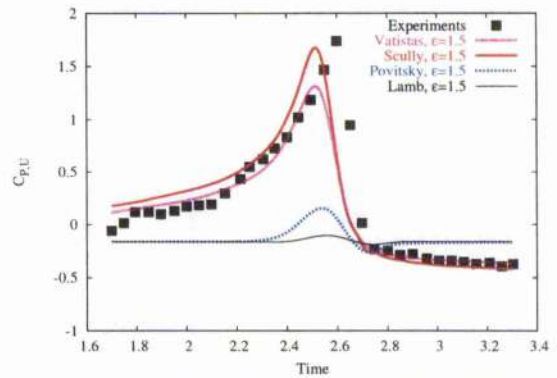
More head-on BVI simulations were carried out in order to assess the effects of three parameters on the vortex characteristics: the minimum density, maximum tangential velocity and finally the maximum ratio  $\omega/\rho$  at the vortex core. The vortex was introduced for different vortex models with either the same density, tangential velocity or  $\omega/\rho$  ratio at the core. This means that the vortex strength was changed accordingly so that the value of the studied parameter corresponds to the Scully model one.

A comparison of the influence of the mentioned parameters on the loads of the aerofoil is given in Figure 4.6. It can be seen from Figures 4.4 and 4.6 that the most important parameter of the introduced vortex in terms of effects on the loads is its strength. It can also be observed that the surface pressure coefficient obtained using the Scully and the Vatistas models match reasonably well the experiments for the ratio  $\omega/\rho$ . As far as the Scully and the Vatistas models are regarded, this suggests that the ratio  $\omega/\rho$  at the vortex core is a valuable quantity for representing the characteristics of the vortex as depicted in Figure 4.6.

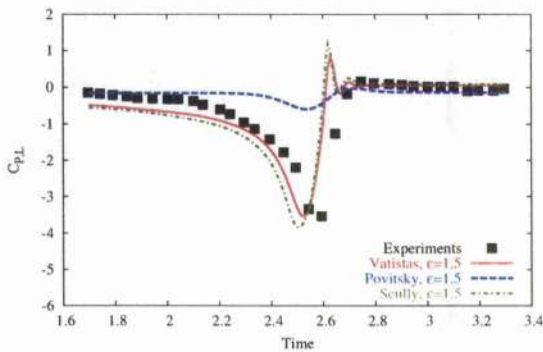
The vortices introduced using the Povitsky or Lamb-like models were found to dissipate very quickly for an  $\epsilon$  parameter of 1.5, the optimum value of which was found to be larger. This is related to the sharp velocity profile of these two models which renders the capture of the initial vortex characteristics more difficult on coarse grid.



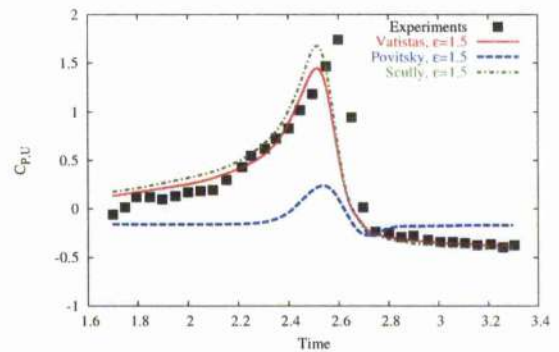
(a) Same initial density at the vortex core



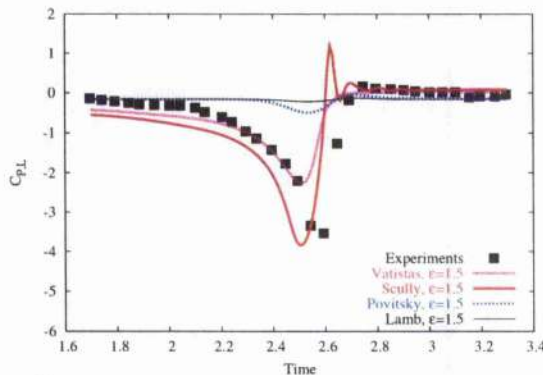
(b) Same initial density at the vortex core



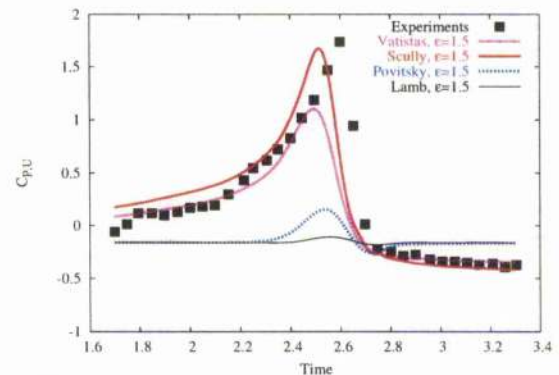
(c) Same initial  $\omega/\rho$  ratio at the vortex core



(d) Same initial  $\omega/\rho$  ratio at the vortex core



(e) Same initial tangential velocity at the vortex core



(f) Same initial tangential velocity at the vortex core

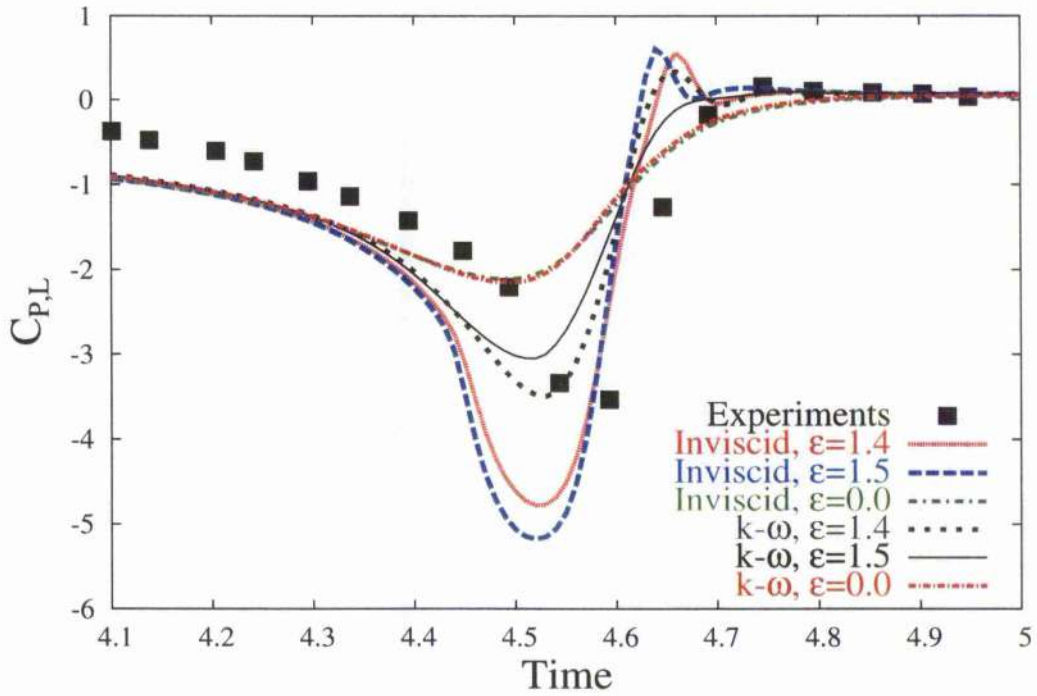
Figure 4.6: Surface pressure coefficient history at the chordwise location  $x/c=0.02$  for vortex models introduced initially with (a-b) the same density, (c-d) the same  $\omega/\rho$  ratio and (e-f) the same tangential velocity at the vortex core. Viscous calculations (k- $\omega$  model),  $Re = 1e + 6$ ,  $M_\infty=0.5$ ,  $\hat{\Gamma} = -0.283$ ,  $R_c = 0.018$ . The vortex introduced at 2.5 chords ahead of the aerofoil. Note that no results are presented for the Lamb-like model in Figures c and d since it was not possible to obtain the initial  $\omega/\rho$  ratio at the vortex core due to the velocity profile of the model.

### 4.2.2 Influence of the CVCM

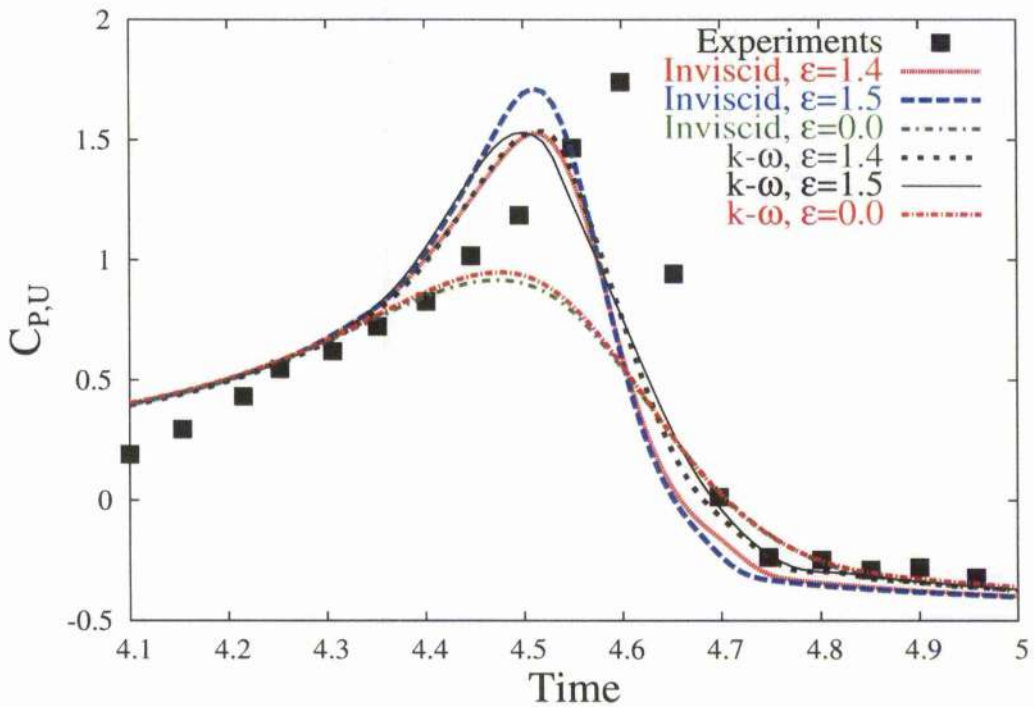
Inviscid and viscous calculations were carried out for different values of  $\epsilon$  for a vortex introduced 4.5 chords ahead of the aerofoil. The  $k-\omega$  model was chosen for the viscous calculations. As shown in Figure 4.7, the pressure coefficients are well predicted for both inviscid and viscous calculations assuming the optimum value of  $\epsilon$  is chosen whereas they are very much underestimated when no CVCM is applied.

The importance of the  $\epsilon$  parameter which determines how the vortex is preserved is highlighted. It appears that the vortex strength increases with  $\epsilon$  for the inviscid calculations. Too high a value of  $\epsilon$  leads to a non physical flow and too low a value does not allow the preservation of the vortex as illustrated in Figure 4.8. The good prediction of the  $C_p$  history shows that the CVCM which uses the  $\epsilon$  scaled with the grid and the vorticity gradient limiter is able to preserve the vortex characteristics for inviscid calculations.

Regarding viscous calculations, too high a value of  $\epsilon$  also makes the vortex too strong as depicted in Figure 4.8. However, the best prediction of the  $C_p$  history was not obtained for  $\epsilon = 1.5$  as for the inviscid calculations but for a value of 1.4. For this case, the dimensionless value of density was 0.62 at the vortex core which is close to the desired 0.6. For  $\epsilon = 1.6$ , a much lower value was obtained as can be seen from the legend of Figure 4.8. The vortex core radius was found to change with the value of  $\epsilon$  and the employed turbulence model. This is discussed in more detail in section 4.2.7. As expected, the Mach number has an influence on the  $\epsilon$  parameter and, in this work, a value of 1.4 was used for the subsonic case. A slightly higher value of 1.8 was used for the transonic case.



(a) Lower surface,  $x/c=0.02$



(b) Upper surface,  $x/c=0.02$

Figure 4.7: Influence of the value of the confinement parameter  $\epsilon$  on the time history of the surface pressure coefficient for inviscid and viscous calculations. The vortex was introduced at 4.5 chords ahead of the aerofoil. Head-on BVI problem, NACA-0012 aerofoil, inviscid calculations,  $M_\infty=0.5$ ,  $\hat{\Gamma} = -0.283$ ,  $R_c = 0.018$ ,  $x/c=0.02$ .

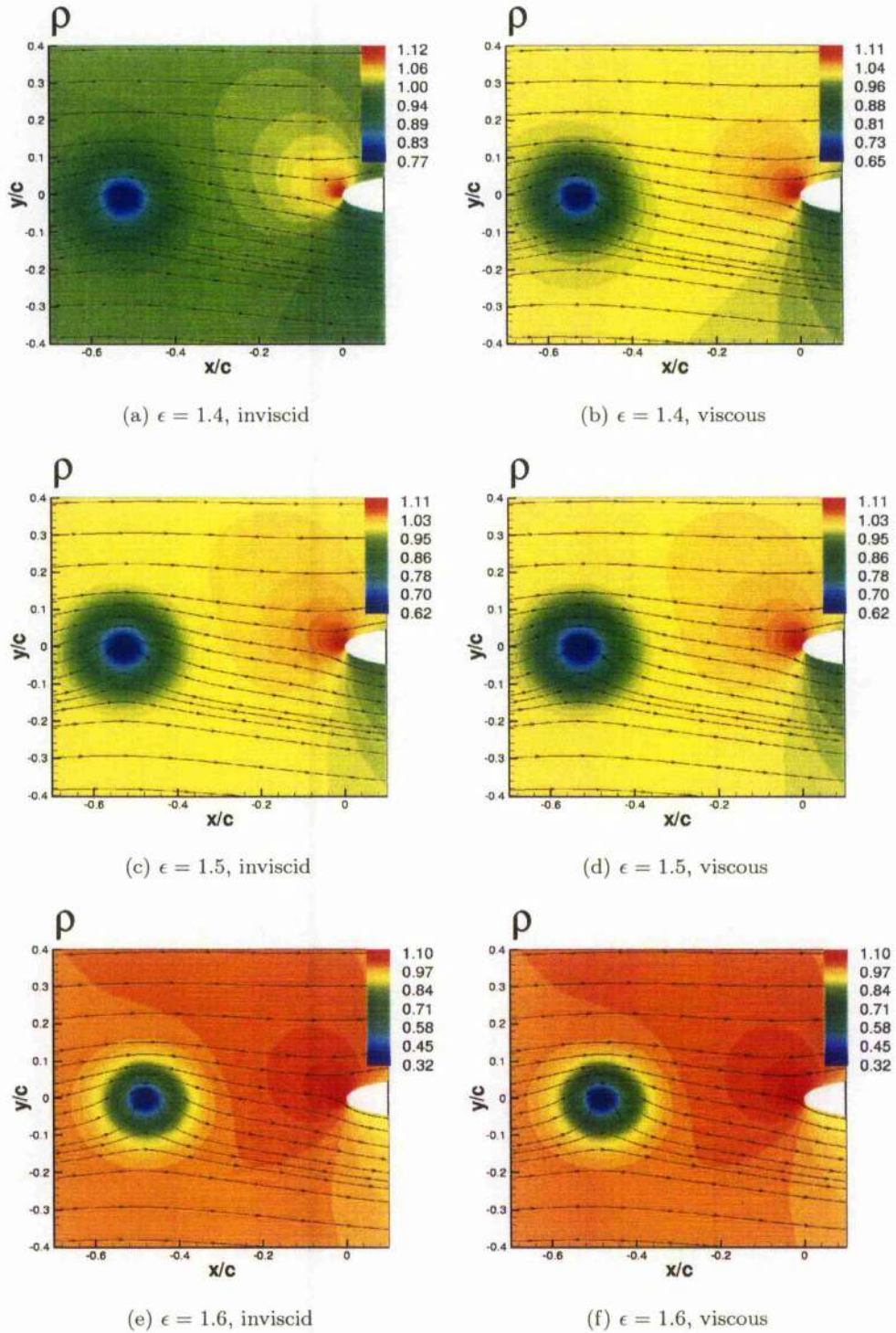


Figure 4.8: Effect of the  $\epsilon$  parameter on the vortex path and on the size of the vortex core for (a, c, e) inviscid and (b, d, f) viscous calculations. Density contours are shown along with streamlines at the same instant  $t(U_\infty/c) = 4.0$ . The vortex was introduced 4.5 chords ahead of the aerofoil. Note that the lower value of density corresponds to the density at the vortex core.

### 4.2.3 Influence of the initial vortex location

The initial vortex location is significant since the vortex model needs to be introduced in a potential-like flow region. Different locations have been tested to check whether the history of the pressure coefficient changes and whether the vortex is preserved in a similar way for different initial locations. Four locations have been used at 1.5, 2.5, 3.5 and 4.5 chords ahead of the aerofoil. Inviscid and viscous calculations were run.

Figure 4.9 presents the surface pressure comparison between the experiments and predictions at the chordwise location  $x/c=0.02$ , on a fine grid of approximately 500k points. The inviscid results using the CVCM compare very well against the experiments for the four vortex locations. The pressure coefficients are well predicted whereas they are very much underestimated when no CVCM is applied.

Viscous calculations were run for the  $k-\omega$  model. Better agreement with experiments is obtained for viscous calculations especially for the pressure coefficient at the lower surface (see Figure 4.10). This is expected as viscosity makes the encounter less impulsive [126]. In fact, viscous calculations can reasonably predict the oscillation of the stagnation point [17] and flow separation [16] which determines the movement of the high-pressure region towards the low-pressure region near the LE of the aerofoil [9]. This is further discussed in section 4.2.6. As explained in [16, 17, 127], a secondary vortex is formed beneath the aerofoil due to the flow separation. The induced velocity of the initial clockwise-rotating vortex makes the stagnation point move up. Then the flow speed decreases on the upper surface and increases on the lower surface leading to the creation of a secondary anti-clockwise rotating vortex. The original and the secondary vortices get weakened after combining and they separate more and more from the aerofoil. This explains why their effect on the flow over the aft of the aerofoil is minimal.

It is interesting to note that, for both inviscid and viscous calculations, the peaks of surface pressure coefficients are not of the same magnitude when the vortex is introduced at different vortex locations for a fixed  $\epsilon$  parameter. This is shown in Figures 4.9 and 4.10 for a vortex introduced at 2.5 and 4.5 chords ahead of the aerofoil. The vortex core radius which should remain of the same size before the interaction appears to vary depending on the value of  $\epsilon$  as depicted by Figures 4.8 (b), (c) and (d). The pressure at the vortex core is indeed lower for a larger confinement parameter, leading to an increase of the vortex strength and, for a value of the confinement parameter which is too large, to a decrease of the vortex core radius. Too low a value of  $\epsilon$  leads to the dissipation of the vortex whose core radius increases while too large a value of  $\epsilon$  changes the characteristics of the initial vortex which gets stronger with a decrease of its radius core for inviscid calculations. However, in the case of too large a value for viscous calculations, the vortex may also get weaker with a larger radius core depending on the nature of the used turbulence model. It seems that the dynamics of the vortex, which are related to the turbulence model and to the CVCM are at the origin of such differences which is discussed in more detail in section 4.2.7. Nevertheless, the vortex location does not seem to affect the prediction of the pressure coefficient assuming the optimum confinement parameter  $\epsilon$  is used. The trace of the interaction on the  $C_p$  is in good agreement with the experiments whereas it is very weak when no confinement is used.

#### 4.2.4 Influence of the spatial refinement

Grids of different density along the vortex path have been used for the inviscid and viscous runs. The coarse and fine grids have respectively around 2 and 4 cells across the core radius, corresponding to a similar grid density as in the benchmark problem. The size of the grid is given in Table 4.1. The vortex was introduced 2.5 chords ahead of the aerofoil.

Again, the  $C_p$  is well predicted on both grids for inviscid calculations (see Figure 4.11). The  $C_p$  predictions are very similar, which indicates that CVCM can predict correctly the loads on coarse and fine grids. However, the presence of a spike in the  $C_p$  for a non-dimensionalised time of 2.65 can be noticed after the interaction. This may be expected for Euler solutions. Indeed, the downwash effect of the vortex generates a small supersonic region at the head of the aerofoil. Then, when the vortex passes the supersonic region, it induces an upwash effect. This may be at the origin of the formation of a second small supersonic region as depicted in Figure 4.12(a). It does not appear for viscous calculations due to the exchange of energy between the vortex and the boundary layer during the interaction. Since the region of high pressure is small and disappears quickly (see Figure 4.12(b)), it is not considered to alter the quality of the BVI simulation, especially in terms of integrated loads.

---

#### Influence of the spatial refinement

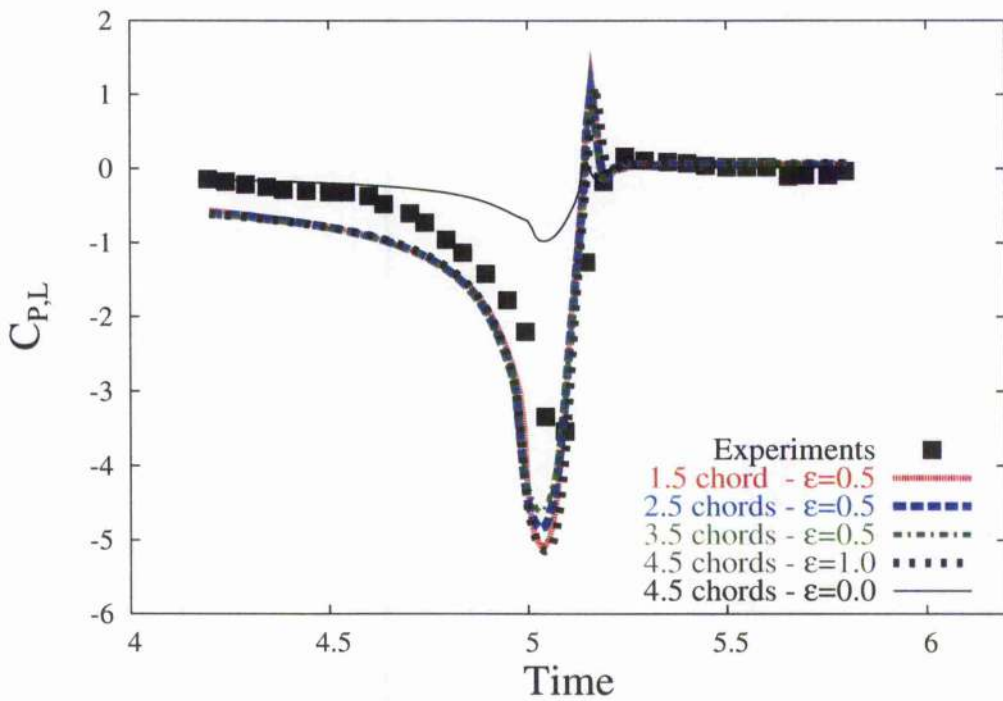
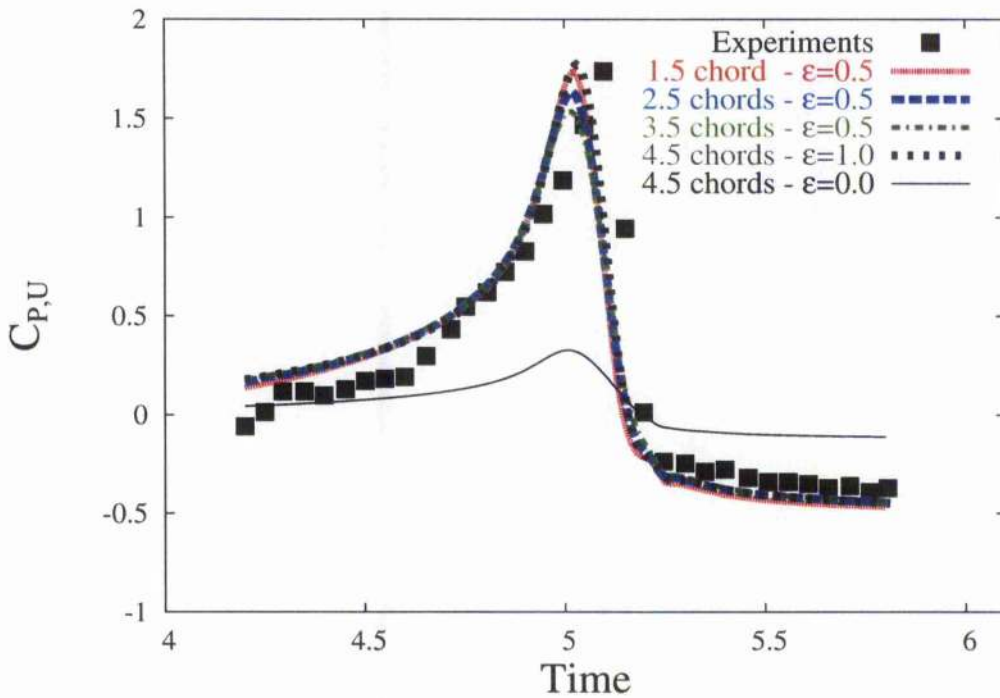
(a) Lower surface,  $x/c=0.02$ (b) Upper surface,  $x/c=0.02$ 

Figure 4.9: Influence of the initial vortex location on the time history of the surface pressure coefficient. Head-on BVI problem, NACA-0012 aerofoil, inviscid calculations,  $M_\infty=0.5$ ,  $\hat{\Gamma} = -0.283$ ,  $R_c = 0.018$ ,  $x/c=0.02$ .

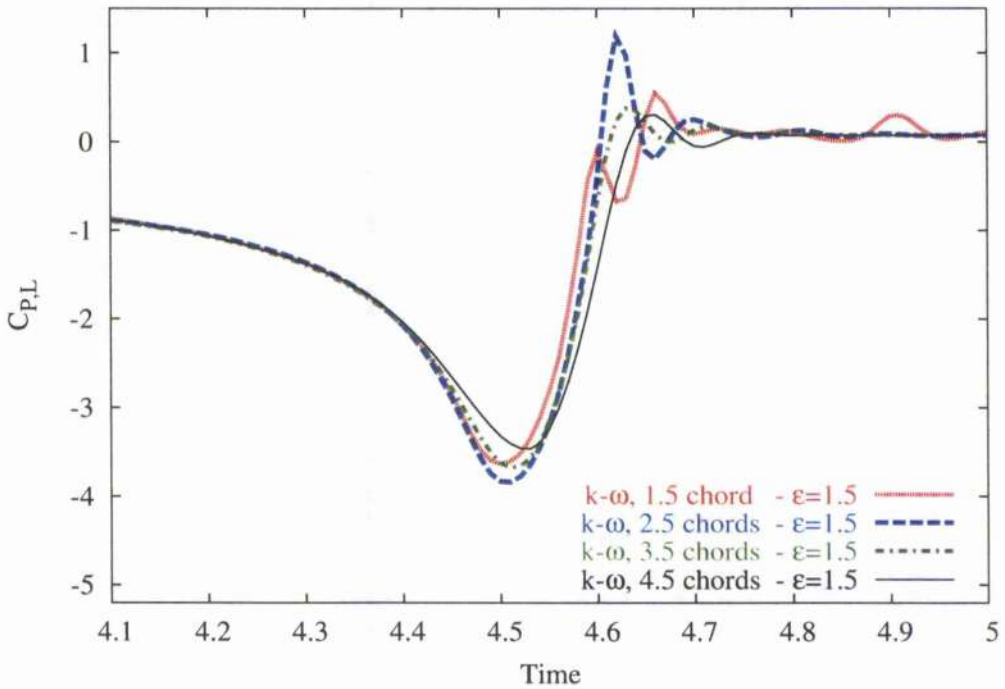
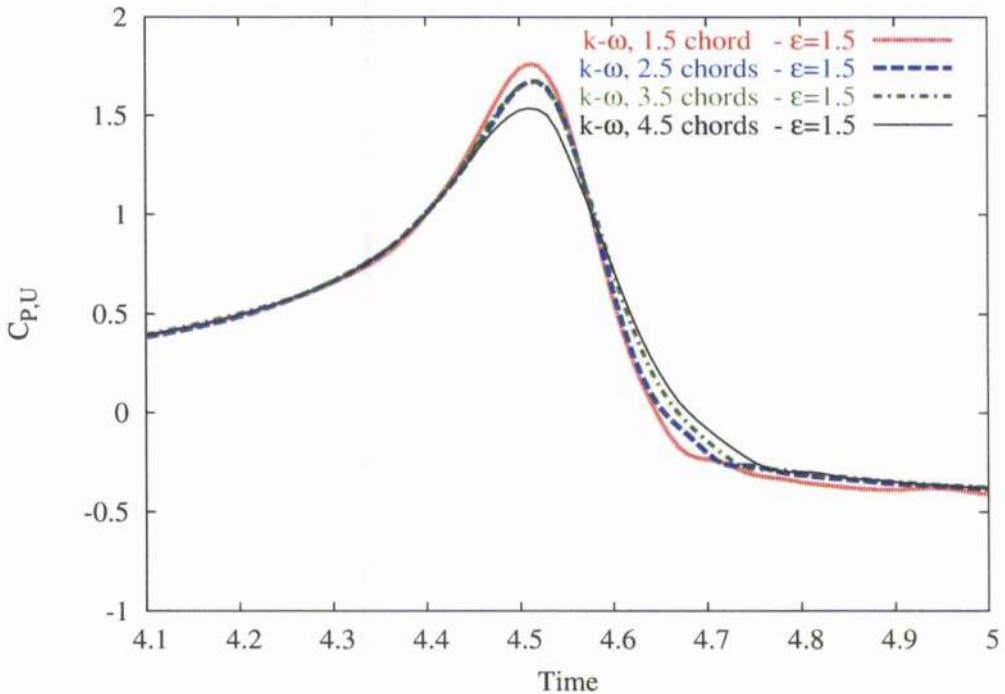
(a) Lower surface,  $x/c=0.02$ (b) Upper surface,  $x/c=0.02$ 

Figure 4.10: Influence of the initial vortex location on the time history of the surface pressure coefficient. Head-on BVI problem, NACA-0012 aerofoil, viscous calculations,  $M_\infty=0.5$ ,  $\hat{\Gamma} = -0.283$ ,  $R_c = 0.018$ ,  $x/c=0.02$ .

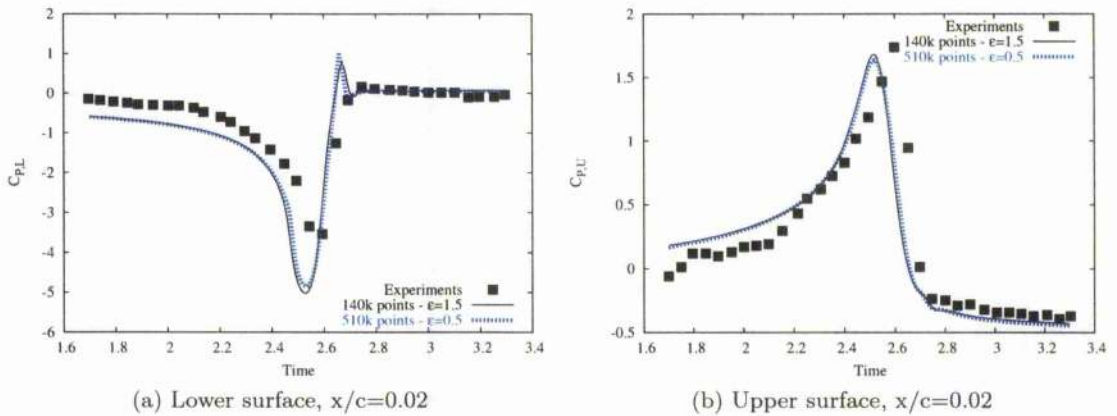


Figure 4.11: Influence of the spatial refinement on the time history of the surface pressure coefficient. Head-on BVI problem, NACA-0012 aerofoil, inviscid calculations,  $M_\infty=0.5$ ,  $\hat{\Gamma} = -0.283$ ,  $R_c = 0.018$ ,  $x/c=0.02$ .

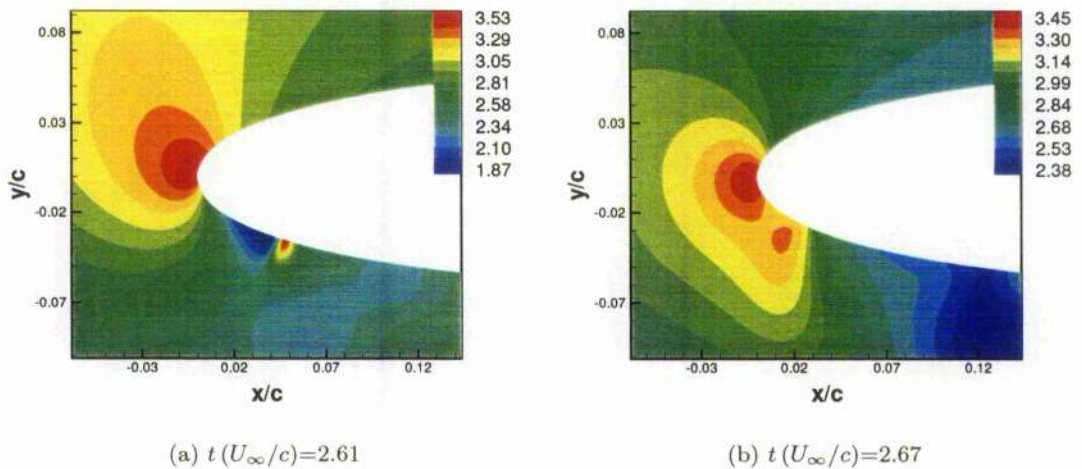


Figure 4.12: Pressure contours on the coarse grid at two different instants. Head-on BVI problem, NACA-0012 aerofoil, inviscid calculations,  $M_\infty=0.5$ ,  $\hat{\Gamma} = -0.283$ ,  $R_c = 0.018$ ,  $x/c=0.02$ . Note that the pressure is non-dimensionalised against the dynamic pressure.

The  $k-\omega$  model was used for viscous calculations on two grids: a coarse grid of 211k points and a fine grid of 819k points. Results are similar on both grids for the main interaction as shown in Figure 4.13. However, as for the inviscid calculations, a spike in the  $C_p$  is present for the coarse grid and some oscillations occur after the main interaction on the fine grid. This can be ascribed to the way the turbulence of the flow is modelled. The non-dimensionalised pressure and the turbulent Reynolds number, indicating how turbulent the flow is, are given in Figure 4.14 for both grids. It can be seen that an excessive amount of turbulence is generated by the turbulence model, especially

**Influence of the spatial refinement**

on the fine grid. On the coarse grid, the region of high pressure which starts to detach from the aerofoil after the oscillation of the stagnation point comes into contact with the LE of the aerofoil. The region of high pressure then affects the surface pressure coefficient on the lower side of the aerofoil at  $x/c=0.02$  due to the excessive amount of turbulent viscosity present at the head of the aerofoil. Note that, as for the inviscid calculations, the phenomenon is not significant enough to alter the BVI simulation.

On the fine grid, a low pressure area which results from the oscillation of the stagnation point is still visible at the LE of the aerofoil whereas it should have detached from the aerofoil after the passage of the vortex. The assumption of isotropy of the flow is not valid any more when the grid is fine enough for the solver to capture the non-linearities of the flow at the LE of the aerofoil. This implies that the eddy-viscosity turbulence model tends to resolve the scales which have already been captured due to the grid refinement, explaining the oscillations of the loads at the chordwise position  $x/c=0.02$ . As explained in [75], this is a known problem for all linear turbulence models. The turbulence kinetic energy is overpredicted near the stagnation point at the LE of the aerofoil. Although the use of non-linear turbulence models will remedy this problem, the BVI loads can be well predicted on the coarse grid, meaning that relatively coarse grids will be used for BVI simulation.

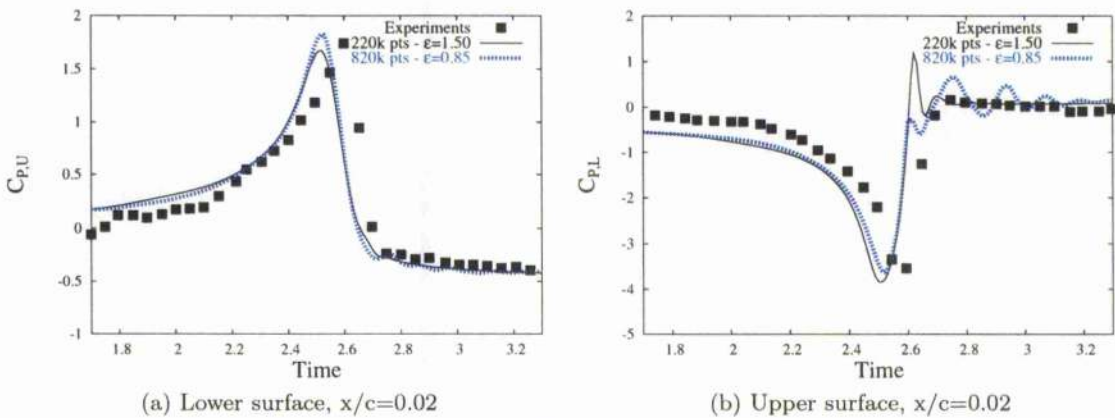


Figure 4.13: Influence of the spatial refinement on the time history of the surface pressure coefficient. Head-on BVI problem, NACA-0012 aerofoil, viscous calculations,  $M_\infty=0.5$ ,  $\hat{\Gamma} = -0.283$ ,  $R_c = 0.018$ ,  $x/c=0.02$ .

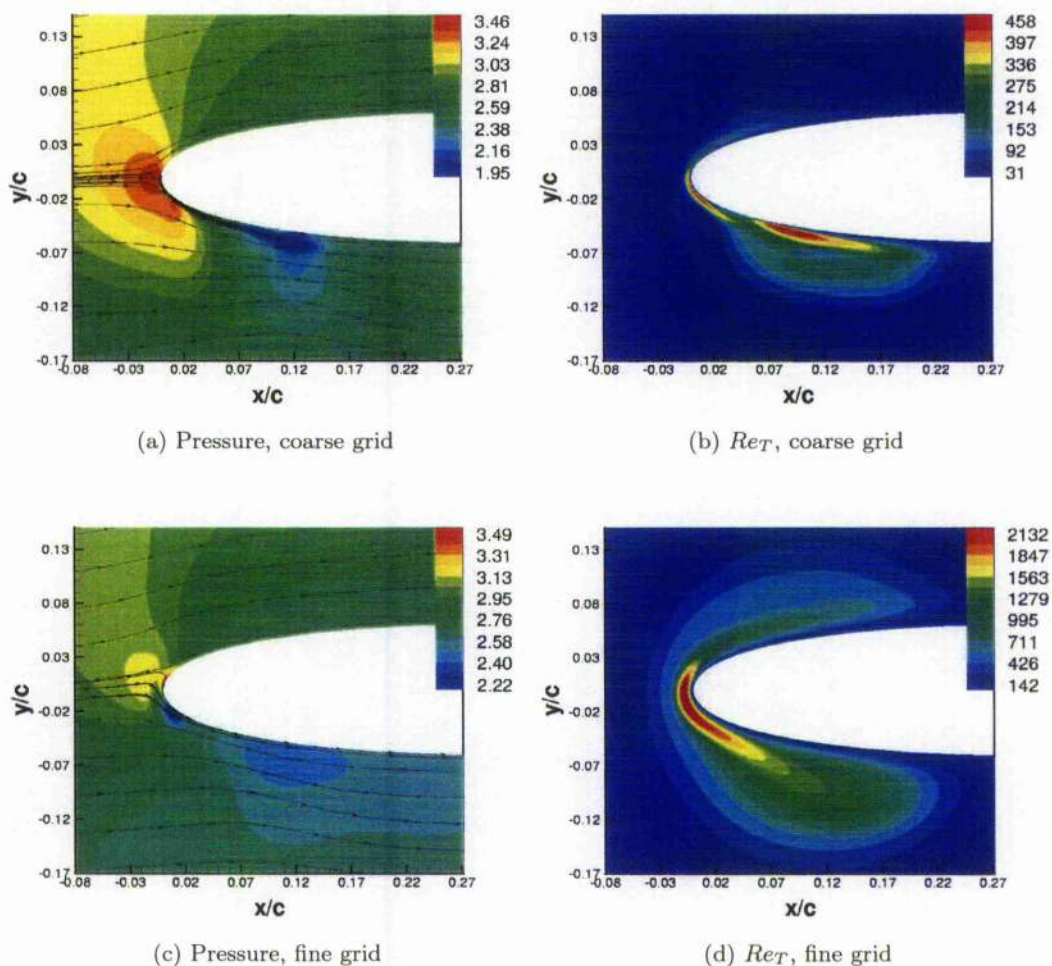


Figure 4.14: Contours of pressure along with the velocity streamlines and of the turbulent Reynolds number for the  $k-\omega$  model on the coarse and fine grid at  $t(U_\infty/c)=2.65$ . The vortex was introduced at 2.5 chords ahead of the aerofoil. Head-on BVI problem, NACA-0012 aerofoil, viscous calculations,  $M_\infty=0.5$ ,  $\hat{\Gamma} = -0.283$ ,  $R_c = 0.018$ .

Note that the  $\epsilon$  parameters for the coarse and fine grids were respectively set to 1.5 and 0.5 for the inviscid calculations. The value of  $\epsilon$  was chosen according to the cell area along the vortex path for a given grid. Knowing the optimum  $\epsilon$  value for a particular grid density, it is possible to estimate the  $\epsilon$  value on another uniform grid by simply assuming it is inversely proportional to the cell area. It was found that the good agreement depends on the choice of the  $\epsilon$  parameter.

#### 4.2.5 Influence of the time refinement

The vortex was introduced at 1.5 chords ahead of the aerofoil and inviscid calculations were carried out on the coarse grid of 126k points. As depicted in Figure 4.15, the  $C_p$  values are very well predicted for the different time steps. Differences appear at the chordwise section  $x/c=0.05$ , that is unlikely to affect the acoustic pressure since the

main interaction near the LE is well predicted. The use of a small time step is advisable only if secondary vortices in the flow are to be captured.

Viscous calculations were run using the  $k-\omega$  model for two different time steps 0.01 and 0.001 with the vortex being introduced at 2.5 chords ahead of the aerofoil. The time refinement was found to modify the strength of the secondary vortex which is generated on the lower side of the aerofoil after the interaction. This is observed in Figure 4.16 which depicts the  $C_p$  value at  $x/c=0.05$ . Viscous calculations using the  $k-\omega$  model are more sensitive to the time refinement than the inviscid calculations. However, the BVI loads are captured in a similar way for both inviscid and viscous calculations at different time refinements (see Figure 4.17), that seems to indicate that a time of 0.01 is sufficient to get an estimation of the BVI loads for this test case.

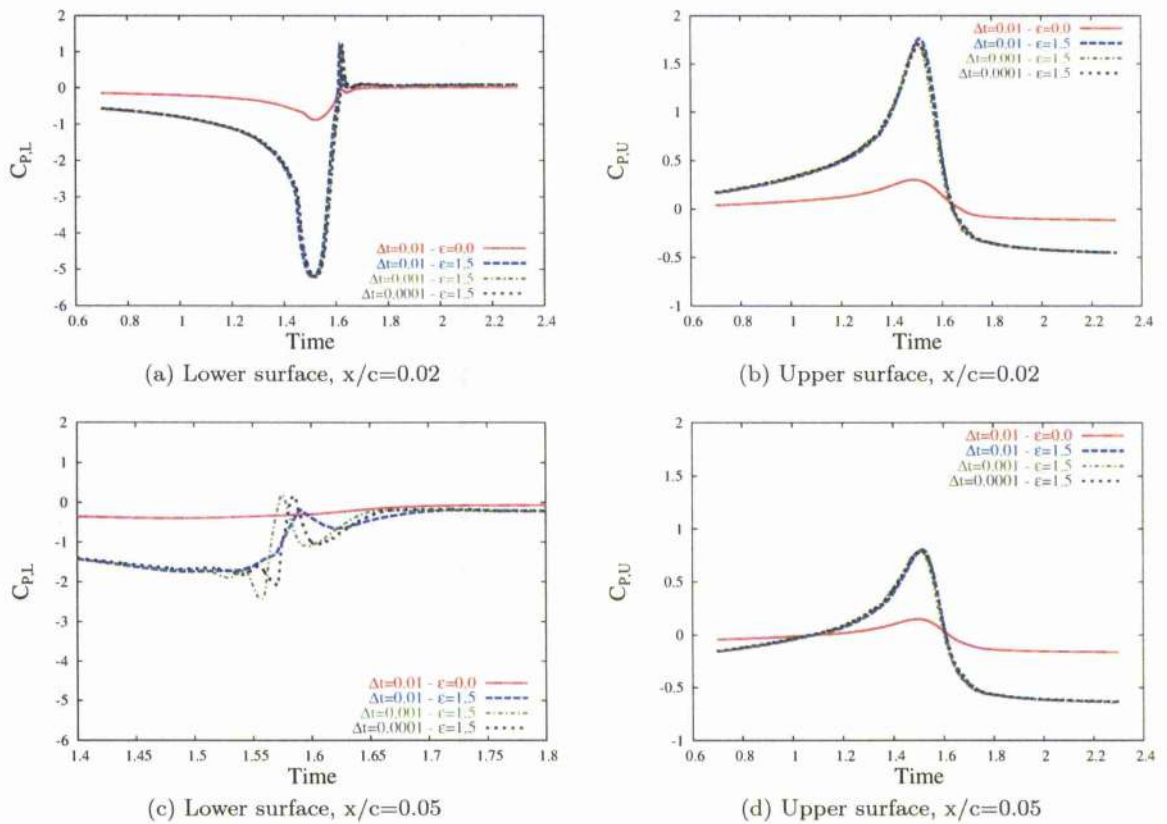


Figure 4.15: Influence of the time refinement on the time history of the surface pressure coefficient for inviscid calculations. Head-on BVI problem, NACA-0012 aerofoil,  $M_\infty=0.5$ ,  $\hat{\Gamma} = -0.283$ ,  $R_c = 0.018$ . (a-b)  $x/c=0.02$ , (c-d)  $x/c=0.05$ . The time step  $\Delta t$  is non-dimensionalised with the freestream velocity ( $U_\infty$ ) and the aerofoil chord (c).

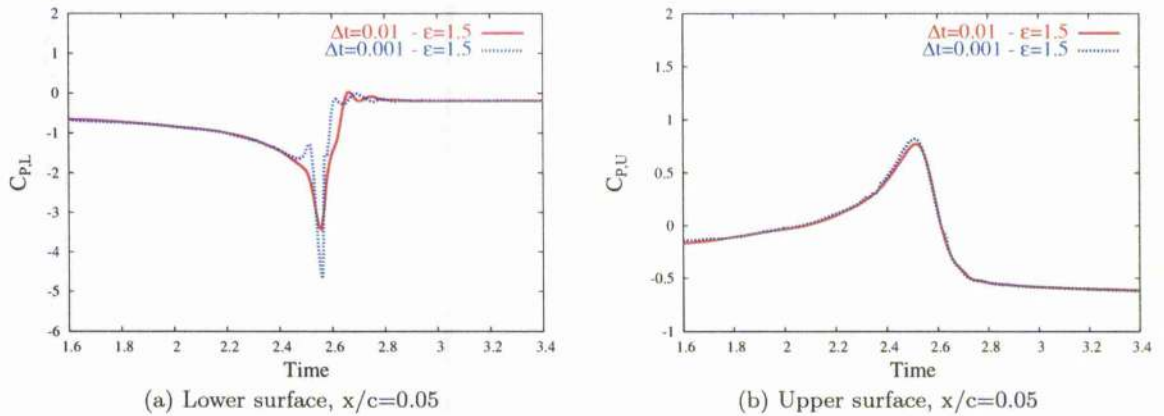


Figure 4.16: Influence of the time refinement on the time history of the surface pressure coefficient for viscous calculations ( $k-\omega$  model). Head-on BVI problem, NACA-0012 aerofoil,  $M_\infty=0.5$ ,  $\hat{\Gamma} = -0.283$ ,  $R_c = 0.018$ ,  $x/c=0.05$ . The time step  $\Delta t$  is non-dimensionalised with the freestream velocity ( $U_\infty$ ) and the aerofoil chord ( $c$ ).

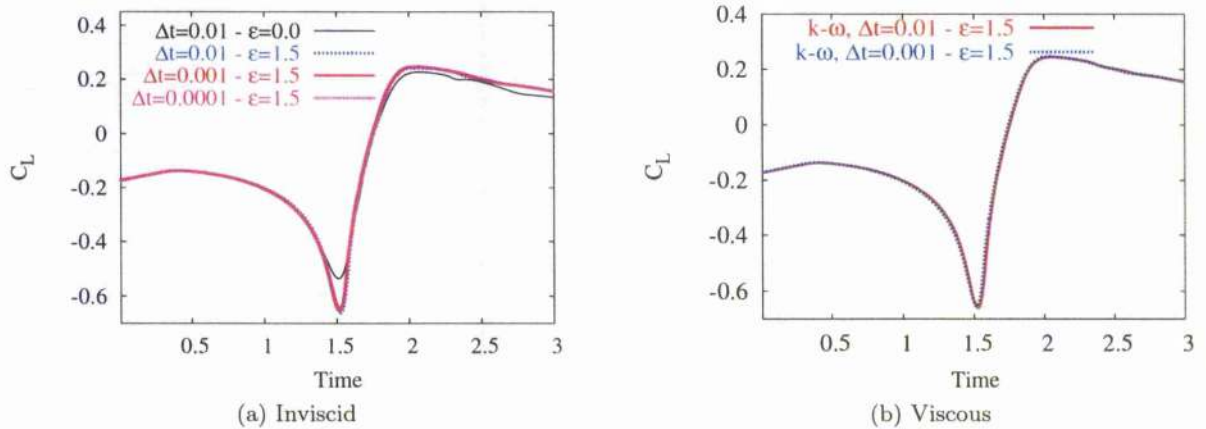


Figure 4.17: Influence of the time refinement on the lift histories for (a) the inviscid and (b) viscous calculations. Head-on BVI problem, NACA-0012 aerofoil,  $M_\infty=0.5$ ,  $\hat{\Gamma} = -0.283$ ,  $R_c = 0.018$ .

### 4.2.6 Influence of the angle of attack

It is noticeable that the computed  $C_p$  pressure does not match the experiments before the interaction as if an angle of attack was present. It was suggested [128] that the clockwise-rotating vortices decrease locally the apparent angle of attack when passing below the aerofoil, i.e. they unload the blade. Therefore two viscous calculations with angles of attack 0.5 and 0.75 degrees were carried out. The  $k-\omega$  model was used and the vortex was introduced at 2.5 chords ahead of the aerofoil. Not only does the presence of a small angle of attack give a better match against the experiments regarding the  $C_p$  history before the interaction, but it also gives weaker  $C_p$  values at sections  $x/c=0.05$  and  $x/c=0.10$ , as illustrated by Figure 4.18. It can be deduced from the lift and drag histories given in Figure 4.19 that the vortex-induced angle of attack for the studied BVI is of  $-0.75$  degrees.

Regarding the  $C_p$  value for  $x/c=0.02$ , the interaction appears stronger for zero angle of attack due to the vortex path. After the vortex splits, a larger part of the vortex propagates on the lower side of the aerofoil (see Figure 4.20), explaining why the anti-clockwise rotating secondary vortex is stronger in the case of zero angle of attack. Then the interaction weakens as the secondary vortex mixes with the original one.

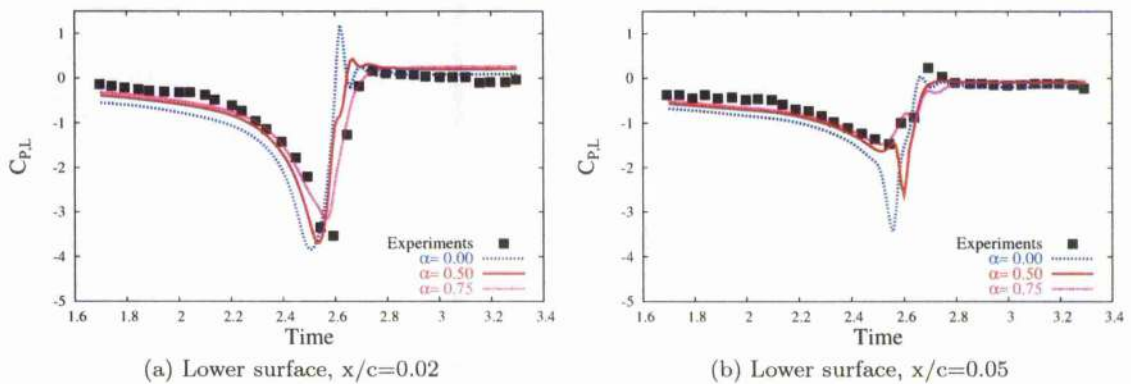


Figure 4.18: Influence of the angle of attack on the time history of the surface pressure coefficient. Head-on BVI problem, NACA-0012 aerofoil, viscous calculations,  $M_\infty=0.5$ ,  $\hat{\Gamma} = -0.283$ ,  $R_c = 0.018$ . (a)  $x/c=0.02$ , (b)  $x/c=0.05$ .

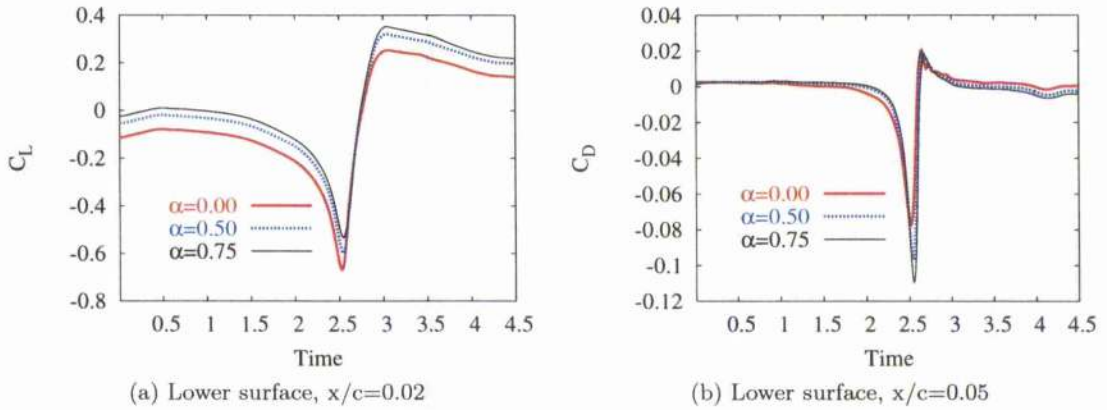


Figure 4.19: Influence of the angle of attack on the lift and drag time histories. Head-on BVI problem, NACA-0012 aerofoil, viscous calculations,  $M_\infty=0.5$ ,  $\hat{\Gamma} = -0.283$ ,  $R_c = 0.018$ . (a)  $x/c=0.02$ , (b)  $x/c=0.05$ .

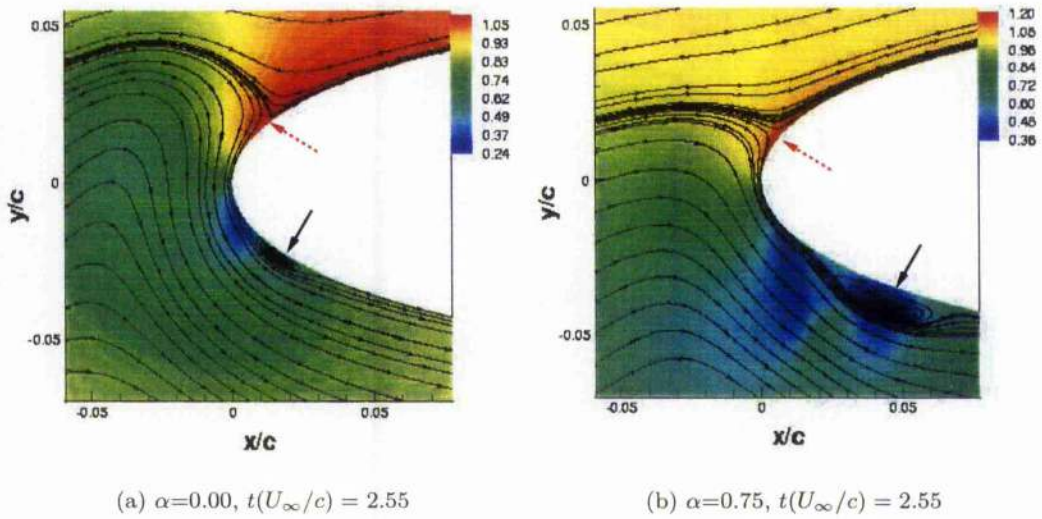


Figure 4.20: Effect of the angle of attack on the location of the stagnation point. Viscous calculations. Density contours are shown along with streamlines at the same time instant. The dotted red arrow indicates the location of the stagnation point and the plain black arrow shows the secondary vortex.

#### 4.2.7 Influence of the turbulence models

Five different turbulence models have been tested: Spalart-Allmaras [129] (1-equation model),  $k-\omega$  [77],  $Pk$  limiter, Menter's Shear Stress Transport (SST) (2-equation models). The  $Pk$  limiter model [81] is a version of the  $k-\omega$  model which uses a limiter for the turbulence kinetic energy to reduce the eddy-viscosity at the vortex cores. The SST model [78] corresponds to the baseline model [79] with the addition of a shear stress limiter. This model blends the  $k-\omega$  and  $k-\epsilon$  models which are respectively applied in the boundary layer and free shear layer zones. A description of the turbulence models is given in Chapter 2. It has to be mentioned that a constant viscosity could have been applied along with the use of the CVCM as a simple turbulence model [98]. This is not covered in this dissertation since the CVCM was only used for overcoming the dissipation of the solver. Note that the optimum value of  $\epsilon$  is set to 1.5 as for the inviscid calculations for this test case.

To the knowledge of the author, this is the first time that a variety of turbulence models have been employed along with the CVCM for BVI cases. A comparison between the results given by the turbulence models gives some interesting features when the CVCM is applied. It is relevant to compare the turbulence models during the interaction as no confinement was applied within a distance 0.1 chord from the aerofoil. Although this implies that, at one moment, only half the vortex belongs to the zone where the CVCM is applied, the grid density was supposed to be finer when the vortex approaches the aerofoil, meaning that the CVCM has its influence decreased due to the grid scaling of the confinement parameter. Figures 4.21-4.22 show that the value of the confinement parameter remains very similar during the convection of the vortex whereas it decreases when the vortex gets closer to the aerofoil to finally become very low just before the interaction as depicted in Figure 4.23.

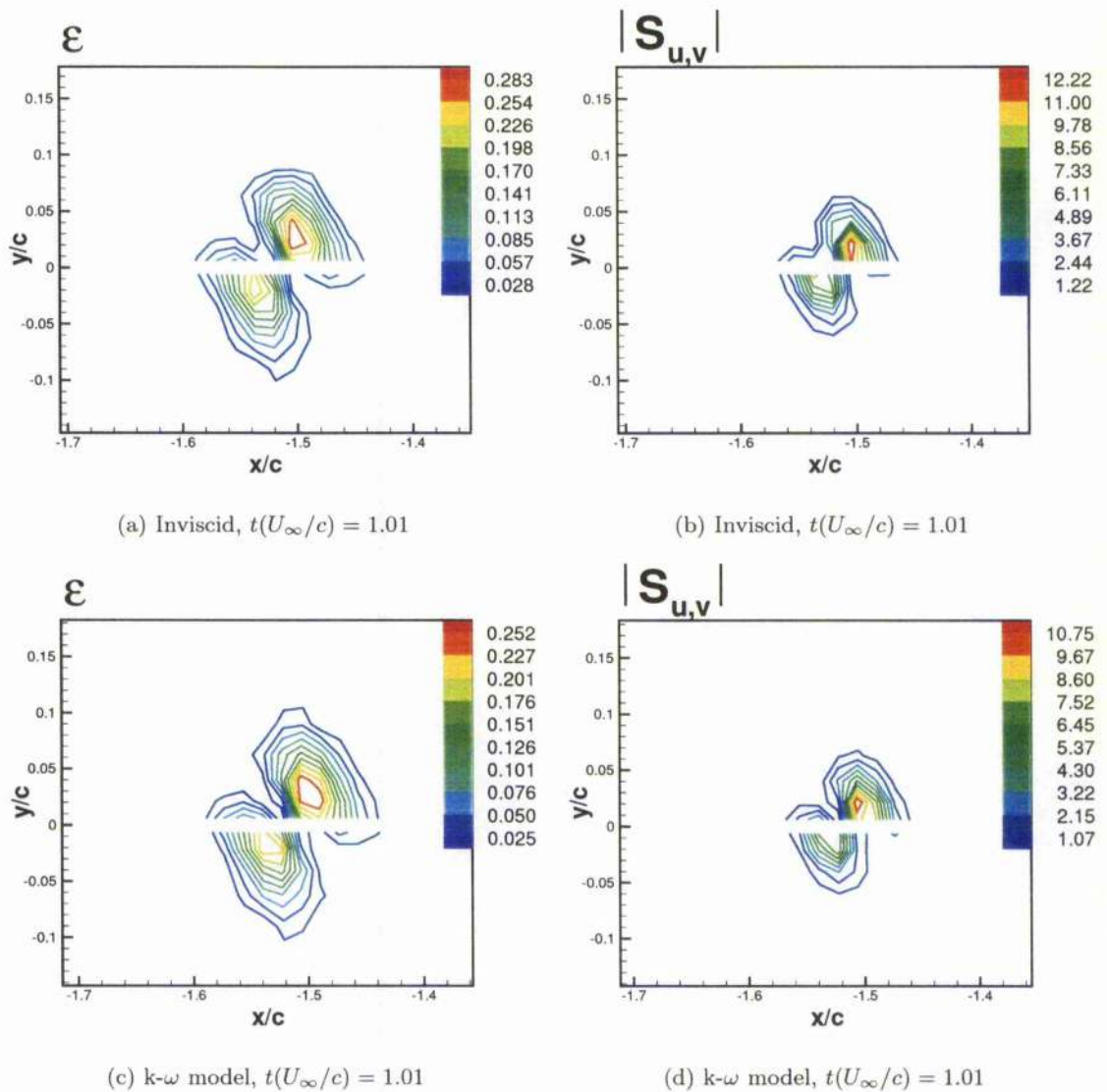


Figure 4.21: (a, c) Contours of the confinement parameter  $\epsilon$  and (b, d) the magnitude of the velocity source term  $S_{u,v} = (S_u, S_v)$  of the CVCM for a non-dimensionalised time  $t(U_\infty/c) = 1.01$ . The grid is uniform along the vortex path. Head-on BVI problem, NACA-0012 aerofoil, viscous calculations,  $M_\infty=0.5$ ,  $\hat{\Gamma} = -0.283$ ,  $R_c = 0.018$ . Note that no value appears on a horizontal line, the variables being cell-centered for the two blocks present along the vortex path.

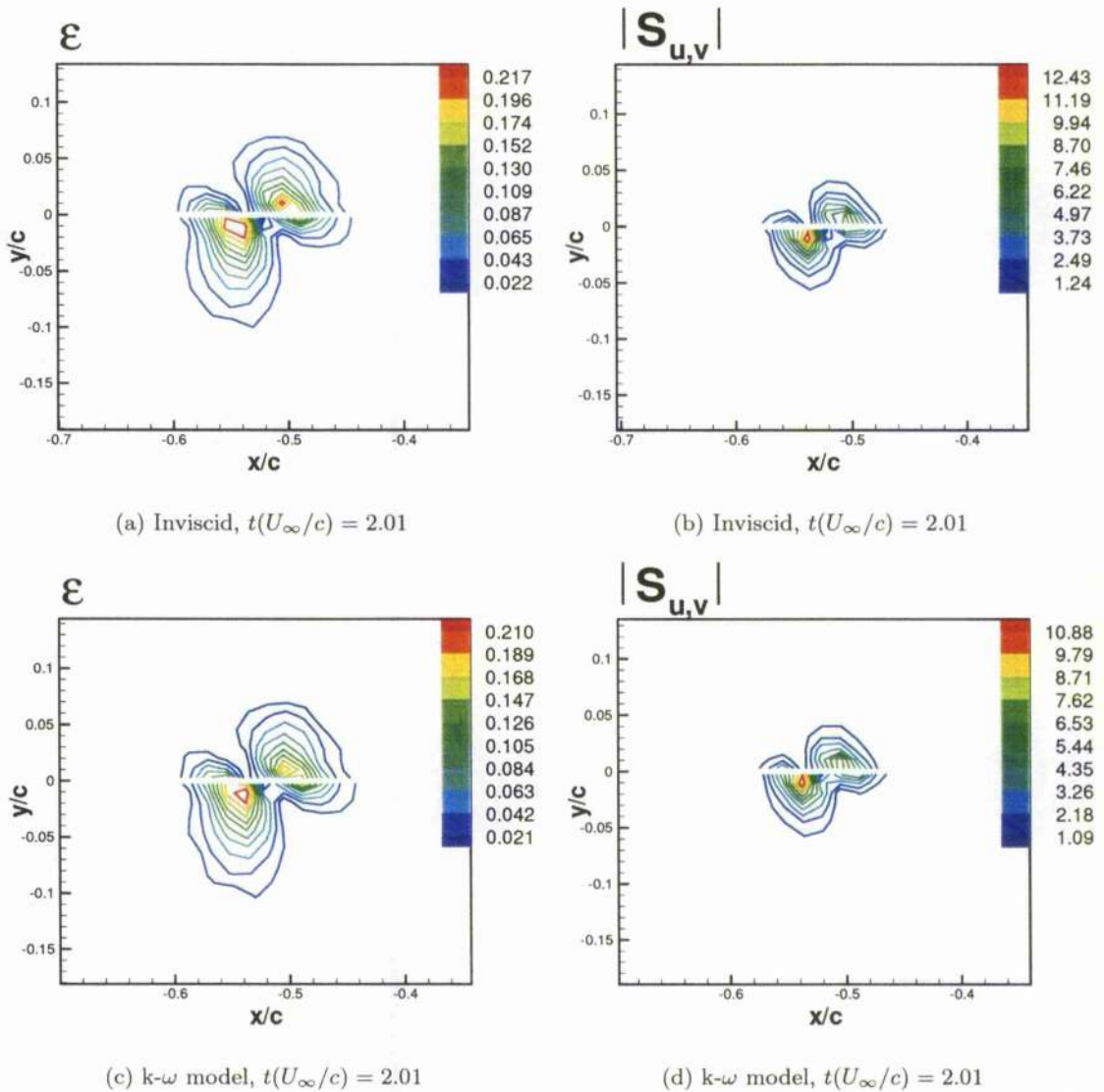


Figure 4.22: (a, c) Contours of the confinement parameter  $\epsilon$  and (b, d) the magnitude of the velocity source term  $S_{u,v} = (S_u, S_v)$  of the CVCM for a non-dimensionalised time  $t(U_\infty/c) = 2.01$ . The grid is uniform along the vortex path. Head-on BVI problem, NACA-0012 aerofoil, viscous calculations,  $M_\infty=0.5$ ,  $\hat{\Gamma} = -0.283$ ,  $R_c = 0.018$ . Note that no value appears on a horizontal line, the variables being cell-centered for the two blocks present along the vortex path.

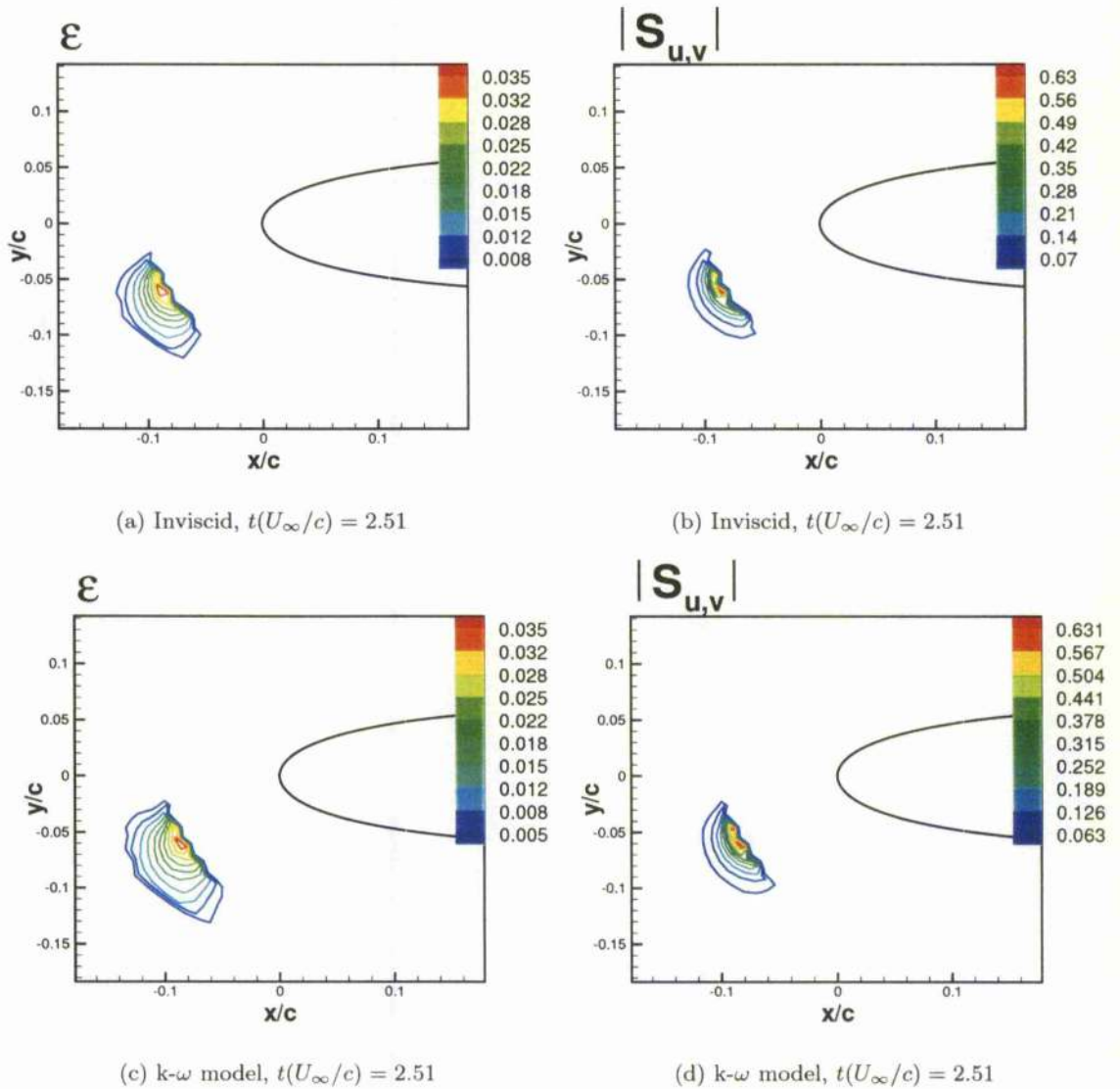


Figure 4.23: (a, c) Contours of the confinement parameter  $\epsilon$  and (b, d) the magnitude of the velocity source term  $S_{u,v} = (S_u, S_v)$  of the CVCM for a non-dimensionalised time  $t(U_\infty/c) = 2.51$ . The grid gets refined when the vortex approaches the aerofoil. Head-on BVI problem, NACA-0012 aerofoil, viscous calculations,  $M_\infty=0.5$ ,  $\hat{\Gamma} = -0.283$ ,  $R_c = 0.018$ ,  $t(U_\infty/c) = 2.51$ . Note that it can be observed that the CVCM was not applied up to a distance 0.1 chord from the aerofoil.

The  $C_p$  history is given in Figure 4.24 for the different turbulence models. On the upper side of the aerofoil, the magnitude of the peaks is similar for all the models but the SST gives a lower value especially at the chordwise section  $x/c=0.02$ . The magnitude of the pressure coefficients given by the other models, and the inviscid calculations, are comparable indicating that the viscous effects are not important on the upper side of the aerofoil.

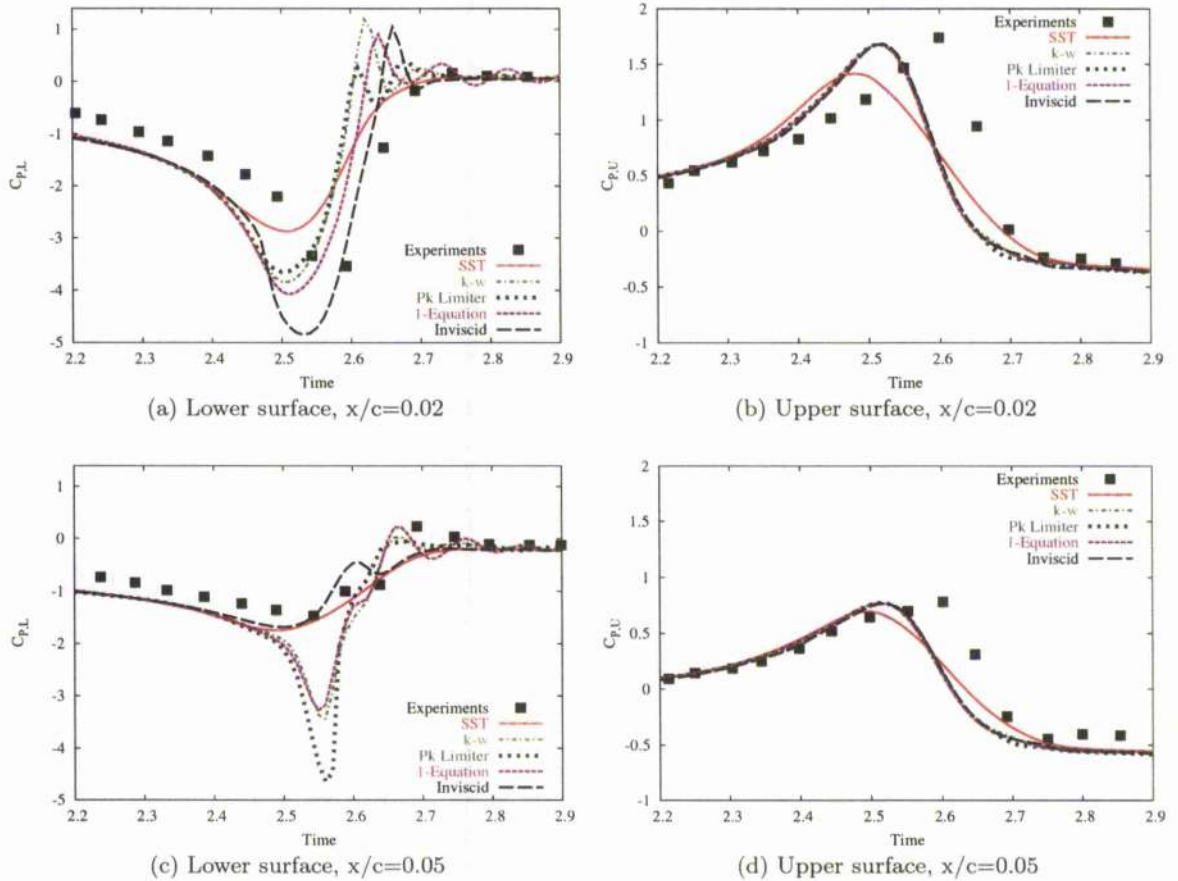


Figure 4.24: Time history of the surface pressure coefficient obtained with various turbulence models. Head-on BVI problem, NACA-0012 aerofoil, viscous calculations,  $M_\infty=0.5$ ,  $\hat{\Gamma} = -0.283$ ,  $R_c = 0.018$ .

The loads given by inviscid and viscous calculations are now compared. The magnitude of the main peak is lower for the viscous calculations since there is a transfer of energy between the original vortex and the boundary layer, leading to a weaker interaction. Regarding the secondary peak, the viscous calculations give a higher surface pressure peak. The secondary vortex remains attached to the aerofoil for the viscous calculations while it does not appear for the inviscid calculations as shown in Figure 4.25, the vortex being generated after the boundary layer detaches.

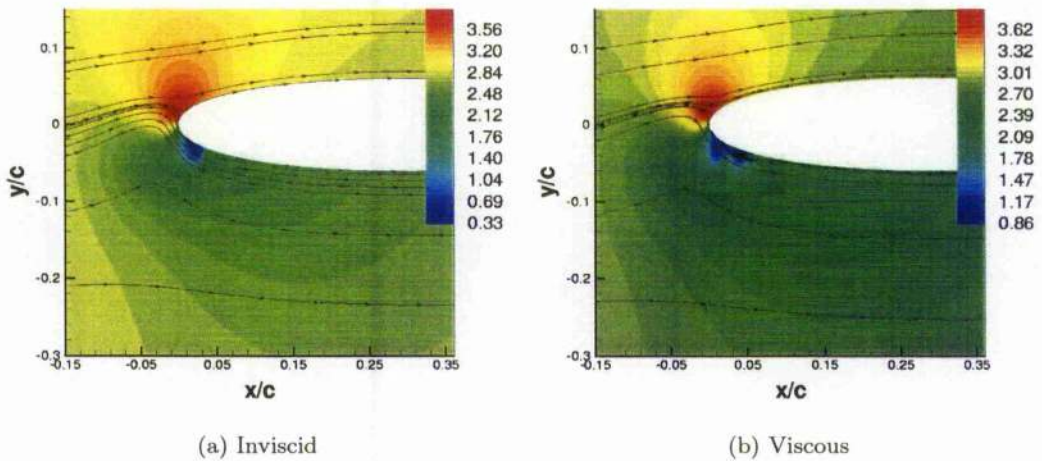


Figure 4.25: Contours of the pressure for (a) inviscid and (b) viscous calculations ( $k-\omega$  model) at time  $t(U_\infty/c) = 2.54$ . Head-on BVI problem, NACA-0012 aerofoil,  $M_\infty=0.50$ ,  $\hat{\Gamma} = -0.283$ ,  $R_c = 0.018$ . Note that the pressure is non-dimensionalised against the freestream pressure.

On the lower side, a similar behaviour is observed for the  $k-\omega$  and 1-equation models which produce similar levels of turbulence. The  $Pk$  limiter model was found to overpredict the strength of the secondary vortex. It can be seen that the  $C_p$  predicted by the SST model is lower than for the other models at the chordwise section  $x/c=0.02$  and  $0.05$ . The difference between the SST and the other turbulence models lies in the shear layer stress limiter of the SST model. The shear layer generated by the SST model gets lower with the vortex strength. Figure 4.26 shows the values of the shear stress in the  $y$  direction for the secondary vortex. The values of the shear stress for the SST and the  $k-\omega$  models are comparable when the  $\epsilon$  parameter is set to 1.25 for the SST and to 1.5 for the  $k-\omega$ , the optimum confinement parameter being 1.5. The fact that the vortex stretches less for a confinement parameter of 1.5 with the use of the SST model explains why the use of a lower value of confinement parameter ( $\epsilon=1.25$ ), which does not allow good conservation of the characteristics of the initial vortex, leads to better prediction of the loads at the chordwise positions  $x/c=0.02$  and  $0.05$ . This is depicted in Figure 4.27.

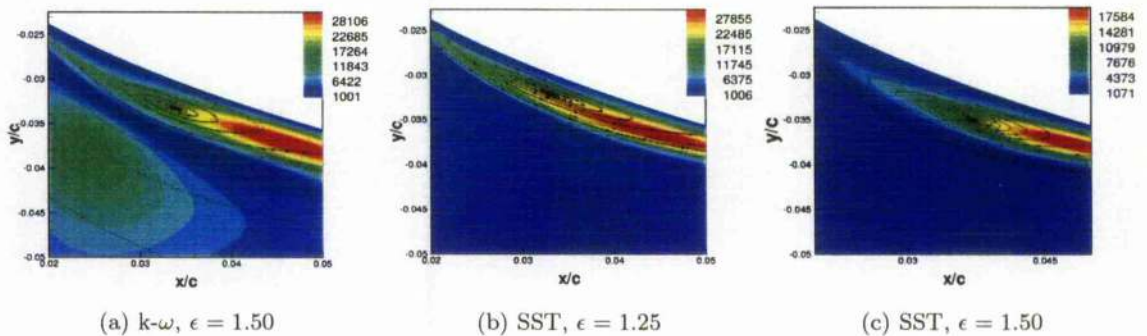


Figure 4.26: Contours of the normal stress  $\tau_{yy}$  along with the velocity streamlines at time  $t(U_\infty/c) = 2.51$  for different  $\epsilon$  for the SST model. The vortex was introduced at 2.5 chords ahead of the aerofoil. Head-on BVI problem, NACA-0012 aerofoil,  $M_\infty=0.5$ ,  $\hat{\Gamma} = -0.283$ ,  $R_c = 0.018$ .

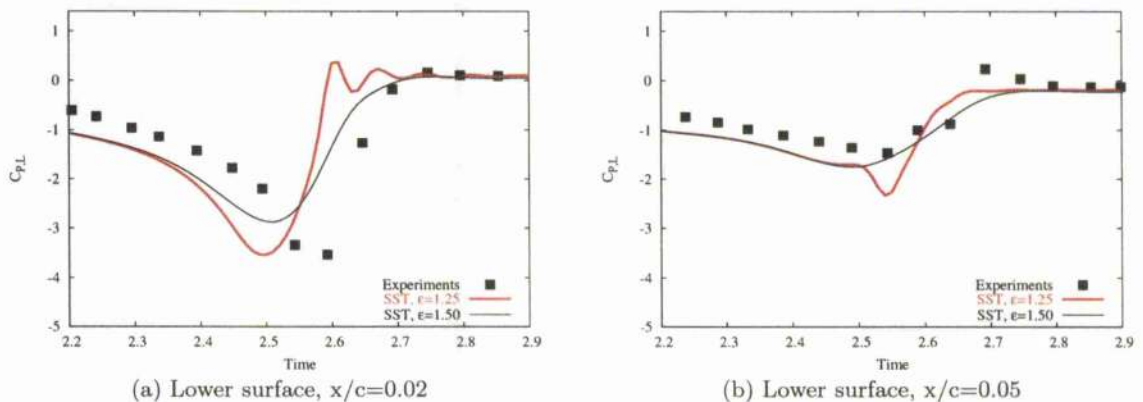


Figure 4.27: Time history of the surface pressure coefficient obtained with two confinement parameters for the SST model. Head-on BVI problem, NACA-0012 aerofoil, viscous calculations,  $M_\infty=0.5$ ,  $\hat{\Gamma} = -0.283$ ,  $R_c = 0.018$ .

It was found that the CVCM is very sensitive to the value of  $\epsilon$  for viscous calculations and that using a higher value than the optimum one did not increase systematically the strength of the vortex, as found for inviscid calculations. The peaks of surface pressure coefficients were actually underpredicted for the  $k-\omega$  model although the value of the  $\epsilon$  parameter was greater than the optimum one. As shown in Figure 4.28, the deformation of the vortex varies with the value of  $\epsilon$ . This stems from the fact that the turbulence models generate some turbulent viscosity which depends on the velocity gradients. The use of too high a value for  $\epsilon$  may amplify the strength of the vortex so that the shear stress at the vortex core is not adapted any more, deforming the shape of the initial vortex. This is manifested as an increase of the vortex core radius, leading to a weaker interaction. Note that the flow is expected to be laminar at the vortex core.

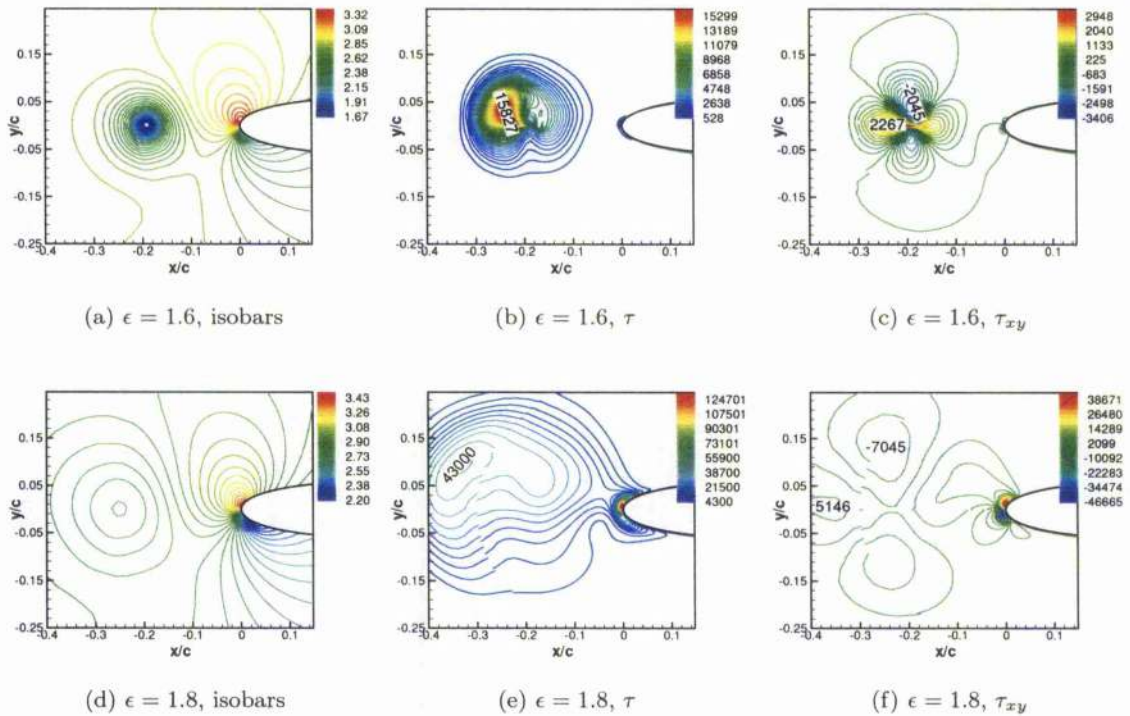


Figure 4.28: Contours of the isobars ( $2p/q_\infty$ ) and the shear stress at time  $t(U_\infty/c) = 4.30$  for different  $\epsilon$  for the  $k-\omega$  model. The vortex was introduced at 4.5 chords ahead of the aerofoil. Head-on BVI problem, NACA-0012 aerofoil,  $M_\infty=0.5$ ,  $\hat{\Gamma} = -0.283$ ,  $R_c = 0.018$ .

The overall shape of the lift coefficient history given in Figure 4.29 is similar for both inviscid and viscous calculations. This suggests that the secondary vortex does not contribute much to the lift. Although the loads near the LE of the aerofoil seem to depend on the nature of the turbulence model, particularly on the lower side of the aerofoil where the viscosity plays an important role, it appears that the lift is predicted in a similar way for inviscid and viscous calculations.

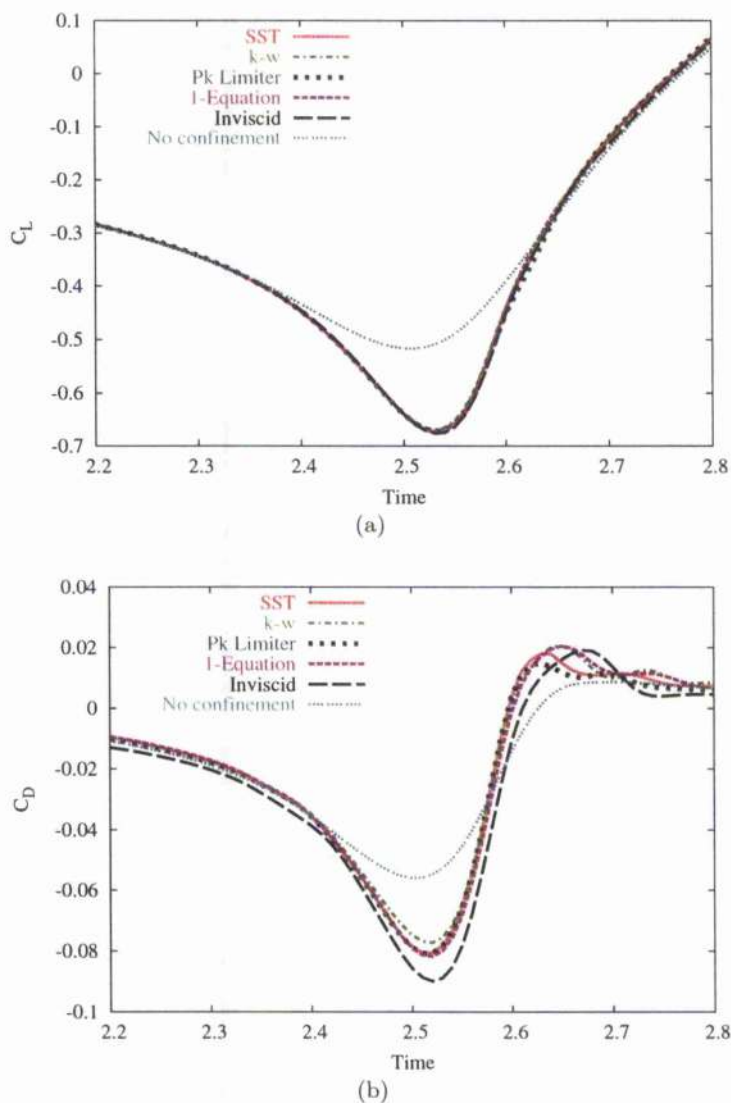


Figure 4.29: Time histories of the lift and drag for inviscid and viscous calculations. Different turbulence models have been used. The confinement parameter was set to 1.5 and the vortex was introduced at 2.5 chords ahead of the aerofoil. Head-on BVI problem, NACA-0012 aerofoil,  $M_\infty=0.5$ ,  $\hat{\Gamma} = -0.283$ ,  $R_c = 0.018$ .

### 4.3 Conclusions

Present results indicate that realistic predictions of BVI can be obtained using the CVCM. First indications reveal that the predictions are not so sensitive to the parameters of the method considering that different grids with the appropriate confinement parameter  $\epsilon$  give similar results. The present calculations demonstrate that accurate prediction of the surface pressure coefficient is possible for head-on BVI cases.

The study confirms that the use of the Euler calculations for the determination of the BVI loads is reasonable, which allows a relative comparison between different BVI cases. However, additional validation cases are necessary to improve the fidelity of the CFD results. Direct comparison between acoustic measurements and CFD would be beneficial and this could reveal further limitations stemming from the order of accuracy of the employed numerical scheme for the capture of the acoustical waves.

## Chapter 5

# Parametric study of BVI aerodynamics

After describing the cases for the BVI parametric study, this chapter discusses the effects of the aerofoil shape, the freestream Mach number, the core radius size, the vortex strength and the miss-distance on BVI aerodynamics.

### 5.1 Introduction

The complex flowfield encountered during BVI is known to produce a very intense impulsive noise [9]. As mentioned in [18], this noise has four main contributions: (i) from the vortex at subsonic speed with its upwash or downwash velocity component, (ii) from the separation and reattachment of the flow when the vortex approaches the aerofoil, (iii) from the oscillation of the stagnation point due to the high pressure region generated at the leading-edge (LE) of the aerofoil (compressibility waves) and (iv) from the development of a supersonic area at the shoulder of the aerofoil (transonic waves). It is known that the magnitude of the BVI noise and its directivity patterns are related to the aerofoil shape, the freestream Mach number, the vortex core radius, the vortex strength and the miss-distance between the vortex core and the surface of the aerofoil.

The effects of the aerofoil shape and the vortex properties have been investigated as depicted in Figure 5.1. The BVI investigation has been confined to 2D simplified flow calculations for two reasons. On one hand, the calculations are capable of predicting reasonably the BVI loads for parallel BVI cases. On the other hand, they are useful to decouple the different acoustic mechanisms of the noise as mentioned by Lent *et al.* [18]. A list of the conditions along with the nature of the calculations is given in Table 5.1. Central to this effort is the Compressible Vorticity Confinement Method (CVCM) which helps traditional CFD methods to preserve vortices. CVCM is used for preserving vortices up to and beyond their interaction with the blade.

Head-on BVI has been simulated for six different aerofoils at subsonic and transonic flow conditions: NACA-0006, NACA-0012, NACA-0018, NACA-001234, NACA-16018 and SC-1095 (see Figure 5.2). The first three sections are symmetric with increasing thickness while the fourth and the fifth ones are NACA 4-digit profiles with a modified leading edge radius. The last one is a cambered section and is representative of the sections currently used in helicopter rotors. For the employed sections the leading edge radius is respectively 0.397%, 1.587%, 3.57%, 0.397%, 1.587% and 0.7% of the aerofoil chord.

The range of Mach numbers under consideration was chosen to highlight the differences between subsonic and transonic flow, which explains why a high Mach number of 0.8 was chosen for the latter. The  $C_p$ , lift and drag histories of the vortex-aerofoil interaction given by Euler and NS calculations are presented for the different types of BVI at different Mach numbers. Note that the Reynolds number was fixed to one million for viscous calculations and the angle of attack was set to zero for all the calculations.

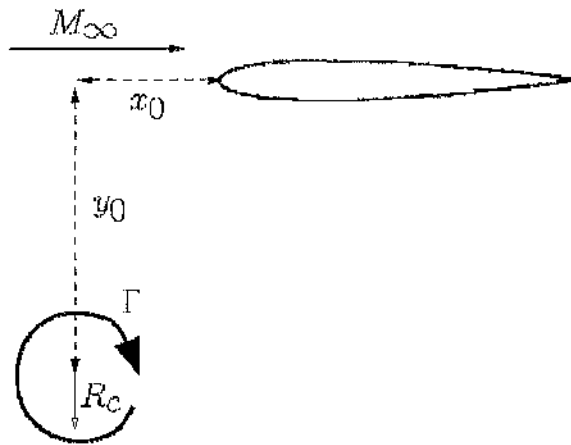


Figure 5.1: Schematic of the BVI parametric study.

Unsteady case	Parameter	$M_\infty$	$y_0$	$\hat{\Gamma}$	$R_c$	Aerofoil
Viscous	Aerofoil Shape	0.50	0.0	-0.283	0.018	NACA-0006
		0.80		-0.177		NACA-0012
Inviscid	Freestream Mach number	0.50	0.0	-0.283 (at $M_\infty=0.50$ )	0.1	NACA-0012
		0.57				
		0.63				
		0.73				
Inviscid	Vortex core radius	0.73	0.00	-0.42	0.04	NACA-0012
			-0.15		0.06	
					0.10	
					0.15	
Inviscid	Vortex Strength	0.50	0.0	+0.283	0.1	NACA-0012
				-0.283		
		0.57	0.0	-0.248	0.1	NACA-0012
				-0.538		
				-1.16		
		-1.80				
Inviscid	Miss-distance	0.57	0.0	-1.80	0.1	NACA-0012
			-0.10			
			-0.15			
			-0.31			
			-0.45			
			-0.60			

Table 5.1: List of the parameters examined.  $M_\infty$ ,  $R_c$ ,  $\hat{\Gamma}$ ,  $(x_0, y_0)$  represent respectively the freestream Mach number, the vortex core radius non-dimensionalised against the chord, the vortex strength non-dimensionalised against the product freestream velocity-chord and the miss-distance non-dimensionalised against the chord. A Mach number of 0.8 was chosen to highlight the differences of behaviour for the different aerofoils. Note that a negative strength  $\hat{\Gamma}$  corresponds to a clockwise-rotating vortex and that the distance from the aerofoil to the vortex core is called miss-distance.

## 5.1. INTRODUCTION

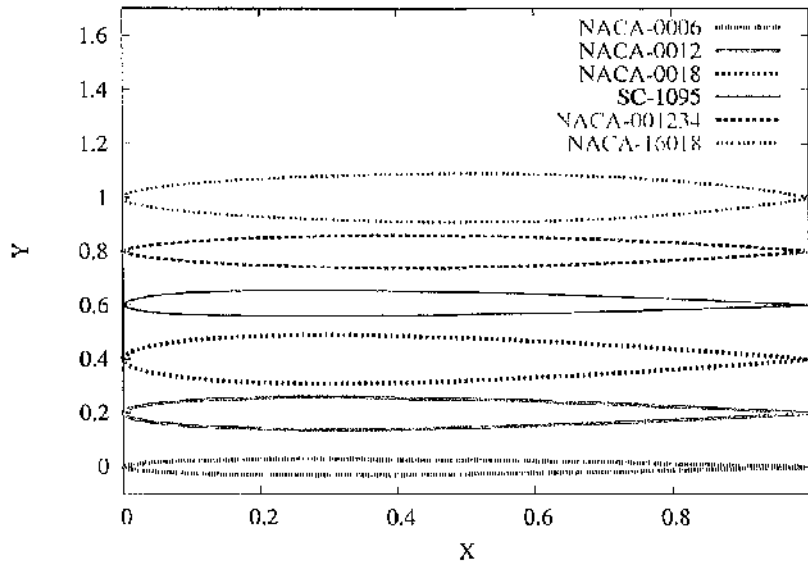


Figure 5.2: Geometry of the different aerofoils. The aerofoils NACA-0012, NACA-0018, SC-1095, NACA-001234 and NACA-16018 are respectively offset by 0.2, 0.4, 0.6, 0.8 and 1.0 for clarity.

## 5.2 Aerodynamics

A parametric BVI study has been done using different grids. The grid density was similar along the vortex path for all the calculations but for the aerofoils study which required a finer grid due to the small size of the initial vortex. Table 5.2 indicates the nature of the BVI along with the size of the grids used. The characteristics of the BVI aerodynamics are presented for various aerofoils, freestream Mach numbers, vortex core radii, vortex strengths and miss-distances.

Type of BVI	Unsteady case	Parameter studied	Number of points
Head-on ( $y_0 = 0.0$ ) Fixed $\hat{\Gamma}$ and $R_c$	Viscous	Aerofoil	230k 234k
Head-on ( $y_0 = 0.0$ ) Fixed $R_c$ , $\hat{\Gamma}$ and aerofoil	Inviscid	Freestream Mach number	168k
Head-on ( $y_0 = 0.0$ ) Fixed $\hat{\Gamma}$ and aerofoil	Inviscid	Vortex core radius	149k
Miss-distance ( $y_0 > 0.0$ ) Fixed $\hat{\Gamma}$ and aerofoil			168k
Head-on ( $y_0 = 0.0$ ) Fixed $R_c$ and aerofoil	Inviscid	Vortex strength	149k
Miss-distance ( $y_0 > 0.0$ ) Fixed $R_c$ , $\hat{\Gamma}$ and aerofoil	Inviscid	Miss-distance	168k

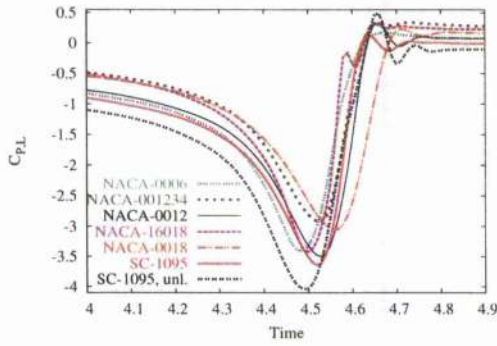
Table 5.2: Size of the grids used for the inviscid and viscous calculations for different types of BVI. The vortex was introduced at 4.5 chords ahead of the aerofoil.

## 5.2. AERODYNAMICS

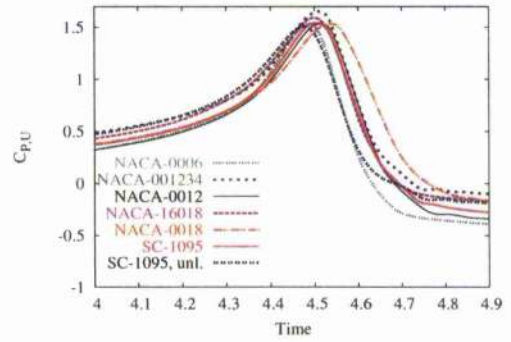
### 5.2.1 Influence of the aerofoil shape

Different NACA profiles were used to highlight the role of the thickness and the LE radius of the aerofoil. Calculations were also run with the SC-1095 aerofoil to investigate the influence a cambered section may have. For this profile (SC-1095), the loaded aerofoil calculations were performed by keeping the angle of attack to  $0^\circ$ . Further runs were also carried out with the aerofoil set at its zero-lift angle (SC-1095 unloaded).

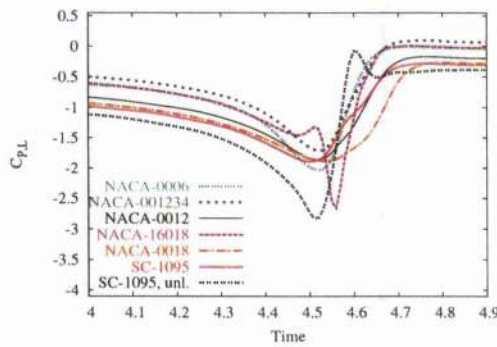
The subsonic BVI cases are first considered. The surface pressure coefficient is given in Figures 5.3-5.4 for six chordwise sections: 0.02, 0.05, 0.10, 0.20, 0.30 and 0.40. The  $C_p$  history at  $x/c=0.02$  on the upper surface is similar for all aerofoils as shown in Figure 5.3(b). It can be seen that the LE radius has a stronger effect on the thinner aerofoils. It is expected that a smaller leading-edge should actually be more sensitive to the vortex-induced "downwash" [130], which is translated into larger fluctuations in the pressure distributions near the LE [44]. The differences on the lower side seem to be driven by the LE radius and the thickness, especially for the chordwise location  $x/c=0.02$  as shown in Figure 5.4(a). This is illustrated by the  $C_p$  of the NACA-0006 and NACA-001234 aerofoils. As depicted in Figure 5.5, the secondary generated vortex is weaker for the NACA-001234, leading to lower  $C_p$ . Although this confirms the idea that the LE radius is more important for thinner aerofoils at subsonic flow, the overall influence of the secondary vortex on the  $C_p$  is small due to its short lifespan (see Figure 5.6). It can be observed that the vortex induces a "downwash" effect on the blade before the interaction and an "upwash" effect after. This results in the generation of the primary BVI wave front which reflects back from the TE, explaining the small kink in the pressure after the main interaction [40] as can be observed in Figure 5.4.



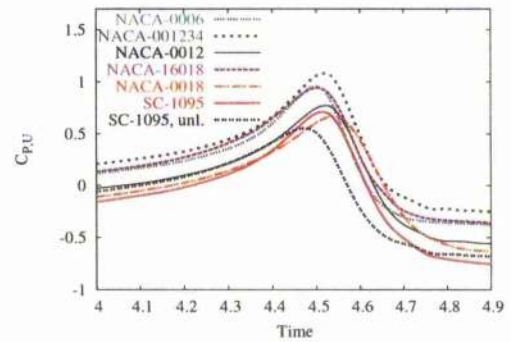
(a) Lower surface,  $x/c=0.02$



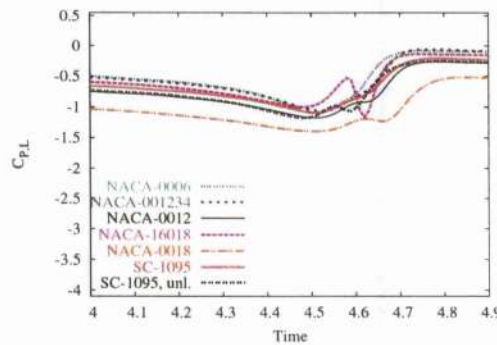
(b) Upper surface,  $x/c=0.02$



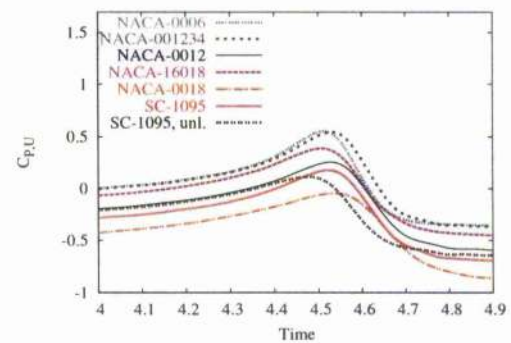
(c) Lower surface,  $x/c=0.05$



(d) Upper surface,  $x/c=0.05$

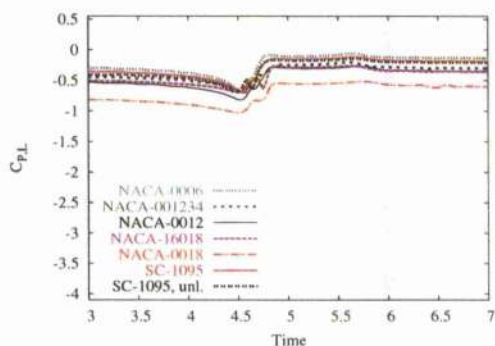


(e) Lower surface,  $x/c=0.10$

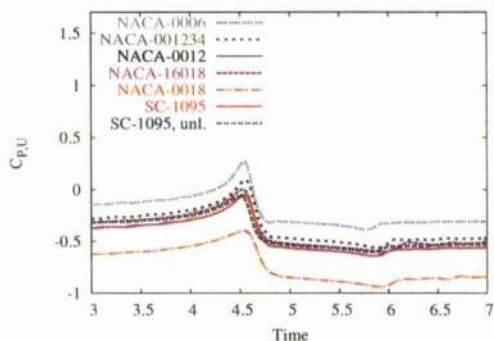


(f) Upper surface,  $x/c=0.10$

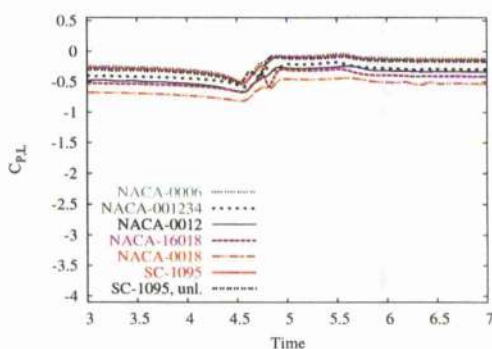
Figure 5.3: Time history of the surface pressure coefficient at different chordwise locations. Head-on BVI problem, six different aerofoils, viscous calculations,  $M_\infty=0.50$ ,  $\hat{\Gamma} = -0.283$ ,  $R_c = 0.018$ . Note that the abbreviation "unl." means unloaded.



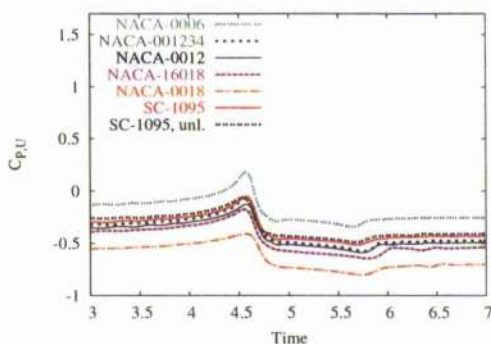
(a) Lower surface,  $x/c=0.20$



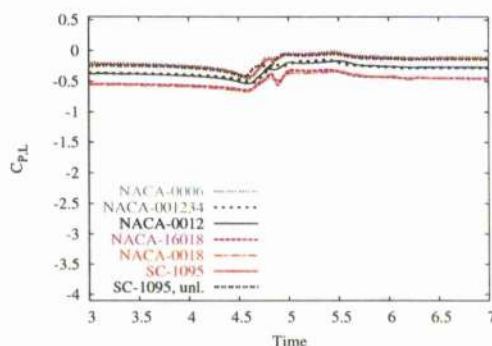
(b) Upper surface,  $x/c=0.20$



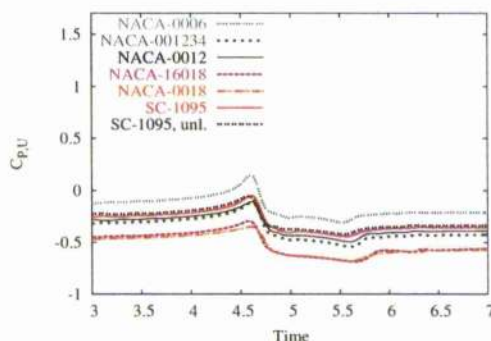
(c) Lower surface,  $x/c=0.30$



(d) Upper surface,  $x/c=0.30$



(e) Lower surface,  $x/c=0.40$



(f) Upper surface,  $x/c=0.40$

Figure 5.4: Time history of the surface pressure coefficient at different chordwise locations. Head-on BVI problem, six different aerofoils, viscous calculations,  $M_\infty=0.50$ ,  $\hat{\Gamma} = -0.283$ ,  $R_c = 0.018$ . Note that the abbreviation "unl." means unloaded.

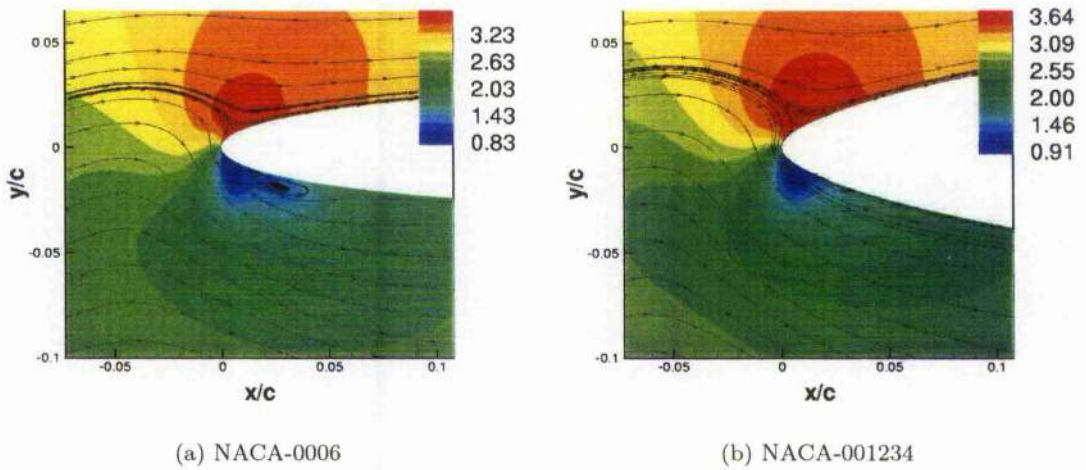


Figure 5.5: Isobars ( $2p/q_\infty$ ) along with the velocity streamlines for the NACA-0006 and NACA-001234 aerofoils. Head-on BVI problem, viscous calculations,  $M_\infty=0.50$ ,  $\hat{\Gamma} = -0.283$ ,  $R_c = 0.018$ .

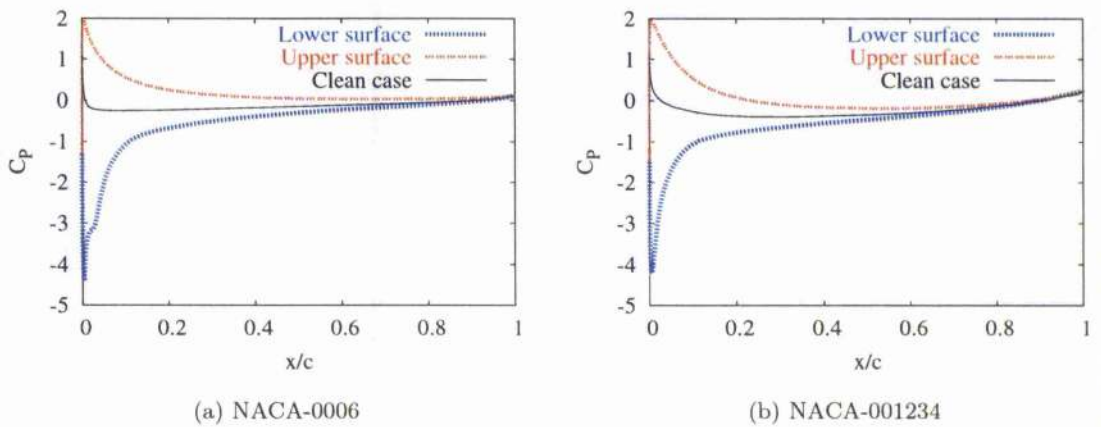


Figure 5.6: Surface pressure coefficient at time  $t(U_\infty/c)=4.51$  for the NACA-0006 and NACA-001234 aerofoils. Head-on BVI problem, viscous calculations,  $M_\infty=0.50$ ,  $\hat{\Gamma} = -0.283$ ,  $R_c = 0.018$ .

Regarding the SC-1095, a similar behaviour was obtained for the NACA-0006 on the lower surface and the NACA-0012 on the upper surface, which is expected due to the similarities of its geometry with these aerofoils (see Figure 5.2). It can be seen from Figure 5.7 that the initial loading of the aerofoil effects the BVI loads before and after the interaction.

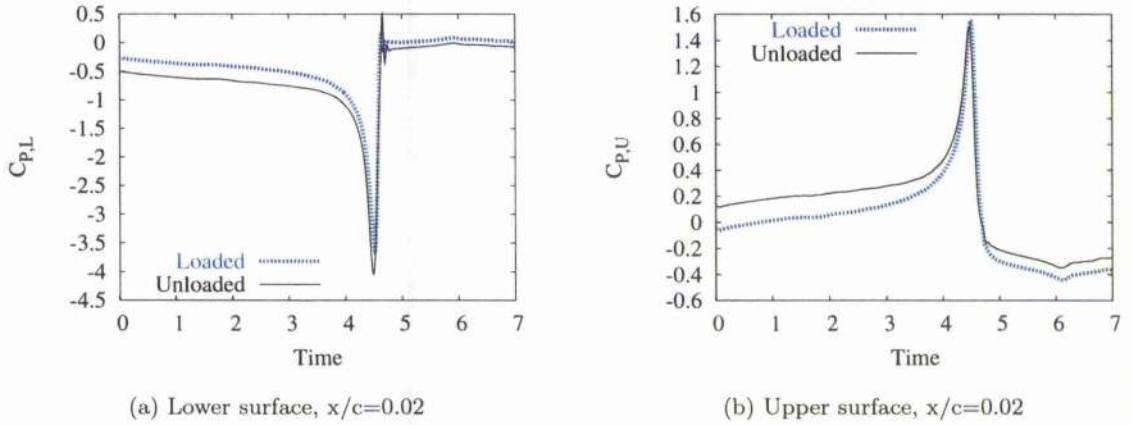


Figure 5.7: Time history of the surface pressure coefficient at different chordwise locations for the loaded and unloaded SC-1095 aerofoil. Head-on BVI problem, SC-1095 aerofoil, viscous calculations,  $M_\infty=0.50$ ,  $\hat{\Gamma} = -0.283$ ,  $R_c = 0.018$ .

Results are now discussed for transonic flow cases at a freestream Mach number of 0.8. The history of the surface pressure coefficient is shown in Figures 5.8-5.9 for the chordwise sections  $x/c=0.02, 0.05, 0.10, 0.20, 0.30, 0.40, 50, 0.60$ . Since the aerofoils have different shock locations, it remains difficult to assess the importance of the thickness and the LE radius. However, the BVI peaks seem to be delayed for thick aerofoils with large LE radius as shown in Figure 5.8(a-b) and it is remarkable that the peaks do not occur at the same time due to compressibility. Note that, although the peaks of the lift coefficients are now lower than the subsonic case, the lift forces exerted on the body are in fact stronger due to the high dynamic head.

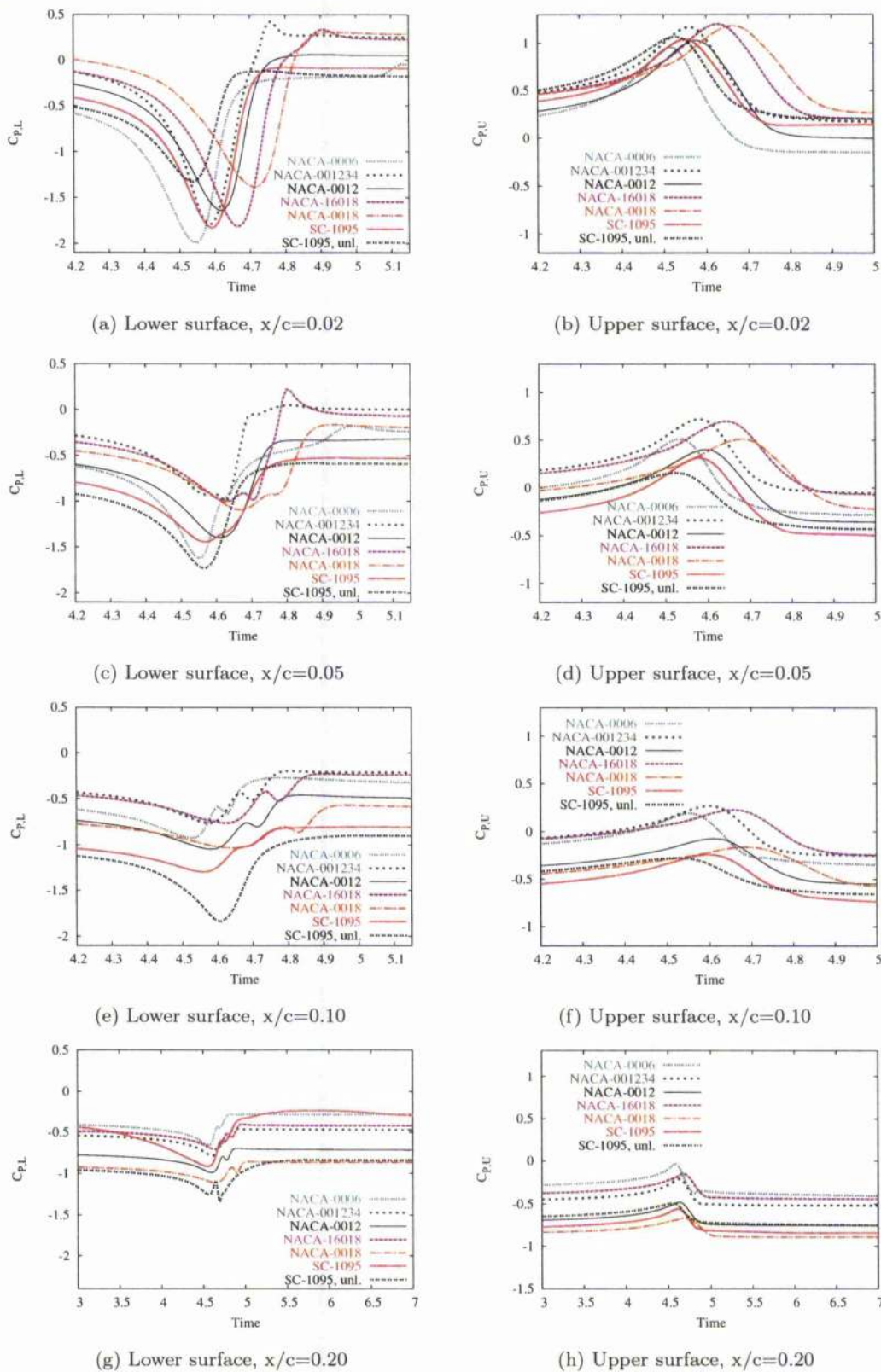


Figure 5.8: Time history of the surface pressure coefficient at different chordwise locations. Head-on BVI problem, six different aerofoils, viscous calculations,  $M_\infty=0.80$ ,  $\hat{\Gamma} = -0.177$ ,  $R_c = 0.018$ . Note that abbreviation "unl." means unloaded.

**Influence of the aerofoil shape**

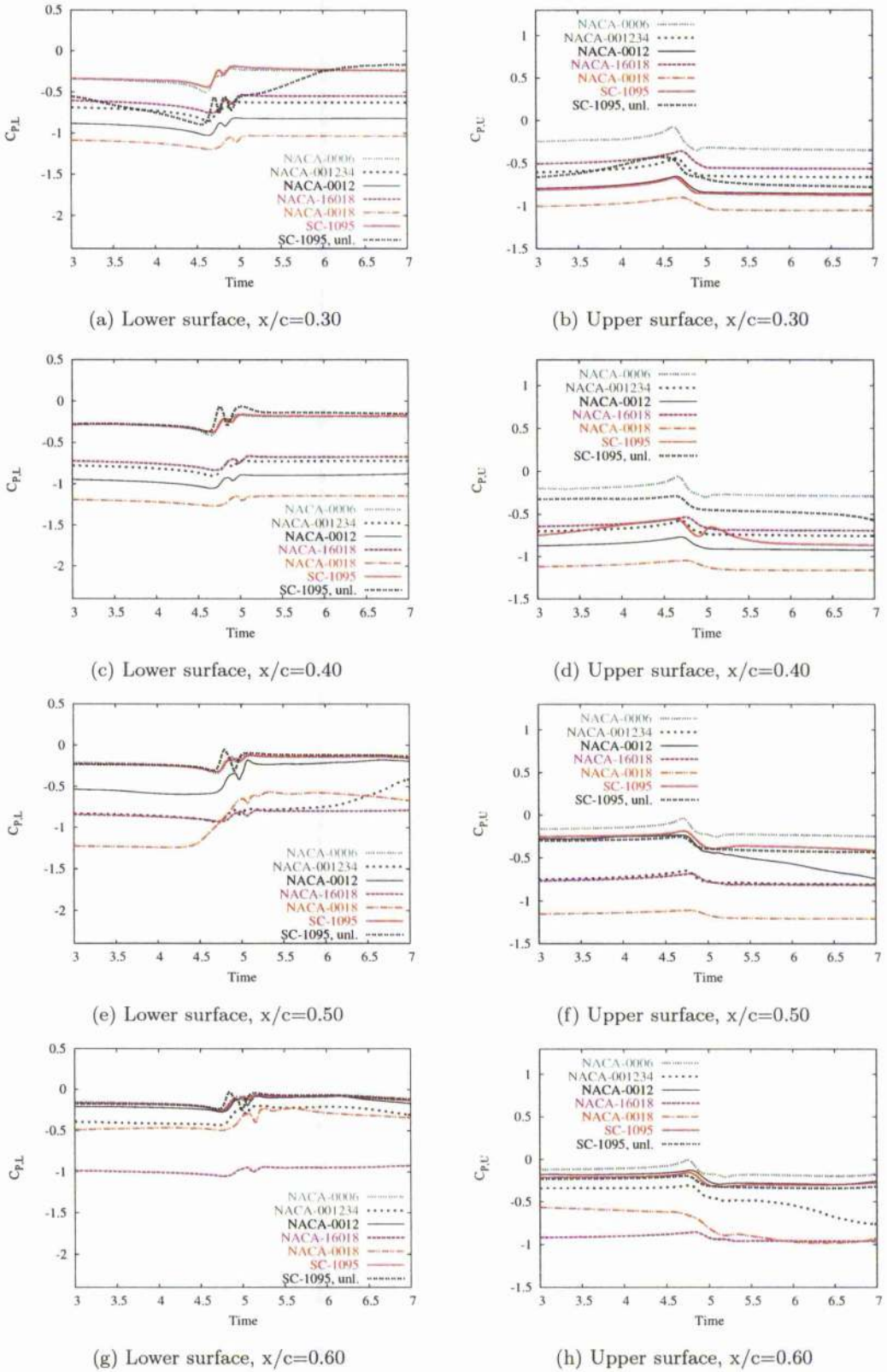


Figure 5.9: Time history of the surface pressure coefficient at different chordwise locations. Head-on BVI problem, six different aerofoils, viscous calculations,  $M_\infty=0.80$ ,  $\hat{\Gamma} = -0.177$ ,  $R_c = 0.018$ . Note that abbreviation "unl." means unloaded.

**Influence of the aerofoil shape**

The presence of the vortex was found to effect the shock. While the vortex is approaching the shock, the boundary layer thickens near the foot of the shock, and the wall pressure near the shock is spread over a distance of order several boundary-layer thicknesses [131] as depicted in Figure 5.10.

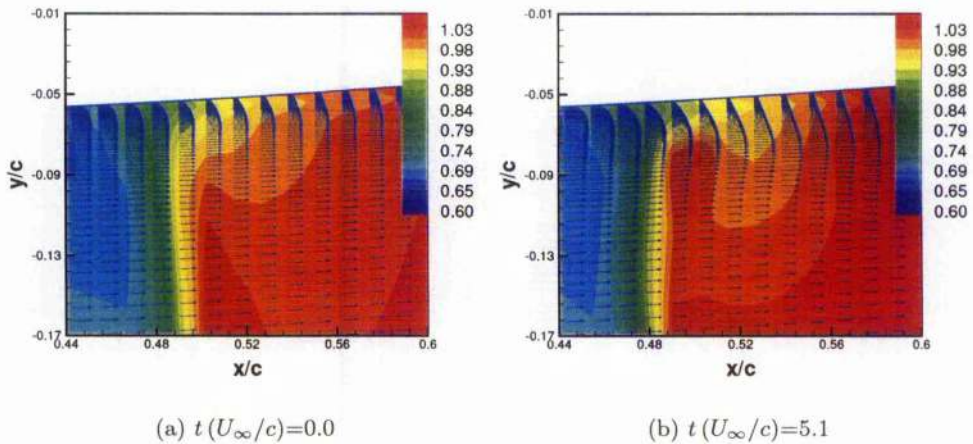


Figure 5.10: Isobars ( $2p/q_\infty$ ) and velocity vectors for (a) the clean case and (b) the vortex-shock interaction. Head-on BVI problem, NACA-0012 aerofoil, viscous calculations,  $M_\infty=0.80$ ,  $\hat{\Gamma} = -0.177$ ,  $R_c = 0.018$ .

The effect of the wall pressure change on the shock wave is to weaken it near the wall and to cause it to bend forward relative to the streamwise direction as depicted in Figure 5.11. Because of the adverse pressure gradient on the wall, the boundary layer is less able to withstand it than for a zero pressure gradient flat wall and hence separates more easily, as a result of the interaction. This explains why the shock is less altered by the passage of the vortex for inviscid calculations.

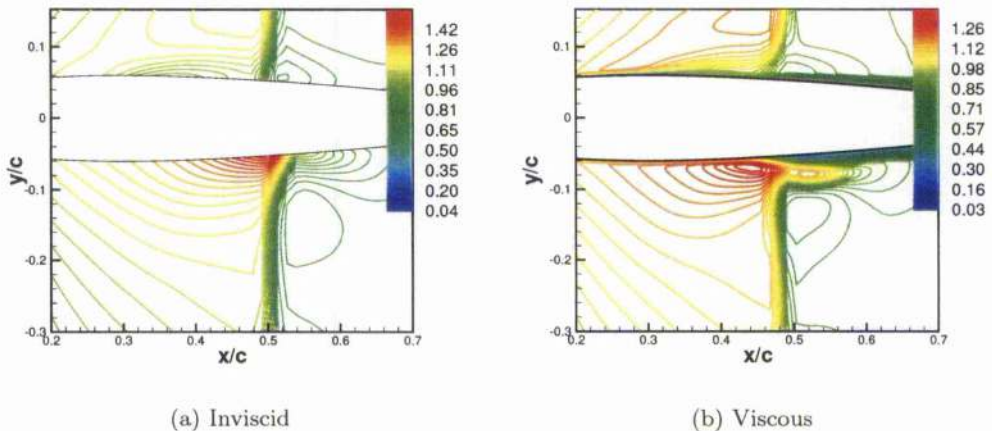


Figure 5.11: Isomachs at  $t(U_\infty/c)=5.0$  for (a) inviscid and (b) viscous calculations. Head-on BVI problem, NACA-0012 aerofoil,  $M_\infty=0.80$ ,  $\hat{\Gamma} = -0.177$ ,  $R_c = 0.018$ .

**Influence of the aerofoil shape**

The vortex-induced angle also explains the difference of loads before the BVI at transonic flow. Indeed, the shock location on the lower side was found to move upstream, which changes the symmetry between the shocks on the lower and upper surfaces and therefore modifies the loads as well. The movement of the shock is depicted in Figure 5.12.

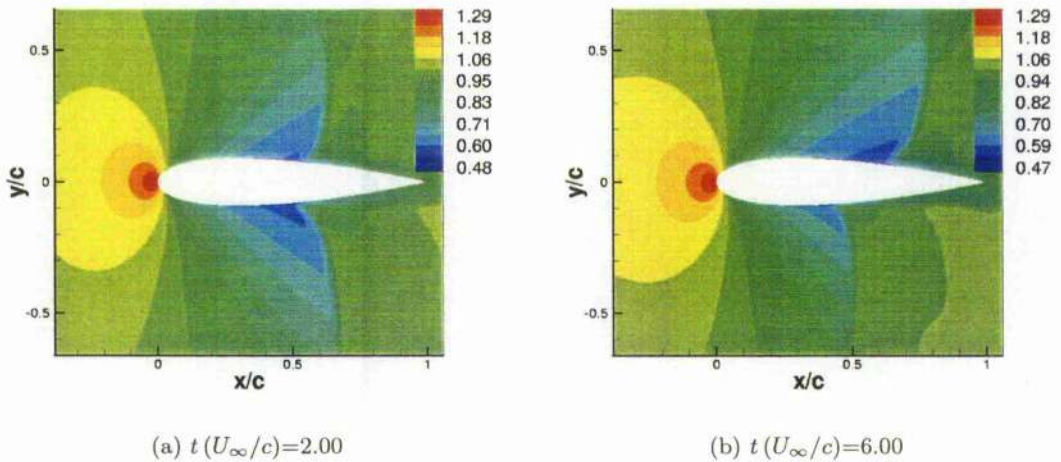


Figure 5.12: Isobars ( $2p/q_\infty$ ) for the clean case at two different time steps. It illustrates the movement of the shocks. Head-on BVI problem, NACA-0018 aerofoil,  $M_\infty=0.8$ ,  $\hat{\Gamma} = -0.177$ ,  $R_c = 0.018$ .

As depicted in Figure 5.13, the lift coefficient is observed to be negative when the vortex induces a downwash at the LE of the aerofoil [59] in both subsonic and transonic flows. Afterwards, when the vortex passes the LE, the lift coefficient rapidly increases due to the "upwash" effect of the vortex. The passage of the vortex generates an impulsive drag for both flows and, in transonic flow, the wave drag which is related to the strength of the shocks can be easily observed in Figure 5.13(f) before the interaction.

It is interesting to establish a comparison between the subsonic and transonic flows for the SC-1095 aerofoil. The initial loading of the aerofoil has an effect on the unsteady loading both before and after the encounter with the vortex, especially in the transonic regime. For the SC-1095 aerofoil, the difference of loads before the interaction at the transonic regime mainly comes from the cambered shape of the aerofoil, the aerofoil inducing a static lift. As expected, the SC-1095 aerofoil has the lowest drag coefficient since the aerofoil offsets strong shocks and, for the unloaded case, it appears to be the less effected by the BVI at the freestream Mach number of 0.8. It is important to notice that the shape of the lift curve for the loaded aerofoil is similar to the one of the unloaded one; the lift coefficient is just offset by a positive value. This suggests that the vortex induced effects are independent, at the first order, to the initial angle of attack of the aerofoil, as shown by Masson *et al.* [132].

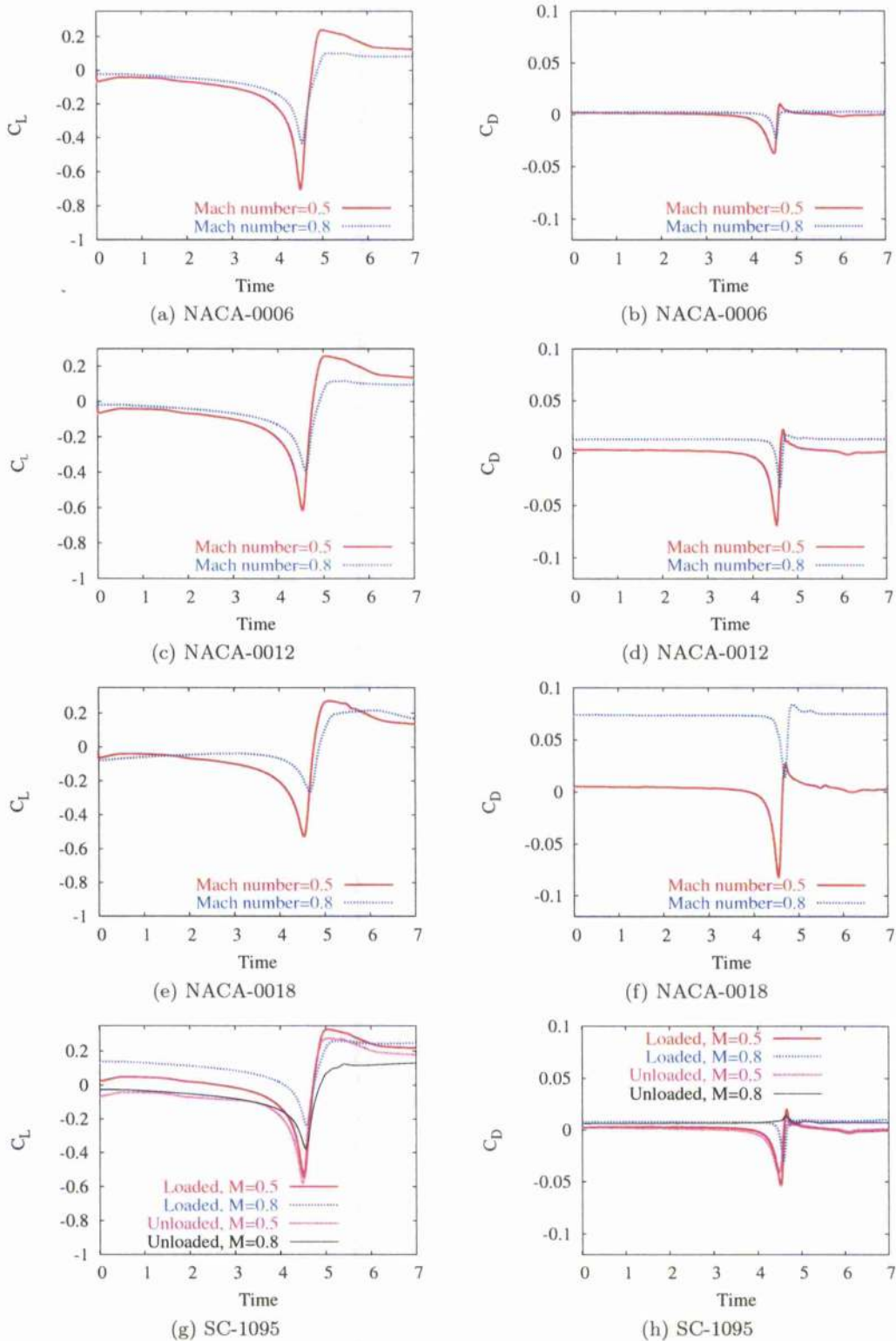


Figure 5.13: Histories of the lift and drag coefficients at freestream Mach numbers of 0.50 and 0.80 for (a-b) the NACA-0006 aerofoil, (c-d) the NACA-0012 aerofoil, (e-f) the NACA-0018 aerofoil, (g-h) the loaded and unloaded SC-1095 aerofoil.  $\hat{\Gamma} = -0.283$  at  $M_\infty = 0.50$ ,  $R_c = 0.018$ . Note that the drag is non-dimensionalised against  $\frac{1}{2}\rho_\infty U_\infty^2 c$ .

**Influence of the aerofoil shape**

The lift history and the lift peaks are given in Figure 5.14 for different aerofoils at the transonic flow. As suggested by Hardin and Lamkin [126], and Booth [10, 32], the vortex decelerates as it approaches the aerofoil, leading to the generation of lift. The thickness of the aerofoils seems also to determine the timing of occurrence of the peaks.

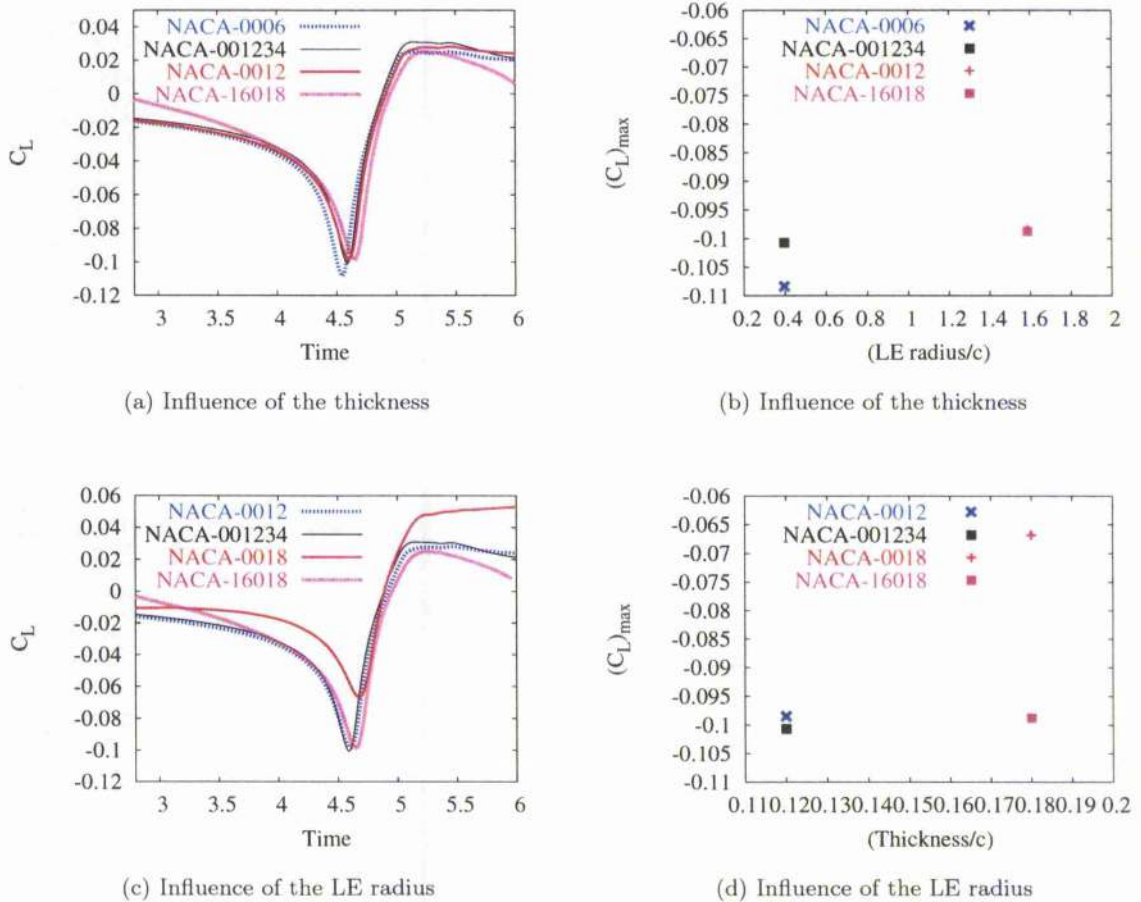


Figure 5.14: (a, c) Lift history and (b, d) maximum difference of lift for different aerofoils of the same thickness or the same LE radius at freestream Mach number 0.80.  $\hat{\Gamma} = -0.177$ ,  $R_c = 0.018$ .

The influence of the aerofoil shape varies with the nature of the flow. At subsonic flow, the BVI affects more the thinner sections for a fixed LE radius and the sections of small LE radius. At transonic flow, the LE radius was also found to have an effect for the thicker sections, especially, which result in strong shocks as shown in Figure 5.14(d).

Note that the same vortex properties were used for both subsonic and transonic flow. Figure 5.15 depicts the time history of the quantity  $\omega/\rho$  before the interaction at the vortex core for the different aerofoils. We can observe that the quantity  $\omega/\rho$  decreases

**Influence of the aerofoil shape**

during the first time steps to finally reach a stable value. This stems from the grid density, i.e. the number of cells per vortex core. Only a few cells have been used to capture the vortex on the given grid. The use of an appropriate confinement parameter overcomes this problem, re-establishing expected levels of density at the vortex core after a few time steps.

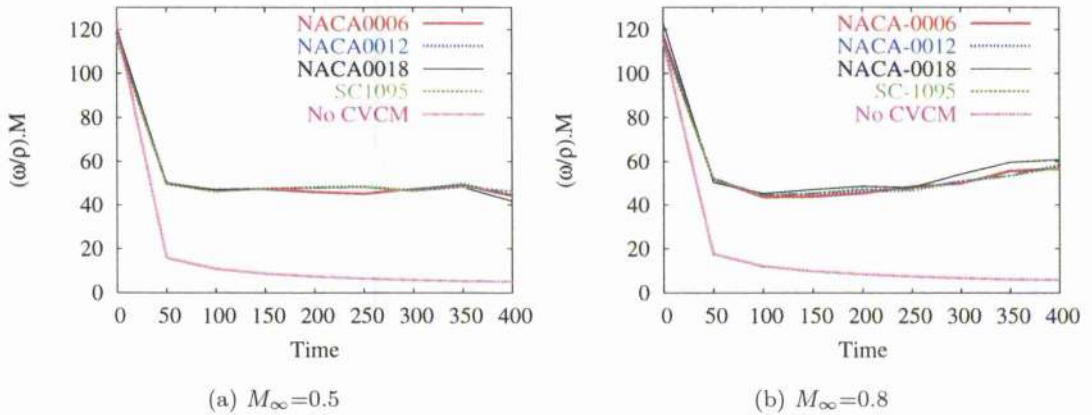
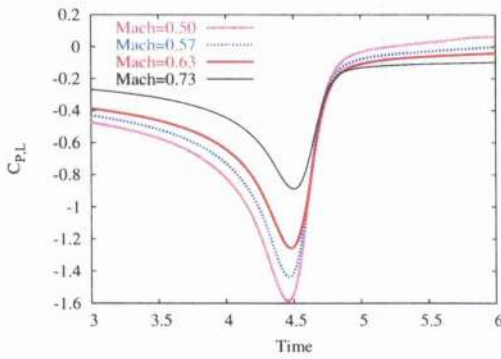


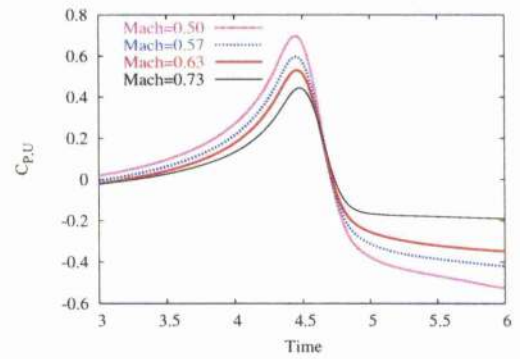
Figure 5.15: Time history of the quantity  $\omega/\rho$  for the four aerofoils at freestream Mach number 0.50 and 0.80.  $\hat{\Gamma} = -0.283$  ( $M_\infty = 0.5$ ),  $R_c = 0.018$ .

### 5.2.2 Influence of the freestream Mach number

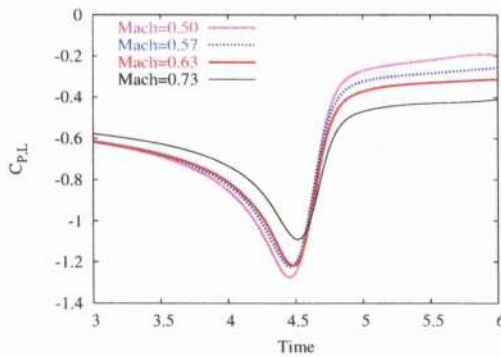
To further assess the effect of Mach number, inviscid calculations were run at four freestream Mach numbers for head-on BVI. The non-dimensionalised vortex strength and core radius were respectively set to  $-0.283$  and to  $0.1$ . The time history of the BVI loads is given in Figure 5.16. It can be observed that the loads magnitude on the lower and upper sides decreases with the Mach number.



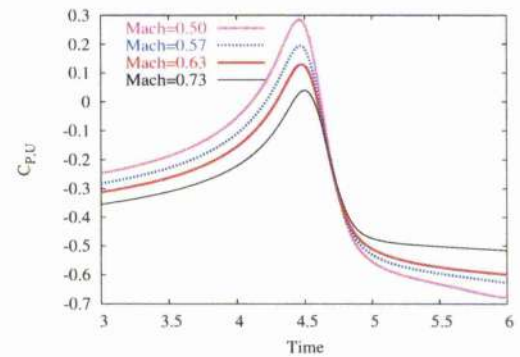
(a) Lower surface,  $x/c=0.02$



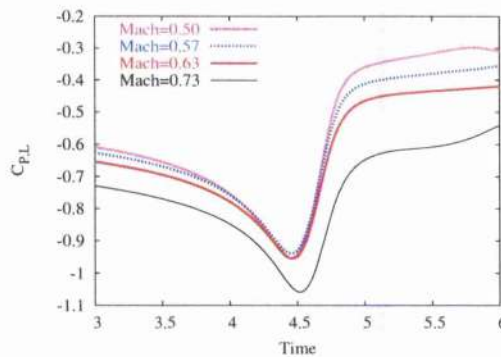
(b) Upper surface,  $x/c=0.02$



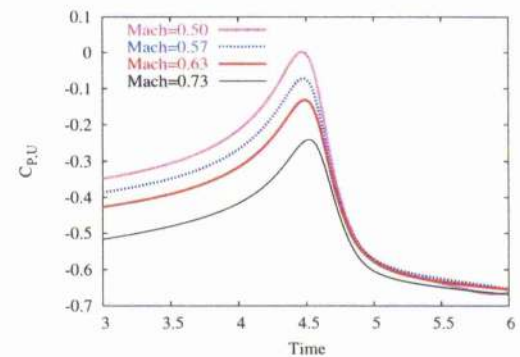
(c) Lower surface,  $x/c=0.05$



(d) Upper surface,  $x/c=0.05$



(e) Lower surface,  $x/c=0.10$



(f) Upper surface,  $x/c=0.10$

Figure 5.16: Time history of the surface pressure coefficients for different freestream Mach numbers at different chordwise locations. Head-on BVI problem, NACA-0012 aerofoil, inviscid calculations.  $\hat{\Gamma} = -0.283$  ( $M_\infty = 0.5$ ),  $R_c = 0.10$

The lift and the drag are shown in Figure 5.17. As expected, the lift and drag coefficients decrease with the freestream Mach number.

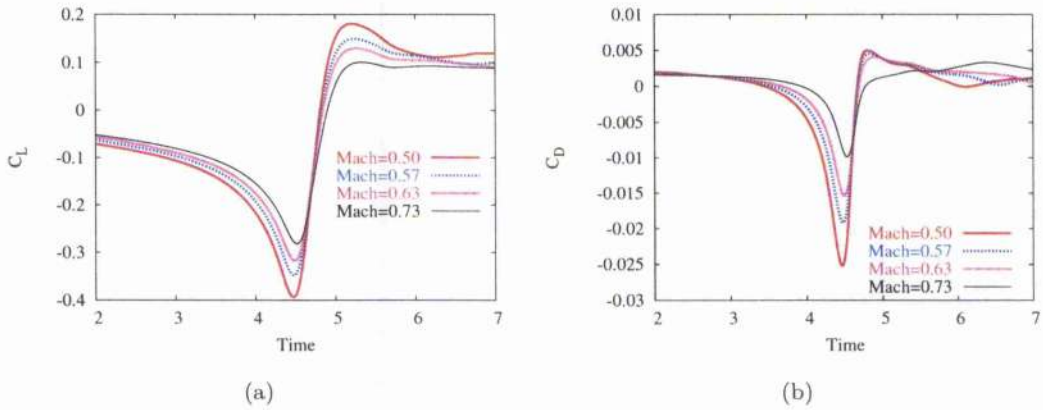


Figure 5.17: Lift and drag histories for a vortex of fixed strength at different freestream Mach numbers. Head-on BVI problem, NACA-0012 aerofoil, inviscid calculations,  $\hat{\Gamma} = -0.283$  ( $M_\infty=0.50$ ),  $R_c = 0.10$ .

The history of the vortex characteristics is given for the range of Mach numbers in Figure 5.18. The fact that the vortex loses its strength before the interaction for higher Mach numbers gives an indication of the compressibility effects near the aerofoil where the pressure increases with the Mach number and is not due to the numerical dissipation of the vortex.

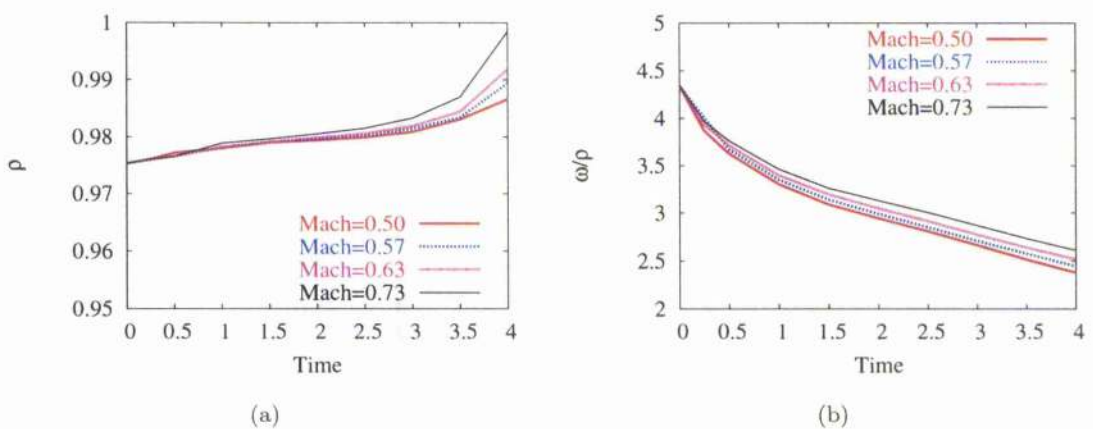


Figure 5.18: (a) Time histories of the density and of (b) the ratio vorticity-density at the vortex core. Head-on BVI problem, NACA-0012 aerofoil, inviscid calculations,  $\hat{\Gamma} = -0.283$  ( $M_\infty=0.50$ ),  $R_c = 0.10$ , various freestream Mach numbers.

**Influence of the freestream Mach number**

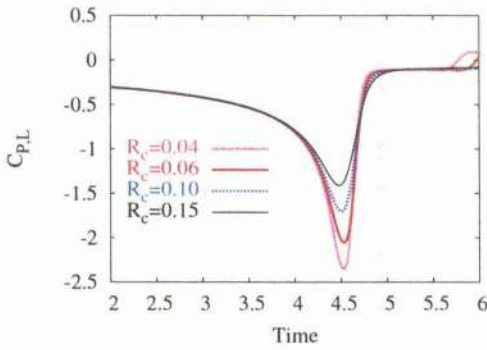
### 5.2.3 Influence of the vortex properties

#### Vortex core radius

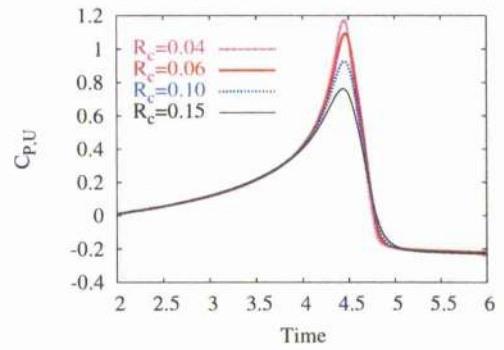
The calculations were run inviscid for head-on and miss-distance BVI cases ( $y_0 = -0.15$ ). The non-dimensionalised vortex strength was set to  $-0.42$  for a freestream Mach number of  $0.73$ .

The surface pressure coefficient is given in Figures 5.19-5.20 for chordwise sections 2, 5 and 10% of the aerofoil chord. A stronger BVI is obtained for a smaller vortex core size. For the head-on BVI, the loads seem to be more sensitive to the vortex core size, the loads magnitude being larger for the smaller vortex. Since the vortex strength was kept the same for the different vortices, it appears that the head-on BVI strongly depends on the core radius. For the miss-distance BVI case, the size of the vortex core is not as important as in the head-on BVI. Although the interaction becomes stronger when the vortex core size decreases, a vortex of smaller core radius is found to have a lesser effect on the loads. This is an important difference between head-on and miss-distance BVI for non-lifting aerofoils as far as the influence of the vortex core size is regarded.

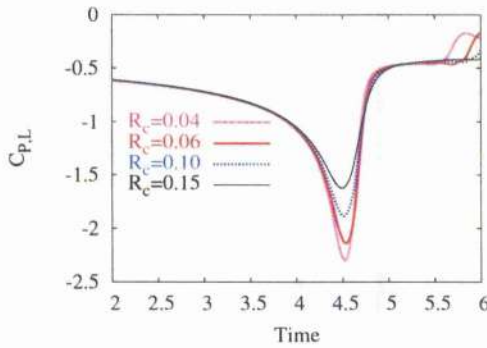
The density at the vortex core dramatically increases with the vortex core size (see Figure 5.21). This may explain the lower  $C_p$  magnitude for a larger core radius size. It can also be observed for both cases that the increase of the vortex radius leads to a weaker decay of the density at the vortex core.



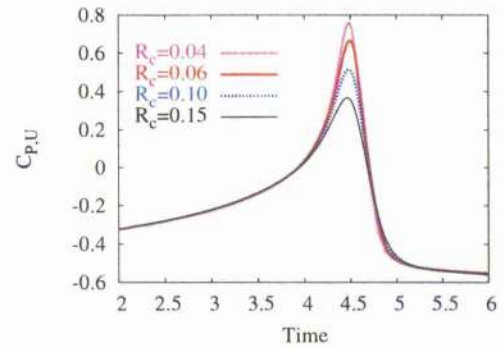
(a) Lower surface,  $x/c=0.02$



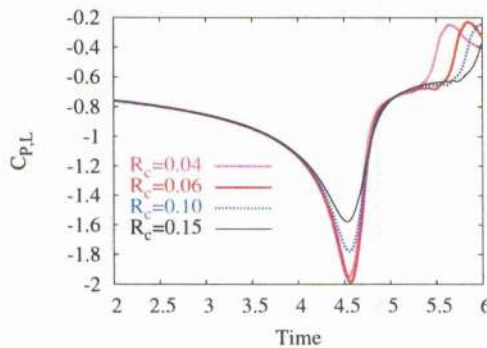
(b) Upper surface,  $x/c=0.02$



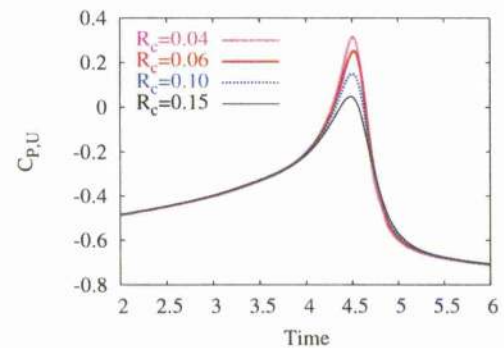
(c) Lower surface,  $x/c=0.05$



(d) Upper surface,  $x/c=0.05$

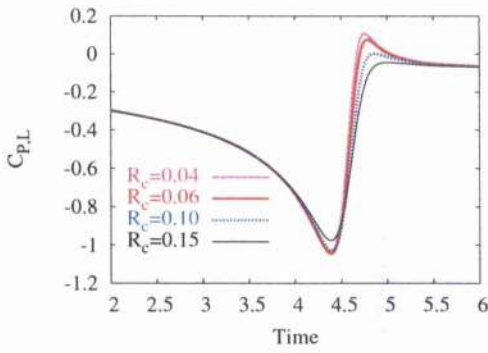


(e) Lower surface,  $x/c=0.10$

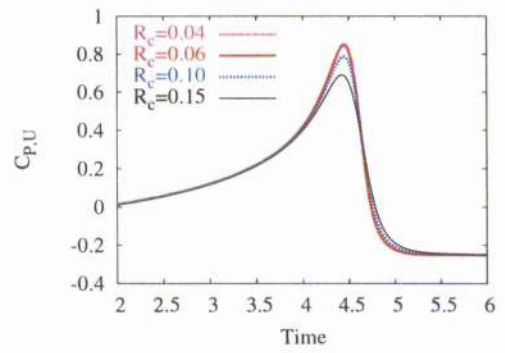


(f) Upper surface,  $x/c=0.10$

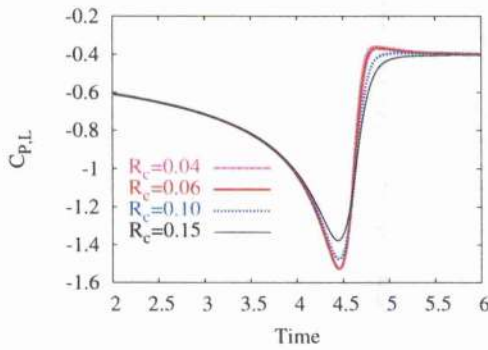
Figure 5.19: Time history of the surface pressure coefficient at different tap locations. Head-on BVI problem, NACA-0012 aerofoil, inviscid calculations,  $M_\infty=0.73$ ,  $\hat{\Gamma} = -0.42$ .



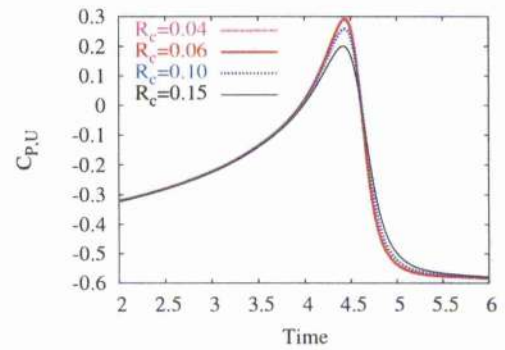
(a) Lower surface,  $x/c=0.02$



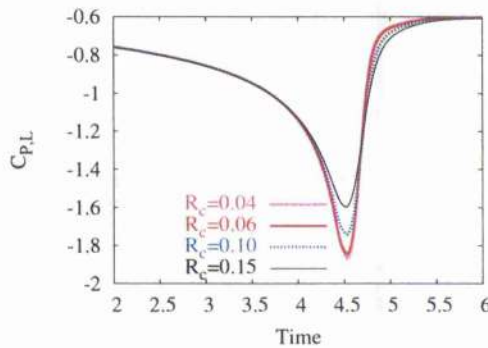
(b) Upper surface,  $x/c=0.02$



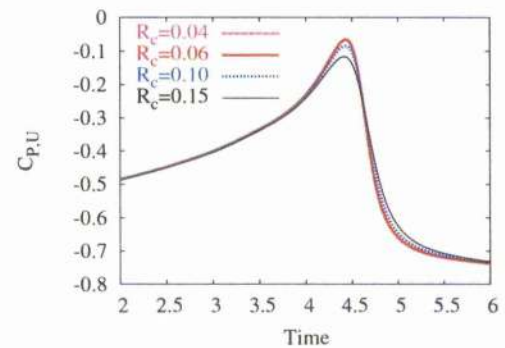
(c) Lower surface,  $x/c=0.05$



(d) Upper surface,  $x/c=0.05$



(e) Lower surface,  $x/c=0.10$



(f) Upper surface,  $x/c=0.10$

Figure 5.20: Time history of the surface pressure coefficient at different tap locations. Miss-distance BVI problem, NACA-0012 aerofoil, inviscid calculations,  $M_\infty=0.73$ ,  $\hat{\Gamma} = -0.42$ ,  $y_0 = -0.15$ .

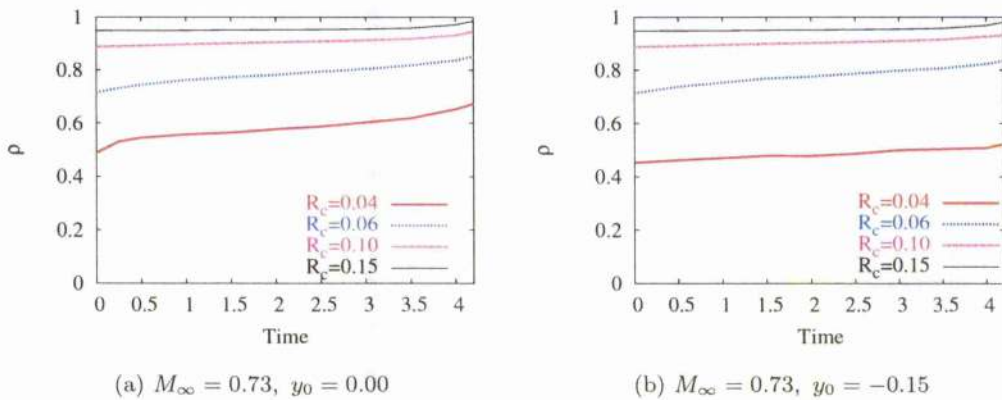


Figure 5.21: Time history of the density  $\rho$  at the vortex core for vortices of different initial core radius. Head-on and miss-distance BVI problems, NACA-0012 aerofoil, inviscid calculations,  $M_\infty=0.73$ ,  $\hat{\Gamma} = -0.42$ . (a)  $y_0 = 0.0$ , (b)  $y_0 = -0.15$ .

The time histories of the lift and pressure drag are shown in Figures 5.22-5.23. The lift tends to increase for vortices of smaller radius but the overall shape of the lift curve remains the same except for the part where the interaction occurs. The apparent angle of attack induced by the vortex is larger for the vortex with the highest tangential velocity and this suggests that the induced angle is primarily a function of the strength of the initial vortex. The same remarks can be made for the drag coefficient: the drag reduces more for the clockwise-rotating vortex of the smaller core radius.

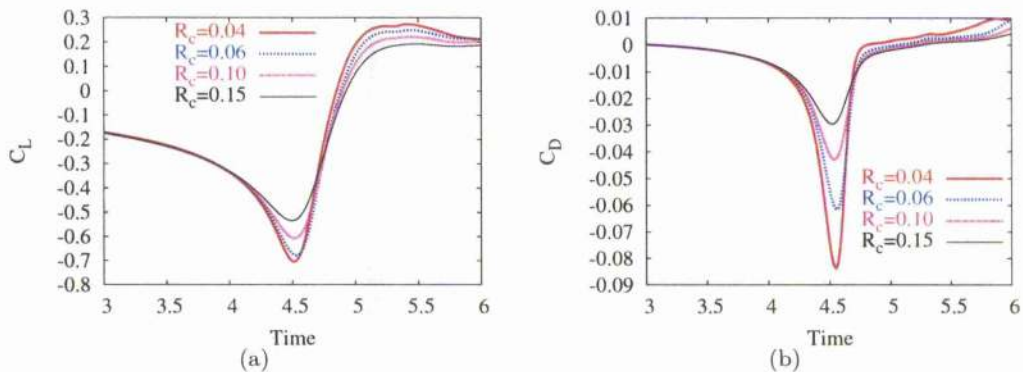


Figure 5.22: Time histories of the lift and drag for four vortices of different initial core radius. Head-on BVI problem, NACA-0012 aerofoil, inviscid calculations,  $M_\infty=0.73$ ,  $\hat{\Gamma} = -0.42$ .

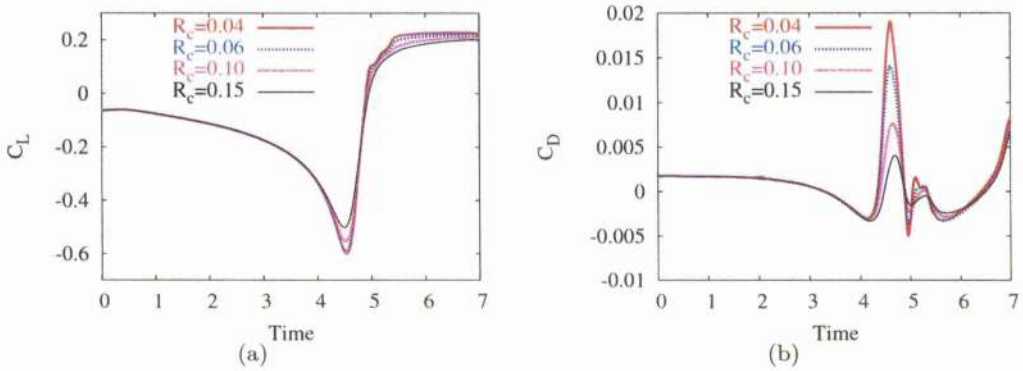


Figure 5.23: Time histories of the lift and drag for four vortices of different initial core radius. Miss-distance BVI problem, NACA-0012 aerofoil, inviscid calculations,  $M_\infty=0.73$ ,  $\hat{\Gamma} = -0.42$ ,  $y_0 = -0.15$ .

An interesting feature of the BVI is the sharpness of the loading pulses. The time history of the core radius before the interaction has been examined for head-on and miss-distance BVI cases and is given in Figure 5.24. An increase of the core radius is observed. This is confirmed by the evolution of the radius along a vertical plane passing by the vortex core as depicted in Figure 5.25. This trend of the vortex shape is consistent with the observations of Booth [10] who reported that the initially circular vortex becomes elliptic when getting closer to the interaction at low speed flow conditions. One possible explanation of the vortex distortion may be the influence of the blade loading on the vortex. Not only the blade loading effects the vortex trajectory and the convection velocity, but it also changes the shape of the circular vortex [10]. Another cause of the change in core radius may also be the non-isotropic diffusion of the solver and effects of the CVCM.

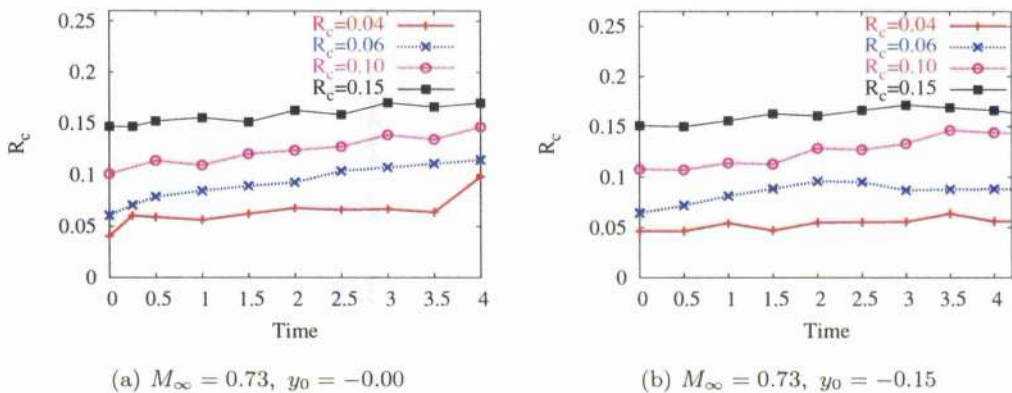


Figure 5.24: Time history of the core radius along a vertical plane passing through the vortex core for four vortices of different initial core radius for two different BVI.  $\hat{\Gamma}=-0.42$ .

**Influence of the vortex properties**

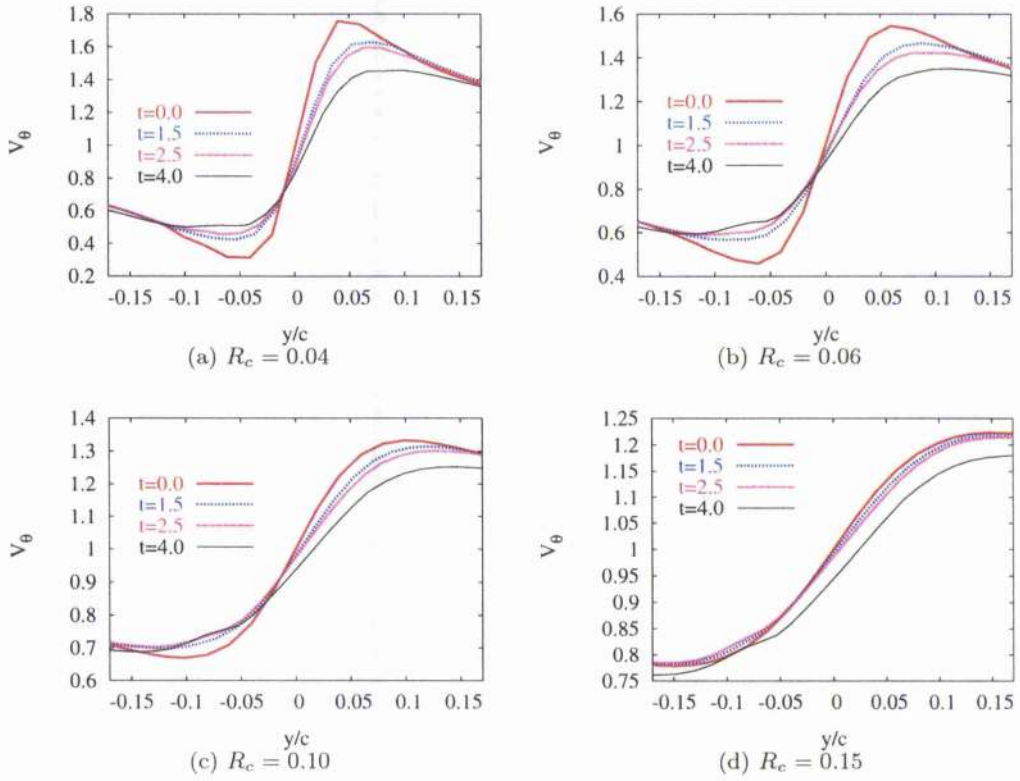


Figure 5.25: History of the tangential velocity profile along a vertical plane passing by the vortex core at four different times. The vortex was introduced at 4.5 chords ahead of the aerofoil. Head-on BVI problem, NACA-0012 aerofoil, inviscid calculations,  $M_\infty=0.73$ ,  $\hat{\Gamma} = -0.42$ .

### Vortex strength

The flow Mach number and the non-dimensionalised core radius were fixed to 0.57 and 0.1, respectively. It is interesting that the apparent angle of attack induced by the incoming vortex is negative before the interaction and becomes positive after reaching the trailing-edge of the aerofoil as shown in Figure 5.26. The clockwise-rotating vortex creates a downwash distribution of vertical velocity before the LE [44] and induces an upwash effect after the TE. It is possible to assimilate the pressure difference across the aerofoil as the response of the flow to a decrease in angle of attack, this means that the vertical velocity field induced by the vortex is negative when approaching the aerofoil and becomes positive after it passes behind the aerofoil as explained by McCroskey and Goorjian [130].

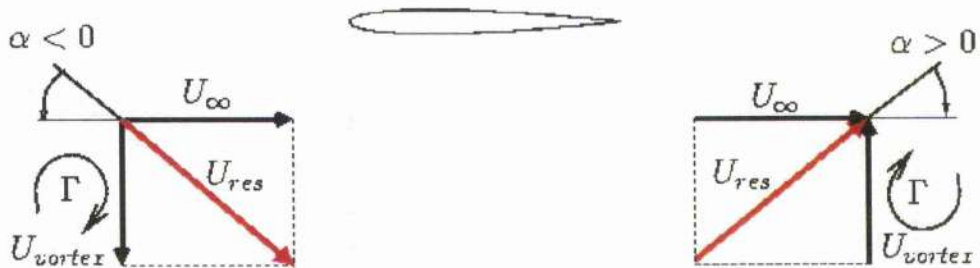
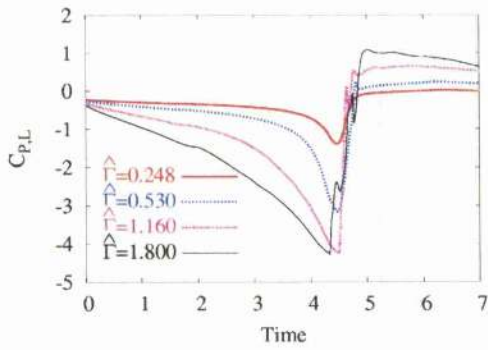
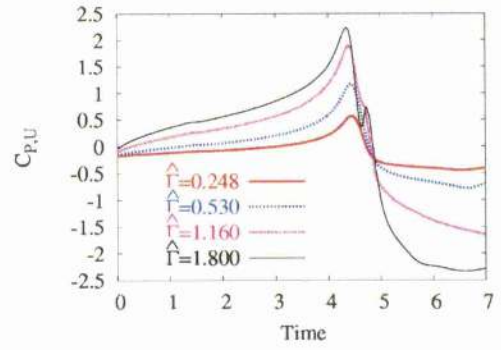


Figure 5.26: Schematic of the vortex-induced angle on the aerofoil before and after the interaction. The vertical velocity component of the vortex induces an apparent angle of attack for the aerofoil.

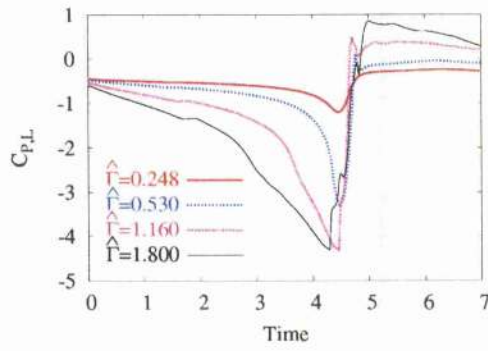
Regarding the  $C_p$  history obtained for different vortex strengths, the amplitude of the  $C_p$  fluctuations increases with the vortex strength for all chordwise sections as shown in Figure 5.27. Another pulse of opposite sign can also be observed for the pressure at the TE [40] after the vortex passes past the TE.



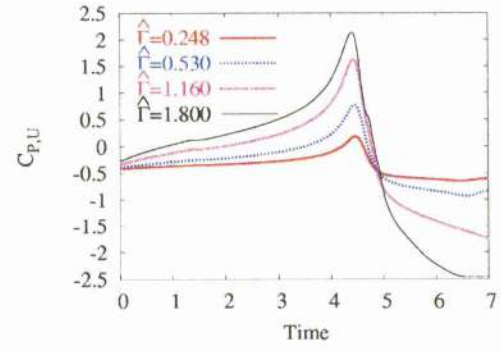
(a) Lower surface,  $x/c=0.02$



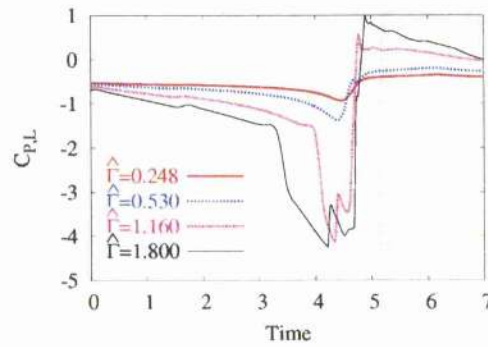
(b) Upper surface,  $x/c=0.02$



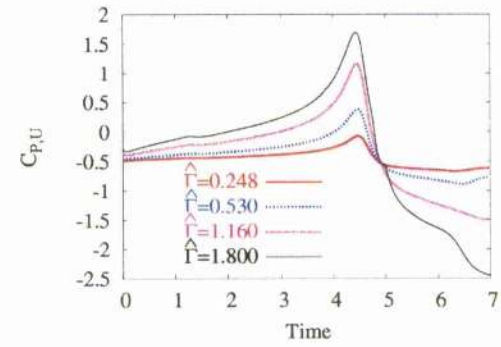
(c) Lower surface,  $x/c=0.05$



(d) Upper surface,  $x/c=0.05$



(e) Lower surface,  $x/c=0.10$



(f) Upper surface,  $x/c=0.10$

Figure 5.27: Time history of the surface pressure coefficient at different tap locations. Head-on BVI problem, NACA-0012 aerofoil, inviscid calculations,  $M_\infty=0.57$ ,  $R_c = 0.10$ .

It is also observed that the lift is driven by the vortex strength as depicted in Figure 5.28. This is also valid for the drag whose magnitude is larger for an initially stronger vortex.

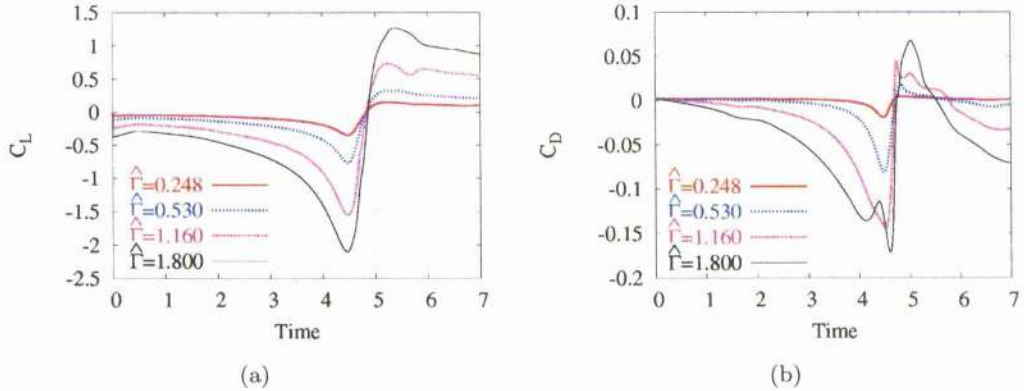


Figure 5.28: Lift and drag histories for vortices of different strengths. Head-on BVI problem, NACA-0012 aerofoil, inviscid calculations,  $M_\infty=0.57$ ,  $R_c = 0.10$ .

As for the vortex core radius, the vortex strength does influence the density at the vortex core as illustrated by Figure 5.29. It was observed that the quantity  $\omega/\rho$  decreases by 55% for the cases where the vortex strength  $\hat{\Gamma}$  was set to -0.248, -0.530 and -1.8 and by 60% when  $\hat{\Gamma}$  was equal to -1.16. This suggests that the vortex strength does not influence significantly the evolution of the density at the vortex core as long as the core radius remains the same.

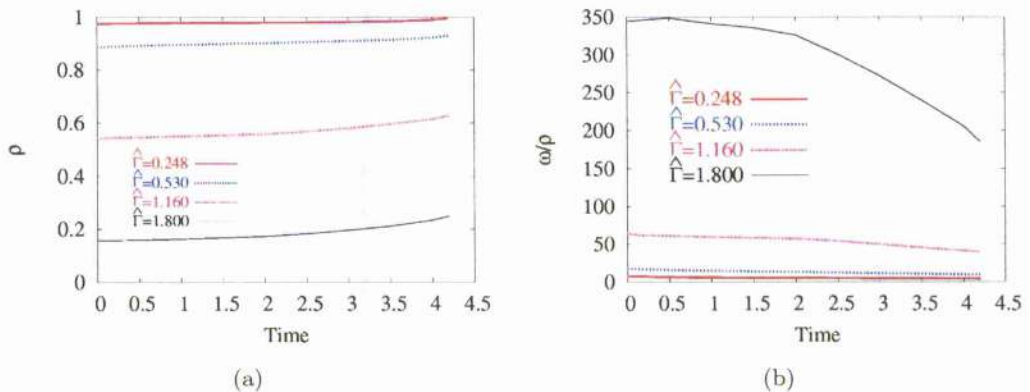


Figure 5.29: Time histories of (a) the density and of (b) the vorticity-density ratio at the vortex core. Head-on BVI problem, NACA-0012 aerofoil, inviscid calculations,  $M_\infty=0.57$ ,  $R_c = 0.10$ , various vortex strengths.

Another test case was run to evaluate the importance of the sense of rotation of the vortex. Two head-on BVI with a clockwise and anti-clockwise rotating vortices were simulated at a freestream Mach number of 0.5. Although the BVI loads in Figure 5.30 are slightly different at the chordwise location  $x/c=0.02$ , the overall shape of the lift history given in Figure 5.31 looks quite symmetric. A slightly higher peak of lift was obtained for the anti-clockwise rotating vortex, which stems from the slight asymmetry of the coarse grid. Note that the BVI case with the anti-clockwise rotating vortex is not included in the BVI noise study presented in Chapter 6 due to the similarities between the results for the two cases.

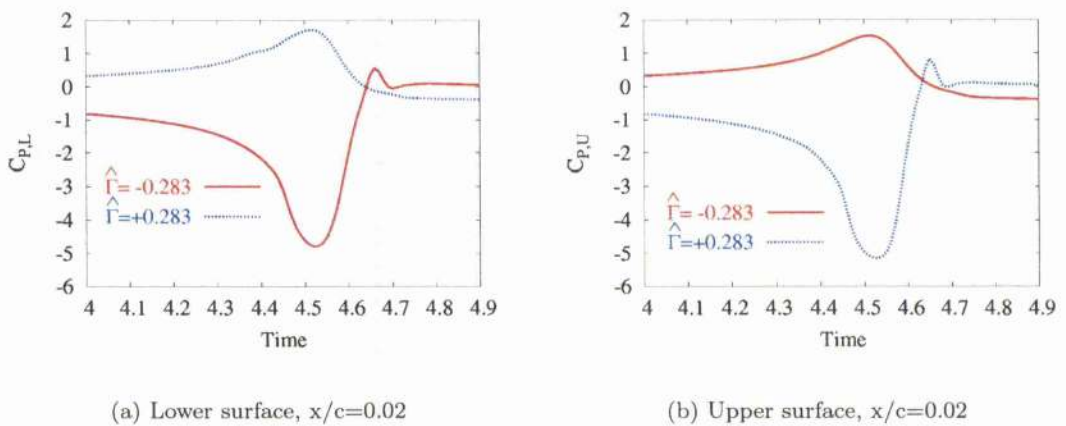


Figure 5.30: Time history of the surface pressure coefficient at the chordwise location  $x/c=0.02$  for a clockwise and anti-clockwise rotating vortex. Head-on BVI problem, NACA-0012 aerofoil, inviscid calculations,  $M_\infty=0.50$ ,  $R_c = 0.018$ .

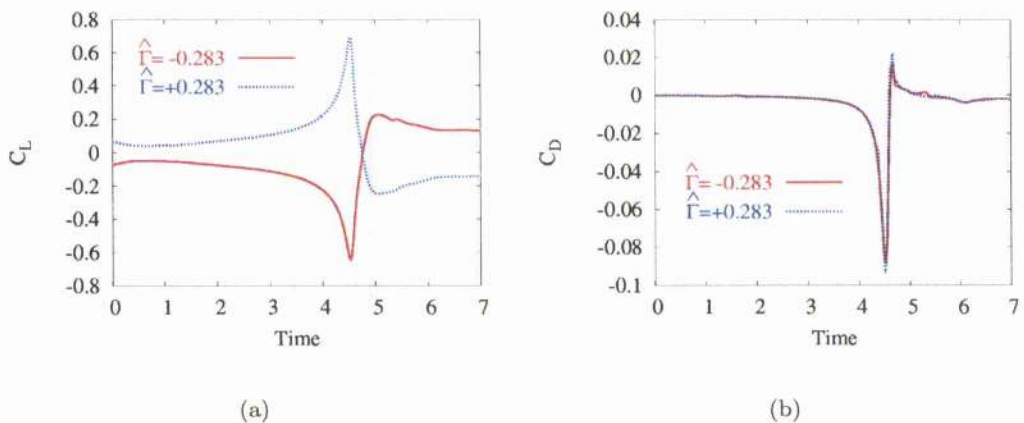


Figure 5.31: Lift and drag histories for clockwise and anti-clockwise rotating vortices. NACA-0012 aerofoil, head-on BVI,  $M_\infty=0.50$ ,  $R_c = 0.018$ .

### Miss-distance

Inviscid calculations were run for two freestream Mach numbers of 0.57 and 0.73 at different miss-distances of 0.00  $c$ , 0.10  $c$ , -0.15  $c$ , -0.31  $c$ , 0.45  $c$ , 0.60  $c$ . The effect of the vortex on the loads is similar for the two types of flow and miss-distances before the interaction starts ( $t(\frac{U_\infty}{c}) = 3.0$ ) as illustrated by Figures 5.32 and 5.33. This indicates that the miss-distance mainly influences the magnitude of BVI, which confirms that BVI is strongly influenced by the effect of proximity [133]. The fact that the decrease in loads for the different chordwise sections for both flows is of the same magnitude seems to indicate that BVI magnitude is a linear function of the miss-distance. However, it can be noticed that the timing of the pressure extrema seems to vary more with the miss-distance than for the low-speed BVI experimental observations from Booth [10]. The  $C_p$  history depicted in Figure 5.33 for the subsonic flow actually shows the stronger interaction for a miss-distance of -0.15  $c$  (see Figure 5.32) on the upper surface of the aerofoil whereas the stronger BVI for the transonic flow is obtained for  $y_0 = 0.0$ . The interaction for  $y_0 = -0.60 c$  is also obtained earlier than the one for the miss-distances  $y_0 = 0.0 c$  and  $-0.10 c$ , i.e. when the vortex is further away from the aerofoil. This suggests that an increase of the miss-distance does not necessarily mean a proportional decrease of the main BVI [134] and that other parameters than  $y_0$  play a role for BVI with different miss-distances. Indeed, the peak in terms of loads occurs earlier for the larger miss-distance BVI with the strength of the supersonic pocket directly related to the proximity of the vortex to the aerofoil.

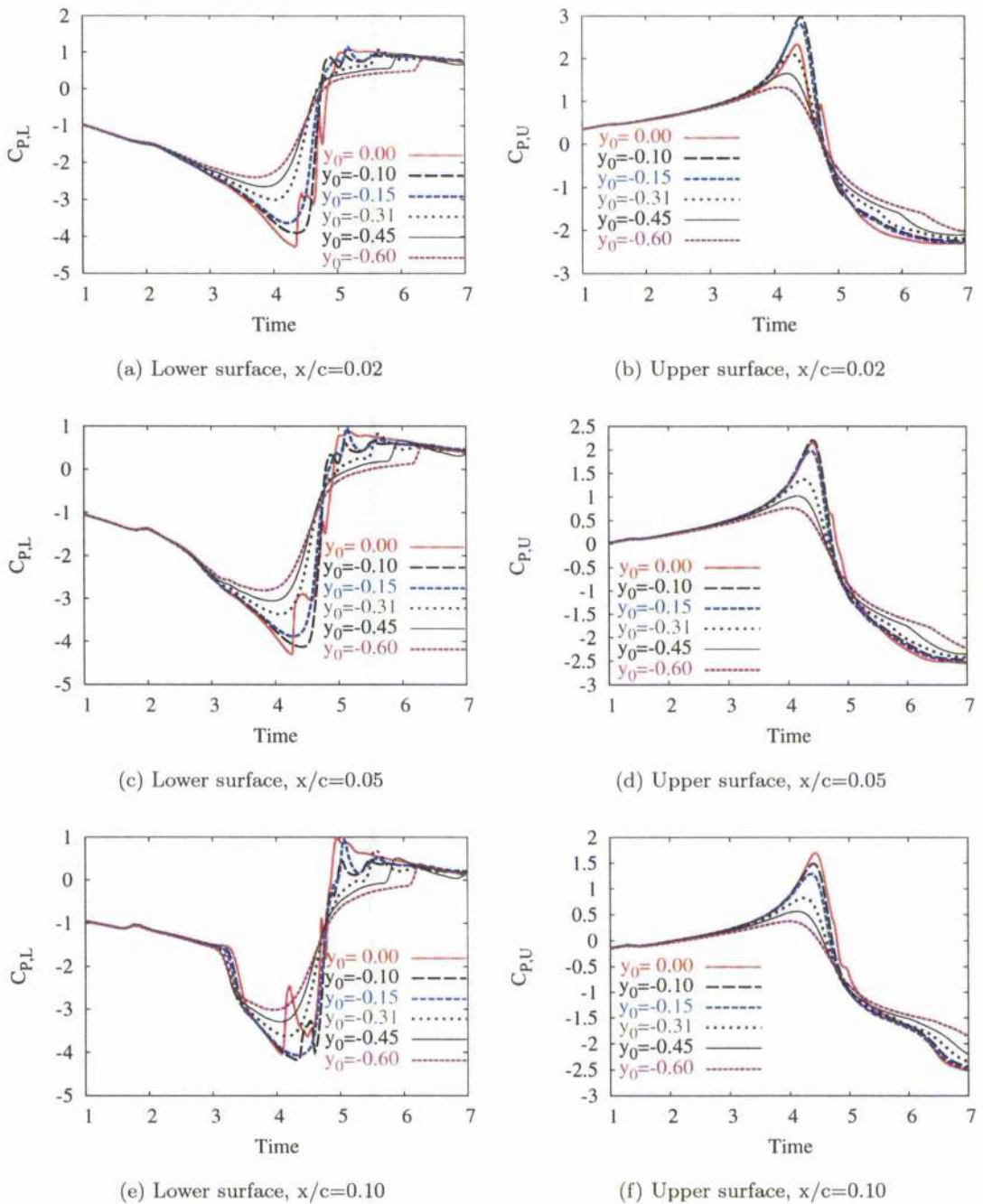


Figure 5.32: Time history of the surface pressure coefficient at different chordwise locations for different miss-distances. Head-on BVI problem, NACA-0012 aerofoil, inviscid calculations,  $M_\infty=0.57$ ,  $\hat{\Gamma} = -1.8$ ,  $R_c = 0.10$ .

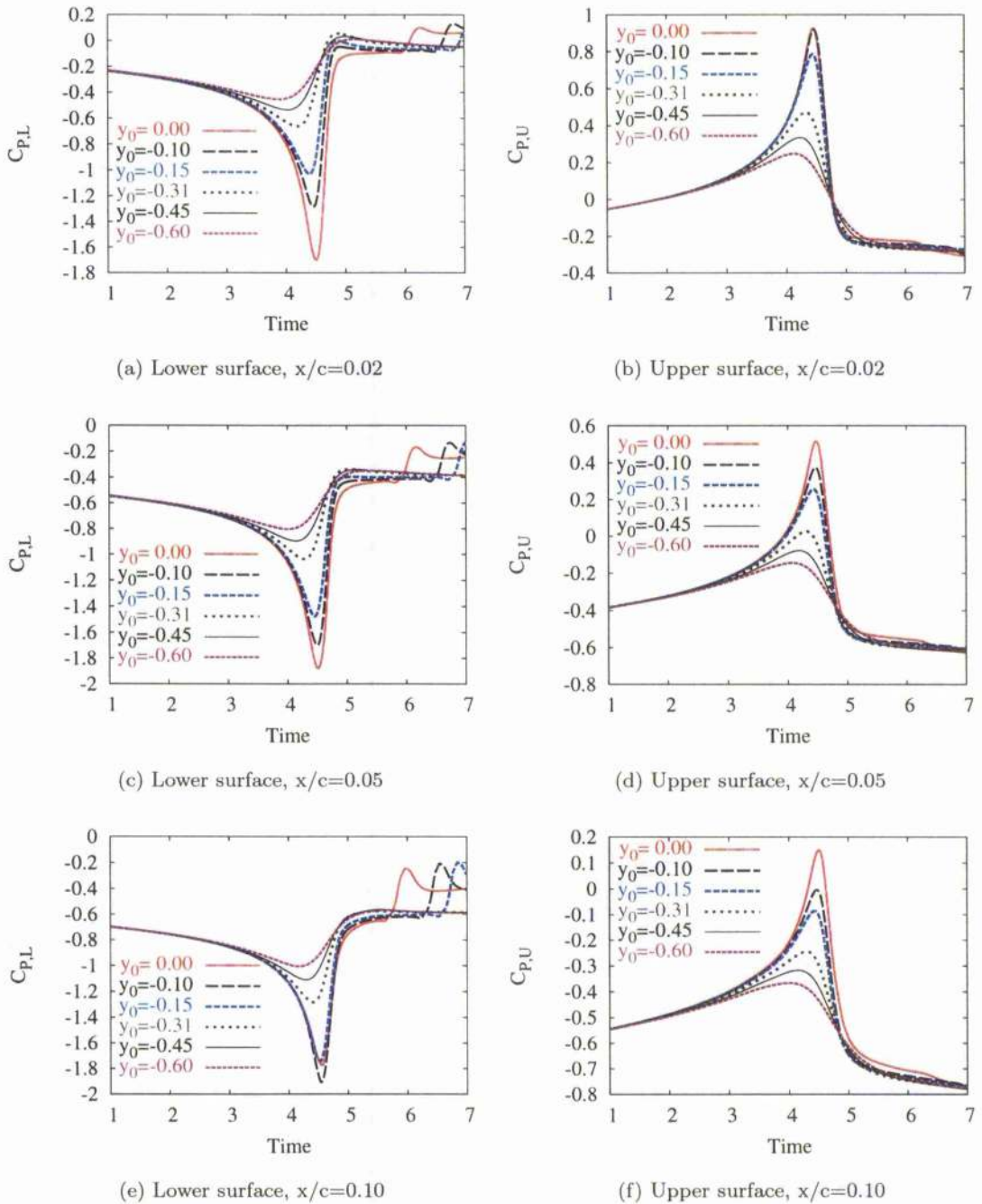


Figure 5.33: Time history of the surface pressure coefficient at different tap locations for different miss-distances. NACA-0012 aerofoil, inviscid calculations,  $M_\infty=0.73$ ,  $\hat{\Gamma} = -0.42$ ,  $R_c = 0.10$ .

The first BVI ( $M_\infty=0.57$ ) was considered in terms of flow visualisation since it is a more severe case. Figure 5.34 shows the pressure contours at the non-dimensionalised time 5.50. It has to be pointed out that a shock wave is generated and propagates upstream. This shock wave is also generated at an early stage and is stronger for small miss-distances.

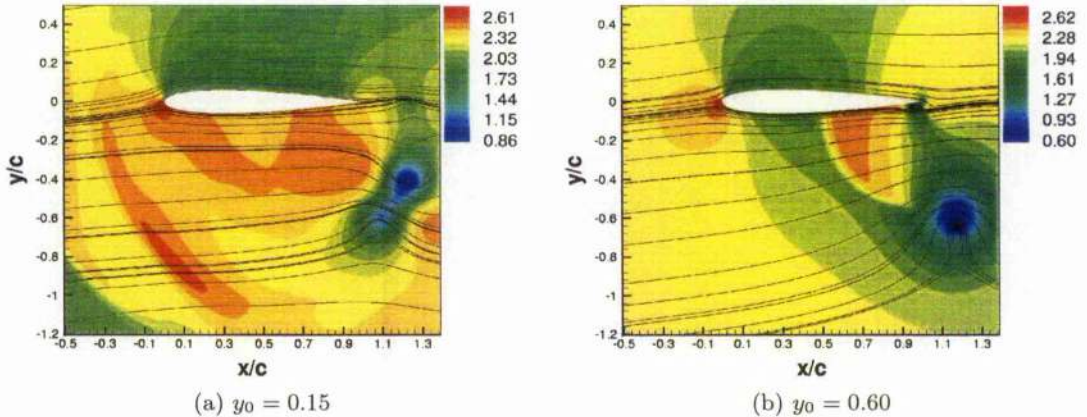
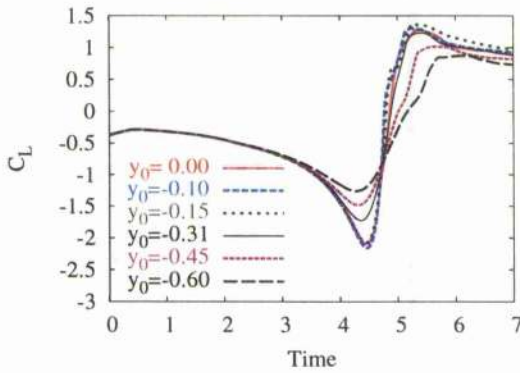
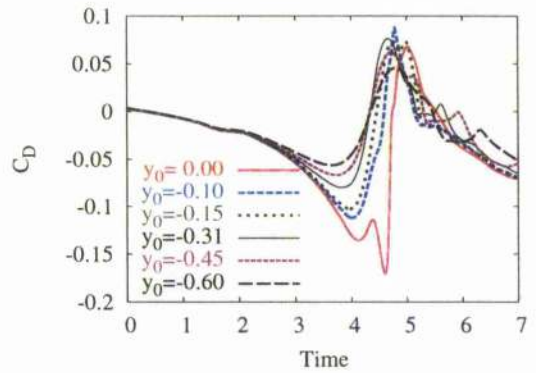


Figure 5.34: Pressure contours along with the velocity streamlines for miss-distances  $y_0 = 0.00$  at time  $t(U_\infty/c) = 5.50$ . Head-on BVI problem, NACA-0012 aerofoil, inviscid calculations,  $M_\infty=0.57$ ,  $\hat{\Gamma} = -1.8$ ,  $R_c = 0.10$ . Note that the pressure is non-dimensionalised against the dynamic pressure.

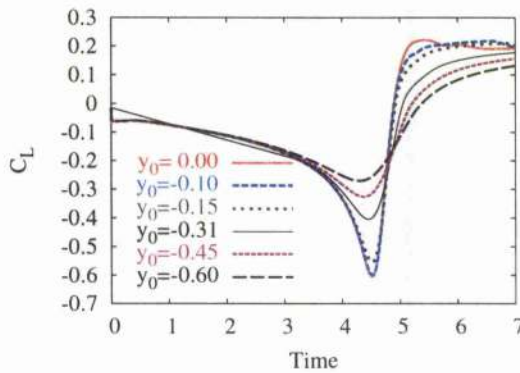
The lift and drag histories are given in Figure 5.35. It is noticeable that the lift history is very similar for the head-on BVI and the BVI case with a miss-distance of  $y_0 = -0.10$ . This verifies that the strongest interaction occurs for head-on BVI and for a miss-distance equal to the core radius. The miss-distance may be an interesting way of alleviating BVI as long as the distance between the vortex and the aerofoil is greater than twice the core radius size. The drag coefficient increases for both types of flow and becomes positive for the transonic flow at miss-distances  $y_0 \geq -0.15$ . This may be due to the vortex-shock interaction since the shock may distort due to the vortex or even gain some strength. It is believed [135] that the drag forces influence the shock motion, more especially their directivity. Although subcritical inviscid flow gives zero drag,  $C_d$  becomes different to zero because of the supersonic pockets.  $C_d$  is affected by the disturbance whereas  $C_l$  is not.



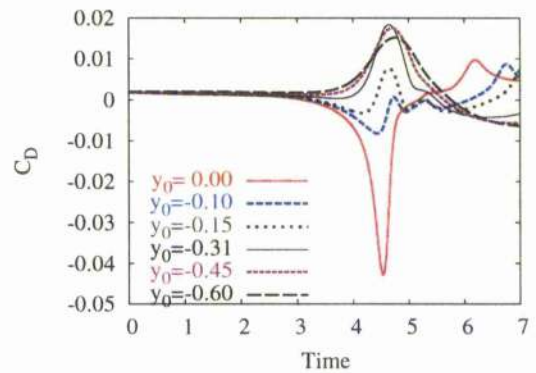
(a)  $M_\infty=0.57$



(b)  $M_\infty=0.57$



(c)  $M_\infty=0.73$



(d)  $M_\infty=0.73$

Figure 5.35: Lift and drag histories for vortex of various miss-distances at two flow conditions. NACA-0012 aerofoil, inviscid calculations.

The evolution of the density at the vortex core is given by Figure 5.36 for the two flow conditions. Again, the vortex characteristics are preserved till the vortex gets closer to the LE of the aerofoil. The vortex strength remains very similar during the time for large miss-distances.

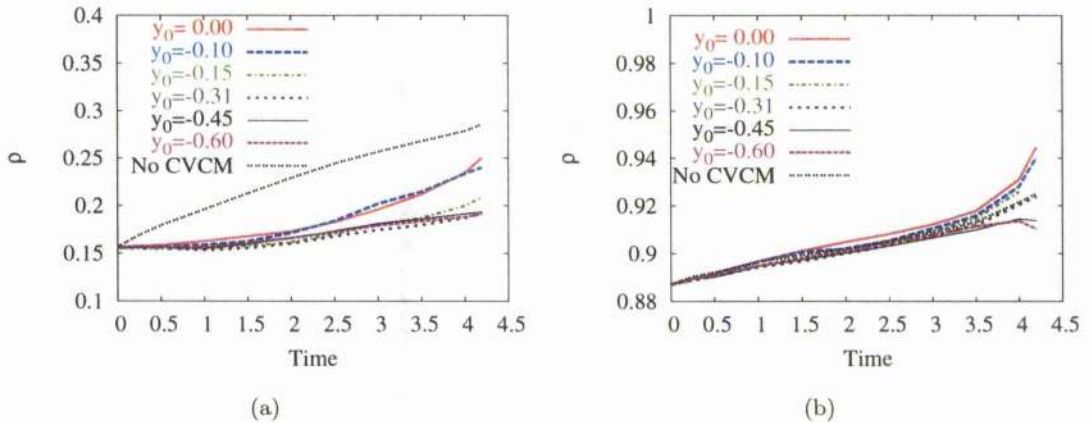


Figure 5.36: Time history of the density at the vortex core for different freestream Mach numbers. (a)  $M_\infty=0.57$ , (b)  $M_\infty=0.73$ . Head-on BVI problem, NACA-0012 aerofoil, inviscid calculations, various miss-distances.

### 5.3 Conclusions

The aerodynamics of various BVI cases have been investigated in terms of surface pressure coefficient, lift and drag histories. It has been shown that the BVI magnitude is related to the vortex-induced angle of attack and that BVI is primarily a LE phenomenon. The loads are affected by the primary BVI, its reflection at the TE of the aerofoil and by the presence of a supersonic pocket generated by the incoming vortex for some cases.

The aerofoil shape at transonic flow, the freestream Mach number and the vortex properties were found to effect the BVI loads. The lift and drag histories reveal that the freestream Mach number, the vortex strength and the miss-distance are important parameters. Different timings of occurrence of the loads were observed. This is influenced by the compressibility effects in front of the aerofoil, mainly by the freestream Mach number and the aerofoil shape.

## Chapter 6

# Parametric study of BVI aeroacoustics

This chapter presents the results of a parametric study revealing the characteristics of both the near-field and far-field acoustics of BVI. The study of the effects of the aerofoil, freestream Mach number and vortex properties on BVI is documented. The originality of this work is the use by the Ffowcs Williams-Hawkings (FW-H) method of the CFD results for the study of farfield noise, the use of the CVCM allowing the vortex to be preserved before its interaction with the blade.

### 6.1 Introduction

Inviscid and viscous calculations have been carried out and the obtained results highlight the differences in the acoustic behaviour of various aerofoil sections and of vortices with different properties. CFD is used to generate the unsteady pressure field around a blade during BVI and this is used as a source in a Computational AeroAcoustics (CAA) method. Once the acoustic waves are generated close to the surface of the blade, the FW-H method is used for assessing their effects on the far-field acoustics of the aircraft. First, the near-field acoustics are investigated using a computational grid sufficiently fine near the blade to capture the acoustic waves provided the vortex in the flow is well-preserved. Finally, the farfield noise is predicted using the FW-H method.

### 6.2 Parametric study of the nearfield noise

So far the aerodynamics of the interaction, as characterised by the surface pressures, have been considered. The differences in acoustics are now discussed for six different aerofoils. The acoustical pressure which corresponds to the pressure fluctuations from the undisturbed medium is studied. This is given by  $P'(\vec{x}, t) = p(\vec{x}, t) - \overline{p(\vec{x}, t)}$  where  $p(\vec{x}, t)$  comes from the CFD solution and  $\overline{p(\vec{x}, t)}$  is the time-averaged pressure.

The first parameter to be assessed for the calculations of the acoustic pressure was the vortex location. Although the pressure coefficient can be correctly predicted for the four different vortex locations (see Section 4.2.3), non physical waves appear. Indeed, during the first time steps, the difficulty of the solver in perfectly assimilating the vortex into the flow solution is manifested by the creation of spurious waves that start to propagate from the aerofoil. Acoustical analysis can be spoiled by the presence of these waves and the vortex must be introduced at least 4.5 chords ahead (see Figures 6.1-6.2).

### 6.2.1 Influence of the aerofoil shape

The high directivity of BVI noise is usually illustrated by two distinct radiation lobes. These two waves are called compressibility waves and are typical for high subsonic flow [8, 136]. They are denoted by A and B in Figure 6.3 and are driven by the compressibility effects at the LE of the aerofoil. The oncoming vortex decelerates the flow on the upper surface. The contrary happens on the lower surface. Then the stagnation point moves upwards to finally move towards the lower side once the vortex has passed the LE of the aerofoil, the vortex inducing an upwash effect. This generates an enlarged high-pressure region which propagates upstream like a steepening shock wave [119]. This wave is denoted by A. Furthermore, the acceleration of the flow generates a confined supersonic pocket on the lower side near the LE which detaches from the aerofoil after the passage of the vortex and the return of the stagnation point to its initial position. This leads to the generation of wave B. It has to be pointed out that the flow deflection at the LE of the aerofoil is actually large enough for the acoustic waves to detach from the aerofoil. Once the compressibility waves reach the trailing-edge (TE), two new waves start to form which propagate upstream contributing to the trailing-edge noise. It is believed [28] that the TE waves are a response to the compressibility waves. Other studies demonstrated that the sound is scattered by the TE of the aerofoil [19, 137], resulting in an increase of the acoustic energy. The TE waves [126] are marked as C and D. The acoustic behaviour of the different aerofoils in subsonic flow is similar in terms of acoustic pressure peak. The acoustic pressure of the main wave which propagates downstream is of the same level (about 3% of the freestream pressure) for the four symmetric aerofoils. However, the pressure difference encountered just after the vortex reaches the aerofoil and again as it reaches the TE seems to increase for the thinner aerofoils.

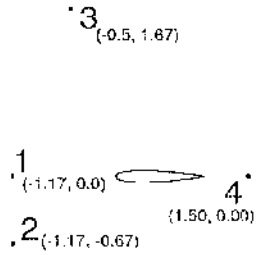


Figure 6.1: Schematic of the probe locations at which the acoustic pressure was calculated for the four initial vortex locations.

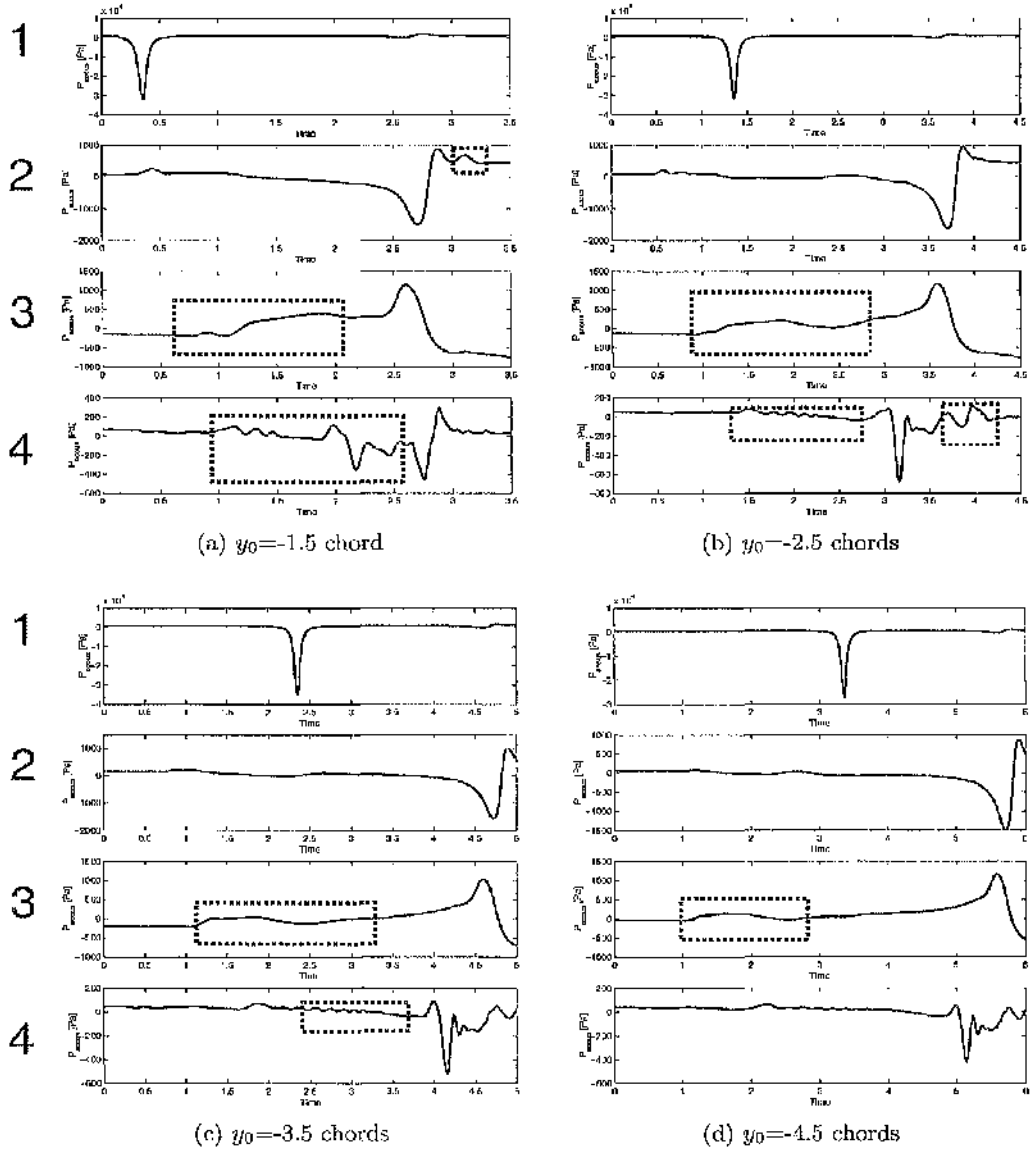


Figure 6.2: Influence of the vortex location on the acoustical signature. The history of the acoustic pressure is given at point 1, 2, 3 and 4. The dotted lines indicates the presence of spurious waves. NACA-0012 aerofoil, viscous calculations,  $M_\infty=0.5$ ,  $\hat{\Gamma} = -0.283$ ,  $R_\tau = 0.018$ .

**Influence of the aerofoil shape**

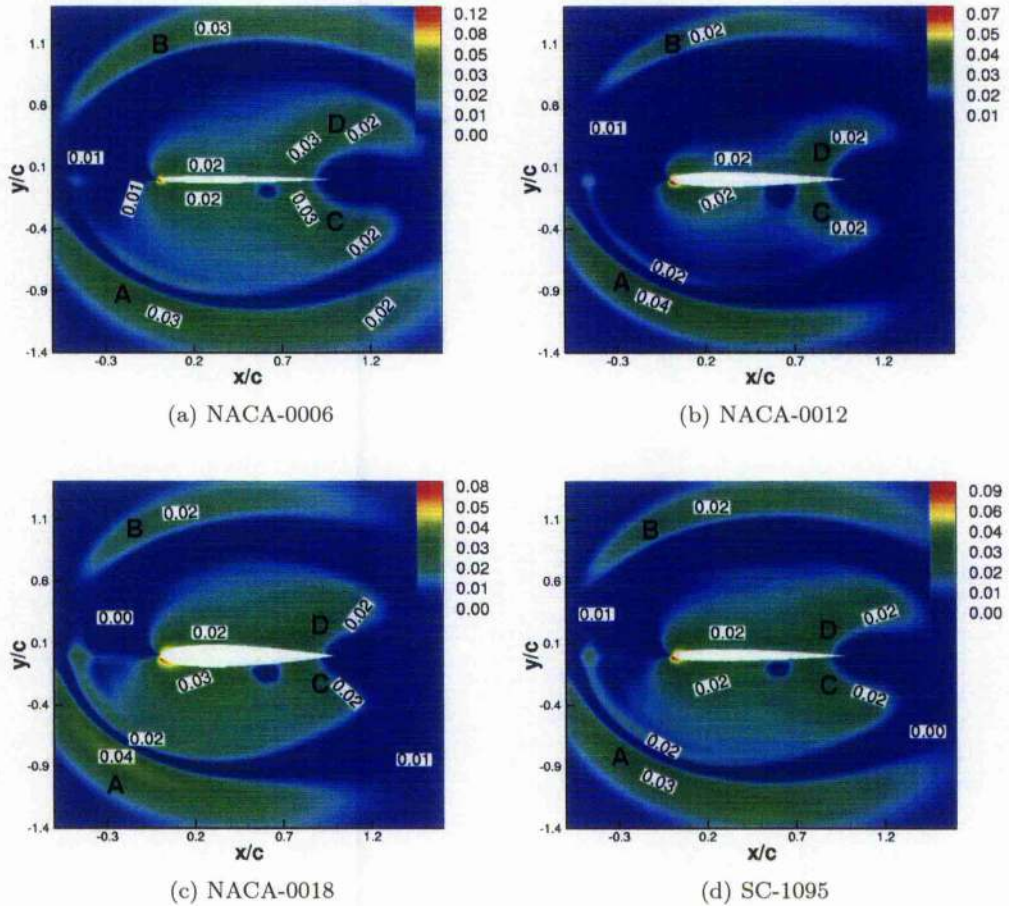


Figure 6.3: Absolute value of the acoustic pressure at  $t(U_\infty/c)=5.10$  and freestream Mach number of 0.5 for the NACA-0006, NACA-0012, NACA-0018, SC-1095. Head-on BVI, viscous calculations,  $\hat{\Gamma} = -0.283$ ,  $R_c = 0.018$ . Note that the acoustic pressure is non-dimensionalised against the freestream pressure.

It is interesting to note that a third acoustical wave is present just behind the compressibility wave denoted by A, which propagates below the aerofoil. Figure 6.4(a) shows the two regions of high and low pressure generated at the head of the aerofoil just after the interaction. These two regions which are at the origin of the compressibility waves detach from the aerofoil and propagate upstream. It appears, in this case, that a secondary vortex is generated on the lower side of the aerofoil after the interaction. When the stagnation point returns to its original position of equilibrium, the area of high pressure which characterises the stagnation point is indeed affected by the presence of the secondary vortex which is generated after the interaction on the lower side of the aerofoil. This results in the detachment of the high pressure region, leading to the generation of the third acoustic wave as depicted in Figure 6.4(b).

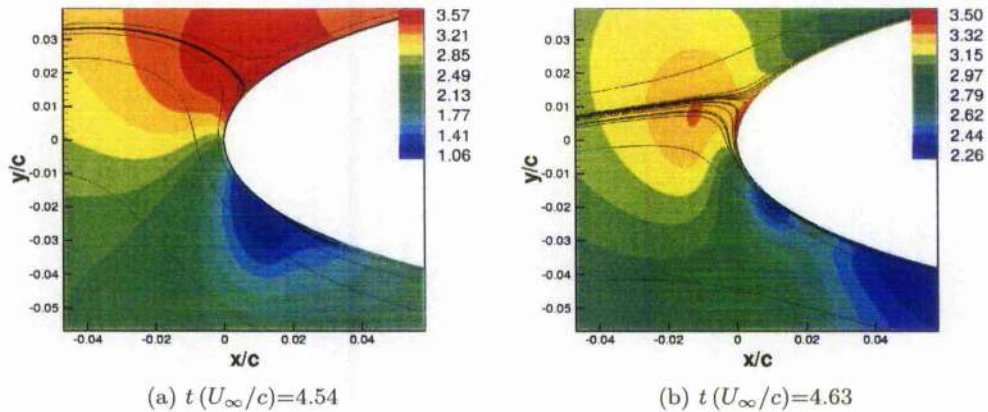


Figure 6.4: Pressure contours of the NACA-0012 aerofoil at two different instants. Head-on BVI case, NACA-0012 aerofoil, viscous calculations,  $M_\infty=0.5$ ,  $\hat{\Gamma} = -0.283$ ,  $R_c = 0.018$ . Note that the pressure is non-dimensionalised against the dynamic pressure.

The acoustic pressure was calculated at four probes marked as  $P_1$ ,  $P_2$ ,  $P_3$ ,  $P_4$  in Figure 6.5(a, c) to allow a comparison of the magnitude and the phase of all acoustic waves present in the flow. The calculation was repeated for all aerofoils and at two freestream Mach numbers. Figures 6.5(b) and 6.5(d) show the typical signature of the waves, in subsonic and transonic flow respectively. The compressibility waves pass through points  $P_1$  and  $P_2$  and look very similar in terms of magnitude and are opposite in phase. The same remark can be made for the TE waves at points  $P_3$  and  $P_4$ . It can be observed for the subsonic case that the TE waves also pass through points  $P_1$  and  $P_2$  at a later time.

Figures 6.6 and 6.8 establish a comparison between the compressibility waves propagating above and below the aerofoil at the two flow regimes whereas Figures 6.7 and 6.9 depict the TE waves propagating upstream. It has to be noticed that there are significant differences in the strength and direction of the acoustical waves between the two freestream Mach numbers. Despite the fact that at low Mach the passage of the vortex does not perturb the loads on the aerofoil as much as in transonic flow, the level of acoustic pressure at the transonic Mach number is higher than the subsonic case. The time history of the acoustic pressure  $P'(\vec{x}, t)$  through the point  $P_1$  at the high Mach number differs from the subsonic one in three aspects. First, the difference of the Sound Pressure Level ( $\text{SPL} = 20 \log_{10}(P'(\vec{x}, t)/2.10^{-5})$ ) for the transonic flow from the subsonic flow is about 10dB. Secondly, the acoustic waves are generated later after the interaction for the transonic case than for the subsonic one. Finally, the acoustic response of the aerofoils after the interaction varies with the location and strength of the shocks which are likely to make the BVI less impulsive as the vortex passes through them. The resulting directivity patterns of the radiated acoustic waves which is a result of the complex interaction between the vortex, the boundary layer and the shocks are all different. The acoustic waves seem to propagate more upstream and to be wider for thicker sections.

### Influence of the aerofoil shape

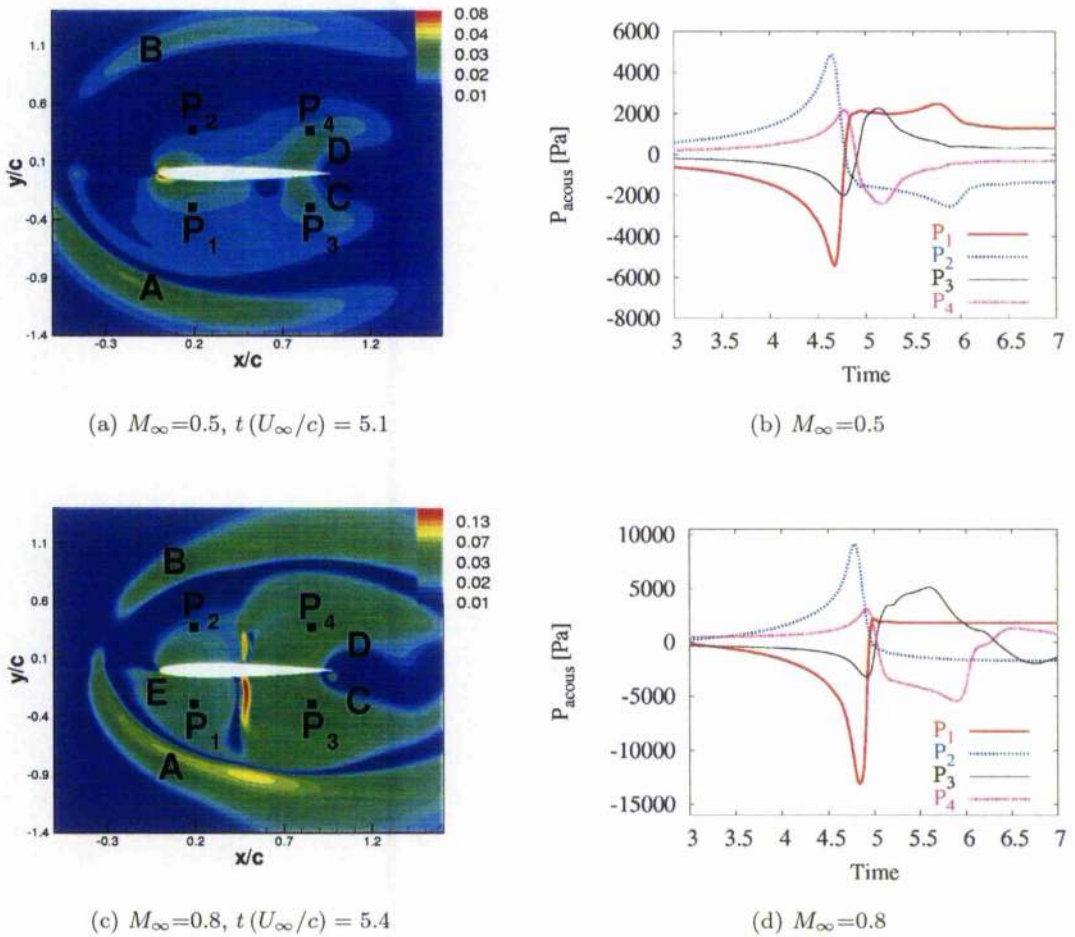


Figure 6.5: (a, c) Contours of the acoustic pressure along with the location of the four probes and (b, d) Time history of the acoustic pressure at the probes. The absolute value of the acoustic pressure is represented for the NACA-0012 at a freestream Mach number of 0.5 (a, b) and 0.8 (c, d). The scale is exponential. Note that the acoustic pressure is non-dimensionalised against the freestream pressure.

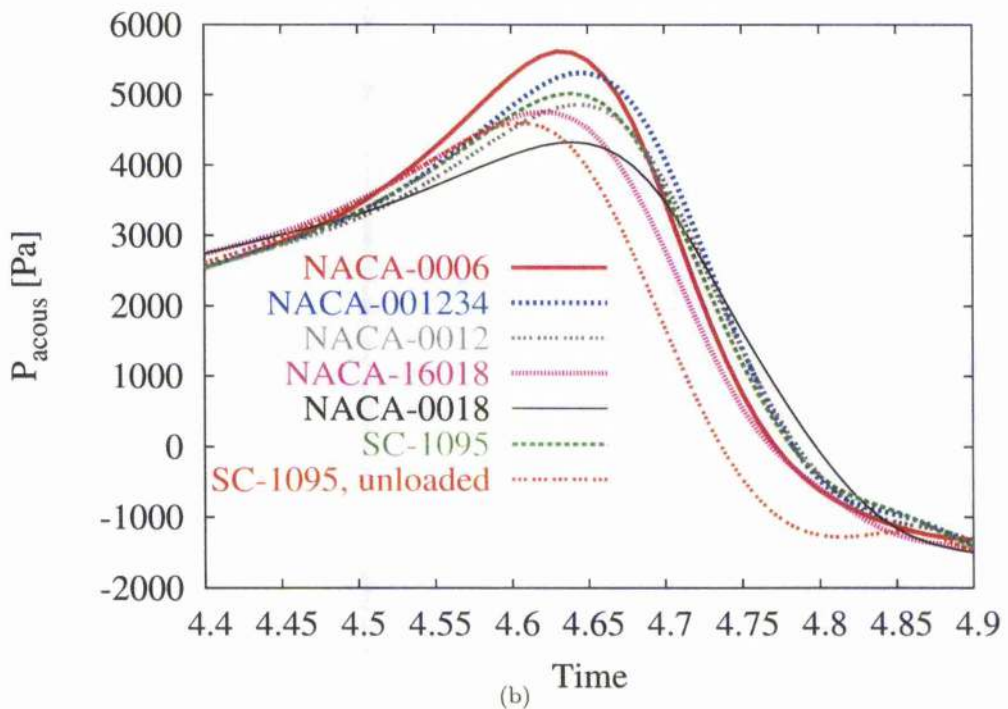
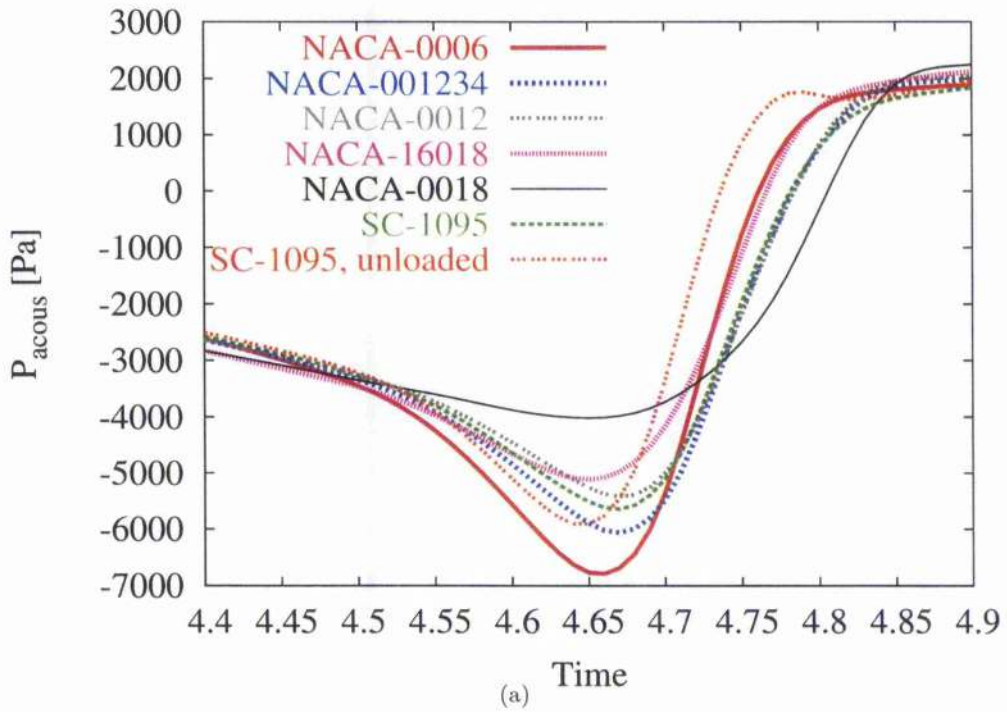


Figure 6.6: Acoustic pressure history for the aerofoils at points  $P_1$  (a) and  $P_2$  (b). Head-on BVI problem, viscous calculations,  $\hat{\Gamma} = -0.283$ ,  $R_c = 0.018$ ,  $M_\infty = 0.5$ . Note that the time is non-dimensionalised with  $U_\infty/c$  and that the abbreviation "unl." means unloaded.

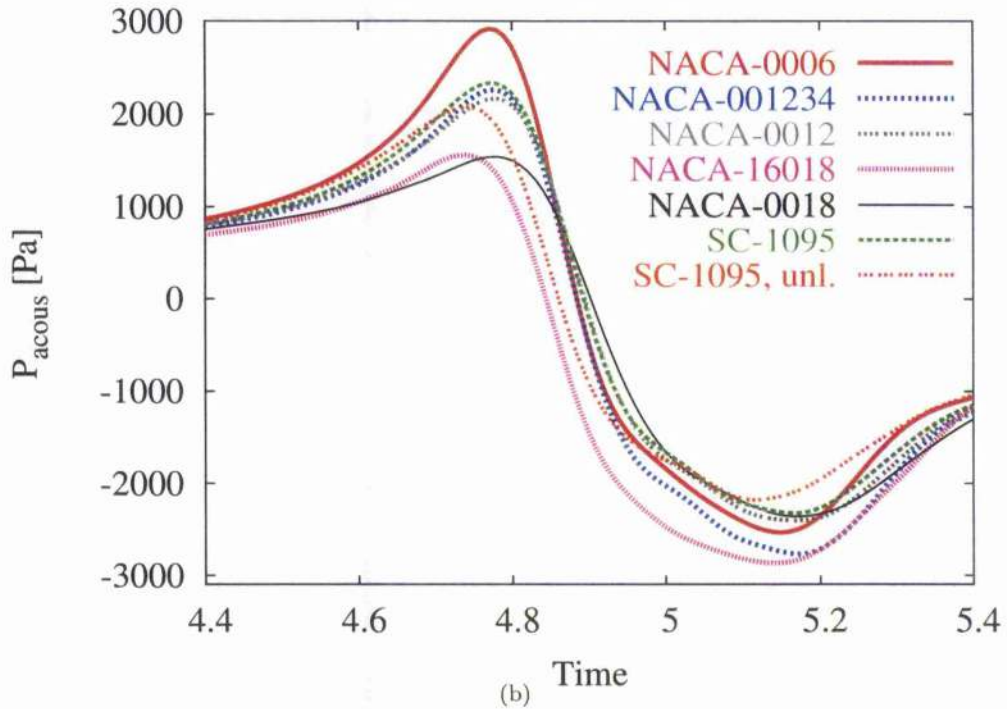
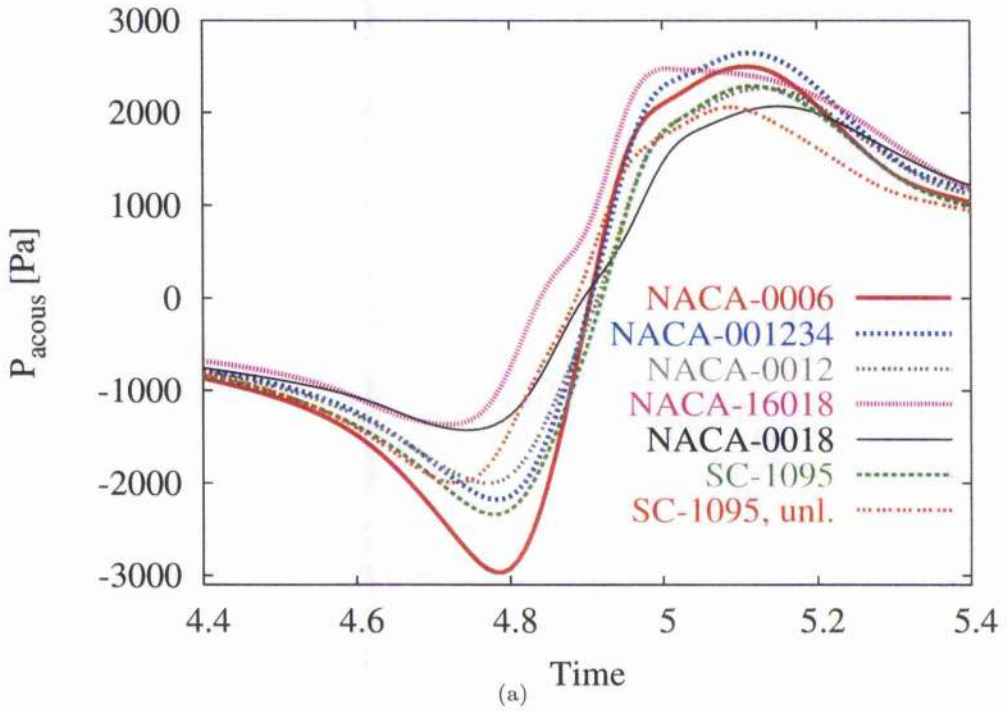


Figure 6.7: Acoustic pressure history for the aerofoils at points  $P_3$  (a) and  $P_4$  (b). Head-on BVI problem, viscous calculations,  $\hat{\Gamma} = -0.283$ ,  $R_c = 0.018$ ,  $M_\infty = 0.5$ . Note that the time is non-dimensionalised with  $U_\infty/c$  and that the abbreviation "unl." means unloaded.

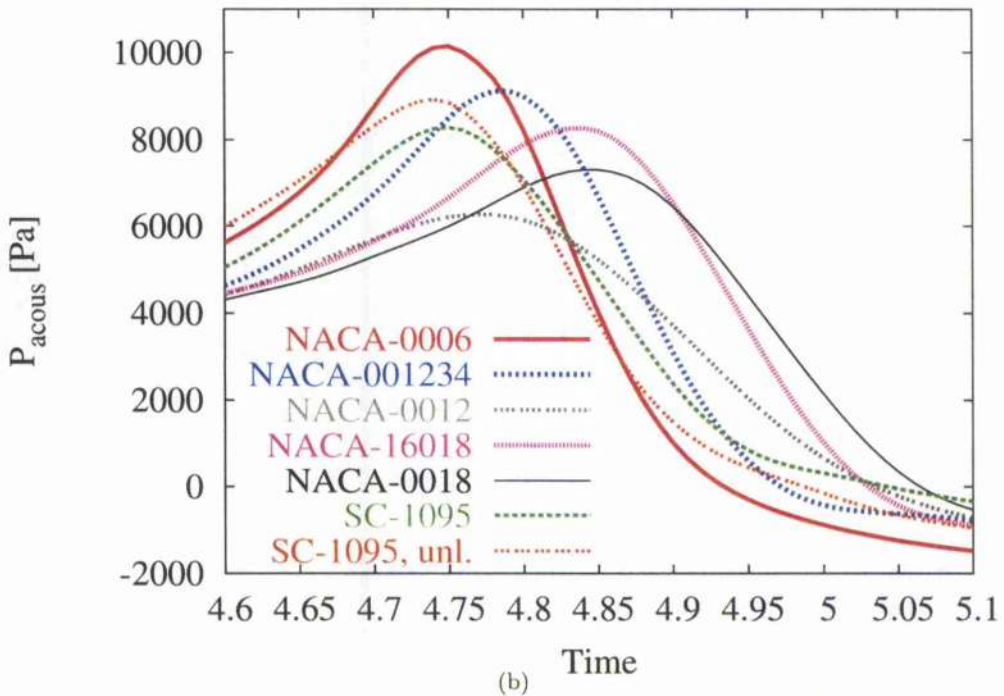
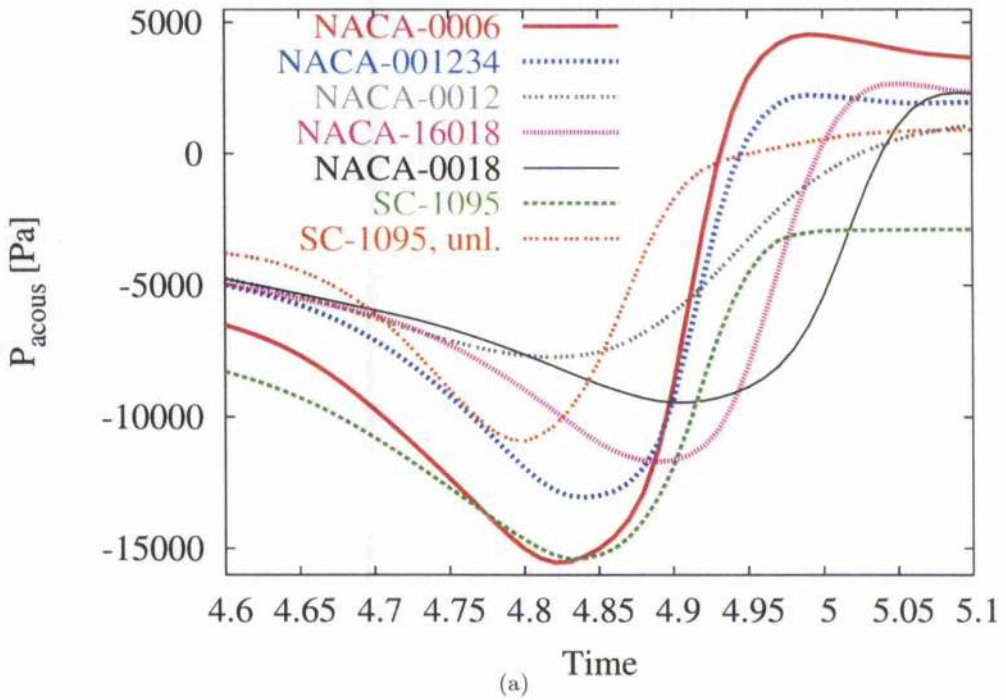


Figure 6.8: Acoustic pressure history for the aerofoils at points  $P_1$  (a) and  $P_2$  (b). Head-on BVI problem, viscous calculations,  $\hat{\Gamma} = -0.177$ ,  $R_c = 0.018$ ,  $M_\infty = 0.8$ . Note that the time is non-dimensionalised with  $U_\infty/c$  and that the abbreviation "unl." means unloaded.

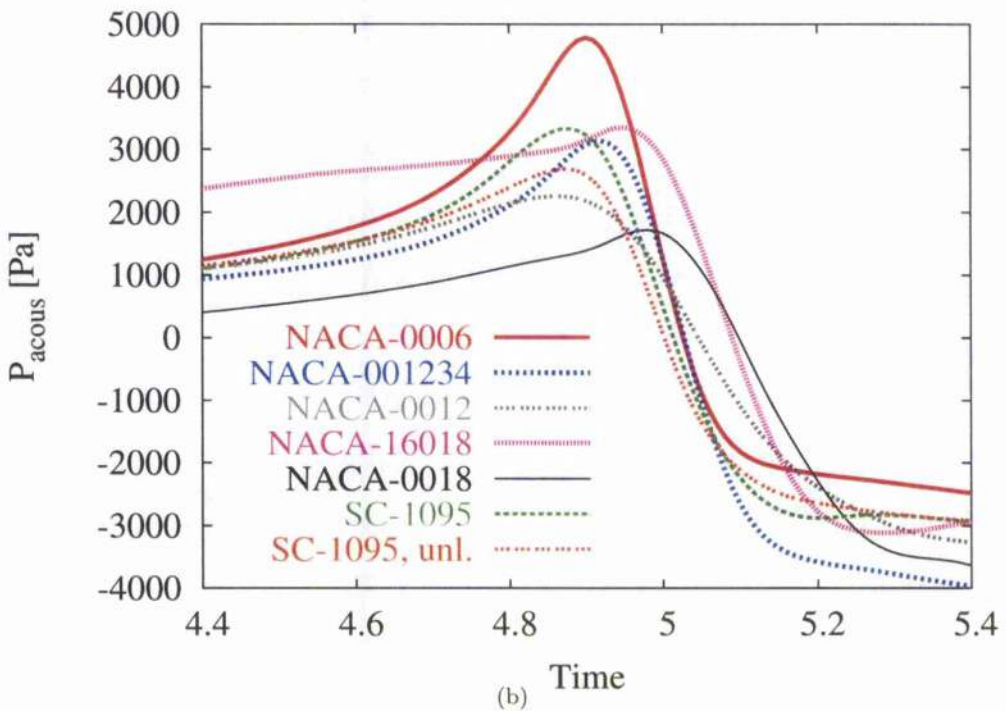
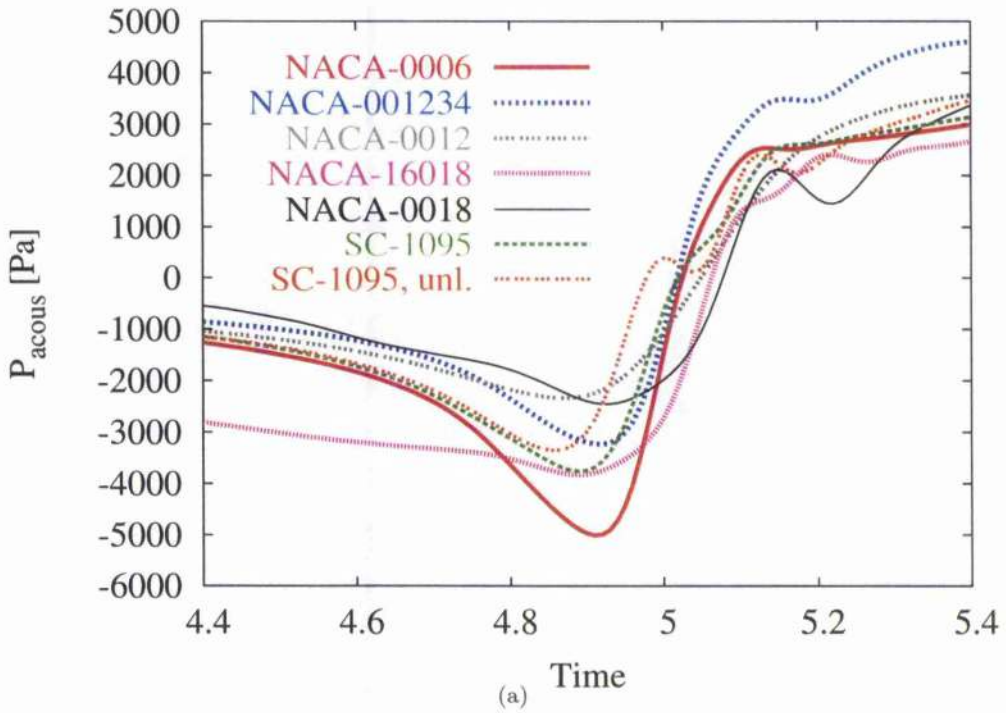


Figure 6.9: Acoustic pressure history for the aerofoils at points  $P_3$  (a) and  $P_4$  (b). Head-on BVI problem, viscous calculations,  $\hat{\Gamma} = -0.177$ ,  $R_c = 0.018$ ,  $M_\infty = 0.8$ . Note that the time is non-dimensionalised with  $U_\infty/c$  and that the abbreviation "unl." means unloaded.

An additional acoustic wave is present for transonic flow. This wave, called the transonic wave, emerges when a supersonic flow region is present on the shoulder of the aerofoil [119]. As explained in [18, 122], a shock wave appears after the vortex reaches the maximum thickness of the aerofoil beyond which the supersonic area collapses. Then the shock wave moves upstream leaving the LE in a downward direction while the stagnation point moves upwards. This results in the generation of a sound wave propagating upstream [136] which is marked by E.

The acoustic pressure and the isomach contours are given for the NACA-4 digit and Sikorsky aerofoils in Figures 6.10(a-b), 6.11(a-b), 6.12(a-b), 6.13(a-b) for the first time instant, and 6.10(c-d), 6.11(c-d), 6.12(c-d), 6.13(c-d) for the second. The compressibility wave propagates upstream at zero angle to the chord of the section while the transonic wave moves in a vertical downward direction [91]. As expected, the compressibility and trailing-edge wave are also present for the transonic flow case.

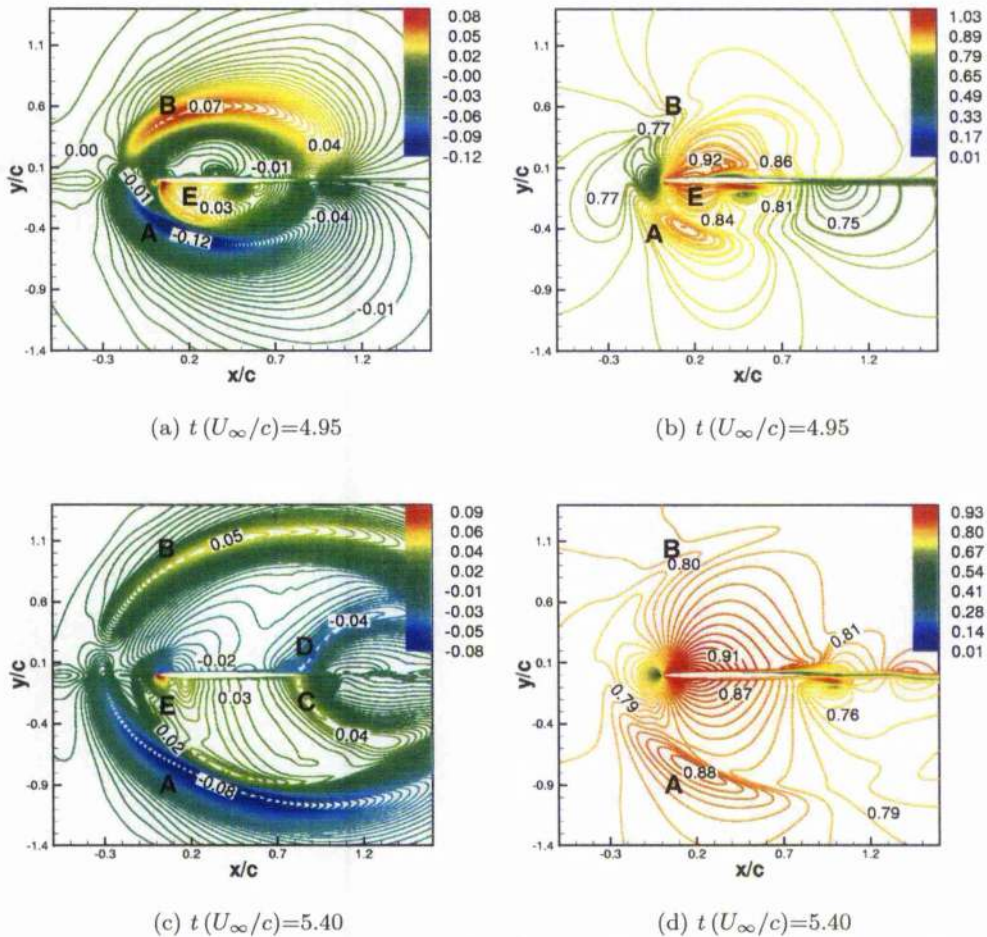


Figure 6.10: (a, c) Acoustic pressure and (b, d) isomachs at two different times. Head-on BVI problem, NACA-0006 aerofoil, viscous calculations,  $M_\infty=0.80$ ,  $\hat{\Gamma} = -0.177$ ,  $R_c = 0.018$ . Note that the acoustic pressure is non-dimensionalised against the freestream pressure.

**Influence of the aerofoil shape**

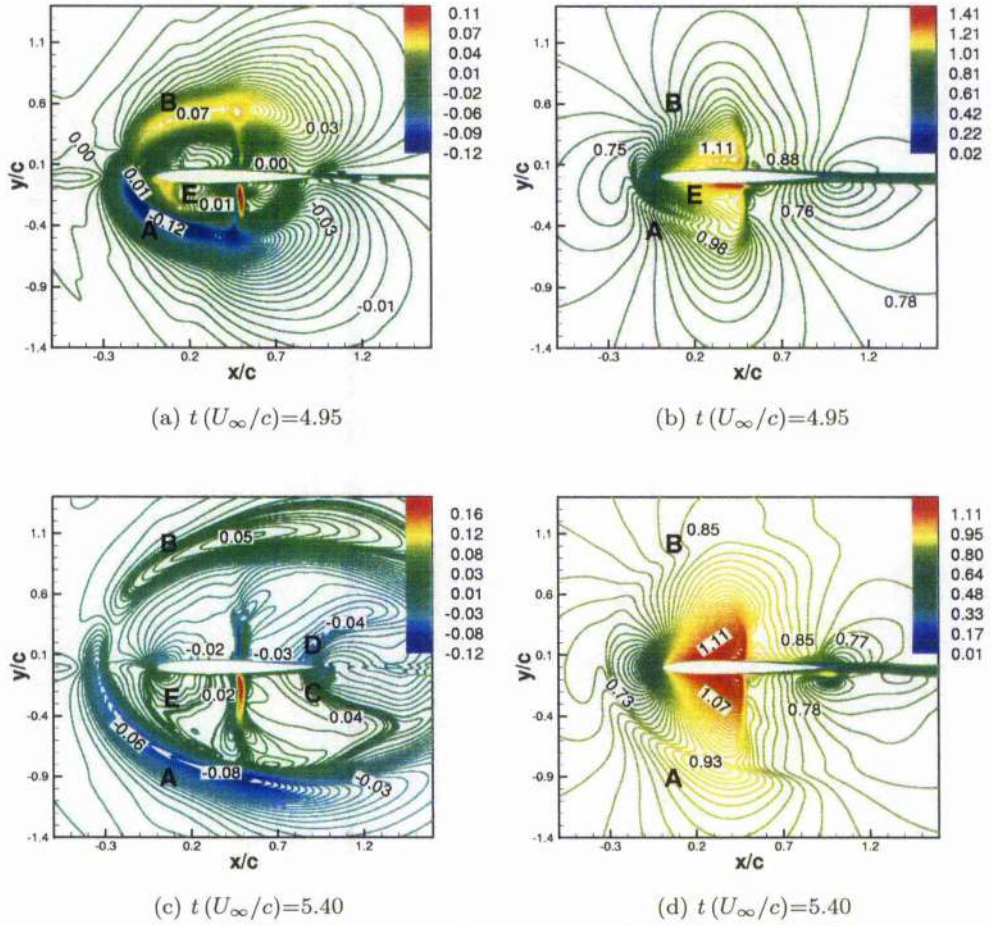


Figure 6.11: (a, c) Acoustic pressure and (b, d) isomachs at two different times. Head-on BVI problem, NACA-0012 aerofoil, viscous calculations,  $M_\infty = 0.80$ ,  $\hat{\Gamma} = -0.177$ ,  $R_c = 0.018$ . Note that the acoustic pressure is non-dimensionalised against the freestream pressure.

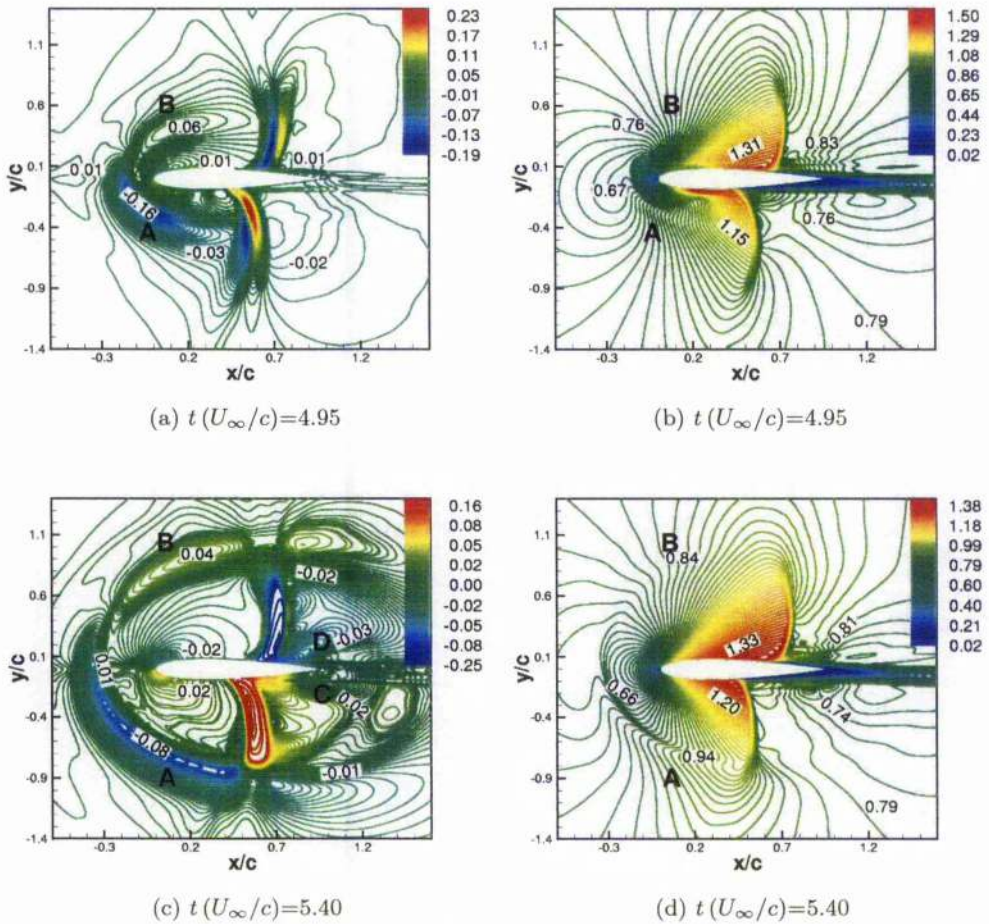


Figure 6.12: (a, c) Acoustic pressure and (b, d) isomachs at two different times. Head-on BVI problem, NACA-0018 aerofoil, viscous calculations,  $M_\infty=0.80$ ,  $\hat{\Gamma} = -0.177$ ,  $R_c = 0.018$ . Note that the acoustic pressure is non-dimensionalised against the freestream pressure.

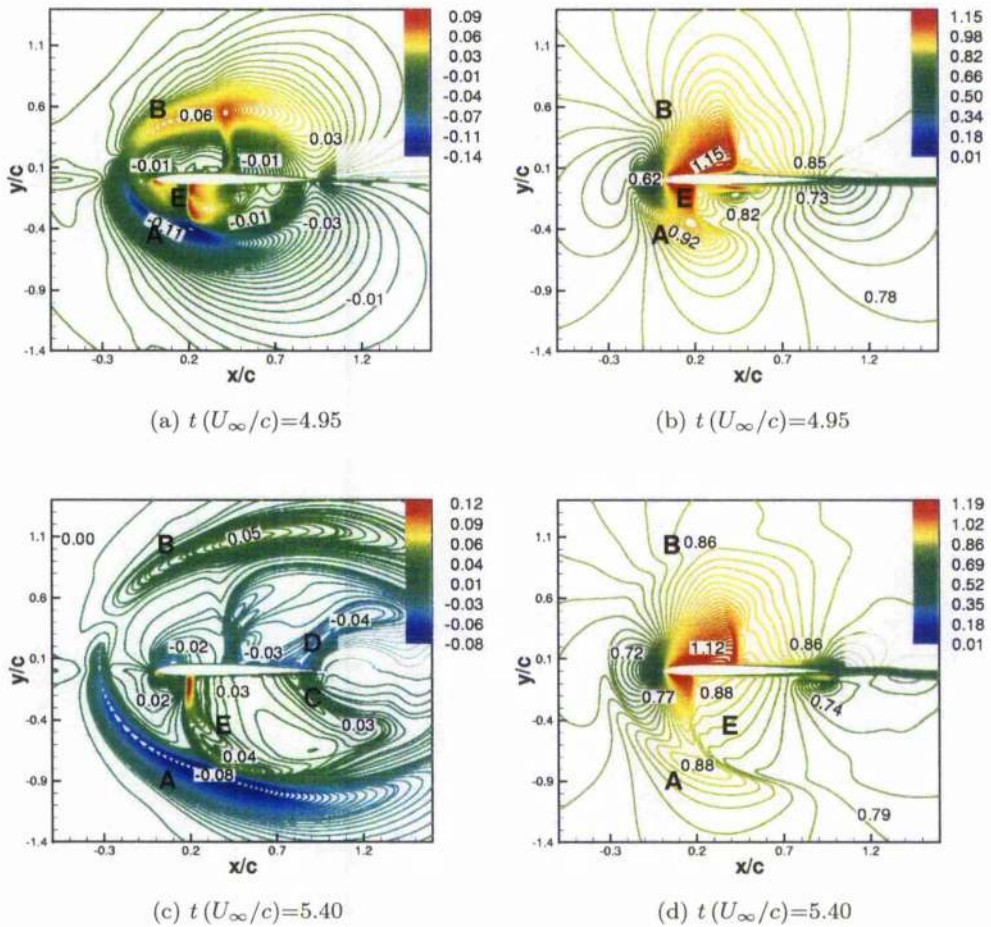


Figure 6.13: (a, c) Acoustic pressure and (b, d) isomachs at two different times. Head-on BVI problem, SC-1095 aerofoil, viscous calculations,  $M_\infty=0.80$ ,  $\Gamma = -0.177$ ,  $R_c = 0.018$ . Note that the acoustic pressure is non-dimensionalised against the freestream pressure.

The influence of the aerofoil shape in terms of thickness and LE radius was investigated for the compressibility and the TE waves, passing by points  $P_1$  and  $P_3$ , respectively. No specific relationship between the SPL and the aerofoil characteristics could be deduced with the NACA-4 digit aerofoils since the thickness and the LE radius both vary for these types of profiles. This is illustrated by Figure 6.14 which depicts the maximum SPL obtained at point  $P_1$ . Therefore, the NACA-001234 and the NACA-01618 have been used to determine the effects of the aerofoil parameters on the BVI noise magnitude. Note that the SPL is significantly larger than normally experienced in standard operating conditions, a head-on BVI representing the worst BVI scenario possible as mentioned by Malovrh *et al.* [22].

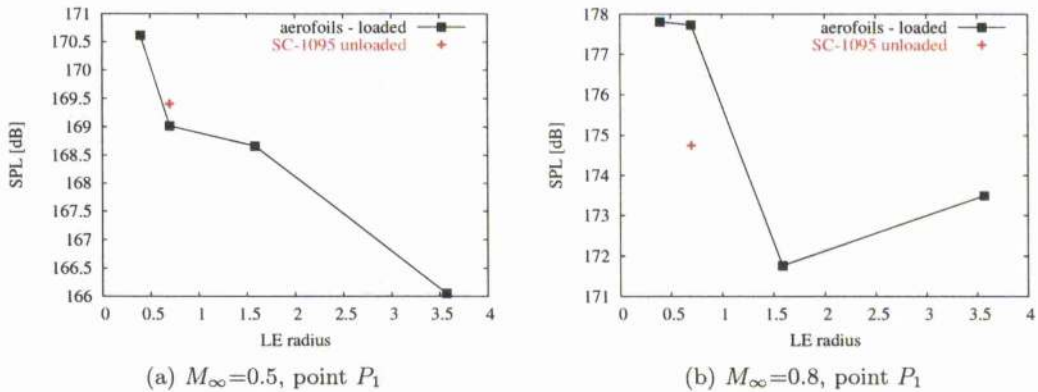


Figure 6.14: Acoustic pressure history for the aerofoils at points  $P_1$  (a-d) and  $P_3$  (e-h) for the NACA-0006, NACA-0012, NACA-0018 aerofoils and the loaded and unloaded SC-1095 aerofoil at two different freestream Mach numbers. Head-on BVI, viscous calculations,  $\hat{\Gamma} = -0.283$ ,  $R_c = 0.018$ . Note that the compressibility wave and the TE wave pass by points  $P_1$  and  $P_3$ , respectively.

Figure 6.15 gives the maximum SPL at points  $P_1$  and  $P_3$  for different thicknesses and LE radii. For the compressibility wave, in subsonic flow, it is observed that the BVI noise increases when the thickness and the LE radius decrease. Regarding the TE wave, the thickness is the more important parameter in subsonic flow and the magnitude of the TE wave actually increases for thinner aerofoils. It is important to note that the role played by the LE radius and the thickness is difficult to assess in the transonic regime due to the different locations of the shocks for the aerofoils. However, it is possible to notice for the transonic flow that the influence of the LE radius seems to increase for thinner aerofoils and that the TE wave is weaker when strong shocks are present.

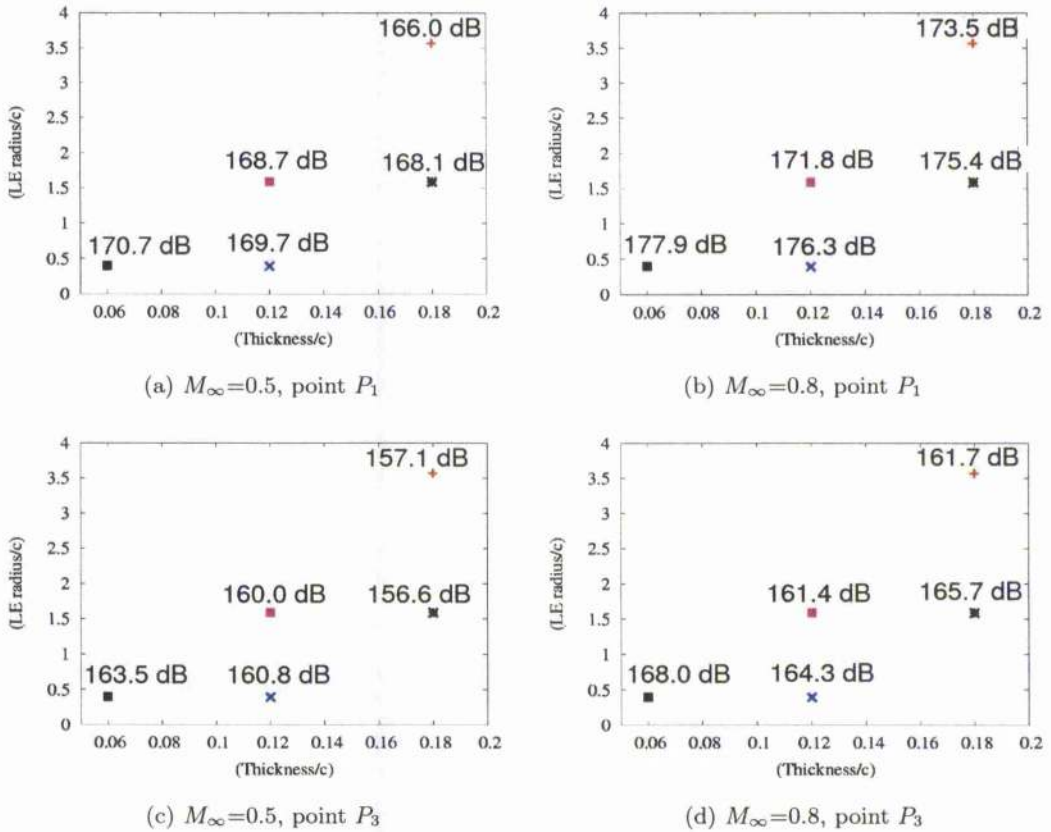


Figure 6.15: Maximum Sound Pressure Level for the aerofoils at points  $P_1$  (a-d) and  $P_3$  (e-h) at two different freestream Mach numbers. Head-on BVI problem, viscous calculations,  $M_\infty = 0.5$ ,  $\hat{\Gamma} = -0.283$  ( $M_\infty = 0.5$ ),  $R_c = 0.018$ .

It is also interesting to note that the BVI magnitude seems to be related to the initial loading of the aerofoil, as shown in Figure 6.16(a) by the different BVI peaks obtained on the loaded and unloaded SC-1095 cases. The acoustical signal at point  $P_1$  is similar in subsonic flow while the unloaded aerofoil seems to be less critical in terms of BVI noise magnitude in transonic flow. The acoustic pressure is also given at point  $P_2$  which is located above the aerofoil at the same distance from the aerofoil than point  $P_1$ . It can be seen in Figure 6.16(b) that the amplitude of the compressibility waves is very similar in the case of the unloaded aerofoil at points  $P_1$  and  $P_2$  for both types of flow. This is not the case for the loaded aerofoil, the compressibility wave passing by point  $P_1$  being the stronger in transonic flow. It is thought that the presence of asymmetrical shocks for the loaded aerofoil explains the observed difference in acoustics. Furthermore, the transonic wave E merges with the compressibility waves for the loaded aerofoil whereas the transonic wave is not present at point  $P_1$  for the unloaded aerofoil, explaining the difference of acoustic pressure levels. This is illustrated in Figure 6.17.

**Influence of the aerofoil shape**

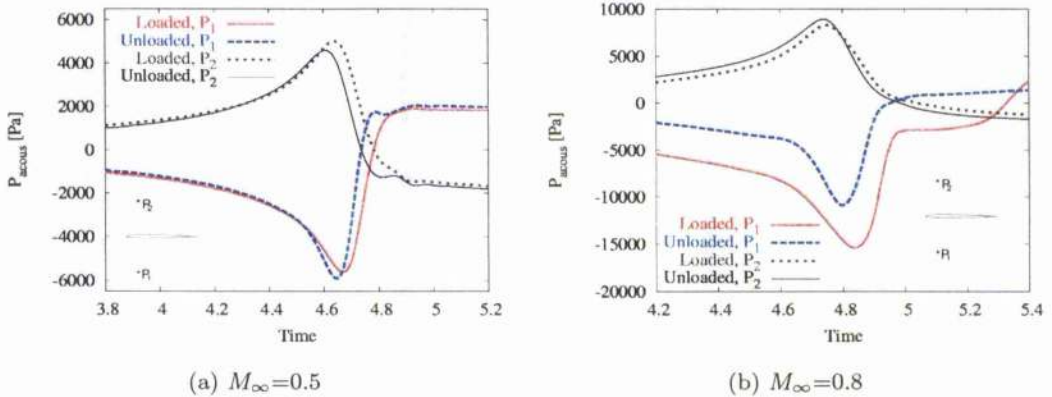


Figure 6.16: Acoustic pressure history at point  $P_1$  and  $P_2$  for the loaded and unloaded SC-1095 aerofoils at two freestream Mach numbers. Head-on BVI case,  $\hat{\Gamma} = -0.283$  ( $M_\infty = 0.5$ ),  $R_c = 0.018$ . Note that point  $P_2$  is at the same distance from the aerofoil than point  $P_1$ .

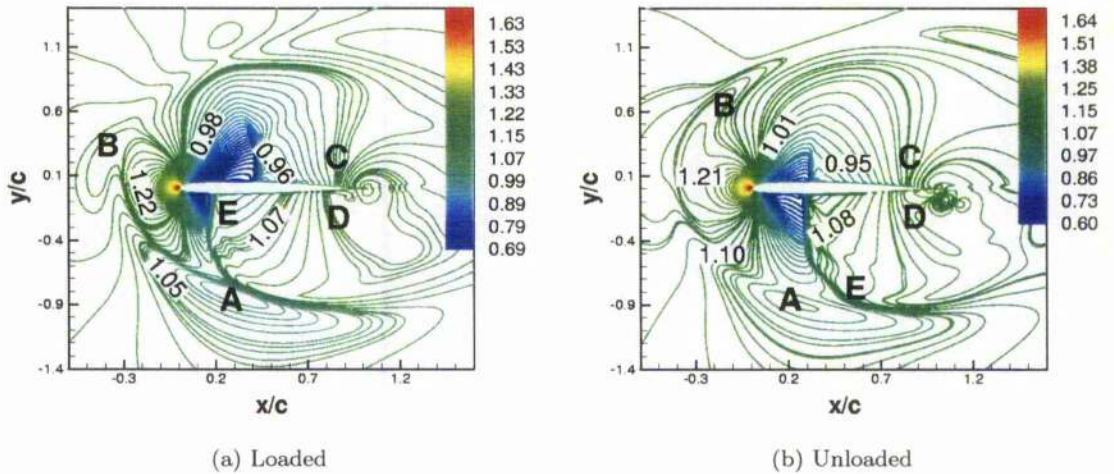


Figure 6.17: Isobars ( $2p/q_\infty$ ) at  $t(U_\infty/c)=5.10$  for (a) the loaded and (b) unloaded SC-1095 aerofoils in transonic flow. Head-on BVI case, viscous calculations,  $M_\infty=0.8$ ,  $\hat{\Gamma} = -0.177$ ,  $R_c = 0.018$ .

6.2.2 Influence of the freestream Mach number

Inviscid calculations have been carried out for different freestream Mach numbers. The isobars ( $2p/q_\infty$ ) and the acoustic pressure are given in Figures 6.18(a-b) and (c-d), respectively. It can be observed that the compressibility waves and the TE waves are present for all types of flow. It can be also deduced that the BVI noise peak increases with the Mach number, which is expected due to the expression of the lift forces  $F_L$  which is proportional to  $\frac{1}{2}\rho_\infty C_L U_\infty^2$ . This is confirmed by Figure 6.19 which shows the acoustic pressure at point P. Although the isobars indicates the presence of the acoustic waves, the directivity patterns of the waves can be distinguished more precisely when the acoustic pressure is plotted.

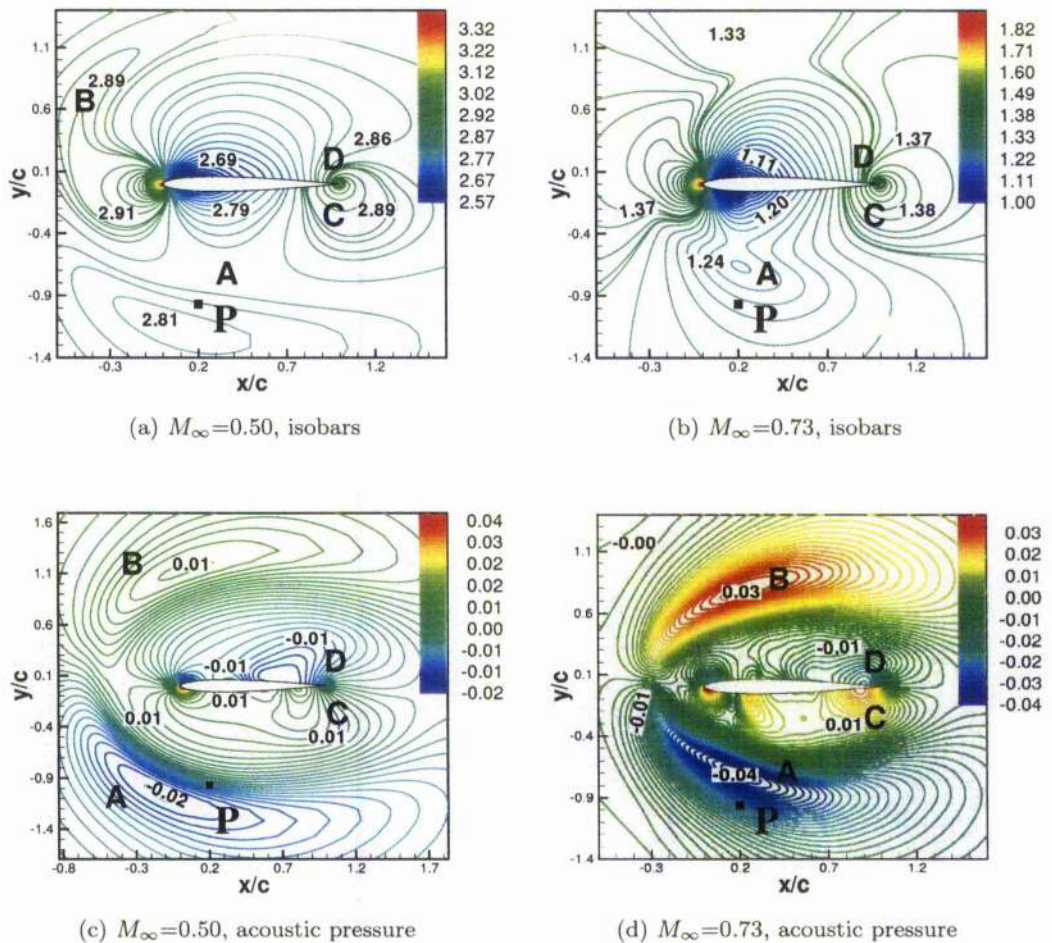


Figure 6.18: (a-b) Isobars ( $2p/q_\infty$ ) and (c-d) isolines of the acoustic pressure at  $t(U_\infty/c)=5.10$  for head-on BVI at different freestream Mach numbers. NACA-0012 aerofoil, inviscid calculations,  $\hat{\Gamma} = -0.283$  ( $M_\infty=0.5$ ),  $R_c = 0.10$ . Note that the acoustic pressure is non-dimensionalised against the freestream pressure.

Influence of the freestream Mach number

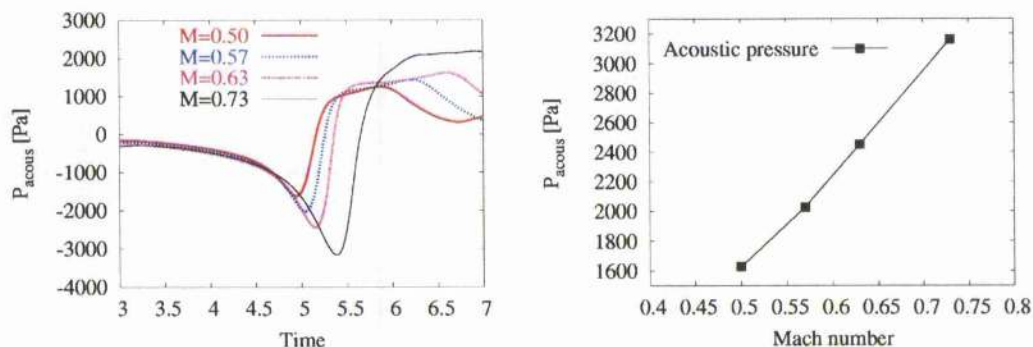


Figure 6.19: (a) Acoustic pressure history and (b) absolute value of the maximum acoustic pressure at point P for head-on BVI at different freestream Mach numbers. NACA-0012 aerofoil, inviscid calculations,  $\hat{\Gamma} = -0.283$  ( $M_\infty=0.5$ ),  $R_c = 0.10$ .

### 6.2.3 Influence of the vortex properties

#### Vortex core radius

Two types of BVI with various core radii are investigated. The first flow is a head-on BVI whereas the second one is a miss-distance BVI case ( $y_0 = -0.15$ ). For both BVI flows, the freestream Mach number was set to 0.73 with a vortex of non-dimensionalised strength -0.42. The values of the different core radii were 0.4, 0.06, 0.10 and 0.15.

The nearfield acoustics are now discussed. The isobars are given in Figure 6.20. For the head-on BVI, the acoustic waves are weaker and wider for vortices of initially larger core radius. For a given miss-distance, the vortex core size also influences the magnitude of the pressure wave with the stronger BVI obtained for the smaller radius. This is expected since the magnitude of the maximum tangential velocity is a function of the core radius to miss-distance ratio.

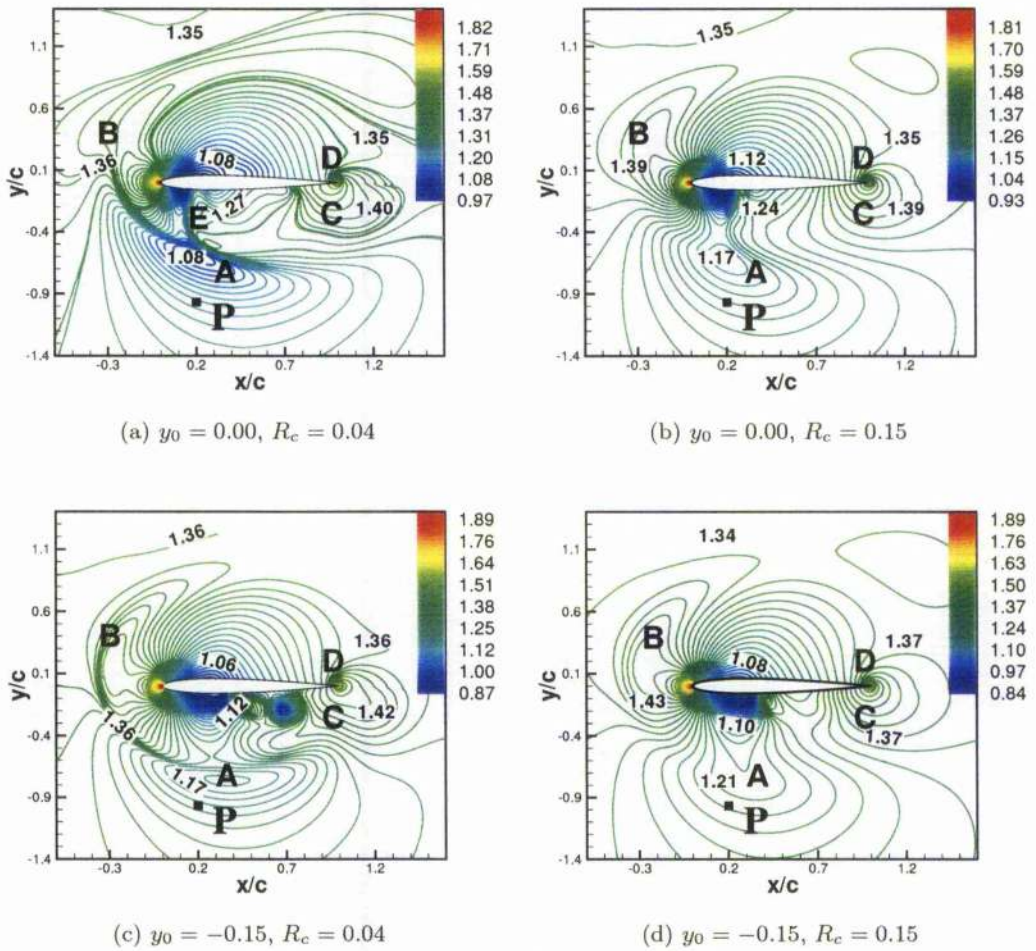


Figure 6.20: Isobars ( $2p/q_\infty$ ) at  $t(U_\infty/c)=5.10$  for different core radii. NACA-0012 aerofoil, inviscid calculations. (a-b)  $y_0 = 0.00$ , (c-d)  $y_0 = -0.15$ .  $M_\infty=0.73$ ,  $\hat{\Gamma} = -0.42$ .

Regarding the acoustic signal passing through point P, the first BVI peak is due to the compressibility wave noted A for the head-on and miss-distance BVI cases. This is illustrated by Figure 6.21. However, the time history of the acoustic pressure differs afterwards. This is due to the difference of location and strength of the transonic wave noted E between the head-on and miss-distance BVI cases as shown in Figure 6.21(a, c). Indeed, for the first BVI, the acoustic pressure starts to decrease after the compressibility waves passes by point P whereas a positive peak of pressure fluctuations which stems from the passage of the strong transonic wave occurs for the second type of BVI.

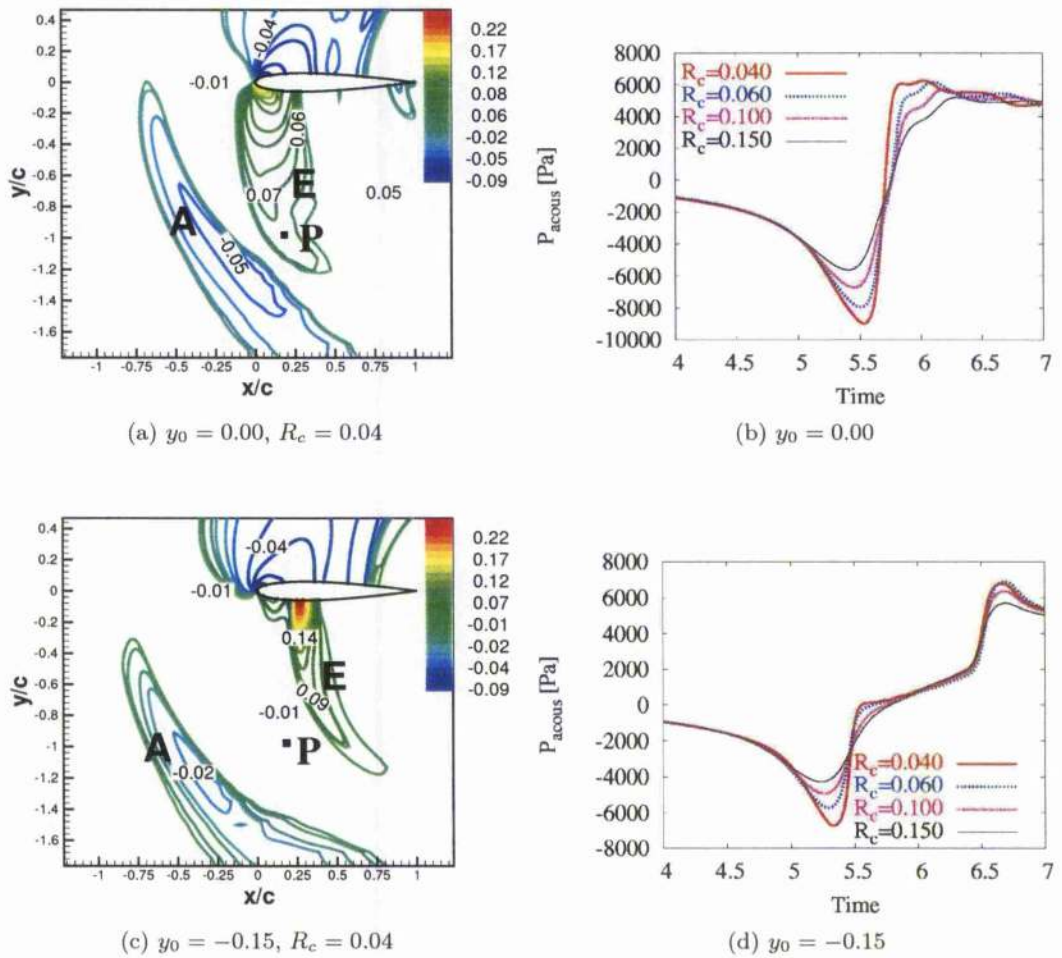


Figure 6.21: (a, c) Isolines of the acoustic pressure at  $t(U_\infty/c)=6.0$  for two miss-distance BVI cases. (b, d) Acoustic pressure history at point P. NACA-0012 aerofoil, inviscid calculations,  $M_\infty=0.73$ ,  $\hat{\Gamma} = -0.42$ . Note that the acoustic pressure is non-dimensionalised against the freestream pressure for the isolines.

### Vortex strength

The freestream Mach number was fixed to 0.57 and the non-dimensionalised core radius to 0.1 for the head-on BVI. Contours of isobars ( $2p/q_\infty$ ) are given in Figures 6.22(a-d). The work of Hardin and Lamkin [31] shows that the acoustic pressure is a linear function of the strength of the incoming vortex. This is verified for the compressibility waves for which amplitude increases with the vortex strength. However, it can be noticed that the direction of propagation is modified with the increase of the vortex strength. This is caused by the presence of a supersonic pocket generated on the lower side of the aerofoil. Indeed, the supersonic pocket gets so strong by the passage of the vortex that the supersonic domain starts to move downstream. This leads to a change of the directivity patterns of the compressibility wave noted A. Thus, the acoustical wave almost propagates in direction normal to the aerofoil chord. Once the vortex has

### Influence of the vortex properties

overtaken the supersonic pocket, this latter changes direction and weakens to finally radiate as a shock wave at the LE of the aerofoil [138]. Note that the directivity patterns of the transonic wave remains similar, which confirms the observations of Ballmann and Körber [122].

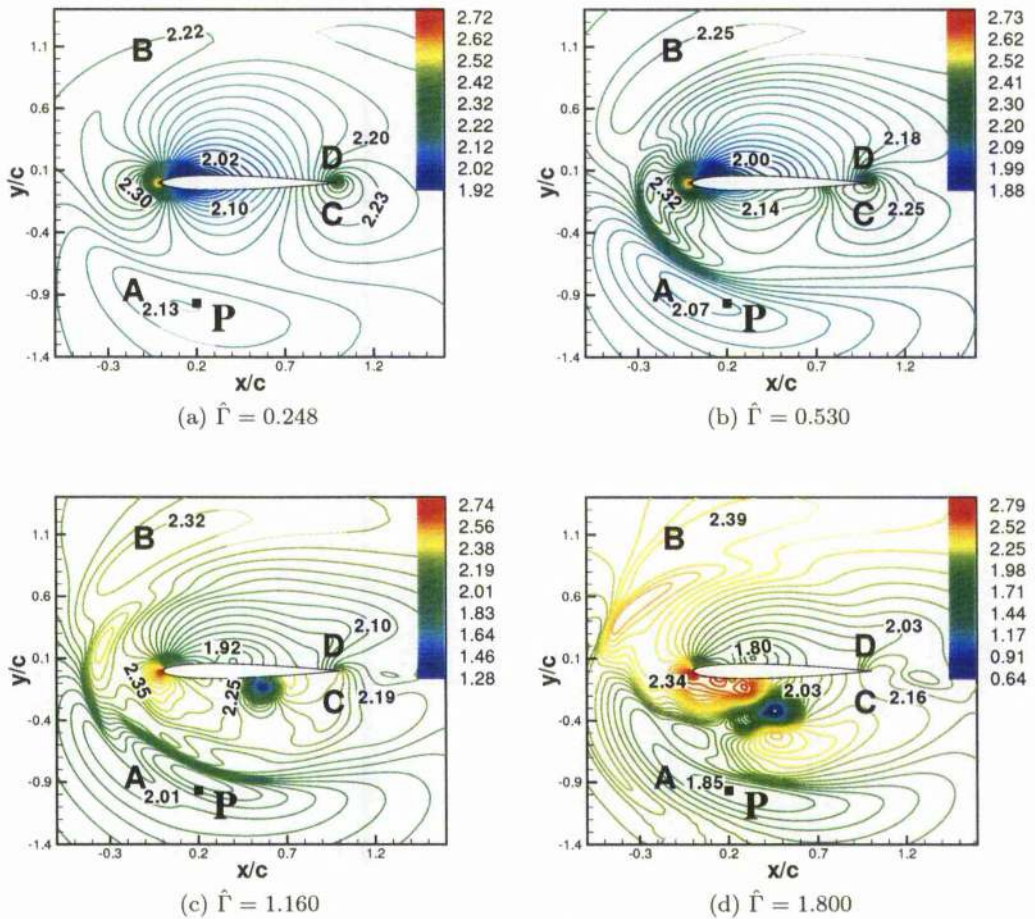


Figure 6.22: Isobars ( $2p/q_\infty$ ) at  $t(U_\infty/c)=5.10$ . Head-on BVI problem, NACA-0012 aerofoil, inviscid calculations.  $M_\infty=0.57$ ,  $R_c = 0.10$ .

The acoustic pressure at the non-dimensionalised time 5.1 and the time history of the acoustic pressure at point P are shown in Figure 6.23. It is apparent that the magnitude of the BVI noise is related to the vortex strength. The transonic wave is clearly observable for  $\hat{\Gamma} > 0.283$ , this is manifested as a positive pressure peak after the main interaction. The fact that the magnitude of the transonic wave increases with the vortex strength suggests that the supersonic pocket which is at the origin of the generation of the transonic shock wave depends on the magnitude of the velocity induced by the vortex, i.e. the vortex strength. Note that the difference of SPL before the interaction indicates that the vortex is a monopole source whose intensity varies linearly with strength as depicted in Figure 6.24. It was verified that the SPL was a function of the square of the vortex strength.

**Influence of the vortex properties**

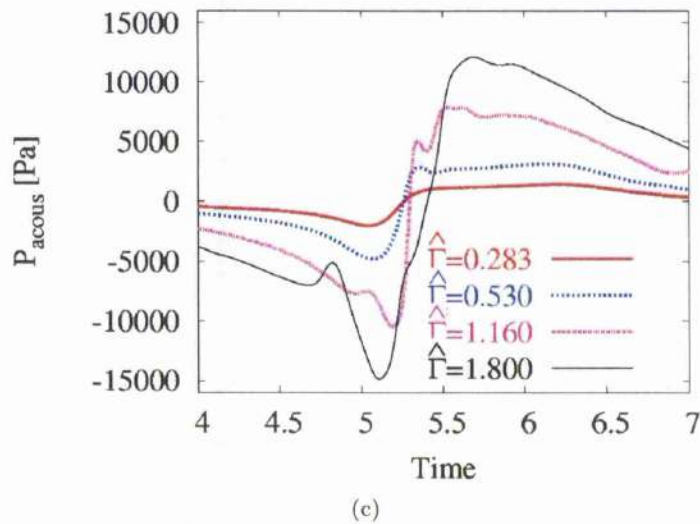
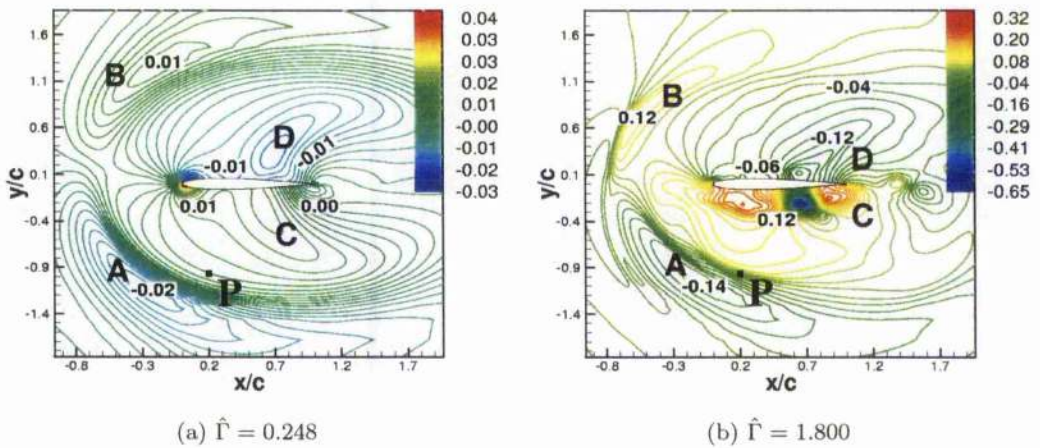


Figure 6.23: (a-b) Isolines of the acoustic pressure at  $t(U_\infty/c)=5.40$  for a vortices of different strengths. (c) Acoustic pressure history at point P. Head-on BVI problem, NACA-0012 aerofoil, inviscid calculations.  $M_\infty=0.57$ ,  $R_c = 0.10$ . Note that the acoustic pressure is non-dimensionalised against the freestream pressure for the isolines.

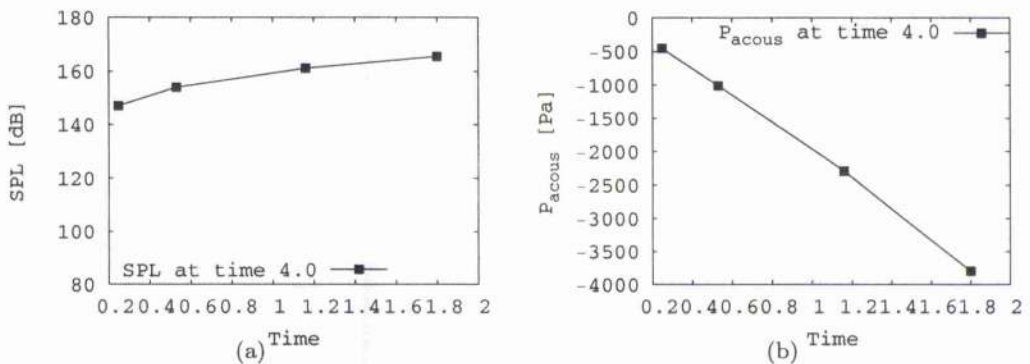


Figure 6.24: (a) Sound Pressure Level and (b) acoustic pressure at point P for vortices of different strengths at time  $t(U_\infty/c)=4.00$ .

**Influence of the vortex properties**

Miss-distance

Two BVI cases were investigated. The non-dimensionalised vortex strength was set to  $-1.80$  and  $-0.42$  for the first and second case, respectively. The non-dimensionalised core radius was fixed to  $0.1$  for both cases. Figures 6.25 and 6.26 show the contours for the BVI problems. Both compressibility waves and transonic waves appear for the two types of flows. The acoustical waves noted A and B weaken with the miss-distance for both types of flow when the miss-distance is greater than the core radius. Indeed, the strongest BVI is expected for a miss-distance equal to the core radius. The vortex-induced downwash also effects the aerofoil at an early time for miss-distance BVI cases. As a result, the acoustical wave generated by miss-distance BVI starts to propagate before the one for head-on BVI.

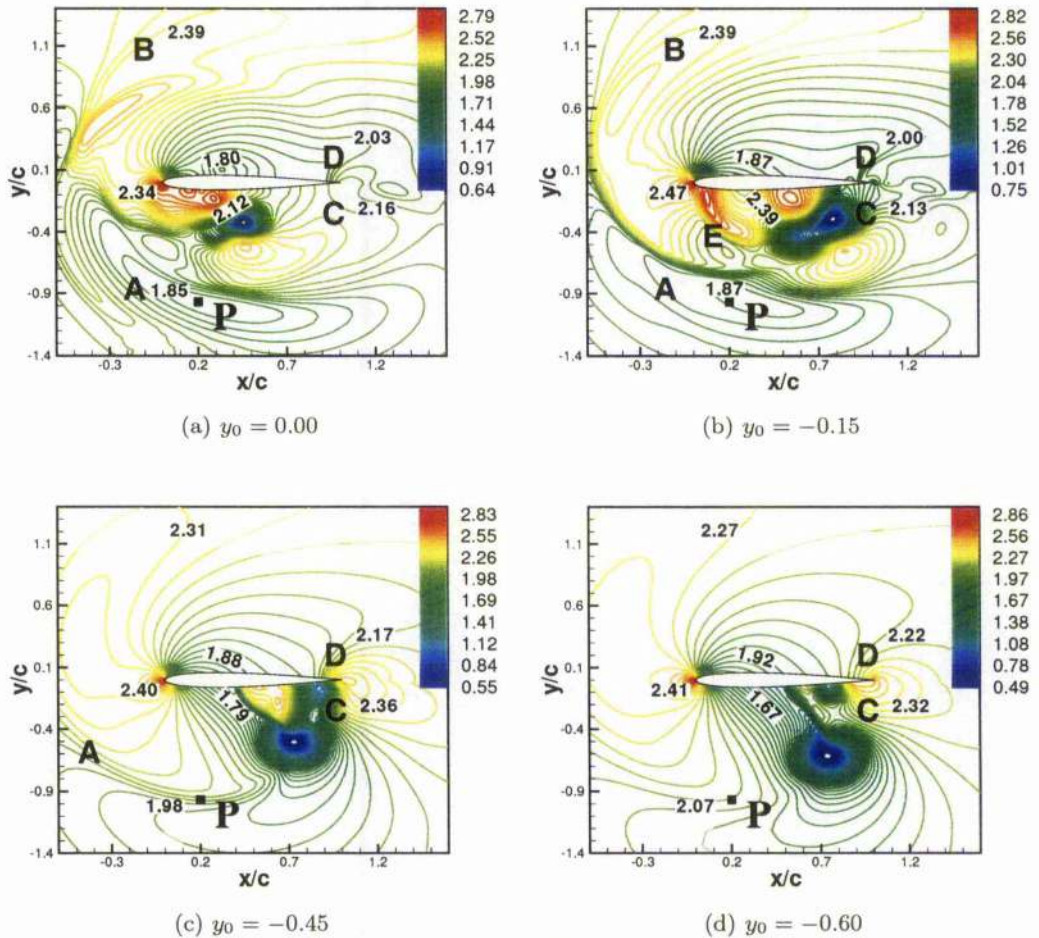


Figure 6.25: Isobars ( $2p/q_\infty$ ) contours for different miss-distance BVI cases at time  $t(U_\infty/c) = 5.10$ . Head-on BVI problem, NACA-0012 aerofoil, inviscid calculations,  $M_\infty=0.57$ ,  $\hat{\Gamma} = -1.8$ ,  $R_c = 0.10$ .

Influence of the vortex properties

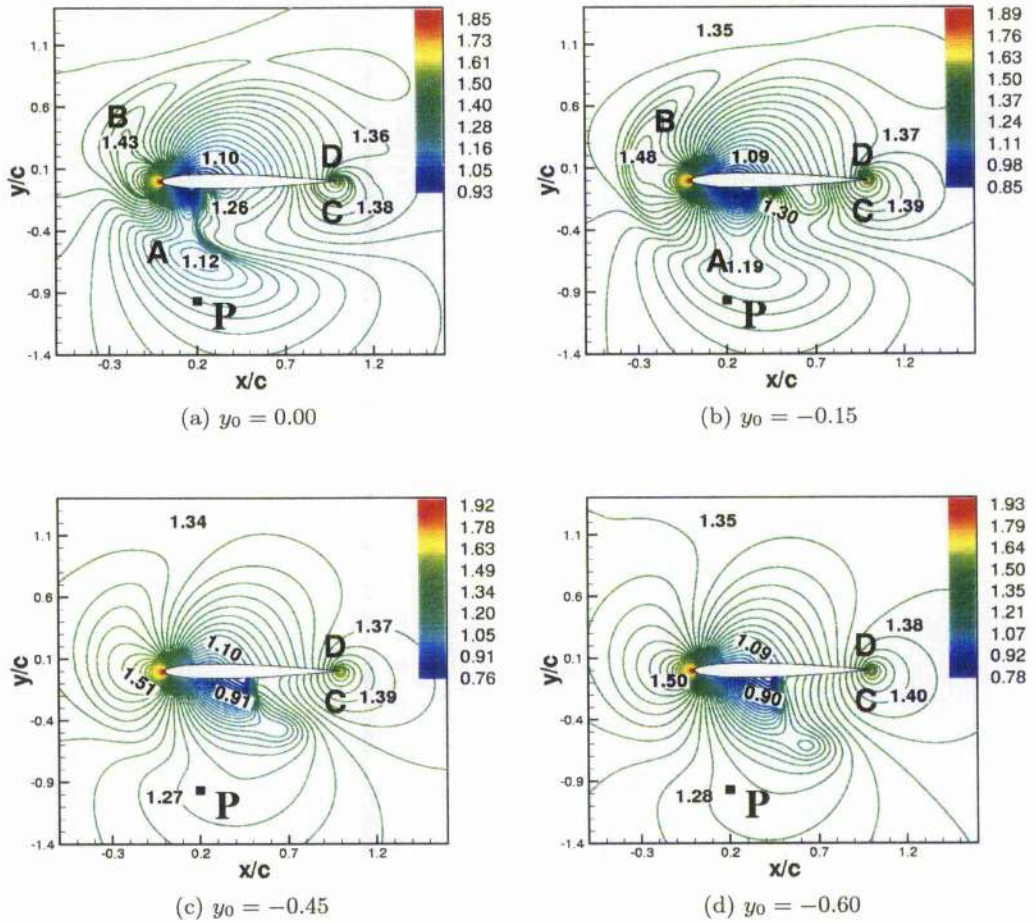


Figure 6.26: Isobars ( $2p/q_\infty$ ) contours for different miss-distance BVI cases at time  $t(U_\infty/c) = 5.10$ . Head-on BVI problem, NACA-0012 aerofoil, inviscid calculations,  $M_\infty=0.73$ ,  $\hat{\Gamma} = -0.42$ ,  $R_c = 0.10$ .

It is also interesting to note that the directivity of the two compressibility waves changes with the miss-distance. As shown in Figure 6.27, they tend to propagate more downstream and to merge for miss-distance BVI cases. As observed by Booth [10], the width of the acoustic waveform seems to be independent of the blade-to-vortex spacing. The compressibility wave is also found to merge with the transonic wave for small miss-distances. It can be observed that the transonic wave disappears for too large miss-distances, i.e. when the generated supersonic pocket is not strong enough to detach as a shock wave and propagate into the farfield.

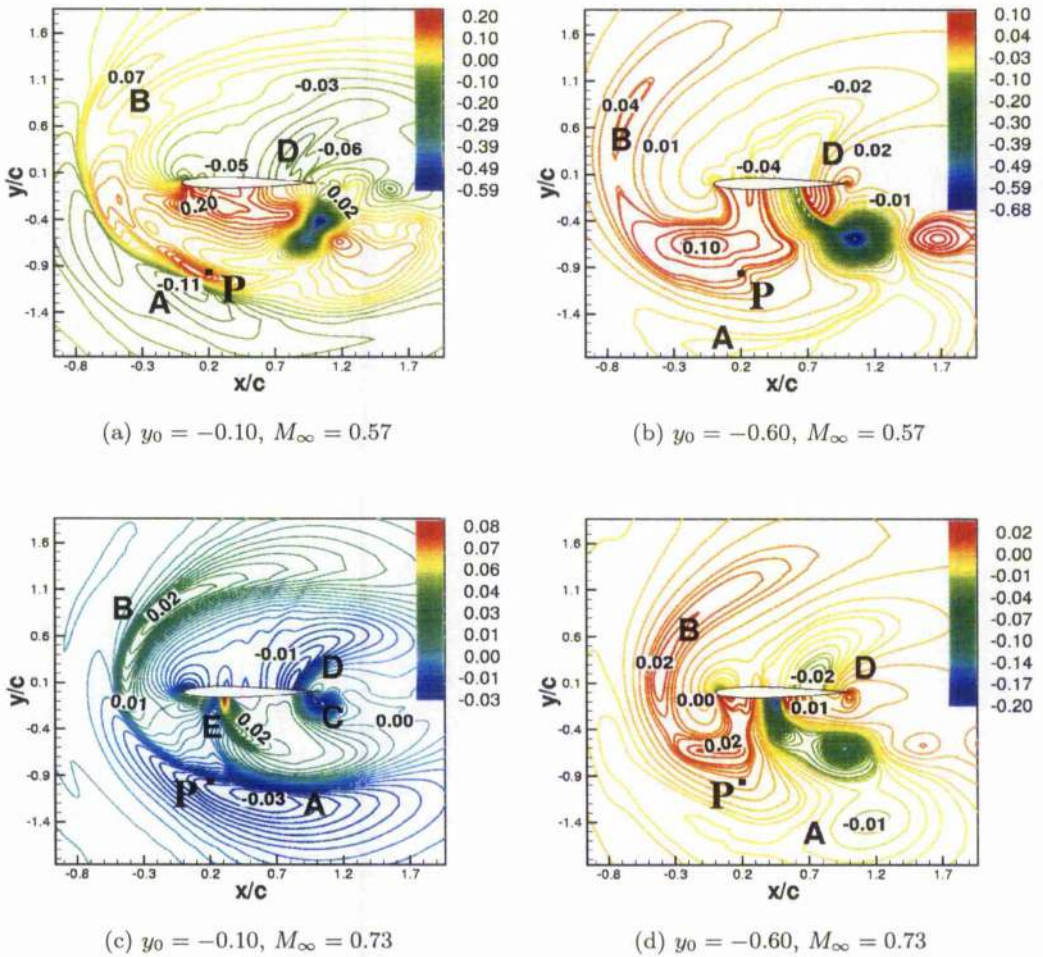


Figure 6.27: Isolines of the acoustic pressure for different miss-distance BVI cases at time (a-b)  $t(U_\infty/c) = 5.40$ . Head-on BVI problem, NACA-0012 aerofoil, inviscid calculations. (a-b)  $M_\infty=0.57, \hat{\Gamma} = -1.8$ , (c-d)  $M_\infty=0.73, \hat{\Gamma} = -0.42$ . Note that the acoustic pressure is non-dimensionalised against the freestream pressure.

It has to be pointed out that the transonic wave may be as strong or even stronger than the compressibility wave as shown in Figure 6.28. The strongest BVI appears to be for a miss-distance of  $-0.15$  due to the transonic wave for case 1 ( $M_\infty=0.57$ ) and for the head-on BVI due to the compressibility wave for case 2 ( $M_\infty=0.73$ ). It seems that a strong transonic wave is more likely to be generated and to dominate the overall noise near the aerofoil for miss-distance BVI cases. The magnitude of the transonic wave, which happens after the first negative peak, gives a good estimation of the BVI magnitude for case 1. For case 2 ( $M_\infty=0.73$ ), the vortex is much weaker, explaining why the negative peak is representative of the BVI strength. Note that, although the maximum peak of acoustic pressure is obtained in case 1 for the largest miss-distance, it does not mean that the compressibility wave is the strongest acoustical wave. This is actually caused by the passage of the vortex near point P.

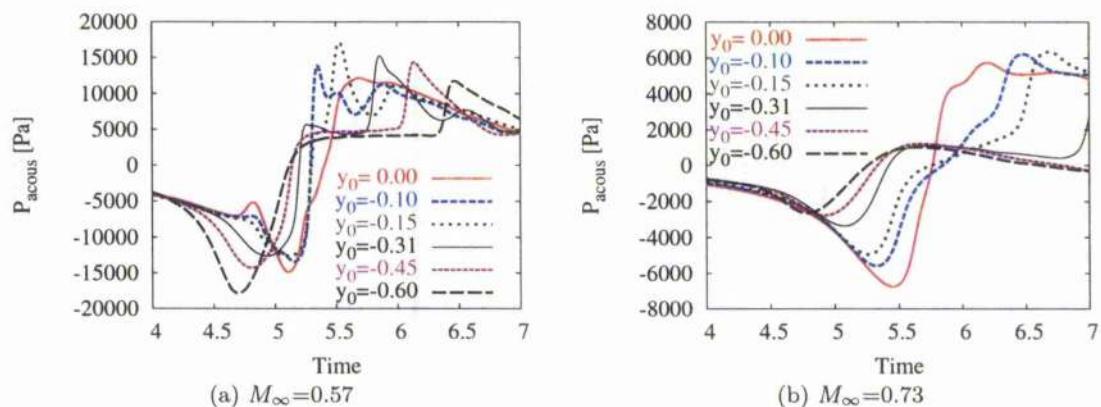


Figure 6.28: Acoustic pressure history at point P at two freestream Mach numbers. (a)  $M_\infty=0.57$ ,  $\hat{\Gamma} = -1.8$ , (b)  $M_\infty=0.73$ ,  $\hat{\Gamma} = -0.42$ . NACA-0012 aerofoil, inviscid calculations, various miss-distances. Note that the acoustic pressure is of a larger magnitude before the interaction for the subsonic case. This is due to the fact that the initial vortex is much stronger for the subsonic case than the transonic one.

### 6.3 Capabilities of the aeroacoustic module

#### 6.3.1 Coupling between CFD and the FW-H module

Two different approaches are common for determining the farfield noise: the Kirchhoff [87] and the Ffowcs Williams-Hawkings (FW-H) [88] methods. A description of these two aeroacoustic methods is given in Chapter 2. Regardless of choice, both FW-H and Kirchhoff methods rely on the accuracy of the nearfield acoustics which in this work are obtained from CFD calculations. Therefore, the ability of the CFD solver for preserving acoustic waves needs to be investigated. As shown in Figure 6.29, acoustic signals dissipate fast, which is purely numerical in origin. The acoustic waves are actually not characterised by any vorticity, rendering the CVCM inactive.

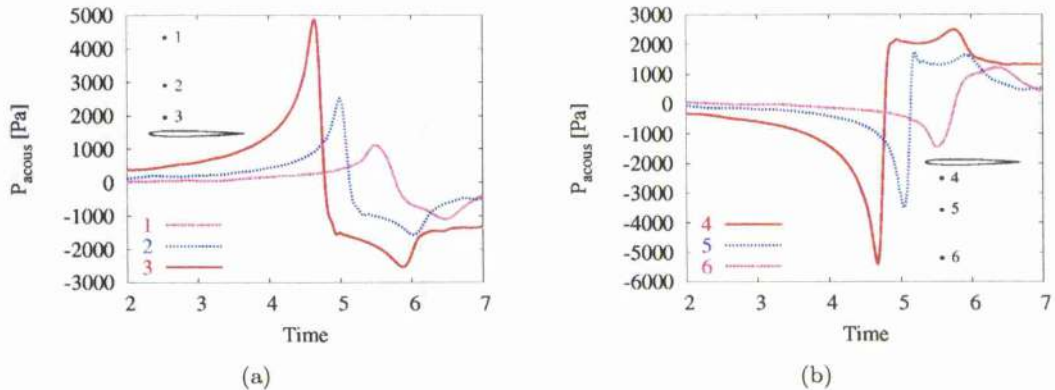


Figure 6.29: (a) Acoustic pressure history at points 1, 2, 3 above the aerofoil. (b) Acoustic pressure history at points 4, 5, 6 below the aerofoil. Head-on BVI problem, NACA-0012 aerofoil, viscous calculations,  $M_\infty=0.5$ ,  $\hat{\Gamma} = -0.283$ ,  $R_c = 0.018$ .

So, despite the fact that the CVCM is capable of conserving vorticity, it does not help the preservation of the acoustical waves. This, of course, is to be expected since only vorticity is confined. This implies that only the near-field close to the aerofoil is correctly captured by CFD and hence can be used as input data for CAA. Since the FW-H method is not as sensitive to the choice of the surface control as the Kirchhoff method, the FW-H is preferred for the study of the farfield noise. Indeed, the Kirchhoff method works better for potential-like flows, implying that the passage of the vortex through the control surface may spoil the solution. Therefore, the loads history, which can be well predicted with the use of the CVCM, was used as input data for the FW-H method. As in most acoustic codes based on the FW-H formulation [27], our approach considers the linear thickness and loading terms of the FW-H equation, neglecting the non-linear quadrupole term. The quadrupole term is not considered since its contribution is known to be negligible in the out-plane region of the rotor [11, 94].

## 6.3.2 Validation test

The acoustic module was tested against data taken from the experiments of Kitaplioglu [30]. A two-bladed rotor of diameter 7.0 feet was used in the experiments. The blades were untwisted with a rectangular platform and NACA-0012 sections of 6-inch chord. The blade tip Reynolds number was of the order of the million. A schematic of the experimental setup is shown in Figure 6.30 while a schematic of the blade with its polar co-ordinates is given in Figure 6.31. The angles  $\Psi$  and  $\theta$  are respectively the azimuth and the elevation angles. The azimuth angle is equal to  $0^\circ$  behind the rotorcraft and to  $180^\circ$  in front of. A point whose elevation is set to  $-90^\circ$  is located just beneath the rotorcraft. The flow conditions were the following:  $\mu = 0.2$ ,  $M_{tip} = 0.71$ ,  $r/R = 0.886$  and the vortex characteristics were  $\hat{\Gamma} = -0.25$ ,  $M_\infty = 0.63$ ,  $R_c = 0.162$ . Since these test cases were used as validation cases in Chapter 3, the loads calculated by CFD were used for the prediction of the BVI noise at microphone 3 for the two miss-distance BVI cases ( $y_0 = 0.0$  and  $y_0 = -0.25$ ). It has to be mentioned that the measurements were carried out in order not to contain any significant contribution from the quadrupole noise.

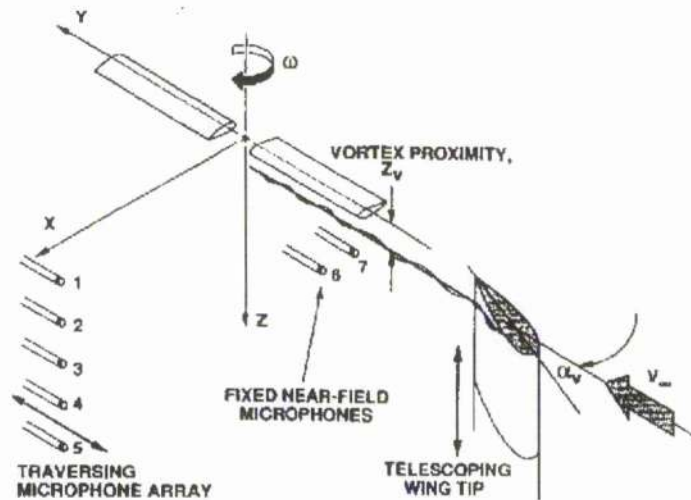


Figure 6.30: Schematic of the BVI rotor test.

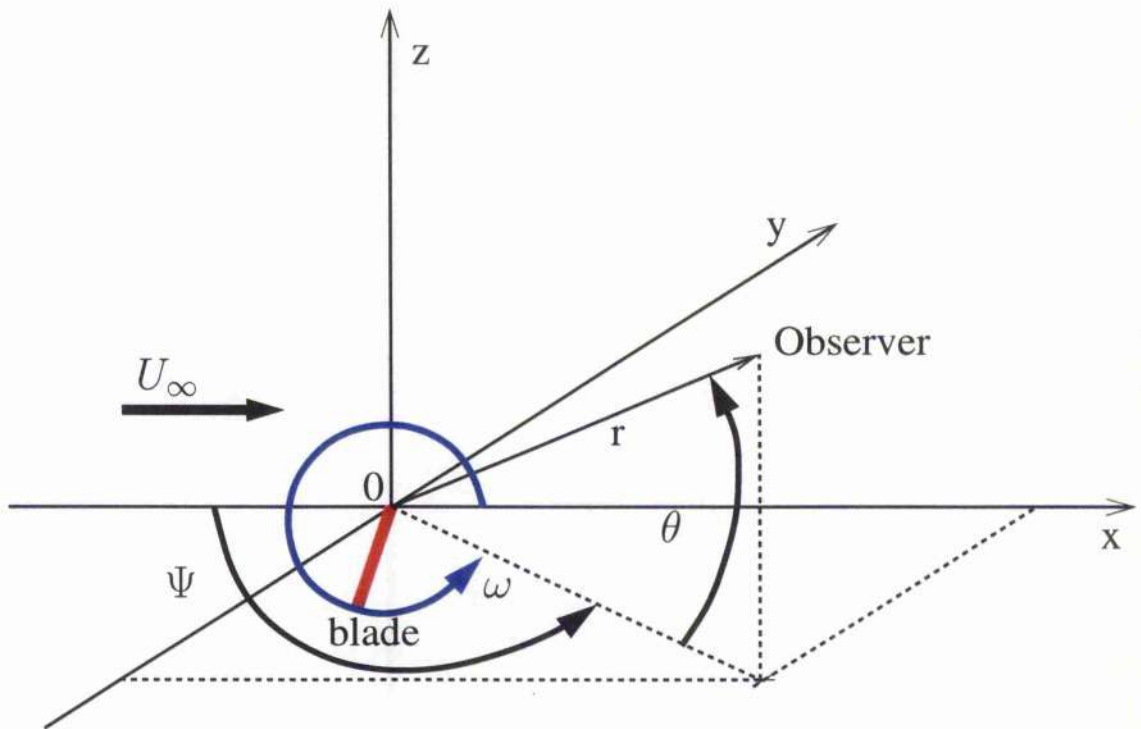


Figure 6.31: Schematic of the blade. The blade rotates anti-clockwise at  $\omega/(2\pi)$  revolutions per second. The spherical coordinates of the observer are  $(r, \theta, \Psi)$ .

Due to the FW-H formulation used, it was necessary to generate 3D loads from the 2D CFD results. Since the blade is less subjected to the compressibility effects than a 2D aerofoil due to the tip relief [139], only a part of the signal was used as input data for the CAA. The BVI loads were selected between two instants: when the vortex was located one chord ahead of the aerofoil and when the maximum amplitude of the loads was reached. Such a choice was made in order to account for the downward and upward effects of the vortex on the blade. The lift was set to the steady lift when the vortex was assumed to be far enough from the blade. Note that linear interpolations were used to get a smooth signal between the steady lift and the selected signal as depicted in Figure 6.32(a).

The second step for the generation of the 3D signal from the 2D one consisted of redistributing the lift signal along the spanwise direction. Special care was taken in order to generate a lift response adequate for 3D flow. Indeed, as mentioned by [7], the inboard blade contributes very little to acoustics. Therefore, the BVI should only influence the loads for a spanwise radius of  $r/R > 0.65$ . Therefore, the chordwise loading distribution along the spanwise directions was generated using simple weighting functions which correspond to given blade sections of a rectangular blade. This is illustrated by Figure 6.32(a).

Calculations were carried out so that the peak of BVI occurs at an azimuth angle of

180°. It was observed that the time during which BVI happens is essential for predicting the correct BVI noise. This was expected since the acoustic pressure is calculated using the derivative of the lift force in the FW-H method. The number of steps for one revolution was therefore set so that the azimuth angle  $\Psi$  of the blade increases by an amount  $d\Psi$  corresponding to the time step of the CFD computations. The distribution of the lift coefficient over the spanwise direction and the blade revolution is given in Figure 6.32(b) for the head-on BVI. Note that a revolution is completed (Rev=1) when the blade has rotated for 360 degrees.

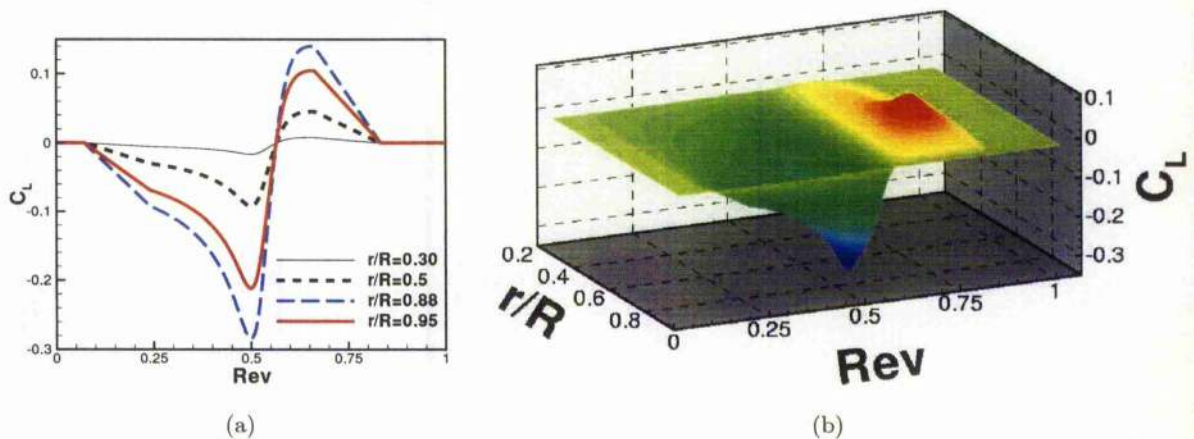


Figure 6.32: (a) Evolution of the lift coefficient against the the revolution of the blade for different spanwise locations. (b) Distribution of the lift along the spanwise direction against the revolution of the blade. Head-on BVI problem, NACA-0012 section.

The acoustic pressure was calculated for the microphone 3 (see Figure 6.30) which is located ahead and below the aircraft. The results are shown in Figure 6.33 and are in good agreement with the experiments, which indicates that the BVI magnitude is correctly predicted by the aeroacoustical module. The computed acoustic pressure differs from the experimental one by its smoother shape. This difference may be ascribed to the way the BVI occurs in the experiments. Although the BVI may be simplified to a 2D problem since the vortex encounters the blade at an azimuth angle of 180° as depicted in Figure 6.30, the 3D effects are important and should be accounted for. The BVI loads are actually affected by the rotational and compressibility effects near the LE of the blade. The generation of the 3D signal from the 2D one may not be appropriate enough to include some of the 3D effects, explaining why the computed signal is not as sharp as the one provided by the experiments. Both loading and thickness noise was calculated and as depicted by Figure 6.33, the slap noise dominates. It has to be pointed out that it takes 0.4 revolution for the acoustical signal to reach probe 3 after the BVI occurs at the azimuth angle of 180°. Note that the distance from the probe 3 to the observer is equal to 3.57 times the rotor, which was assumed to be large enough to consider the observer in the farfield [95].

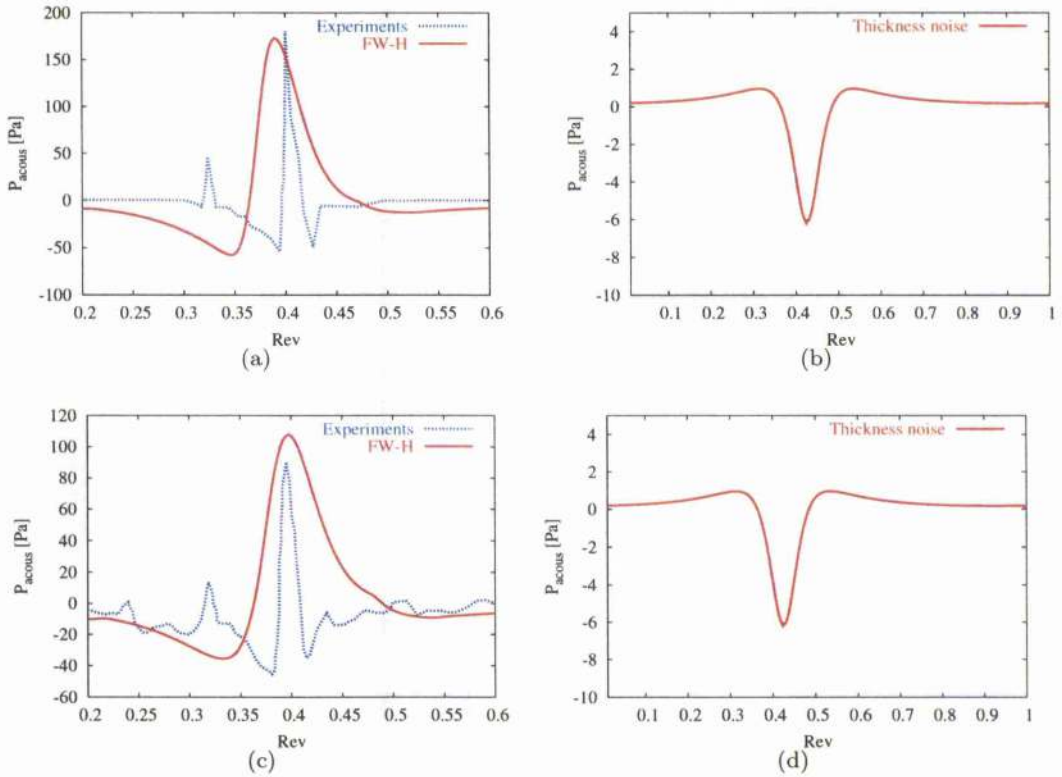


Figure 6.33: Acoustic pressure corresponding to the loading and thickness noises for (a-b) the head-on BVI and (c-d) the miss-distance BVI.  $M_\infty=0.63$ ,  $\hat{\Gamma} = -0.25$ ,  $R_c = 0.162$ .

## 6.4 Parametric study of the farfield noise

It is important to note that the parametric study only concerns the compressibility waves of the BVI.

### 6.4.1 Description of the rotor flight conditions

The flight conditions were chosen to be representative of manoeuvres where BVI is likely to occur. It is known, that the advancing side BVI dominates the overall radiation pattern [7] with most of the noise directed downwards, beneath the helicopter in the direction of forward flight. As reported by Preissier *et al.* [140], the blade undergoes multiple interactions on the advancing side due to the tip vortices of the blade on the retreating side, especially at lower speeds since there are more vortices present in the rotor blade. Therefore, the advance ratio was set to a relatively low value of 0.2 for a blade of 6.2 metres of radius, the tip Mach number ranging from 0.5 to 0.8.

A non-lifting rotor based on the NACA-0012 aerofoil was chosen for most calculations. However, a small lift coefficient was considered for the loaded SC-1095 aerofoil in both subsonic and transonic flows and for the NACA-0018 aerofoil in transonic flow.

## 6.4. PARAMETRIC STUDY OF THE FARFIELD NOISE

The tip-path-plane angle was also fixed to zero for a rectangular blade with a chord of around 40 cm length. Even though the local pitch angle was set to zero, it was not expected to have a large impact in terms of directivity [96] since the angle on the advancing side of an helicopter is small.

The location of the BVI was set at an azimuth  $\Psi = 90^\circ$  since the primary sources of BVI were experimentally located between  $70^\circ$  and  $90^\circ$  of azimuth angle as mentioned by Hardin and Lamkin [31]. The Overall Average Sound Pressure Level (OASPL) was calculated at different observer positions to investigate the magnitude and the directivity patterns of the BVI noise. The OASPL is defined as  $10 \log_{10} \left( \sum_{i=1}^{i=N} 10^{\frac{SPL_i}{10}} \right)$ ,  $N$  being the number of time steps. The observers have been positioned below and above the rotor for both advancing and retreating blades. The directivity of BVI has been highlighted using an  $(\theta, \Psi)$  map which represents the OASPL of BVI for different rotational and azimuthal angles. Therefore, the OASPL was calculated for observers located all around the aircraft as shown in Figure 6.34.

Although it has been shown previously that the transonic waves may be as strong or even stronger than the compressibility waves, it is assumed that they will not effect as much an observer below the rotorcraft than the compressibility waves due to the fact that they propagate upstream the aerofoil. Therefore, it is acceptable to say that the present calculations are representative of the BVI characteristics for the specified flight conditions. Note that 1024 points were sampled per rotor revolution.

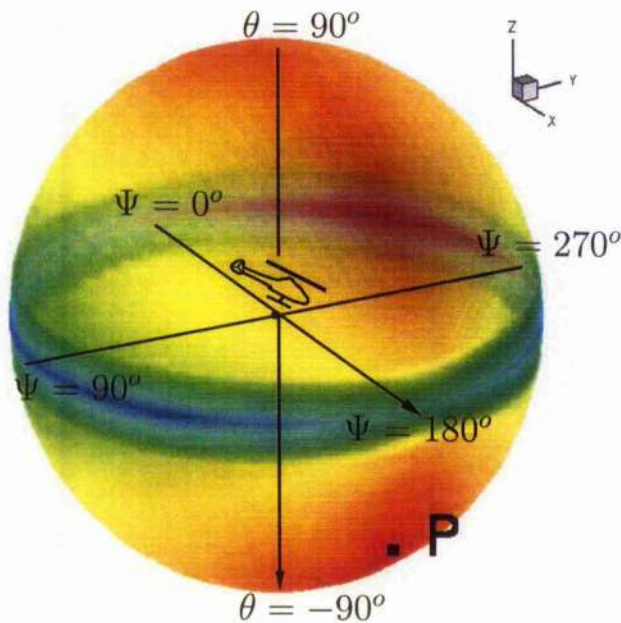


Figure 6.34: Schematic of the acoustical mapping for the helicopter. The OASPL is represented around a sphere passing by point P. The acoustic pressure has been calculated at point P (50, 0, -50) for the parametric study.

### 6.4.2 Influence of the aerofoil shape

The loading distribution along the spanwise direction for a head-on BVI is given in Figure 6.35. It can be seen that BVI takes place at 0.25 revolution and that the lift coefficient is equal to the static lift before and after the BVI, meaning that it is zero for symmetrical aerofoils.

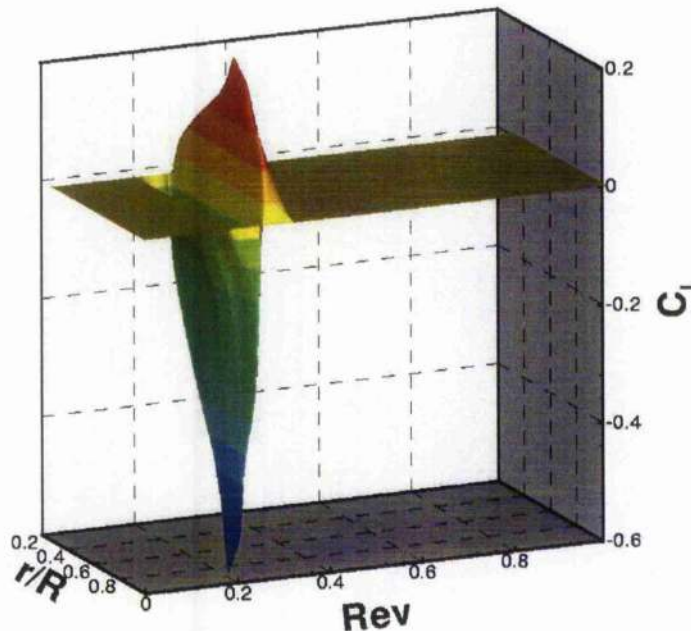


Figure 6.35: Distribution of the lift along the spanwise direction against the revolution of the blade. The BVI takes place at  $90^\circ$  of azimuth. NACA-0012 section,  $M_\infty=0.5$ .

The farfield noise levels are given for an observer located 50 metres below and 50 metres ahead of the aircraft which corresponds to point P indicated in Figure 6.34. A comparison of the acoustic pressure for the different aerofoils (see Figure 6.36) shows that only slight differences in terms of BVI noise magnitude appear for a Mach number of 0.5, the NACA-0018 remaining the least noisy, the three others giving similar acoustical response. It is interesting to note that the unloaded SC-1095 aerofoil is slightly less noisy than the loaded SC-1095 at point P, suggesting that the induced loads effect the BVI noise directivity. The levels of thickness noise are negligible against the loading noise levels as depicted in Figure 6.36.

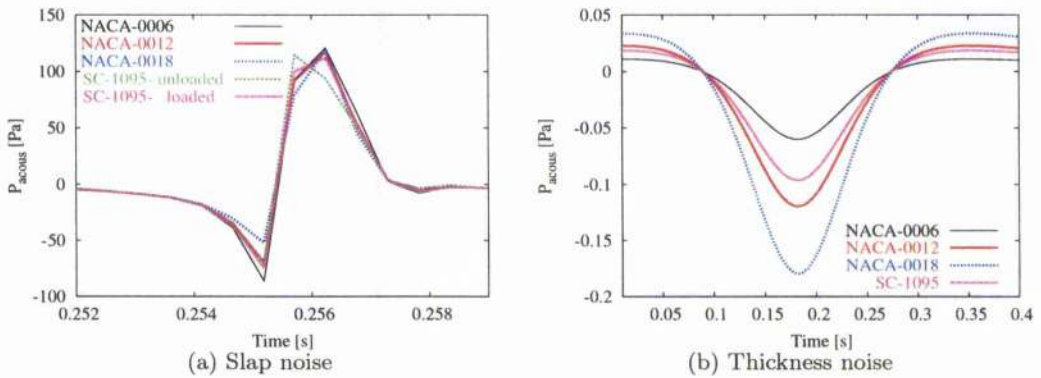


Figure 6.36: Acoustic pressure for different aerofoils at the location (50.0,0.0,-50.0). (a) Slap noise, (b) thickness noise.

The importance of the aerofoil shape [91] is verified for transonic flow at which the behaviour of the BVI noise for the non-symmetric aerofoil SC-1095 and the NACA-0018 is different from the other NACA-4 digit aerofoils as depicted in Figures 6.37 and 6.38. The difference of directivity patterns between the aerofoils is clear from Figure 6.39 which shows the trends of the OASPL evolution over the azimuth angle for a fixed distance aircraft-observer and elevation angle. The noise is radiated in some preferred direction in transonic flow. The similar acoustical behaviour between the SC-1095 and NACA-0018 aerofoils suggests that the camber and the movement of strong shocks which induce loads around the aerofoil modify the directivity of the BVI noise. Note that the OASPL signals of Figure 6.39 are not smooth, implying that the time and spatial resolution was not refined enough. However, the purpose of such plots is to show the directivity patterns of the BVI noise for different aerofoils in the transonic regime, where the present formulation of the FW-H method allows a relative comparison between the BVI cases (see Chapter 2).

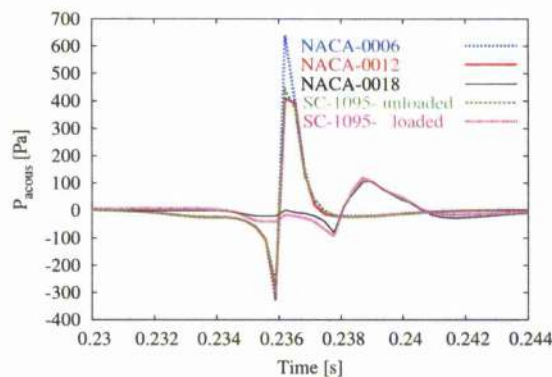


Figure 6.37: Acoustic pressure for different aerofoils at the point  $P$  (50.0,0.0,-50). Results corresponds to an azimuth angle of  $180^\circ$ .

**Influence of the aerofoil shape**

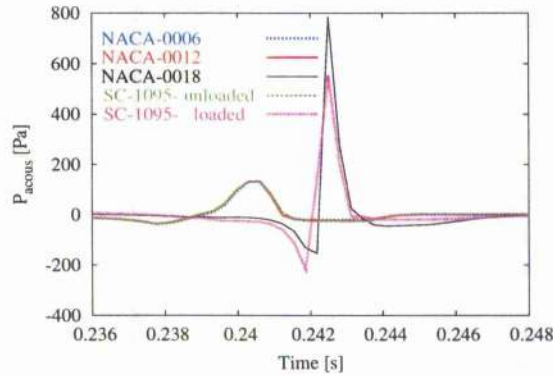
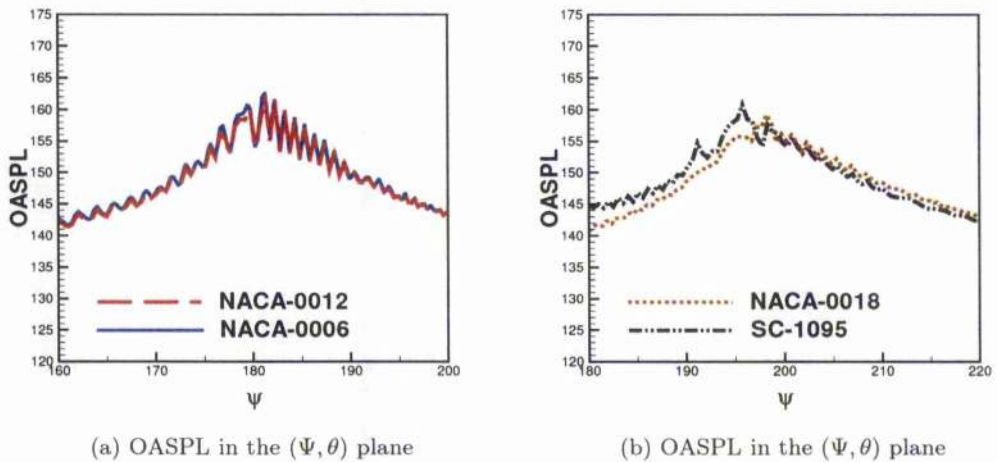


Figure 6.38: Acoustic pressure for different aerofoils at point  $P'$  (47.0,17.1,-50.0). Results corresponds to an azimuth angle of  $200^\circ$ . The distance aircraft-observer is the same as point P.



(a) OASPL in the  $(\Psi, \theta)$  plane

(b) OASPL in the  $(\Psi, \theta)$  plane

Figure 6.39: Contours of the OASPL at the transonic freestream Mach number for the range of azimuth angles  $\Psi$  where the BVI occurs. The elevation angle  $\theta$  was fixed to  $-30^\circ$  (below the aircraft) and the distance aircraft-observer to 50 metres.  $\hat{\Gamma}=-0.177$ ,  $M_\infty=0.8$  - (a) NACA-0006, NACA-0012, (b) NACA-0018, SC-1095.

The effects of the camber, thickness and LE radius on the BVI noise amplitude have been investigated. Regarding the influence of the camber, it is apparent from Figure 6.40 that the initial loading effects the BVI magnitude. Indeed, the Sikorsky seems to behave more like the other aerofoils when it is unloaded. Since the Sikorsky aerofoil could be expected to be as noisy as the NACA-0006 due to the similar geometry on the lower side, the present results suggest that the loads of the cambered aerofoil effect the BVI directivity pattern, especially in transonic flow.

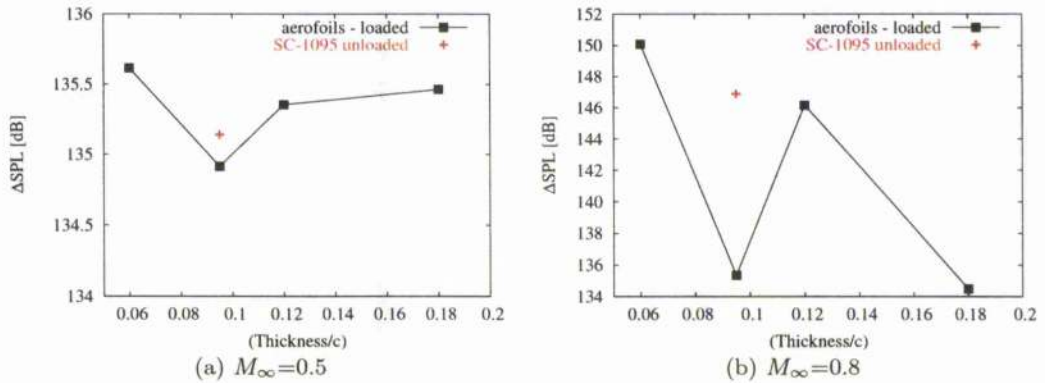


Figure 6.40: Maximum BVI noise amplitude in terms of Sound Pressure Level for different thicknesses of aerofoils at two freestream Mach numbers. The square points corresponds to the NACA-0006, NACA-0012, NACA-0018 and the SC-1095 sections. The cross corresponds to the unloaded SC-1095 aerofoil. Note the  $\Delta SPL$  is deduced from the maximum value of the acoustic pressure at point P.

As no specific trends could be deduced for the thickness and the LE radius, which are linked for the NACA 4-digit profiles, the NACA-001234 and the NACA-16018 aerofoils were used. It appears from Figure 6.41 that both LE radius and thickness do not make much of a difference in terms of noise in subsonic flow. However, it can be observed that the leading-edge radius plays a more important role for thinner aerofoils whereas the thickness influences more the BVI magnitude for aerofoils of larger LE radius. For the transonic flow, it remained difficult to assess the role of the thickness and of the LE radius due to the difference of BVI noise directivity of the aerofoils. It is also necessary to use a very small time step for the CFD calculations for this head-on BVI in order to take into account the Doppler effects, which is not required for a relative comparison between the aerofoils in transonic flow. Nevertheless, it is suspected that the amplitude of the BVI noise tends to increase when the thickness or the LE radius decreases, depending on the presence of shocks which change the directivity of the acoustic waves. This was highlighted when the near-field acoustic was analysed in Section 6.2.1.

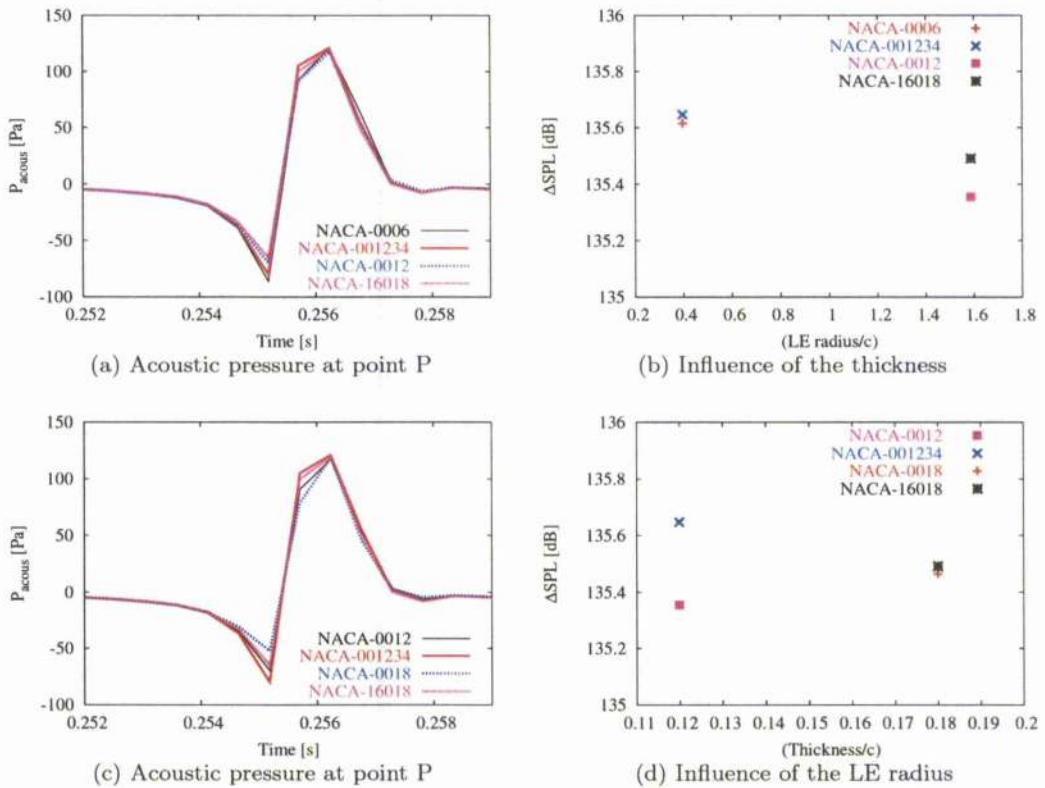


Figure 6.41: Acoustic pressure and maximum BVI noise amplitude at point (50,0,-50) in terms of Sound Pressure Level for (a-b) different thicknesses and (c-d) LE radii of aerofoil in subsonic flow.  $M_\infty=0.5$ ,  $\hat{\Gamma} = -0.283$ ,  $R_c = 0.018$ .

It is observed for the two different types of flow that the OASPL is a function of  $20 \log_{10}(r)$ ,  $r$  being the distance from the aircraft to the observer. This is shown in Figure 6.42. For the transonic case, an increase of the tip Mach number also increases the amplitude of the BVI radiation [7] through the Doppler factor [95]. It can be seen that the directivity patterns of the BVI noise is different for the two regimes of flow, the maximum noise occurring for an elevation angle of  $-50^\circ$  in subsonic regime and of  $-30^\circ$  for the transonic one. It is verified that the OASPL also increases by around  $10 \times [\log_{10}(0.8/0.5)^6 - \log_{10}(1 - 0.8 * \sin(30)) + \log_{10}(1 - 0.5 * \sin(50))]$  dB for the most intense BVI noise, the strength of the dipole type source being related to  $M^6$  and  $1/(1 - M_r)^4$  [86]. This shows that the source of the BVI noise can be assimilated to a dipole far away from the aerofoil.

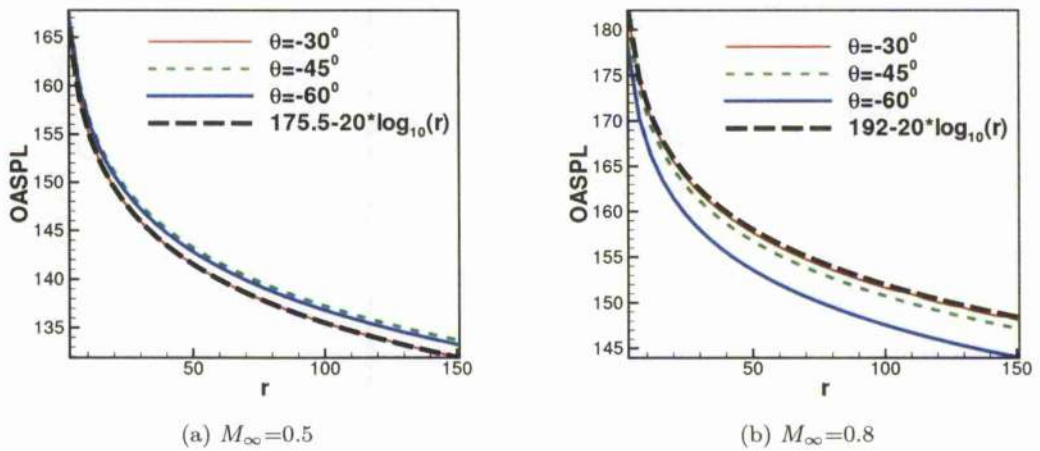


Figure 6.42: Evolution of the OASPL against (a, c) the square of the distance observer-aircraft and the logarithm of the distance at  $\Psi = 180^\circ$  for three different azimuth angles at two freestream Mach numbers. NACA-0012 section,  $\hat{\Gamma} = -0.283$  ( $M_\infty=0.5$ ),  $R_c = 0.018$ . (a)  $M_\infty=0.5$ , (b)  $M_\infty=0.8$ .

### 6.4.3 Influence of the freestream Mach number

A different range of Mach numbers was applied for a head-on BVI with an initial vortex of strength  $\hat{\Gamma} = -0.283$  and core radius  $R_c = 0.018$ . The acoustical signature at point P is shown in Figure 6.43. As expected, the increase of the Mach number leads to a signal which propagates faster and which is perceived earlier for an observer located at point P.

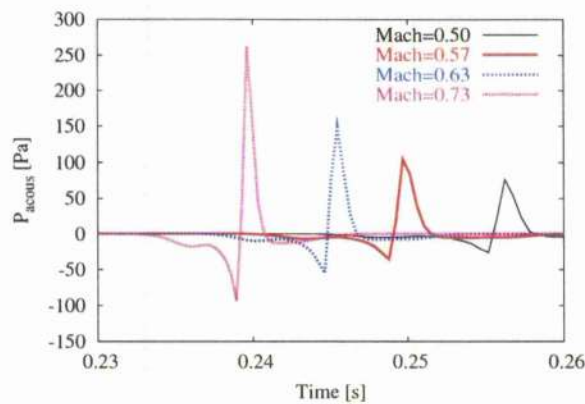


Figure 6.43: Acoustic pressure at different freestream Mach numbers at the location  $(50.0,0.0,-50.0)$ . NACA-0012 section,  $\hat{\Gamma} = -0.283$  at a freestream Mach number of 0.5,  $R_c = 0.01$ .

The slope of the SPL against the freestream Mach number was plotted. This was used by Gallman who conducted a BVI parametric study [95] for investigating the correlation between the SPL evolution and some parameters studied. The expression of the slope, i.e. the logarithmic decrement is given by

$$slope = \frac{SPL_n - SPL_{n-1}}{10 \log_{10}(X_n) - 10 \log_{10}(X_{n-1})} \quad (6.1)$$

with  $X_n$  being the studied parameter of indice n.

It can be observed from Figure 6.44(a) that the magnitude of the BVI noise peak increases linearly with the Mach number. This means that there may be a law between the values of the SPL and the freestream Mach numbers. As depicted in Figure 6.44(b), the slope varies from 5.0 to 7.5. The value of 5.0 can be explained by the fact that the difference in acoustics is small for the lowest Mach numbers whereas the value of 7.5 may express the importance of the acceleration effects as mentioned by Gallman [95]. It is thought that the slope is different from the value of 6 which was suggested by Lawson [86] for a dipole-type phenomenon since the logarithmic decrement was regarded in terms of the BVI noise peak and not in terms of the OASPL.

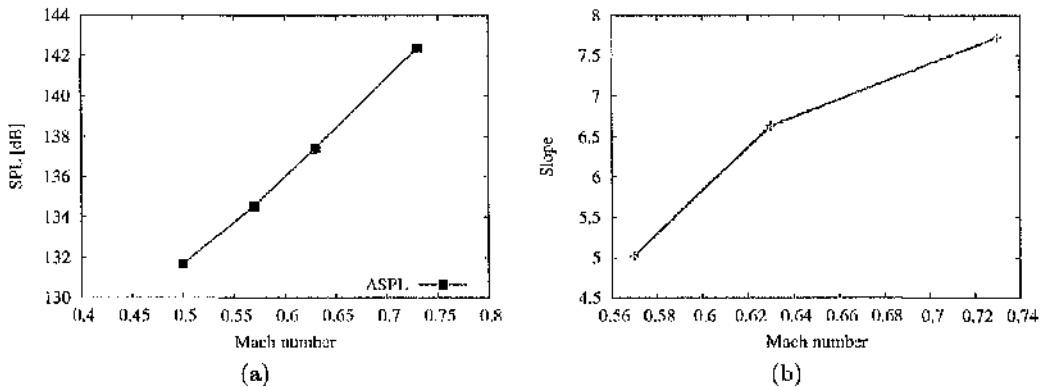


Figure 6.44: (a) Maximum BVI noise amplitude in terms of Sound Pressure Level for different Mach numbers. (b) Slope of the SPL-Mach curves.  $\hat{\Gamma} = -0.283$ ,  $M_\infty = 0.50$ ,  $R_c = 0.10$ .

6.4.4 Influence of the vortex properties

The influence the core radius size, the vortex strength and the miss-distance on the BVI noise signature is now investigated.

Vortex core radius

The acoustic pressure at an observer located at point P is given in Figure 6.45 for different radii for three cases. The first and second BVI cases were set at a Mach number of 0.73 for a miss-distance of 0.00 and -0.15, respectively. The vortex strength was fixed to -0.42. As shown in Figure 6.45, the stronger BVI remains for the vortex of smaller core radius which is characterised by the higher tangential velocity magnitude.

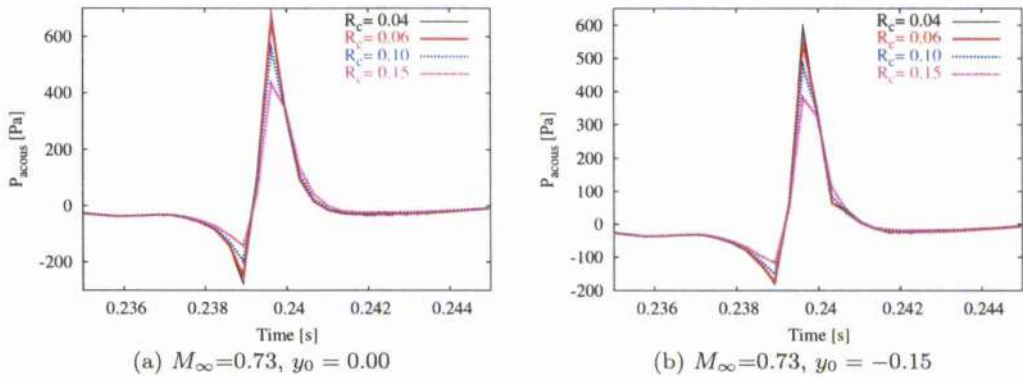


Figure 6.45: Acoustic pressure for different vortex core radii at the location (50.0,0.0,-50.0) for (a) head-on and (b) miss-distance BVI cases.  $\hat{\Gamma} = -0.42$ ,  $M_\infty=0.73$ . (a)  $y_0 = 0.00$ , (b)  $y_0 = -0.15$ .

It is noticeable that the decrease of the core radius effects the head-on and miss-distance BVI cases in terms of peak magnitude (see Figure 6.46). The noise is actually less and less affected by the core radius size for small enough vortices, which is expected since the expression for the tangential velocity can then be approximated by

$$\frac{v_\theta}{V_\infty} = \frac{\hat{\Gamma}}{2\pi r} \quad \text{for } R_c \ll r$$

This confirms that the SPL decay rate with core radius gets smaller when the core radius is less than the miss distance [95]. In other words, the distance from the blade to the aerofoil is a more important parameter for the BVI noise than the core radius when the miss-distance is greater than the core radius ( $y_0 \gg R_c$ ). Figure 6.46 illustrates that the decay rate of the SPL is small when the core radius is smaller than the miss-distance [95]. For head-on BVI, the distance separating the vortex to the aerofoil just before the interaction may play a similar role than  $y_0$  for miss-distance BVI cases when the core radius is very small. Regarding the miss-distance BVI case, the SPL was found to evolve in a similar way as for the head-on BVI for the largest core radii. This is verified in Figure 6.46(b) which illustrates that the decay rate gets close to -1 for large radii.

Influence of the vortex properties

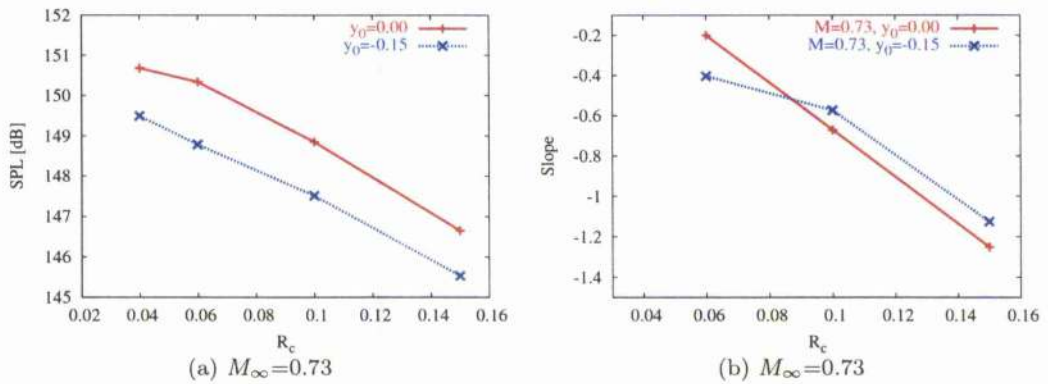


Figure 6.46: (a) Maximum BVI noise amplitude in terms of Sound Pressure Level for different vortex core radii at two flow conditions. (b) Slope of the SPL-viscous core radius.  $\hat{\Gamma} = -0.42, M_\infty=0.73$ . (a)  $y_0 = 0.00$ , (b)  $y_0 = -0.15$ . Note that  $R_c$  is the non-dimensionalised core radius.

As depicted in Figure 6.47, the BVI directivity patterns are more likely to enlarge for an initial vortex of larger viscous radius. The lobes of the head-on BVI noise get larger and the overall magnitude tends to decrease with the vortex core size. It may suggest that an increase of the core radius leads to a more spread-out radiated noise for head-on BVI. Since BVI is more likely to happen for a descending flight, i.e. when the the tip-path-plane of the rotor is tilted rearward [11], the BVI noise more often results from the interaction of the blade with an older vortex. This implies that a head-on BVI with the tip vortices may lead to enlarged lobes of radiated noise, the core size increasing in wake age [97].

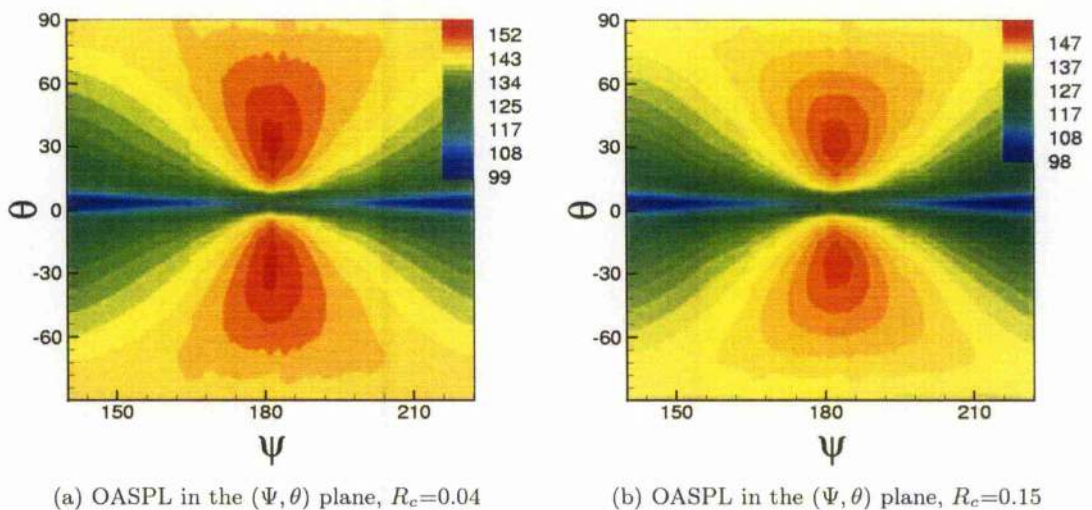


Figure 6.47: Contours of the OASPL for the range of azimuth angles  $\Psi$  where the BVI occurs. The elevation angle  $\theta$  indicates the directivity patterns of the BVI noise below ( $\theta < 0$ ) and above ( $\theta > 0$ ) the helicopter. Head-on BVI problem, NACA-0012 section,  $\hat{\Gamma} = -0.42, M_\infty=0.73$ . (a)  $R_c=0.04$ , (b)  $R_c=0.15$ .

Vortex strength

The noise levels perceived by an observer located at point P for the four different types of BVI are shown in Figure 6.48. As mentioned by Lyrantzis and George [91], the disturbances increase more than linearly with the vortex strength. Indeed, a "slightly superlinear" dependence is found for the BVI peaks [41]. However, Figure 6.49(a) suggests that the dependence of the BVI peak on the vortex strength decreases for very strong vortices. This is confirmed by Figure 6.49(b) which shows the decrease of the decay rate of SPL for stronger vortices. Then it is reasonable to say that the vortex strength has to be significantly reduced [22] to alleviate the peaks in the loads, especially when the vortices are strong.

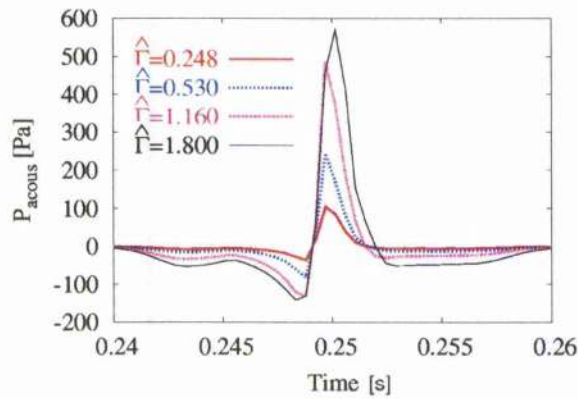


Figure 6.48: Acoustic pressure for different vortex strengths at point P (50.0,0.0,-50.0).

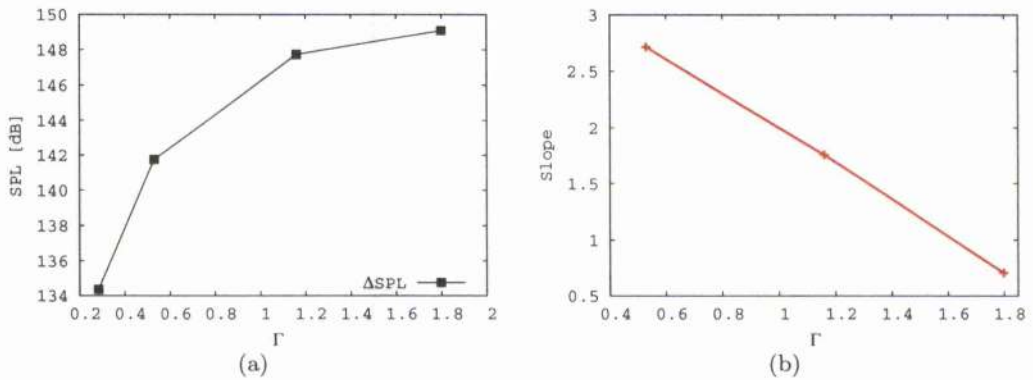
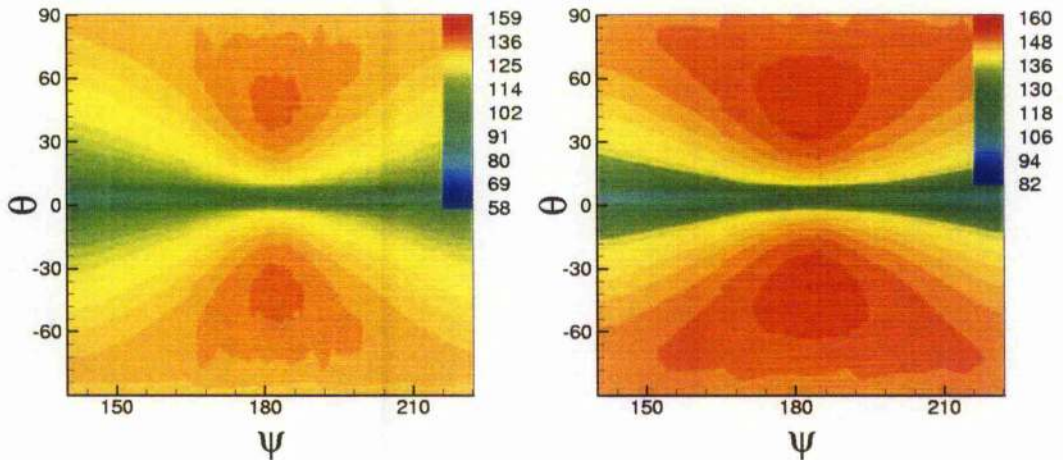


Figure 6.49: (a) Maximum BVI noise amplitude in terms of Sound Pressure Level for different vortex strengths. (b) Slope of the SPL-vortex strength.

The directivity of the BVI noise is related to compressibility effects. Head-on BVI propagates more uniformly for a stronger initial vortex as shown by the size of the lobes of the radiated noise of Figure 6.50.



(a) OASPL in the  $(\Psi, \theta)$  plane,  $\hat{\Gamma}=-0.283$

(b) OASPL in the  $(\Psi, \theta)$  plane,  $\hat{\Gamma}=-1.80$

Figure 6.50: Contours of the OASPL for the range of azimuth angles  $\Psi$  where the BVI occurs. The elevation angle  $\theta$  indicates the directivity patterns of the BVI noise below ( $\theta < 0$ ) and above ( $\theta > 0$ ) the helicopter. NACA-0012 section, (a)  $\hat{\Gamma}=-0.283$ ,  $M_\infty=0.57$  - (b)  $\hat{\Gamma}=-1.80$ ,  $M_\infty=0.57$ .

### Miss-distance

Results are discussed for two types of BVI. The first BVI was simulated at a freestream Mach number of 0.73 for an initial vortex of non-dimensionalised strength -0.42. The second case was for a freestream Mach number of 0.57 with a vortex strength -1.8. The non-dimensionalised radius  $R_c$  of the initial vortex was fixed to 0.1. First, it is interesting to note that the maximum BVI noise occurs when the miss-distance is equal to the vortex core size. BVI amplitude also shows a linear dependence on the miss-distance [41] as long as the miss-distance is greater than  $R_c$  (see Figure 6.51(a-b)). However, the linear dependence of the BVI noise with the miss-distance is only valid for miss-distances greater than  $-0.15c$  for the second BVI as shown in Figure 6.51(c-d). The interaction between the vortex and the generated supersonic pocket may be at the origin of this behaviour.

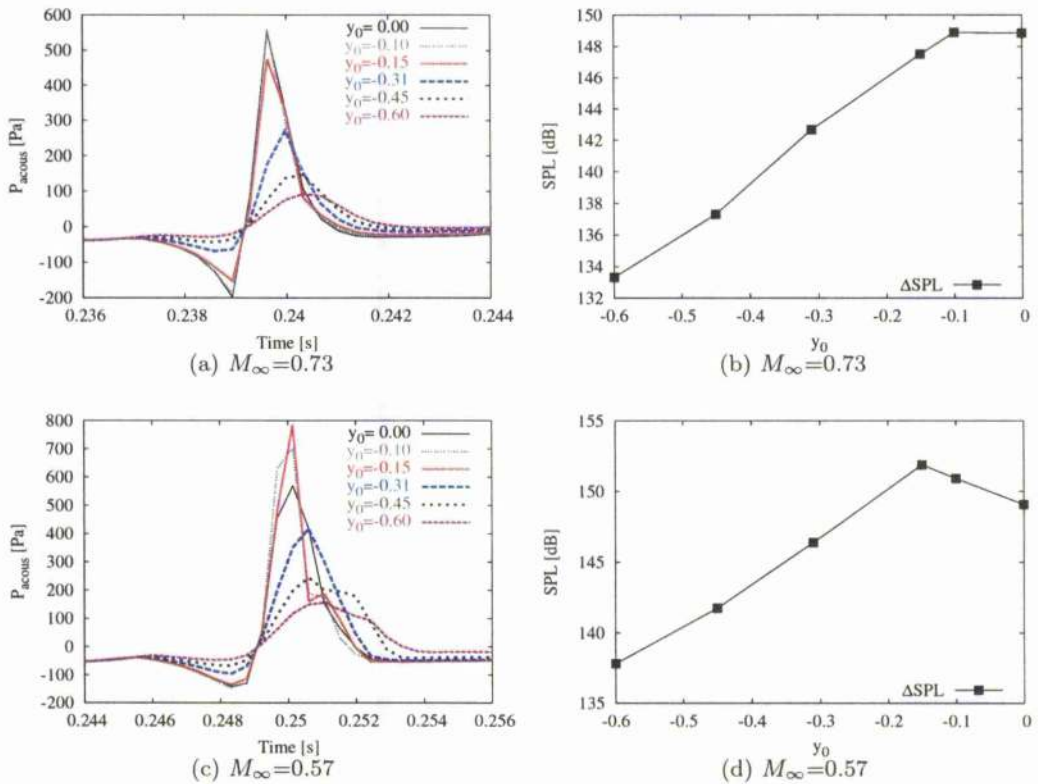


Figure 6.51: Influence of the miss-distances on the farfield noise for two different BVI cases. (a-b)  $\hat{\Gamma} = -0.42$ ,  $M_\infty = 0.73$ , (c-d)  $\hat{\Gamma} = -1.8$ ,  $M_\infty = 0.57$ . (a, c) Acoustic pressure for different aerofoils at the location (50.0,0.0,-50.0). (b, d) Maximum BVI noise amplitude in terms of Sound Pressure Level for different miss-distances. Note that  $y_0$  is non-dimensionalised with the chord of the aerofoil.

Figure 6.52 which depicts the values of the slope of the SPL-miss-distance curves shows that the decay rate is of -1 when the miss-distance is approximately equal to the radius core and that it decreases and stabilises for larger miss-distances towards a value of -3. This is in agreement with the expression of the acoustic pressure derived by Hardin and Lamkin for BVI, which shows that the noise can be approximately a function of the miss-distance of the power of three when the induced lift is relatively high. This implies that the miss-distance is a more important parameter than the core radius for BVI alleviation when it is greater than the radius core.

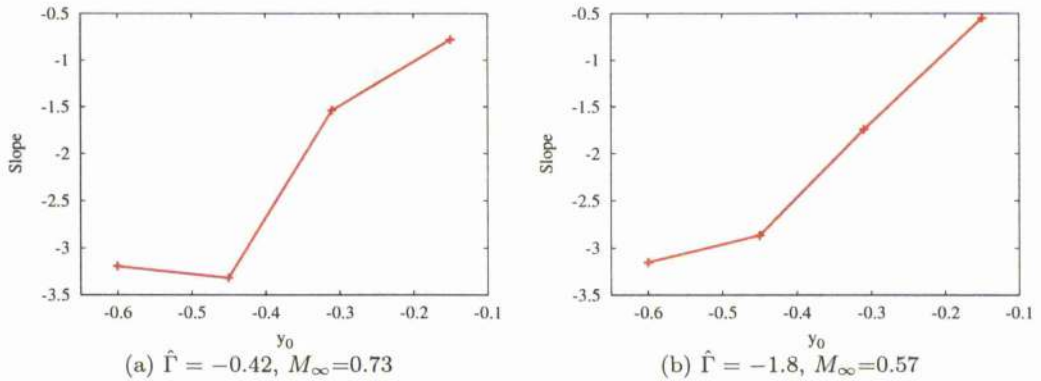


Figure 6.52: Slope of the SPL for two miss-distance BVI cases. NACA-0012 section. The acoustic pressure was taken for different miss-distance BVI cases at the location (50.0,0.0,-50.0). Note that  $y_0$  is the non-dimensionalised miss-distance.

Figure 6.53 shows the BVI trends for head-on and miss-distance BVI. It appears that the size of lobes of radiated noise increases with the miss-distances, the OASPL decreasing. This just means that the BVI noise energy is more spread-out in the case of increasing miss-distances.

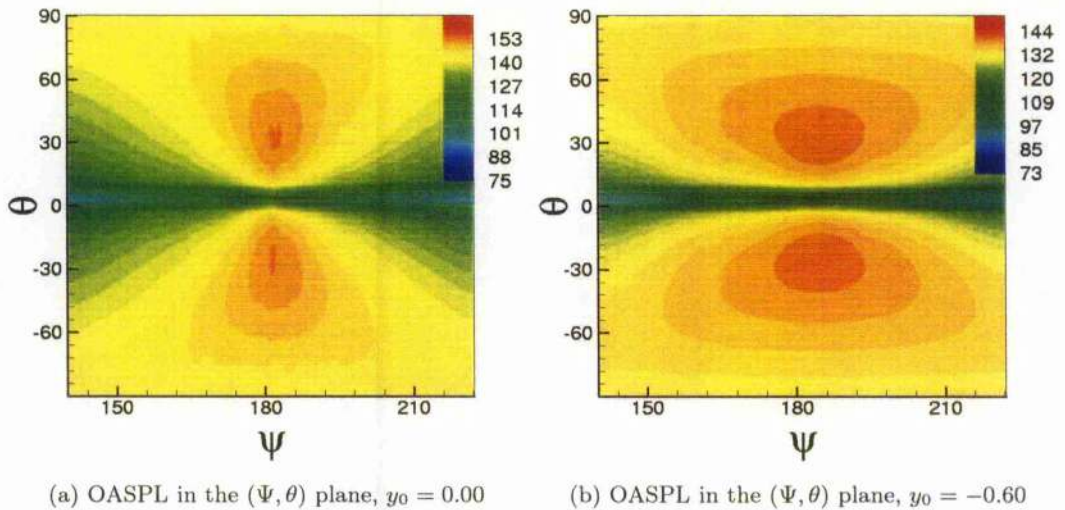


Figure 6.53: Contours of the OASPL for the range of azimuth angles  $\Psi$  where the BVI occurs. The elevation angle  $\theta$  indicates the directivity patterns of the BVI noise below ( $\theta < 0$ ) and above ( $\theta > 0$ ) the helicopter. NACA-0012 section,  $M_\infty = 0.73, \hat{\Gamma} = -0.242$ . (a)  $y_0 = 0.00$ , (b)  $y_0 = -0.60$ .

## 6.5 Conclusions

A combination of CFD and CAA methods has been used for the study of the BVI problem. The potential of the method has been demonstrated for several flow cases suggesting that the CVCM is a valid, low-cost and easy to implement technique in comparison with high order CFD methods. The obtained results highlight the importance of the aerofoil shape in the emitted sound during BVI and the complex relationship between the vortex characteristics and the resulting acoustic field. The magnitude of the computed acoustic pressure shows that the vortex strength and the miss-distances remain the most important parameters for alleviating the BVI noise. Of importance is the relationship between the radius of the vortex core and the intensity of BVI. The current set of results indicates that alleviation or even total control of the sound is possible provided that the vortex core properties can be modified in an efficient way.

The directivity of the BVI for the different aerofoils seems to be similar in subsonic flow. For transonic flow, the BVI noise directivity changes with the loading of the aerofoil which can either happen for a cambered aerofoil or for an aerofoil with strong moving shocks. The directivity trends of BVI show that the size of the lobes for the BVI noise is mainly related to the size of the vortex core and to the miss-distance. The noise is more spread-out for larger core radii and larger miss-distances.

# Chapter 7

## Conclusions

This chapter presents the achievements of the present work and suggestions for the further work.

### 7.1 Achievements

This work has highlighted the capabilities of numerical methods for the prediction of BVI. The time-stepping implicit unfactored method was shown to be robust for steady and unsteady calculations. Its efficiency is based on the fact that the system of linear equations to be solved is not factorised, removing the influence of the factorisation error. Furthermore, the use of the Conjugate Gradient method allows a rapid and efficient resolution of the linear system. Regarding the spatial discretisation, the typical second-order accuracy spatial solver was found to dissipate vortices. The dissipation rate was found to be related to the number of cells per vortex core radius and to the vortex strength. The Compressible Confinement Method was used to remedy this problem. This method was assessed as robust, cheap in terms of CPU time, with the only remaining issue the optimisation of the confinement parameter. The use of the grid scaling for the  $\epsilon$  parameter helped to find the optimum parameter which was found to be inversely proportional to the core radius of the vortex on a given grid.

The flowfield around a rotor was reasonably predicted for three-dimensional flows and successfully simulated for two-dimensional flows. The CVCM was shown to be useful for capturing vortices on a coarse grid and/or for preserving strong vortices which tend to dissipate fast. Since the use of the CVCM made possible a BVI parametric study, the BVI aerodynamics was investigated for different aerofoil shapes, freestream Mach numbers, vortex core radii, vortex strengths and miss-distances. The vortex introduced was clockwise-rotating, which is supposed to be representative of the BVI on the advancing side of a helicopter. A comparison between the BVI loads for the different cases showed the importance of the aerofoil shape for transonic flow. The BVI loads were strongly influenced by the vortex properties which determine the vortex-induced angle of attack.

A BVI noise parametric study was then carried out using the Ffowcs Williams-Hawkings (FW-H) method. CFD and CAA were used to predict the nearfield and farfield acoustics, respectively. In terms of nearfield acoustics, the CVGM is, of course, unable to preserve acoustic waves, with the use of a high-order scheme or adaptive grid refinement techniques remaining the only alternatives for high-fidelity acoustics prediction. Although the nearfield acoustics of the BVI were found to dissipate, a relative comparison between different BVI was possible. Three acoustical waves were observed. The first waves, called the compressibility waves, were present for all BVI cases. They propagate upstream of the aerofoil, above and below the aerofoil. These two waves characterise BVI noise at subsonic flow since they dominate. They are also observed in transonic flow. Their magnitude depends strongly on the freestream Mach number and the vortex properties. The wave propagating downwards was found to be the stronger for both head-on and miss-distance BVI cases. The aerofoil shape was found to affect the BVI noise, especially in transonic flow, an aerofoil of smaller LE radius being more likely to generate high levels of noise. Their directivity is influenced by the aerofoil shape near the LE in subsonic flow and also by the locations of the shock in transonic flow. They were found to bend downwards for miss-distance BVI cases.

Two other acoustical waves, named the TE waves, are generated once the compressibility waves reach the TE of the aerofoil. These waves propagate upstream of the aerofoil and their intensity was found to be secondary compared to the compressibility waves for all types of flow conditions. The directivity patterns of these waves was not altered by the nature of the BVI in subsonic flow whereas the presence of the shock influences their directivity in transonic flow.

For high subsonic or transonic flow, the induced velocity of the vortex can be sufficient to generate a supersonic pocket along the shoulder of the aerofoil on the lower side. A shock wave is generated, weakening until it reaches the LE of the aerofoil to finally detach from the aerofoil. This wave, the transonic wave, was found to be noisier than the compressibility waves when the initial vortex strength was large, especially for miss-distance BVI cases. Although the transonic wave, in most cases, propagates perpendicularly to the freestream flow direction, it was observed that the presence of the shock or of the supersonic pocket could change its directivity. The most critical BVI case was obtained when the miss-distance was equal or slightly greater than the radius core.

The farfield noise was then investigated for the BVI cases using the FW-H method. The BVI noise was regarded in terms of the compressibility waves. The BVI loads provided by CFD were therefore used by the CAA method for determining the magnitude of the compressibility wave for an observer located below and in front of the aircraft. The study showed that the BVI noise magnitude is directly related to the

---

## 7.1. ACHIEVEMENTS

freestream Mach number. This also confirmed that the compressibility waves can be considered as a dipole type phenomenon as long as no transonic wave, i.e. quadrupole component, is present. The vortex strength and the miss-distance were found to be very important parameters. Linear dependence of the BVI noise peak was observed for the miss-distance as long as the miss-distance is larger than the vortex core radius. The BVI noise magnitude was also found to be dependent on the vortex strength, the SPL decay rate decreasing for very strong vortices. Furthermore, the sharpness of the compressibility wave seems to be driven by the vortex core size, the BVI noise intensity decreasing more for larger radii. It was also shown that the BVI loads are offset by a positive value in the case of a clockwise-rotating vortex in the transonic regime when the aerofoil is cambered and/or when asymmetrical shocks are present before the interaction. This causes a change in the time occurrence of the BVI peaks, leading to different azimuthal BVI locations.

## 7.2 Further work

It has to be remembered that BVI is a highly three-dimensional phenomenon. Although some critical parameters controlling BVI noise have been highlighted, the study of the influence of the parameters which determine the location on the blade of the BVI is essential for a complete understanding of BVI [22]. It is known that the directivity of BVI is highly sensitive to rotor advance ratio and disk attitude [140]. Furthermore, interaction with the rotor tail should also be investigated since it controls the overall noise in the absence of blade slap [4]. The problems of interaction with the aeroelasticity and the aerodynamic of the helicopter should also be borne in minds [5].

The BVI noise was regarded in terms of its compressibility waves which were assumed to dominate the noise below the rotorcraft for the specified flight conditions. It would be interesting to assess the contribution of the transonic waves to test this assumption and to investigate its directivity at different flight conditions since they can propagate into the farfield [4]. It is indeed suspected that it could dominate the overall noise levels for descending flight and affect an observer at the ground, depending on the atmospheric conditions which can actually change the directivity patterns of the acoustical waves. Only a three-dimensional study of BVI considering the environment of the helicopter could reveal the contribution of the different acoustical waves for some specific flight conditions. Although such calculations would be expensive in terms of CPU time, more especially at transonic flow which requires a high resolution in the time domain to take into account the Doppler effects, the use of the CVCM could make it feasible since coarse grids could be used.

Although this work has suggested the usefulness of the CVCM for BVI study, the

priority should remain the optimisation of the method, i.e., the optimisation of the confinement parameter. It is thought that such optimisation would be possible by taking into account the properties of the spatial scheme and the characteristics of the vortices. The first step should consist in the optimisation of the method on uniform grids as attempted in [110]. The determination of the truncation error of the spatial scheme may indicate how the dissipation of the scheme is related to the local Mach number. The second step should emphasize on the effects of the grid stretching. Since it would be difficult to calculate the truncation error on non-uniform grids, parameters such as the number of cells per radius core may be used to express the dissipation of the scheme related to the grid cell size.

In terms of robustness, the code can preserve its characteristics as long as some inherent dissipation is still present for damping any disturbances which may lead to some problems of instability. The CVCM can be therefore used with upwind schemes which are dissipative by nature. The condition to be fulfilled is to avoid flow regions characterised by high values of vorticity, i.e., boundary layer and wake. This can be handled by the use of limiters such as zones. It is thought that a suitable limiter for viscous calculations could be the ratio shear stress magnitude over vorticity.

The capture of the near-field acoustics currently requires the use of adaptive grid refinement or high-order accurate schemes. This is especially needed in the transonic regime where the transonic wave may dominate. The implementation in CFD solvers of any of these methods is, however, difficult and most of the times is associated with a long period of validation and in practice it may result in loss of efficiency and stability during calculations. This suggests that the CVCM should gain popularity for CFD solvers once optimised and, in conjunction with the use of techniques capable of capturing the near-field acoustics, should allow the solution of high-fidelity aeroacoustics for rotorcraft.

# References

- [1] K.S. Brentner and F. Farassat. Modeling aerodynamically generated sound of helicopter rotors. *Progress in Aerospace Sciences*, Vol. 39, pp. 83-120, 2003.
- [2] A.T. Conlisk. Modern helicopter aerodynamics. *Progress in Aerospace Sciences*, Vol. 37, pp. 419-476, 2001.
- [3] B. Edwards and C. Cox. Revolutionary concepts for helicopter noise reduction-S.I.L.E.N.T. program. *NASA/CR-2002-211650*, 2002.
- [4] J.W. Leverton. 25 years of rotorcraft aeroacoustics: historical perspective and important issue. *Journal of Sound and Vibration*, Vol. 133, No. 2, pp. 261-287, 1989.
- [5] F.H. Schmitz. Reduction of blade-vortex interaction (BVI) through X-force control. *Journal of the American Helicopter Society*, Vol. 43, No. 1, pp. 14-24, 1998.
- [6] F.H. Schmitz, G. Gopalan and B.W.-C. Sim . Flight path management and control methodology to reduce helicopter blade-vortex interaction (BVI) noise. In *American Helicopter Society Vertical Lift Design Conference, San Francisco*, January 2000.
- [7] B.W.-C Sim and F.H. Schmitz. Blade vortex interaction (BVI) noise: retreating side characteristics, sensitivity to chordwise loading and unsteady aerodynamics. *American Helicopter Society (AHS), Aeromechanics Specialists Meeting, Atlanta, Georgia*, November 13-14 2000.
- [8] Y.H. Yu. Rotor blade-vortex interaction noise. *Progress in Aerospace Sciences*, Vol. 36, pp. 97-115, 2000.
- [9] S. Lee and D. Bershadcr. Head-on parallel blade-vortex interaction. *AIAA Journal*, Vol. 32, No. 1, pp. 16-22, 1994.
- [10] E.R. Booth Jr. Experimental observations of two-dimensional blade-vortex interaction. *AIAA Journal*, Vol. 28, No. 8, pp. 1353-1359, 1990.
- [11] F.H. Schmitz and Y.H. Yu. Helicopter impulsive noise: theoretical and experimental status. *Journal of Sound and Vibration*, Vol. 109, No. 3, pp. 361-422, 1986.
- [12] G. Arnaud and H.-J. Marze. Helicopter noise and public acceptance: a stressed relationship today, a better balance tomorrow, Friedrichshafen, Germany. In *29<sup>th</sup> European Rotorcraft Forum, Special Session*, September 2003.

- [13] K.S. Brentner and F. Farassat. Helicopter noise prediction: the current status and future direction. *Journal of Sound and Vibration*, Vol. 170, No. 1, pp. 79-96, 1994.
- [14] S. Lewy and M. Caplot. Review of some theoretical and experimental studies on helicopter rotor noise. *Vertica*, Vol. 8, No. 4, pp. 309-321, 1984.
- [15] S.N. Wagner. Aeroacoustics of wind turbines and helicopter rotors. *Seventh International Congress on Sound and Vibration*, July 2000.
- [16] N. Ng and R. Hillier. Numerical investigation of the transonic blade-vortex interaction. In *28<sup>th</sup> AIAA Fluid Dynamics Conference, 4<sup>th</sup> AIAA Shear Flow Control Conference, Snowmass Village, CO*. AIAA 97-1846, June-July 1997.
- [17] C. Tung and Y.H. Yu. Aerodynamic aspects of blade-vortex interaction (BVI). In *27<sup>th</sup> AIAA Fluid Dynamics Conference*. AIAA 96-2010, June 17-20 1996.
- [18] H.-M. Lent, G.E.A. Meier, K.J. Muller, F. Obermeier, U. Schievelbusch and O. Shurmann. Mechanisms of transonic blade-vortex interaction noise. *Journal of Aircraft*, Vol. 30, No. 1, pp. 88-93, Jan.-Feb., 1993.
- [19] K.S. Brentner B.A. Singer and D.P. Lockard. Simulation of acoustic scattering from a trailing-edge. *Journal of Sound and Vibration*, Vol. 230, No. 3, pp. 541-560, 2000.
- [20] J. Prieur and W.R. Splettstoesser. ERATO - an ONERA-DLR cooperative programme on aeroacoustic rotor optimisation. *25<sup>th</sup> European Rotorcraft Forum, Rome, Italy, September 14-16, 1999*.
- [21] A. Hassan, F.K. Straub and B.D. Charles. Effects of surface blowing/suction on the aerodynamics of helicopter rotor BVI - a numerical simulation. *Journal of the American Helicopter Society*, Vol. 42, No. 2, pp. 182-194, 1998.
- [22] B. Malovrh, F. Gandhi and J. Tauszig. Sensitivity of helicopter BVI-induced and vibration to variations in individual interaction-parameter. In *57<sup>th</sup> Annual Forum, Washington, DC*. American Helicopter Society, May 9-11 2001.
- [23] F.X. Caradonna, R.C. Strawn and J.O. Bridgeman. An experimental and computational study of rotor-vortex interactions. *Vertica*, Vol. 12, No. 4, pp. 315-327, 1988.
- [24] C. Tung, R. Kube, T.F. Brooks and G. Rahier. Prediction and measurement of blade-vortex interaction. *Journal of Aircraft*, Vol. 35, No. 2, pp. 260-266, March-April 1998.
- [25] B.G. van der Wall. The effect of HHC on the vortex convection in the wake of a helicopter rotor. *Aerospace Science and Technology*, Vol. 4, No. 5, pp. 321-336, 2000.
- [26] R. Kube, W.R. Splettstoesser, W. Wagner, U. Seelhorst, Y.H. Yu, C. Tung, P. Beaumier, J. Prieur, G. Rahier, P. Spiegel, A. Boutier, T.F. Brooks, C.L. Burley, D.D. Boyd, E. Mercker and K. Pengel. HHC aeroacoustic rotor test in the german-dutch wind tunnel: improving physical understanding and prediction code. *Aerospace Science and Technology*, Vol. 2, No. 3, pp. 177-190, 1998.

- [27] J.M. Gallman, K.J. Schultz, P. Spiegel and C.L. Burley. Effect of wake structure on blade-vortex interaction. Phenomena: acoustic prediction and validation. *Journal of Aircraft*, Vol. 35, No. 2, pp. 267-273, 1988.
- [28] D. Nellessen, G. Britten and J. Ballmann. Numerical simulation of individual blade control. In *22<sup>nd</sup> European Rotorcraft Forum*, paper No. 84, Brighton, UK. The Royal Aeronautical Society, September 1996.
- [29] W.R. Spletstoeser, B. Junker, K.-J. Schultz, W. Wagner, W. Weitemeyer, A. Protosaltis and D. Fertis. The HELINOISE Aeroacoustic Rotor Test in the DNW. Test documentation and representative results. Technical report, DLR-Mitt. 93-09, 1993.
- [30] C. Kitaplioglu, F.X. Caradonna and C.L. Burley. Parallel blade-vortex interactions: an experimental study and comparison with computations. *Journal of the American Helicopter Society*, Vol. 46, No. 3, pp. 272-281, July 1997.
- [31] J.C. Hardin and S.L. Lamkin. Concepts for reduction of blade/vortex interaction noise. *Journal of Aircraft*, Vol. 24, No. 2, pp. 120-125, 1986.
- [32] E.R. Booth Jr. and J.C. Yu. Two-dimensional blade-vortex flow visualization investigation. *AIAA Journal*, Vol. 24, No. 9, pp. 1468-1473, September 1986.
- [33] R. Mahalingam, O. Wong and N. Komerath. Experiments on the origins of tip-vortices. *AIAA paper 2000-0278*, 2000.
- [34] C. Kitaplioglu and F. Caradonna. Aerodynamics and acoustics of blade-vortex interaction using an independently generated vortex. *American Helicopter Society Aeromechanics Specialists Conference*, San Francisco, CA, January 1994.
- [35] A. Bagai and J.G. Leishman. Rotor free-wake modeling using a pseudo-implicit technique including comparisons with experimental data. *Journal of the American Helicopter Society*, Vol. 40, No. 3, pp. 29-41, 1995.
- [36] G. Rahier and Y. Delrieux. Blade-vortex interaction noise prediction using a rotor wake roll-up model. *Journal of Aircraft*, Vol. 34, No. 4, pp. 522-530, July-August 1997.
- [37] F. Caradonna, C. Kitaplioglu, M. McCluer, J. Baeder, J.G. Leishman, C. Berizin, J. Visintainer, J. Bridgeman, C. Burley, R. Espien, A. Lyrintzis, E. Koutsavdis, G. Rahier, Y. Delrieux, J. Rule and D. Bliss. Methods for the prediction of blade-vortex interaction. *Journal of American Helicopter Society*, Vol. 45, No. 4, pp. 303-317, 2000.
- [38] T.S. Beddoes. Unsteady aerodynamics application to helicopter noise and vibration sources. Technical report, Westland Helicopter Ltd, Yeovil, Somerset BA20 2YB, UK, 1990.
- [39] R.I. Lewis. *Vortex element methods for fluid dynamic analysis of engineering systems*, chapter 8. Cambridge University Press, 1991.
- [40] F. Caradonna, C. Kitaplioglu, M. McCluer, J. Baeder, J.G. Leishman, C. Berizin, J. Visintainer, J. Bridgeman, C. Burley, R. Epstein, A. Lyrintzis, E. Koutsavdis,

- G. Rahier, Y. Delrieux, J. Rule and D. Bliss. Methods of the prediction of blade-vortex interaction noise. *Journal of the American Helicopter Society*, Vol. 45, No. 4, pp. 303-317, October 2000.
- [41] A.S. Lyriutzis and E.K. Koutsavdis. Rotorcraft impulsive noise prediction using a rotating Kirchhoff formulation. *Journal of Aircraft*, Vol. 33, No. 6, pp. 1054-1061, Nov.-Dec. 1996.
- [42] T. Wang. *Unsteady aerodynamic modelling of horizontal axis wind turbine performance*. PhD thesis, University of Glasgow, Department of Aerospace Engineering, James South Building, Glasgow, November 1999.
- [43] J. Sidès, K. Pahlke and M. Costes. Numerical simulation of flows around helicopters at DLR and ONERA. *Aerospace Science and Technology*, Vol. 5, No. 1, pp. 35-53, 2001.
- [44] W.J. McCroskey and G.R. Srinivasan. Unsteady interactions of transonic airfoils with gusts and concentrated vortices. In *Advisory Group for Aerospace Research & Development, Neuilly sur Seine, France*. AGARD, 6-9 May 1985.
- [45] W.S. Oh, J.S. Kim and O.J. Kwon. An unstructured dynamic mesh procedure for 2-d unsteady viscous flow simulations. In *40<sup>th</sup> AIAA Aerospace Sciences Meeting & Exhibit, Reno, NV*. AIAA 2002-0121, January 2002.
- [46] W.S. Oh, J.S. Kim and O.J. Kwon. Numerical simulation of two-dimensional blade-vortex interactions using unstructured adaptive meshes. *AIAA Journal*, Vol. 40, No. 3, pp. 474-480, 2002.
- [47] Z.J. Wang and R.F. Chen. Optimized weighted essentially nonoscillatory schemes for linear waves with discontinuity. *Journal of Computational Physics*, Vol. 174, pp. 381-404, 2001.
- [48] D.S. Balsara and C.-W. Shu. Monotonicity preserving weighted essentially non-oscillatory schemes with increasingly high order of accuracy. *Journal of Computational Physics*, Vol. 160, pp. 405-452, 2000.
- [49] X. Deng and H. Zhang. Developing high-order weighted compact nonlinear schemes. *Journal of Computational Physics*, Vol. 165, pp. 22-44, 2000.
- [50] X. Deng and H. Maekawa. Compact high-order accurate nonlinear schemes. *Journal of Computational Physics*, Vol. 130, pp. 77-91, 1997.
- [51] J.A. Ekaterinaris. Implicit, high resolution, compact schemes for gas dynamics and aeroacoustics. *Journal of Computational Physics*, Vol. 156, pp. 272-299, 1999.
- [52] D.V. Gaitonde, J.S. Shang and J.L. Young. Practical aspects of higher-order numerical schemes for wave propagation phenomena. *International Journal For Numerical Methods in Engineering*, Vol. 45, pp. 1849-1869, 1999.
- [53] M.H. Kobayashi. On a class of padé finite volume methods. *Journal of Computational Physics*, Vol. 156, pp. 137-180, 1999.
- [54] S.K. Lele. Compact finite difference schemes with spectral-like resolution. *Journal of Computational Physics*, Vol. 103, No. 1, pp. 16-42, 1992.

- [55] J.M.C. Pereira, M.H. Kobayashi and J.C.F. Pereira. A fourth-order-accurate finite volume compact method for the incompressible Navier-Stokes solutions. *Journal of Computational Physics*, Vol. 167, pp. 217-243, 2001.
- [56] W.F. Spitz and G.F. Carey. Formulation and experiments with high-order compact schemes for nonuniform grids. *International Journal of Numerical Methods for Heat and Fluid Flow*, Vol. 8, No. 3, pp. 288-303, 1998.
- [57] H.C. Yee. Explicit and implicit multidimensional compact high-resolution shock-capturing methods: formulation. *Journal of Computational Physics*, Vol. 131, pp. 216-232, 1997.
- [58] S. Lee and D. Bershader. An experimental and computational study of 2-d parallel blade-vortex interaction. In *AIAA 19<sup>th</sup> Applied Aerodynamics Conference*. AIAA 91-3277, September 1991.
- [59] M.M. Rai. Navier-Stokes simulations of blade-vortex interaction using high-order accurate upwind schemes. In *AIAA 25<sup>th</sup> Aerospace Sciences Meeting, Reno, NV*. AIAA 87-0543, January 1987.
- [60] M.J. Lighthill. On sound generated aerodynamically I. General theory. In *Proceedings of the Royal Society of London*, Vol. A., No. 211, pp. 564-587, 1952.
- [61] J. Delfs and H. Heller. Aeroacoustics research in Europe-1996 highlights: a summary of last year's activities in the six ceas countries. *Journal of Sound and Vibration*, Vol. 204, No. 4, pp. 609-622, 1997.
- [62] F. Farassat and G.P. Succi. The prediction of helicopter rotor discrete frequency noise. *Vertica*, Vol. 7, No. 4, pp. 309-320, 1983.
- [63] R. Renzoni, A. D'Alascio, N. Kroll, D. Peshkin, M. Hounjet, J.-C. Boniface, L. Vigevano, L. Morino, C.B. Allen, K.J. Badcock, L. Mottura, M. Scholl and E. Kokkalis. A common european Euler code for the analysis of the helicopter rotor flowfield. *Progress in Aerospace Science*, Vol. 36, pp. 437-485, 2000.
- [64] M.H.L. Hounjet (Ed.), A. Pagano, A. D'Alascio, L. Gasparini, L. Vigevano, C.B. Allen and S.P. Fiddes. Precoding of a grid generator for a rotorcraft simulation method. Technical report, NLR-TR-98049, February 1998.
- [65] M.H.L. Hounjet. User manual of a grid generator for rotorcraft simulation methods - GEROS version 1.0. Technical report, NLR-TR-99490, 1999.
- [66] K.J. Badcock and B.E. Richards. Implicit time-stepping methods for the Navier-Stokes equations. *AIAA Journal*, Vol. 34, No. 3, pp. 555-559, 1996.
- [67] K.J. Badcock, B.E. Richards and M. Woodgate. Factored-unfactored method for 3d transonic flows. *Computational Fluid Dynamics 96*, pp. 605-610. J.-A. Désidéri et al. John Wiley & Sons (Editors), 1996.
- [68] A. Jameson, W. Schmidt and E. Turkel. Numerical solutions of the Euler equations by finite volume method using Runge-Kutta time stepping scheme. *AIAA 81-1259*, 1981.
- [69] P.L. Roe. Approximate Rieman solver, parameters vectors and difference schemes. *Journal of Computational Physics*, Vol. 43, pp. 357-372, 1981.

- [70] H.C. Yee and A. Harten. Implicit TVD schemes for hyperbolic conservation laws in curvilinear coordinates. *AIAA Journal*, Vol. 25, pp. 266-247, 1987.
- [71] F. Cantariti, L. Dubuc, B. Gribben, M. Woodgate, K.J. Badcock and B.E. Richards. Approximate Jacobians for the solution of the Euler and Navier-Stokes equations. *Aero report, University of Glasgow, Aerospace Eng. Dept.*, 1997.
- [72] A. Jameson. Time dependent calculations using multigrid with applications to unsteady flows past airfoils and wings. *Proceedings of the AIAA. 91-1596, Honolulu, HI*, June 1991.
- [73] J.E. Bardina, P.G. Huang and T.J. Coakley. Turbulence modeling validation, testing, and development. Technical report, NASA Technical Memorandum 110446, April 1997.
- [74] E.G. Tulapurkara. Turbulence models for the computation of flow past airplanes. *Progress in Aerospace Sciences*, Vol. 33, pp. 71-165, 1997.
- [75] G.N. Barakos. *Study of unsteady aerodynamics phenomena using advanced turbulence closure*. PhD thesis, University of Manchester Institute of Science and Technology, Department of Mechanical Engineering, Manchester, April 1999.
- [76] P.R. Spalart and S.R. Allmaras. A one-equation turbulence model for aerodynamic flows. *La Recherche Aéronautique*, Vol. 1, pp. 5-21, 1994.
- [77] D.C. Wilcox. Turbulence modelling for CFD. *DCW Industries, Inc., La Cañada, California*, 1993.
- [78] F.R. Menter. Zonal two-equation  $k-\omega$  turbulence models for aerodynamic flows. In *AIAA 24<sup>th</sup> Fluid Dynamics Conference, Orlando Florida*. AIAA 93-2906, July 6-9 1993.
- [79] F.R. Menter. Two-equation eddy-viscosity turbulence models for engineering applications. *AIAA Journal*, Vol. 32, No. 8, pp. 1598-1605, 1994.
- [80] W.P. Jones and B.E. Launder. The prediction of laminarization with a two-equation model of turbulence. *International Journal of Heat and Mass transfer*, Vol. 15, pp. 301-314, 1972.
- [81] A.M. Mitchell, J.C. Kok, H.S. Dol and A. Elsenaar. A leading-edge vortex flow computations and comparison with DNW-HST wind tunnel data. *RTO/AVT Vortex Flow Symposium, Loen, Norway*, 2001.
- [82] F.J. Brandsma, J.C. Kok, H.S. Dol and A. Elsenaar. Leading-edge vortex flow computation and comparison with DNW-HST wind tunnel data. Technical report, RTO/AVT Vortex Flow Symposium, Loen, Norway, 2001.
- [83] M. Allan. *A CFD Investigation of wind tunnel interference on Delta wing aerodynamics*. PhD thesis, University of Glasgow, Department of Aerospace Engineering, James South Building, Glasgow, October 2002.
- [84] M.S. Howe. Sound generated by fluid-structure interactions. *Computers and Structures*, Vol. 65, No. 3, pp. 433-446, 1997.

- [85] J.E. Ffowcs Williams. Aeroacoustics. *Journal of Sound and Vibration*, Vol. 190, No. 3, pp. 387-398, 1996.
- [86] M.V. Lowson. Basic mechanisms of noise generation by helicopters, v/stol aircraft and ground effect machines. *Journal of Sound and Vibration*, Vol. 3, No. 3, pp. 454-466, 1966.
- [87] F. Farassat. Generalized functions and Kirchhoff formulas. In *2<sup>nd</sup> AIAA/CEAS Aeroacoustics Conference, State College, PA*. AIAA 96-1705, May 1996.
- [88] F. Farassat. Theory of noise generation from moving bodies with an application to helicopter rotors. Technical report, NASA TR R-451, December 1975.
- [89] L.N. Long, F. Souliez and A. Sharma. Aerodynamic noise prediction using parallel methods on unstructured grids. In *7<sup>th</sup> AIAA/CEAS Aeroacoustics Conference, Maastricht, The Netherlands*. AIAA 2001-2196, May 2001.
- [90] J.E. Ffowcs Williams and D.L. Hawkings. Sound generation by turbulence and surfaces in arbitrary motion. *Philosophical Transactions of the Royal Society of London*, Vol. A, No. 264, pp. 321-342, 1969.
- [91] A.S. Lyrantzis and A.R. George. Farfield noise of transonic blade-vortex interaction. *Journal of American Helicopter Society*, Vol. 34, No. 3, pp. 30-39, July 1989.
- [92] J. Prieur and G. Rahier. Aeroacoustic integral methods, formulation and efficient numerical implementation. *Aerospace Science and Technology*, Vol. 5, No. 7, pp. 457-468, 2002.
- [93] J. Prieur and G. Rahier. Aeroacoustic integral methods, formulation and efficient numerical implementation (vol 5, pg 457, 2001). *Aerospace Science and Technology*, Vol. 6, No. 5, pp. 323-323, 2002.
- [94] R.K. Singh and J.D. Bacder. Transonic effects on acoustics of blade-vortex interaction. *AIAA 2000-1921*, June 2001.
- [95] J.M. Gallman. Parametric computational study of isolated blade-vortex interaction noise. *AIAA Journal*, Vol. 32, No. 2, pp. 232-238, February 1994.
- [96] K.S. Brentner, C.L. Burley and M.A. Marcolini. Sensitivity of acoustic prediction to variation of input parameters. *Journal of the American Helicopter Society*, Vol. 39, No. 3, pp. 43-52, July 1994.
- [97] B.W.-C Sim, F.H. Schmitz and T. Aoyama. Near/far-field radiation of advancing side helicopter blade vortex interaction (BVI) noise. *American Helicopter Society (AHS) 56<sup>th</sup> Annual National Forum, Virginia Beach, Virginia*, May 2-4 2000.
- [98] J. Steinhoff and G.K. Raviprakash. Navier-Stokes computation of blade-vortex interaction using vorticity confinement. In *33<sup>rd</sup> Aerospace Sciences Meeting and Exhibit, Reno, NV*. AIAA 95-0161, January 1995.
- [99] J. Steinhoff, Y. Wenren, L. Wang, M. Fan, M. Xiao and C. Braun. The computation of flow over helicopter rotors and complex bodies using vorticity confinement. Technical report, TN 37388, University of Space Institute, Tullahoma, USA, pp. 699-707, 2001.

- [100] J. Steinhoff and D. Underhill. Modification of the Euler equations for vorticity confinement: application to the computation of interacting vortex rings. *Journal of Physics Fluid*, Vol. 6, No. 8, pp. 2738-2744, 1994.
- [101] R. Löhner and C. Yang. Tracking vortices over large distances using vorticity confinement. *ECCOMAS CFD 2001, Swansea, Wales, September, 2001*.
- [102] M. Murayama, K. Nakahashi and S. Obayashi. Numerical simulation of vortical flows using vorticity confinement coupled with unstructured grid. In *39<sup>th</sup> AIAA Aerospace Sciences Meeting & Exhibit, Reno, NV. AIAA 2001-0606*, January 2001.
- [103] Y. Weren, M. Fan, W. Dietz, G. Hu, C. Braun, J. Steinhoff and B. Grossman. Efficient Eulerian computation of realistic rotorcraft flows using vorticity confinement. In *39<sup>th</sup> AIAA Aerospace Sciences Meeting and Exhibit, Reno, NV. AIAA 2001-0996*, January 2001.
- [104] M. Biava and L. Vigevano. Assessment of the vorticity confinement technique applied to rotorcraft flows. In *21<sup>st</sup> Applied Aerodynamics Conference, Orlando, Florida. AIAA 2003-352*, 23-26 June 2003.
- [105] W. Dietz, M. Fan, J. Steinhoff and Y. Wenren. Application of vorticity confinement to the prediction of the flow over complex bodies. In *AIAA CFD Conference, Anaheim, CA. AIAA 2001-2642*, June 2001.
- [106] G. Hu and B. Grossman. The computation of massively separated flows using compressible vorticity confinement methods. *AIAA paper 2002-0136*, January 2002.
- [107] R. Fedkiw, J. Stam and H.W. Jensen. Visual simulation of smoke. In *Siggraph 2001 Conference Proceedings, Computer Graphics*, pp. 15-22. Assoc Computing Machinery, New York, 2001.
- [108] G. Hu and B. Grossman. Numerical method for vorticity confinement in compressible flow. *AIAA Journal*, Vol. 40, No. 10, pp. 1945-1953, October 2002.
- [109] G. Hu. *The development and applications of a numerical method for Compressible Vorticity Confinement in vortex-dominant flows*. PhD thesis, Virginia Polytechnic Institute and State University, Blacksburg, Virginia, June 2001.
- [110] M. Costes and G. Kowani. An automatic anti-diffusion method for vortical flows based on vorticity confinement. *Aerospace Science and Technology*, Vol. 7, pp. 11-21, 2003.
- [111] M. Fan, Y. Weren, W. Dietz, M. Xiao and J. Steinhoff. Computing blunt body flows on coarse grids using vorticity confinement. *Journal of Fluid Engineering*, Vol. 124, pp. 876-885, December 2002.
- [112] Y. Wenren, M. Fan, L. Wang, M. Xiao and J. Steinhoff. Application of vorticity confinement to the prediction of the flow over complex bodies. *AIAA Journal*, Vol. 41, No. 5, pp. 809-815, May 2003.
- [113] A. Gangwar, B. Lukovic and P.D. Orkwis. Modeling unsteadiness in steady cavity simulations. Part I: parametric solutions. In *39<sup>th</sup> Aerospace Sciences Meeting and Exhibit, Reno, NV. AIAA 2001-0153*, 2001.

- [114] P. Eremenko, C.A. Mouton and H.G. Hornung. The pressure drag of blunted cones in supersonic flow. In *41<sup>st</sup> Aerospace Sciences Meeting and Exhibit, Reno, NV*. AIAA, January 2003.
- [115] K.W. McAlister and R.K. Takahashi. NACA-0015 wing pressure and trailing vortex measurements. Technical report, NASA TP 3151, November 1991.
- [116] J. Bridgeman. In *BVI workshop, 52<sup>nd</sup> American Helicopter Society Annual Forum, Washington, DC*, June 1996.
- [117] M. Damodaran and D. A. Caughey. Finite-volume calculation of inviscid transonic airfoil-vortex interaction. *AIAA Journal*, Vol. 26, No. 11, pp. 1346-1353, November 1988.
- [118] J.L. Ellzey and M.R. Henneke. The shock-vortex interaction: the origin of the acoustic wave. *Fluid Dynamics Research*, Vol. 21, No. 3, pp. 171-184, 1997.
- [119] J.L. Ellzey and M.R. Henneke. The acoustic wave from a shock-vortex interaction: comparison between theory and computation. *Fluid Dynamics Research*, Vol. 27, No. 1, pp. 53-64, 2000.
- [120] K.G. Powell, E.M. Murman, E.S. Perez and J.R. Baron. Total pressure loss in vortical solutions of the conical Euler equations. *AIAA Journal*, Vol. 25, No. 3, pp. 360-368, 1986.
- [121] E.H. Hirschel. Vortex flows: some general properties, and modelling, configurational and manipulation aspects. AIAA 96-2514, June 1996.
- [122] S. Körber and J. Ballmann. Mechanisms and acoustics of blade-vortex-interactions. *Z. Flugwiss. Weltraumforsch.* Vol. 19, pp. 397-406, Springer-Verlag, 1995.
- [123] J.A. Rule and D.B. Bliss. Prediction of viscous trailing vortex structure from basic loading parameters. *AIAA Journal*, Vol. 36, No. 2, February 1998.
- [124] G.H. Vatistas, V. Kozel and W.C. Mih. A simpler model for concentrated vortices. *Experiments in Fluids*, Vol. 11, pp. 73-76, 1991.
- [125] G.R. Srinivasan, W.J. McCroskey and J.D. Beader. Aerodynamics of two-dimensional blade-vortex interaction. *AIAA Journal*, Vol. 24, No. 10, pp. 1569-1576, October 1986.
- [126] J.C. Hardin and S.L. Lamkin. Aeroacoustic interaction of a distributed vortex with a lifting Joukowski airfoil. In *AIAA/NASA 9<sup>th</sup> Aeroacoustics Conference, Williamsburg, Virginia*. AIAA 84-2287, October 1984.
- [127] M. Mandella and D. Bershader. Quantitative study of the compressible vortex: generation, structure and interaction with airfoils, Reno, NV. In *AIAA 25<sup>th</sup> Aerospace Sciences Meeting*. AIAA 87-0328, January 1987.
- [128] M.C. Wilder and D.P. Telionis. Parallel blade-vortex interaction. *Journal of Fluid and Structure*, Vol. 12, pp. 801-833, 1998.

- [129] P.R. Spalart and S.R. Allmaras. A one-equation turbulence model for aerodynamic flows. In *AIAA, Aerospace Sciences Meeting, 30<sup>th</sup>, Reno, NV*. AIAA 92-0439, January 1992.
- [130] W.J. McCroskey and P.M. Goorjian. Interactions of airfoils with gusts and concentrated vortices in unsteady transonic flow. *AIAA paper 83-1691*, July 1983.
- [131] Introduction to transonic aerodynamics of aerofoils and wings. Technical report, Engineering Sciences Data Unit, ESDU-90008, 1990.
- [132] C.A. Masson, R.B. Green, R.A.McD. Galbraith and F.N. Coton. Experimental investigation of a loaded rotor blade's interaction with a single vortex. *The Aeronautical Journal of the Royal Aeronautical Society*, December 1998.
- [133] F.X. Caradonna, J.L. Lautenschlager and M.J. Silva. An experimental study of rotor-vortex interactions. *AIAA paper 88-0045*, January 1988.
- [134] A.R. George and S.-B. Chang. Flow field and acoustics of two-dimensional transonic blade-vortex interactions. *AIAA paper, 84-2309*, 1984.
- [135] A.S. Lyrintzis and Y. Xue. Noise mechanisms of transonic blade-vortex interaction. In *AHS 46<sup>th</sup> Annual Forum, Washington, DC*. American Helicopter Society, May 1990.
- [136] W.S. Kaminski and A.P. Szumowski. Acoustic effects of parallel vortex-airfoil interaction. *Journal of Sound and Vibration, Vol. 183, No. 2, pp. 209-220*, 1995.
- [137] M.S. Howe. Trailing-edge noise at low mach numbers. *Journal of Sound and Vibration, Vol. 225, No. 2, pp. 211-238*, 1999.
- [138] J. Ballmann and C.S. Kocaaydin. Some aerodynamic mechanisms of impulsive noise during blade-vortex interaction. In *16<sup>th</sup> European Rotorcraft Forum, paper No. II 10, Glasgow, UK*, September 1990.
- [139] R.W. Prouty. *Helicopter aerodynamics*. Rotor and Wing International, 1985.
- [140] J.S. Preisser, T.F. Brooks and R.M. Martin. Recent studies of rotorcraft blade-vortex interaction. *Journal of Aircraft, Vol. 31, No. 5, pp. 1009-1015*, Sept.-Oct. 1994.